A Study of The Relationship Between Monocotyledonous Plant Anatomy and Water

Dylan Hugo Edward Andrew Jones

Thesis submitted to the University of Nottingham for the degree of Doctor of Philosophy

The University of Nottingham

School of Biosciences

Sutton Bonington Campus

Leicestershire,

LE12 5RD

March 2023

Acknowledgements

I would like to first express my tremendous gratitude to my brilliant quartet of supervisors, Darren Wells, Jonathan Atkinson, Tony Bishopp, and Ute Voß, for their valued teaching, guidance, and support.

I would also like to effusively thank the many collaborators and colleagues that made the work on this thesis possible; the teams at IRD and ISRA, Malcolm Bennett, Eze Benson, Riccardo Fusi, and Brian Atkinson to name but a few. With special thanks to Alex Ware for his counsel, insight, and teamwork, in all things duckweed and beyond. I am deeply grateful to the many past and present lab members that have provided help and encouragement over the past years, and who made this such an enjoyable time.

Finally, thanks to my parents, family, and friends, for their continued support and inspiration.

Abstract

Plant anatomy is known to significantly affect many aspects of organ function, as well as the metabolic cost of maintenance and production of plant tissues. Of particular importance is the role of anatomy in plants ability to uptake, transport and utilize water efficiently. Despite this, it remains an unexploited target in crop improvement. The anatomy of duckweeds (aquatic plants with an evolutionary trajectory towards rootlessness) was investigated. Significant root anatomical reduction (particularly in the vasculature) was accompanied by a significant reduction in the functions of the root tested, concluding that duckweed roots have lost their ancestral function and can be considered vestigial. In larger plants it can be more technically challenging to investigate anatomical traits, particularly in a high throughput manner. This requires the development of new methods. Using the novel method of Laser Ablation Tomography (LAT), anatomical phenotyping pipelines were developed and tested on brachypodium, maize, gamagrass, and pearl millet. This included the production of deep-learned fully automatic root image analysis software. These methods were then employed in an investigation of water stress tolerance in pearl millet lines from an association panel. This showed that there was significant root and leaf anatomical variation in this collection, and that anatomical traits were affected by water stress. Further analysis showed that several root anatomical traits were highly correlated with agronomic traits, and genomic analysis was able to identify several single nucleotide polymorphisms associated with these anatomical traits.

Table of Contents

1 Chapter 1: Introduction and Literature Review 29

1.1 Introduction 30

1.1.1 Plant anatomy 30

1.1.2 Water and roots 31

1.2 Plant root traits 32

1.2.1 Root architecture 32

1.2.2 Root anatomy 33

1.2.3 Significance and control of root anatomy 38

1.3 Plant anatomical phenotyping 40

1.3.1 Techniques for anatomical phenotyping 40

1.3.2 Previous studies of root anatomy in monocots 44

1.3.3 Monocot leaf anatomy 47

1.3.4 Drought and Anatomy 47

1.4 Studied species I: Pearl Millet Exemplar species for water stress studies 49

1.4.1 Biology 49

1.4.2 Pearl millet as a crop 51

1.5 Studied Species II: Duckweed 52

1.5.1 Description 53

1.5.2 Vestigiality 54
1.5.3 Anatomy 57
1.6 Aims and objectives 58
2 Chapter Two: Analysis of Duckweed Root Anatomy and Vestigialization 59
2.1 Introduction 60
2.2 Aims 61
2.2.1 Phenotyping methods development 61
2.2.2 Root vestigialization 61
2.3 Materials and methods 63
2.3.1 Duckweed growth and culture 63
2.3.2 µCT anatomical protocol development 65
2.3.3 Histological anatomical protocol development 77
2.3.4 Whole population area imaging 79
2.3.5 Clearing 80
2.3.6 Vestigiality analysis methods 80
2.4 Results 86
2.4.1 µCT protocol development 87
2.4.2 Root vestigialization 99
2.5 Discussion 116
2.5.1 Phenotyping methods development 117
2.5.2 Root vestigialization 122
2.5.3 Future work 124

3 Chapter Three: Novel Approaches to Anatomical Phenotyping 126

3.1 Introduction 127

3.2 Aims 127

3.2.1 Anatomical imaging 128

3.2.2 Anatomy image analysis 128

3.2.3 Use cases 129

3.3 Biological material 130

3.3.1 Pearl millet (Senegal) 130

3.3.2 Pearl millet (Nottingham) 131

3.3.3 Maize and gamagrass 134

3.3.4 Brachypodium 135

3.4 Sample preparation 136

3.4.1 Wet sectioning 136

3.4.2 Critical point drying 138

3.4.3 Optimal sample preparation methods 141

3.5 Laser ablation tomography 145

3.5.1 LAT set up 145

3.5.2 Pearl millet roots 150

3.5.3 Pearl Millet leaves 153

3.5.4 Gamagrass and maize roots 157

3.5.5 Brachypodium 157

3.6 Image analysis 158

3.6.1 Pearl millet root quality assessment 158

3.6.2 Pearl millet leaf image processing and measurement 160

3.6.3 Gamagrass and maize root image analysis 162

3.6.4 *Brachypodium* image analysis 162

3.7 Development of root anatomical analysis software 163

3.7.1 Training set generation 163

3.7.2 Model development 165

3.7.3 Software deployment 168

3.8 Results 170

3.8.1 Pearl millet 170

3.8.2 Gamagrass and Maize 173

3.8.3 Brachypodium 185

3.9 Discussion 189

3.9.1 Evaluation of developed methods 189

3.9.2 Pearl millet whorl selection 192

3.9.3 Effect of combination of microbiome and water stress treatments on maize and gamagrass root anatomy 193

3.9.4 Conclusions 196

4 Chapter Four: The Anatomical Basis of Drought Tolerance in Pearl Millet 198

4.1 Introduction 199

4.2 Aims 200

4.3 Materials and Methods 201

4.3.1 Germplasm 201
4.3.2 Plant Growth 201
4.3.3 Plant Anatomy Sampling 204
4.3.4 Anatomy Sample Preparation, Imaging, and Measurement 206
4.3.5 Root Architecture 207
4.3.6 Leaf Ionome 209
4.3.7 Soil ionomic profiling 209
4.3.8 Physiological Measurements 210
4.3.9 Genotyping 211
4.3.10 Statistical analysis 211
4.4 Results 212
4.4.1 Year 0 213
4.4.2 Year 2 219
4.4.3 Year 3 233
4.5 Discussion 241
4.5.1 Discussion of results from pilot year 241
4.5.2 Discussion of results from year two 242
4.5.3 Discussion of results from year three 245
5 Chapter Five: Discussion 247
5.1 Introduction 248
5.2 Analysis of duckweed root anatomy to determine function and root vestigialization 248

5.3 Novel approaches to anatomical phenotyping 251

5.3.1 LAT methods 251

5.3.2 AI image analysis 253

5.3.3 Maize and gamagrass and the microbiome on the LAT and in root anatomy 254

5.3.4 *Brachypodium* root anatomy 255

5.4 The anatomical basis of drought tolerance in pearl millet 255

5.4.1 Discussion of field trials 255

5.4.2 Anatomical traits in pearl millet 257

5.4.3 Future work 259

5.5 Conclusions 262

Appendix 1 : LAT Imaging resolutions and Image Sizes 287

Appendix 2: Excerpts from gamagrass and maize grant 287

Appendix 3: Map showing soil sampling sites 289

Appendix 4: Macros for leaf image processing 290

Appendix 5: List of pearl millet lines in PGiMAP and used during thesis 292

Appendix 6: R Script used for spatial field correction and to generate BLUPs 303

Appendix 7: R Script used for GWAS 309

Appendix 8: Agronomic, physiological, and architectural measurements used in field trials 311

Appendix 9: Leaf anatomical trait measurements 311

Appendix 10: Leaf anatomical trait block effect visualization 312

List of Figures

Figure 1-1. Illustration of Cellular Organization of Maize Primary Root. (A) Longitudinal section showing functionally distinct zones, (B) Transverse section of Differentiation Zone, (C) Magnified subsection of stele and endodermis; DZ, differentiation zone; EZ, elongation zone; MZ, meristem zone. (Adapted from Yu et al., (2016)) 33

Figure 1-2. Illustration showing the relationship between tracheary element (TE) diameter and relative water conductance. (Redrawn from Mauseth (1988) and Crang et al., (2018)) 35

Figure 1-3. Collection of illustrations from early publications on plant anatomy. (A) Horseradish root from "The anatomy of plants" by Nehemiah Grew (1682), (B) Chestnut tree stem from "*Anatome plantarum"* by Marcello Malpighi,(1675). ... 40

Figure 1-4. Photomicrograph of a section of a plant stem from a solar microscope. Image of possibly either a horsetail or elm stem section, captured on salted paper using a solar microscope by William Henry Fox Talbot in 1838 (The William Henry Fox Talbot Catalogue Raisonné). 41

Figure 1-5. Cladogram showing phylogenetic relationships and photosynthetic subtypes of millets and other Poaceae species. Black, gray and red taxa names represent millets, major crops and model grasses, respectively. Millet lineages are also highlighted in yellow. Green, red, purple, and black branch colors represent three subtypes of C4 (NADP-malic enzyme, NAD-malic enzyme and phosphoenolpyruvate phosphatase) and C3 photosynthesis respectively. Dashed colors represents mixed subtypes of C4. Reproduced from Huang et al., (2016), using phylogeny from Grass Phylogeny Working Group II (2012). 48

Figure 1-6. Map of North Africa. Map of North Africa showing the Sahara desert (pale green) the Sahel region (dark green), and Senegal (Senegalese flag coloured),

with a dashed line denoting the are of the country considered to be in the Sahel. 50

Figure 1-7. Morphological variation between duckweed subfamilies Lemnoideae and Wolffoideae. Representative species of each genus within Lemnoideae: *Spirodela*, *Landoltia*, *Lemna* (left to right). Plants were cleared and stained with Fluorescent Brightener 28 (calcofluor) following the protocol described by (Kurihara et al., 2015) and imaged on a Leica TCS SP5 confocal microscope. Scale bars: A, B =1000 µm, C, D= 500 µm, E=100 µm. 52

Figure 1-8. Representative phylogeny of the duckweed genera and *Pistia*. Highlighting the progressive loss of roots of roots and loss of individual root traits as genera diverge (indicated by + and -; arrows next to cortical cell layers indicate the progressive reduction in layer number as the genera diverge) (after Tippery and Les, 2020). Representative images (not to scale) of species from each genera are shown for illustrative purposes. 54

Figure 2-1. Preparation and embedding of plant material for µCT scanning. (A–G) Rooted plant preparation and embedding; (A, B) Pre-preparation of plant material; (A) Plant transferred by petrolatum coated inoculating loop to blotting paper. (B) Plant rinsed in mineral oil then transferred to blotting. (C–G) Rooted plant embedding (C) Syringe barrel cap cut and removed, and barrel two thirds filled with molten petrolatum. (D) Plant transferred to syringe with loop and allowed to partially solidify. (E) Additional molten petrolatum added to barrel, covering plant. (F) Syringe transferred to ice bath. (G) Syringe plunged, and petrolatum core trimmed to region of interest (ROI). (H–O) Rootless plant embedding and preparation; (H, I) Pre-preparation of plant material; (H) Plants removed from media and transferred to blotting paper, (I) Plants rinsed in mineral oil and decanted to blotting paper. (J–O) Rootless plant embedding (J) Syringe barrel cap

cut and removed and cut in half along barrel length, two thirds filled with molten petrolatum and allowed to cool. (K) Small plants pressed gently into petrolatum with inoculating loop. (L) Plunger replaced and barrel resealed with microporous tape. (M) Remainder of syringe filled with molten petrolatum. (N) Petrolatum allowed to solidify, cooling in ice bath. (O) Syringe plunged and petrolatum core trimmed to ROI. 67

Figure 2-2 Duckweed embedded in petrolatum core mounted in µCT scanner. (A) X-ray detector panel Hamamatsu CMOS Flat Panel (C7942SK-05). (B) Petrolatum core, (C) Rotation stage, (D) X-ray tube (Source). 70

Figure 2-3. Two-dimensional (2D) slice Image segmentation procedure. Carried out in ImageJ, step instructions using ImageJ process commands. The starting point (A) is an 8-bit image, or image stack (referred to interchangeably as image). (1) Gaussian Blur 2.5 pixel sigma radius (2) Threshold 0-155, Invert (3) Fill Holes, Open (4) Analyze Particles (Pixel size:1000-∞, Circularity 0–1, Show Mask) (5) Invert, Dilate, Close, Fill Holes, Erode (6) [((B)Add 1)-F] (7) Threshold 225–255; Analyze Particles 30-Infinity, Invert (8) Threshold 126–224, Invert (9) Threshold 1–125, Invert (10) A–H (11) A–I (12) (A: Invert)-J (13) Merge Channels: C4 (gray) = 'K' (14) Merge Channels: C2(green) = 'L'; (15) Merge Channels:C3(blue) = 'M'. All values given are suggested for described scan settings. 73

Figure 2-4. Preparation of samples in petrolatum provides the most stable method for CT imaging. (A) Representative images of *Spirodela polyrhiza* condition under different preparation methods over time. (B) Percentage change in frond area after 1 and 6 h under different preparation methods, * significant difference in mean area from start point $p < 0.05$, n.s. = No Significance in mean area change from start, n = 32 ANOVA with a Tukeys multiple comparison test. 87

Figure 2-5. Representative images of duckweed genera showing render capabilities and segmentation of micrographs. (A,B) *Spirodela* intermedia, (A) Render clipped

to midpoint of frond, (B) Micrograph and segmentation of micrograph of midpoint slice (White: Starch rich tissue Green: Tissue Blue: Gas), (C) Render of *Landoltia* punctata, (D–F) *Lemna* minor, (D) Render clipped to back half of frond, daughter frond (df), granddaughter frond (gd), (E) Micrograph and segmentation of micrograph, (F) Render clipped to partially remove adaxial frond surface revealing stipe (s), nerves (n), and daughter frond pocket (p), mauve dashed line shows clipping plane of (D,E), (G,H) *Wolffiella* lingulata, (G) Render clipped twice, revealing meristem and internal anatomy of daughter frond, (H) Render clipped to midpoint showing longitudinal section of frond, (I,J) *Wolffia* arrhiza, (I) render of whole plant, (J) Render clipped twice to reveal internal gas spaces. Scale bars (A,B,C): 1 mm, (D,E): 0.75 mm, (F): 0.5 mm, (G–J): 0.3 mm. 88

Figure 2-6. Three-dimensional (3D) particle analysis of *Spirodela intermedia* shows number and volume of each gas space within frond. (A) Render showing internal air spaces of *Spirodela intermedia* frond colored by individual gas space. (B) Render showing internal air spaces of *Spirodela intermedia* frond, colored by volume, clipped to reveal variation in volume between inner and outer gas spaces within the frond (green). (C) Frequency histogram showing distribution in volume of gas spaces within *Spirodela intermedia* frond. Scale bars: 1 mm. Graduated color scale from 4.25×10^{-7} mm^3 to 0.0285 mm^3. 92

Figure 2-7. Localized thickness of each gas space within *Spirodela intermedia* frond. Frond tissue in green, gas spaces from Blue–White in graduated scale from 0.012 mm to 0.465 mm in thickness at each point within each gas space in the frond. Scale bar: 1 mm. 94

Figure 2-8. MicroCT imaging confirms that the extracellular spaces seen in root sections are filled with gas. (A) µCT micrograph of *Spirodela* intermedia root embedded in petrolatum, with air bubble inclusions (ab), 16bit greyscale

micrograph representing xray density from white (high density, to black (low density). (B) Confocal image of a *Spirodela* intermedia root section, 150 µm thick, stained with calcofluor (green) (C) Segmentation of (A) using the method described in Figure 3 Green = tissue, Blue= intra plant gas region, (D) Recolored root section (B) showing the classification of extracellular spaces based on segmentation in (B) green= calcofluor stained cell walls, b= aerenchyma, Scale Bars: (A,C) = 200 µm (C,D) = 50 µm. 95

Figure 2-9. Buoyant Spirodela polyrhiza turions contain a higher percentage of gaseous extracellular space than those that are submerged. (A–C) Mid slice of three µCT micrographs of stacks of three turions, collected under differing conditions. (D–F) Segmentation of images from (A) following steps in Figure 3. Green: Tissue, Blue: Gas, White: Starch (A,D) Turions floating at surface, (B,E) Turions sunk to bottom of flask, (C,F) cold treated turions showing petrolatum (p), Starch (s), Tissue (t), and gas spaces (gs). (G) Expanded micrograph of Cold treated turion. (H) Expanded segmentation of micrograph of Cold treated turion showing petrolatum (p), Starch (s), White, Tissue (t), green, and gas spaces (gs), blue, recolored as determined by segmentation. (I) Composition values of each turion set under each treatment as determined by processing and analysis pipeline. Dots represent data points, horizontal line the mean value. Scale Bars (A–F): 1 mm, (G,H): 0.1 mm. 97

Figure 2-10. Representative root sections from 20 duckweed lines encompassing 13 species, and *Pistia* stratiodes main and lateral roots. Images were obtained via fresh tissue sectioning and confocal imaging from a representative portion of the mid point of the length of the root. The *Pistia* stratiodes and Landoltia punctata roots are counter-stained with fuschin to highlight lignified tissue, Scale bar for whole roots= 100 µM, Scale bar for magnified stele =10um 99

Figure 2-11. Comparison of root anatomical traits across almost all extant duckweeds reveals a highly reduced anatomy. (A) Rose diagram displaying the

width of each cell layer (µm) for roots of 20 duckweed lines encompassing 13 species, denoted at the outside of the circle. B) Rose diagram displaying the number of cells in cell layer for roots of the aforementioned lines, denoted at the outside of the circle, with P. stratiotes main roots (C) in a separate bar chart for ease of resolution. Background colour underlying the species labels represents genera; yellow represents *Pistia*, purple *Spirodela*, pink *Landoltia*, and green *Lemna*. E) Colour coded key to the different cell layers displayed on the rose diagrams. CCL stands for cortical cell layer. n = 10 root sections derived from different plants, except for *Pistia* stratiotes (main) and L. trisulca where n = 5 root sections derived from individual plants. 103

Figure 2-12. Basic fuchsin staining of duckweed vasculature highlights lignification in the endodermis and central xylem. Entire root section and accompanying close up of the vasculature of Spirodela polyrhiza 9509 with cell wall staining (calcofluor white; green) and lignin staining (0.01% Basic Fuchsin; magenta). Scale bar = 50 µM for entire roots; 10 µM for vasculature close-up. 104

Figure 2-13. Principal coordinates analysis of duckweed anatomical traits highlights interspecies differences and a gradient of reducing root anatomical complexity. A) PCoA based on 21 components, with 210 rows, derived from an anatomical analysis of fresh root sections from 20 duckweed lines, encompassing 13 species, and main and lateral roots of *Pistia* stratiotes. Clusters have been manually highlighted and numbered for ease of further discussion. The percentage of variance explained by each PC is indicated on the relevant axis. 107

Figure 2-14. PCA details and cortical cell layer number analysis. A) Loadings plot of PCA in 2-13 B) Summary of the 22 variables used to generate the PCA. *n* = 10 root sections derived from different plants, except for *Pistia stratiotes* (main) and *L.*

trisulca where *n* = 5 root sections derived from individual plants. C) Mean number of cortical cell layers for representative species of each genus. 109

Figure 2-15. Growth and nutrient uptake of six duckweed species is not impacted by continual root removal, unlike the aroid *Pistia* stratiotes. Plants were subjected to continuous root removal and growth and elemental ionomic composition of fronds was compared to untreated controls. A) Growth measured as area of fronds (or aerial tissues for *Pistia*), derived from daily imaging from beneath, and plotted as a percentage increase relative to the initial (day 1) area value. Species are indicated on the graphs. n = 10 flasks, each initially seeded with 3 colonies for duckweed and 1 plant for *Pistia*. Asterisks show statistically significant (P< 0.05) differences as assessed by two-way repeated measures ANOVA followed by Šidák's multiple comparisons. Error bars = 95% CI. Lines show the best fit of an exponential (Malthusian) growth curve. B) Dry weights of frond or aerial tissue harvested from the final timepoint of the growth series shown in A. Asterisks show statistically significant (P< 0.05) differences as assessed by one-way ANOVA followed by Šidák's multiple comparisons. Error bars = SEM. 110

Figure 2-16 Reduction in Lemna minor root length causes an increase in movement speed under wind stimulus 111

Figure 2-17. Effect of root removal on duckweed ionome. Heatmap showing the log2 fold change of elemental concentrations in the frond for rooted versus rootless treatments for each species. Significance (P <0.05) was determined by one-way ANOVA followed by Šidák's multiple comparisons test. n = 5 flasks, each initially seeded with 3 colonies for duckweeds; n = 7 flasks, each initially seeded with 1 plant for *Pistia*..... 113

Figure 2-18. Expression of the NRT1, NRT2 and PHT nutrient transporter gene families shows root bias in A. thaliana and Z. mays, but not S. polyrhiza. A) Mean TSI (tissue-specificity index) was calculated as per Julien et al. (2012) and Brawand

et al. (2011) for all members of the PHT, NRT1 and NRT2 family as identified by orthology analysis across 4 tissues encompassing root, root tip, shoot apical meristem (SAM) and leaf in each species. For each gene, expression levels per tissue type were normalized against total expression across all tissues. For Z. mays, data for root tip and mature root was unavailable so instead 2 separate root types of differing maturity level were used. B) Corresponding heatmap of the individual gene TSI values for each tissue type in the three species. 114

Figure 2-19. PCA showing clustering of replicates of the four tissue types sampled in the *S. polyrhiza* bulk RNA-sequencing experiment. 115

Figure 2-20. Transcriptomic response of *S. polyrhiza* 9509 to 24 hours phosphate starvation. A) Heatmap showing Log2 fold change of PHT and PHO genes in *Spirodela* fronds and roots subjected to 24 hours of phosphate starvation versus control groups grown with phosphate. Stars indicate genes with a Bonferroni corrected p value < 0.05 as per DESeq2. B) Total number of DEGs for the same groups, showing the total number alongside those up and down regulated. C) Genes enriched with the GO term 'transporters' for the same groups, ag their regulation is up or down. 116

Figure 3-1. Illustration of maize and gamagrass experimental design. provided by Valeria Custodio..... 135

Figure 3-2. CO_2 Phase diagram. Showing the temperature and pressure conditions required for CO_2 to exist in its different states 139

Figure 3-3. Schematic showing simplified layout of Nottingham Laser Ablation Tomograph Unit. A: Laser galvanometer, B Z-axis Linear actuator for sample (nanometer precision PI stage), C: X axis linear actuator, D: Y axis linear actuator, E:Sample stage F: Magnetic sample holder F: Root sample G: Laser sheet H: Heat

sink and debris collector I:Microscope turret and objectives J: Microscope body, K: machine vision camera K: camera focusing stage. 146

Figure 3-4. Image of the user interface of the LAT image control software. 149

Figure 3-5 LAT Recipe “Slow_focus”, SPC recipe for small step ablation and sample progression to focus the sample 151

Figure 3-6. LAT Recipe “Polish_Cut_Loop”, SPC recipe for sequential ablation, imaging and sample progressing, repeated three times for imaging coverage .. 152

Figure 3-7. LAT Recipe “Leaf_Cutter”, SPC recipe for sequential ablation, imaging and sample progressing, repeated three times for imaging coverage 154

Figure 3-8. Leaf imaging regions. (A) Composite whole leaf image stitched from multiple frames captured using 1X magnification, with boxes showing regions imaged in B (left) and C (Right), (B) Midrib leaf image captured using 5X magnification, (C) Lamina portion of leaf imaged using 10X magnification (50 images captured at 5 µm *Z*-intervals, Scale Bar A=10 mm, B=1 mm, C=0.5mm . 155

Figure 3-9. Whole leaf imager 1X recipe..... 156

Figure 3-10. Leaf midrib imager 5X recipe 156

Figure 3-11. Leaf lamina portion 10X recipe 157

Figure 3-12. Median projection of 50 pearl millet leaf lamina images. Taken 5 µm apart in the *Z* plane, with asterisk marking more prominently highlighted stomatal files..... 162

Figure 3-13. Representative images of pearl millet organs. Scanned using the methods developed in 3.5.2, and 3.5.3. (A), Pearl millet stem from internode immediately beneath panicle, (B) Fourth whorl crown root, (C) Flag leaf midrib, Scale bars: A=5 mm, B&C= 1 mm 170

Figure 3-14. Paneled image showing the Outputs from ROOTSCAN's measurements of different whorls from the Nottingham grown samples, Images organized into table showing the input images and three types of output from ROOTSCAN for four different adventitious root classifications under two different treatment groups. STR: Water stressed, ETM: Well-watered, Magnification: Mitutoyo lens used on LAT camera, Circle_approx: circle approximated by ROOTSCAN based on mean distance from outermost cell layers cell centroids to root centroid, Convex_Hull: polygon outlining the outermost cell layer of each cell type, Processed: Segmented and recolored image produced by ROOTSCAN representing the identified cells in the sample image. 171

Figure 3-15. Nottingham grown root image quality scores. Stacked Bar chart showing the distribution of sample quality image scores for the different whorls and treatments of pearl millet crown roots obtained from the Nottingham grown plants, scoring system described in Table 3-6 (1: Totally damaged unusable root – 5: Perfectly preserved root), ETM = Well watered, STR = Water stressed..... 172

Figure 3-16. Senegal grown root image quality score. Stacked Bar chart showing the distribution of sample quality image scores for the different whorls and treatments of pearl millet crown roots obtained from the Senegal field trial pilot year, Scoring system described in Table 3-6 (1: Totally damaged unusable root – 5: Perfectly preserved root), ETM = Well watered, STR = Water stressed..... 173

Figure 3-17. Effects of water stress and mesocosm source on gamagrass crown root anatomical traits Gamagrass grown in 6 different mesocosms containing soil from sources contrasting in annual rainfall (TRI=18 in, SVR=19 in, HAY=24 in, KNX=33 in, CWR=37 in, WEL= 40 in), grown under well-watered and water stressed conditions, Blue bars = control well-watered conditions, Red bars = Water stress treatment, Mean values shown, *n*= 8, Error bars = Standard deviation, Comparisons

given are 2-way ANOVA with Tukey's multiple comparison test correction, calculated in Prism 9 (GraphPad), reporting differences only either between different soils of the same water treatment or between water treatments in the same soil, Significant differences; *=P<0.05, **=P<0.01, ***=P<0.001 176

Figure 3-18 Effects of water stress and microbiome on gamagrass root anatomical traits, Gamagrass root anatomy of plants grown in sand inoculated with 24 different microbe communities (derived from soil collected from 6 different locations contrasting in rainfall (TRI=18 in, SVR=19 in, HAY=24 in, KNX=33 in, CWR=37 in, WEL= 40 in) following a period of gamagrass host (G) or free living adaptation (N) in combination with well-watered (W), or water stressed (D) adaptation), grown under well-watered and water stressed conditions, Blue bars = control well-watered conditions, Red bars = Water stress treatment, Mean values shown, *n*= 8, Error bars = Standard deviation, Pairwise comparisons given are multiple T-tests comparing water treatments for the same microbiome inoculations, with multiple comparison corrections using the Holm-Šidák method (Šidák, 1967) calculated in Prism 9 (GraphPad), Significant differences; *=P<0.05, **=P<0.01, ***=P<0.001 177

Figure 3-19. Subset of gamagrass root anatomy data presented in Figure 3-18 presenting only measurements of drought stressed plants. Blue ascending striped bars = microbiome history of well-watered conditions, Red descending striped bars = microbiome history of water stress treatment, Mean values shown, *n*= 8, Error bars = Standard deviation, Pairwise comparisons given are multiple T-tests comparing difference between traits when grown with microbiome adapted to contrasting water levels, with multiple comparison corrections using the Holm-Šidák method (Šidák, 1967) calculated in Prism 9 (GraphPad), Significant differences; *=P<0.05, **=P<0.01, ***=P<0.001 178

Figure 3-20. Subset of gamagrass root anatomy data presented in Figure 3-18 presenting only measurements of well-watered plants. Blue ascending striped bars

= microbiome history of well-watered conditions, Red descending striped bars = microbiome history of water stress treatment, Mean values shown, *n*= 8, Error bars = Standard deviation, Pairwise comparisons given are multiple T-tests comparing difference between traits when grown with microbiome adapted to contrasting Figure 3-19. Cont. water levels, with multiple comparison corrections using the Holm-Šidák method (Šidák, 1967) calculated in Prism 9 (GraphPad), Significant differences; *=P<0.05, **=P<0.01, ***=P<0.001 179

Figure 3-21. Effects of water stress and microbiome on maize root anatomical traits, Maize root anatomy of plants grown in sand inoculated with 24 different microbe communities (derived from soil collected from 6 different locations contrasting in rainfall (TRI=18 in, SVR=19 in, HAY=24 in, KNX=33 in, CWR=37 in, WEL= 40 in) following a period of gamagrass host (G) or free living adaptation (N) in combination with well-watered (W), or water stressed (D) adaptation), grown under well-watered and water stressed conditions, Blue bars = control well-watered conditions, Red bars = Water stress treatment, Mean values shown, *n*= 8, Error bars = Standard deviation, Pairwise comparisons given are multiple T-tests comparing water treatments for the same microbiome inoculations, with multiple comparison corrections using the Holm-Šidák method (Šidák, 1967) calculated in Prism 9 (GraphPad), Significant differences; *=P<0.05, **=P<0.01, ***=P<0.001 181

Figure 3-22. Subset of maize root anatomy data presented in Figure 3-21 presenting only measurements of water stressed plants. Blue ascending striped bars = microbiome history of well-watered conditions, Red descending striped bars = microbiome history of water stress treatment, Mean values shown, *n*= 8, Error bars = Standard deviation, Pairwise comparisons given are multiple T-tests comparing difference between traits when grown with microbiome adapted to contrasting water levels, with multiple comparison corrections using the Holm-

Šidák method (Šidák, 1967) calculated in Prism 9 (GraphPad), Significant differences; *=P<0.05, **=P<0.01, ***=P<0.001 183

Figure 3-23. Subset of maize root anatomy data presented in Figure 3-21 presenting only measurements of well-watered plants. Blue ascending striped bars = microbiome history of well-watered conditions, Red descending striped bars = microbiome history of water stress treatment, Mean values shown, *n*= 8, Error bars = Standard deviation, Pairwise comparisons given are multiple T-tests comparing difference between traits when grown with microbiome adapted to contrasting water levels, with multiple comparison corrections using the Holm-Šidák method (Šidák, 1967) calculated in Prism 9 (GraphPad), Significant differences; *=P<0.05, **=P<0.01, ***=P<0.001 184

Figure 3-24. Composite root image comprised of quadrants from images of well-watered and water stressed, wild type and PIN1a mutant *Brachypodium distachyon*. Scale bar= 100 µm 185

Figure 3-25. Root anatomical traits of wild type and *PIN1a Brachypodium distachyon* under well- watered and water stressed conditions. WW= Well watered plants, DS= Water stressed plants, Mean values shown, WT_WW&DS *n*= 6, PIN1a_WW *n*= 5, PIN1a_DS *n*= 4 Error bars = Standard deviation, Comparisons given are one-way ANOVA with Tukey's multiple comparison test correction, calculated in Prism 9 (GraphPad), reporting differences only either between the same ecotype or water treatment, Significant differences; *=P<0.05, **=P<0.01, ***=P<0.001, ****=P<0.0001 187

Figure 4-1. Images of field trial site. Images of the Year 3 (2022) field sites at the ISRA Bambey field station, showing the water stressed (STR) field on the left, and the well-watered field (ETM) on the right 204

Figure 4-2 Sample harvesting, subsampling, and root architecture phenotyping stations for the Year 3 (2022) field trials in Bambey, Senegal 206

Figure 4-3. Root Architecture Phenotyping Setup. (Left) Image of setup of root architecture phenotyping station used in Year 3 of field trials, DSLR camera mounted in wooden frame facing a blue felt board with a mounting nail, scale reference, and sample labels attached, (Right), image of bisected root crown used for architecture imaging and representative of anatomy sampling material 208

Figure 4-4. Plot map showing field layout from pearl millet field trials. Top block ETM (Well-watered), Bottom STR (Water stressed) soil sampling locations shown by red dots 210

Figure 4-5. Root anatomical traits of pearl millet pilot year subset lines grown under well-watered, and water stressed conditions. Traits defined in table 3.7 as given by ROOTSCAN, Mean values shown, n between 1- 12 dependent on presence or absence of traits in sample, Error bars = Standard deviation, black = control well-watered conditions, Orange = Water stress treatment, Pairwise comparisons given are multiple T-tests comparing water treatments for the same line, with multiple comparison corrections using the Holm-Šidák method (Šidák, 1967) calculated in Prism 9 (GraphPad), Significant differences; *=P<0.05, **=P<0.01, ***=P<0.001, ****=P<0.001 216

Figure 4-6. Principal component analysis of pilot year root anatomical data. Principal component analysis showing two clusters, one largely containing the ETM/Well-watered datapoints (left, black) and the other containing the STR/Water stressed datapoints (right, orange), separated by PC1 of 35.02%, and PC2 of 16.55%..... 217

Figure 4-7 Correlation matrix of root anatomical traits with agro-morphological and root architectural traits. Pearson's correlation matrix showing correlation of traits measured, Details of measurements given in Table 3.7 and Appendix 8. Separated to show full correlation data, and significance level. Bottom-left triangle shows

significance level: Dark Blue=Significant negative correlation at P<0.05, Light blue= No significant correlation, Pink= Significant positive correlation at P<0.05. Top-Right triangle shows Pearson correlation R value, graduated colour scale shown. 218

Figure 4-8. Anatomical diversity of pearl millet roots in Year 2. Column chart showing the mean trait value of nine root anatomical traits, from plants grown under well-watered conditions (Pink), water stressed conditions (Orange), and the percentage change in each trait between well-watered and water stressed (Plasticity) (Blue), for each line. Error bars = Standard Deviation..... 220

Figure 4-9. Correlation matrices of Year 2 phenotypic data and plasticity. Pearson correlation matrices showing the relationship between root anatomical traits, agromorphological traits, root architecture, and the plasticity (Pla) of these traits under water stress from Year 2 field data. Details of measurements given in Table 3.7 and Appendix 8, Matrix split to four quadrants for clarity. Recoloured to show significant positive or correlation at P<0.05 level, Cyan =Significant negative correlation at P<0.05, Light blue = No significant correlation, Orange = Significant positive correlation at P<0.05 222

Figure 4-10. Manhattan plots of GWAS of root anatomical traits from Year 2. Manhattan plots showing genome wide association study results from analysis of root anatomy of pearl millet panel lines grown under well-watered conditions, water stress, and trait plasticity Traits investigated: Stele bounding circle area, Sclerenchyma area pixel area, cortex bounding circle, aerenchyma area, count, total and mean metaxylem and vascular bundle area, and total root bounding circle area. Produced in R using GAPiT, FarmCPU model. 225

Figure 4-11. Leaf anatomical traits of pearl millet Year 2 water use efficiency lines subset grown under well-watered, and water stressed conditions. Mean values shown, Error bars = Standard deviation, Red = control well-watered conditions,

Yellow = Water stress treatment, Pairwise comparisons given are multiple T-tests comparing water treatments for the same line, with multiple comparison corrections using the Holm-Šidák method (Šidák, 1967) calculated in Prism 9 (GraphPad), Significant differences; *=P<0.05, **=P<0.01, ***=P<0.001, ****=P<0.001 227

Figure 4-12 Correlation matrix of leaf and root anatomical data from Year 2 field trials. Pearson correlation matrix showing the relationship between root and leaf anatomical traits. Details of measurements given in Table 3.7 and Appendix 9, Recoloured to show significant positive or correlation at P<0.05 level, Black =Significant negative correlation at P<0.05, Grey = No significant correlation, Purple = Significant positive correlation at P<0.05 231

Figure 4-13. Anatomical diversity of pearl millet roots in Year 3. Column chart showing the mean trait value of nine root anatomical traits, from plants grown under well-watered conditions (Pink), water stressed conditions (Orange), and the percentage change in each trait between well-watered and water stressed (Plasticity) (Blue), for each line. Error bars = Standard Deviation..... 233

Figure 4-14. Correlation matrices of Year 3 phenotypic data and plasticity. Pearson correlation matrices showing the relationship between root anatomical traits, agromorphological traits, root architecture, and the plasticity (Pla) of these traits under water stress from Year 3 field data. Details of measurements given in Table 3.7 and Appendix 8, Matrix split to four quadrants for clarity. Recoloured to show significant positive or correlation at P<0.05 level, Cyan =Significant negative correlation at P<0.05, Light blue = No significant correlation, Orange = Significant positive correlation at P<0.05 235

Figure 4-15. Leaf anatomical traits of pearl millet Year 3 water use efficiency lines subset grown under well-watered, and water stressed conditions. Line IP-12116

samples unavailable in Year 3, intentionally included for comparisons to Year 2, Mean values shown, Error bars = Standard deviation, Black = control well-watered conditions, Yellow = Water stress treatment, Pairwise comparisons given are multiple T-tests comparing water treatments for the same line, with multiple comparison corrections using the Holm-Šidák method (Šidák, 1967) calculated in Prism 9 (GraphPad), Significant differences; *=P<0.05, **=P<0.01, ***=P<0.001, ****=P<0.001 237

List of Tables

Table 2-1 List of duckweed and *Pistia* lines used and provenance 62

Table 2-2 Standard scan settings used for embedded duckweed cores (of different genera) used at high throughput and an example of high image quality settings. 71

Table 2-3. Results of 3D particle analysis of gas spaces within representative fronds scanned 90

Table 3-1 Critical Point Dryer settings optimized for smaller root samples 143

Table 3-2 Critical Point Dryer settings optimized for larger root samples 143

Table 3-3 Critical Point Dryer settings optimized for leaf samples 144

Table 3-4 Critical Point Dryer settings optimized for stem and cotyledon samples 145

Table 3-5 LAT Laser hardware settings 147

Table 3-6 Root quality scoring scheme 159

Table 3-7 Example measurements exported by ROOTSCAN, and the method of measurement 168

Table 4-1 SNPs identified significantly explaining phenotypic variance of total aerenchyma area in well-watered roots 244

Table 4-2 SNPs identified significantly explaining phenotypic variance in sclerenchyma plasticity under water stress 245

Chapter 1:

Introduction and Literature Review

1.1 Introduction

This introduction will focus on three main themes, plant anatomy and its significance in plant function with regard to water stress, methods of investigating plant anatomy, and introducing plant species from contrasting water environments that would benefit from anatomical research.

1.1.1 Plant anatomy

Plant anatomy is the study of the tissue and cell structure of plant organs, with a particular focus on internal and microscopic structures (Simpson, 2019). Recent technological advancements have enabled the identification of genetic control of plant anatomical traits and identified their functional effects. This knowledge can be utilized to develop more productive plant and crop varieties, and those better suited to their environment. This is a necessary goal as there is increasing food insecurity globally, a rapidly growing population, and a prevalence of climate instability (Atkinson *et al.,* 2019*)*. Analysis of plant anatomy, anatomical phenotyping (also called anatomics), is a relatively unexplored method of identifying traits for crop improvement and has been shown to have great potential in a range of species. This suggests there is much to be gained in increasing our understanding of plant anatomy and developing new techniques for its study.

Monocots

Food & global relevance

Monocotyledons, commonly referred to as monocots, are grass and grass-like flowering plants (angiosperms), the seeds of which typically contain only one embryonic leaf, or cotyledon *(c.f.* dicotyledons).

As a target for improvement via anatomical selection, monocot crops represent an ideal starting point for several reasons. Firstly, they are of extreme importance to the global food system; 2.3 billion tons of cereals are produced annually, accounting for over half the world's harvest area, and over 50% of the global caloric daily intake is cereal grains (Awika, 2011; FAOSTAT, 2023). While the majority of this is from three species: wheat, maize, and rice, cereals are diverse and can be found in a wide range of environments. In particular, regional crops are of great importance to local food security, especially in challenging environments. This is particularly true in the Sahelian region and greater West Africa where, millet, sorghum, fossa, and African rice are extremely important due to their increased drought tolerance. Here, food and climate security are significant problems, only due to worsen in the coming years.

Biology

Monocots are defined by their single cotyledon, normally succeeded by pinnate leaves and are generally found to have an absence of secondary meristems or woody growth. Monocots are often found with a largely adventitious root system, stemming from the absence of secondary root meristems. As monocot root anatomy is set down largely in the root apical meristem and elongation zone, post this region it is less variable, making anatomy more consistently comparable.

Monocots, beyond cereals, have a wide ecological range, covering the globe and nearly all ecosystems, ranging from desert conditions to freshwater and seawater. Suggesting by exploring the diversity present in their phylogenetic tree, genes and traits related to their specific adaptations can be identified.

1.1.2 Water and roots

Water is an essential nutrient for plant growth, its roles in the plant are fundamental and wide ranging, though in particular it provides the mechanical structure of the plant, enables, photosynthesis, and facilitates nutrient uptake and

transport (Blatt et al., 2014). A reduction in the availability of water diminishes the plants' ability to function in these ways, and a sufficient interruption to water availability can cause a break in the columns of water that run continuously upwards within the plant. This disturbance to the hydraulic lift responsible for transporting water can be enough to cause the vessel to cease to function and inhibit further water uptake through a process of cavitation (Tyree et al., 1986; Lens et al., 2022).

In the majority of plants, roots are responsible for water uptake, which constitutes one of their primary functions alongside mechanical plant support, nutrient uptake, storage, and metabolite synthesis. Therefore, developing a root system better suited to low water conditions may help to address challenges faced by plants in drought prone environments.

1.2 Plant root traits

The diverse functions of plant roots are reflected in a diversity of measurable traits. This thesis will focus predominantly on anatomical, developmental and architectural features, though there are metabolic, compositional, biotic, and photosynthetic factors, that have an interplay with the traits chosen for investigation but will not be addressed directly.

1.2.1 Root architecture

Monocot root architecture

Root architecture is the presentationand arrangement of the root system in space. In monocots, the root system is made up of seminal (seed derived), and adventitious (stem derived) roots. Bornfrom these are several orders of lateral roots. Following germination, the seminal root is produced often in tandem with the cotyledon. In cereals and many other species, following development of the

stem proper, adventitious (crown) roots, form in concentric rings (whorls) around the stem. The earliest start at a lower portion of the stem, and later forming whorls develop sequentially further upwards. Once tillers are produced, they produce their own crown root system in the same way (termed tiller roots). Further to the development of these root systems, plants are capable of producing additional types of adventitious roots which are classified based on their site of genesis and function such as brace roots.

Significance of root architecture

Root architectural traits have been shown to significantly affect plant performance in a number of ways. The current swathe of literature on root architecture promotes a “steep, cheap, and deep” ideotype for root system architecture (and anatomy) (Lynch, 2013). This has arisen from a number of papers (Lynch, 1995, 2007, 2022; Lynch et al., 2021; Strock et al., 2022) showing that deeper rooting systems, with a more vertical angle to the root crown, confer a higher degree of water stress tolerance. However, there are many different types of soil profile, which can be highly heterogenous in and of themselves. An optimal root system in one environment may not be well suited to another, so an architecturally plastic root system may be most advantageous (Correa et al., 2019).

1.2.2 Root anatomy

Root anatomy is the arrangement of cells and cell types within the root. Due to roots generally being cylindrical in profile and having rotational symmetry, their anatomy is usually viewed in longitudinal and transverse sections Figure 1-1. At the root tip, containing the root apical meristem (RAM), root cap, quiescent center (QC), and elongation zone (EZ), it is typical to visualize this in the longitudinal to see all these regions more clearly where possible. In the differentiated region, transverse sections are standard.

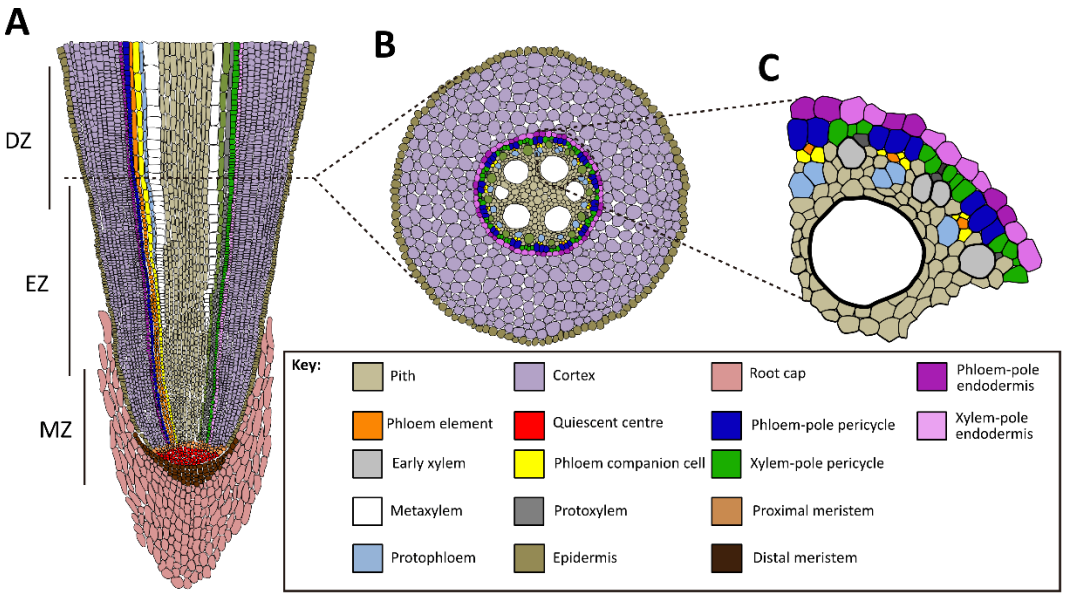


Figure 1-1. Illustration of Cellular Organization of Maize Primary Root. (A) Longitudinal section showing functionally distinct zones, (B) Transverse section of Differentiation Zone, (C) Magnified subsection of stele and endodermis; DZ, differentiation zone; EZ, elongation zone; MZ, meristem zone. (Adapted from Yu et al., (2016))

Most of the anatomy of a root is set down in each roots RAM, with a varying degree of alteration in the EZ. This is particularly the case in monocots as they tend to lack secondary meristems within the root. Within a transverse section of a mature region of a monocot root anatomical analysis generally considers the presentation of the following cell types and tissues.

Stele

The stele, also known as the vascular cylinder, is primarily responsible for the transport of water, nutrients, and sugars, it is also the region from which lateral roots develop. Within the stele of monocots there can be xylem, phloem, pericycle, and pith cell types. The arrangement of the stele varies between species and root types however there are reoccurring motifs, particularly within the cereals.

Primary roots often have a single or small number of central metaxylem, surrounded by pith, then with a spaced circular arrangement of alternating xylem and phloem radially outwards from the center, and beyond this, the pericycle encircling the outer edge of the stele. Crown roots are similar, however typically rather than a central metaxylem, have a number of metaxylem arranged in a circular pattern within the ring of xylem and phloem and a pith center.

Pith

Within the stele pith cells are ground tissue, originating from ground meristem, they are not purported to have significant function in water or nutrient transport.

Xylem

Xylem are the cell type responsible for the transport of water and water transported nutrients, they are also important in providing structure and support to the plant (however more so in shoots than roots). In angiosperms they are normally in the form of vessel elements rather than tracheid or fibers as the increased diameter allows for much greater unimpeded water conductance (Figure 1-2).

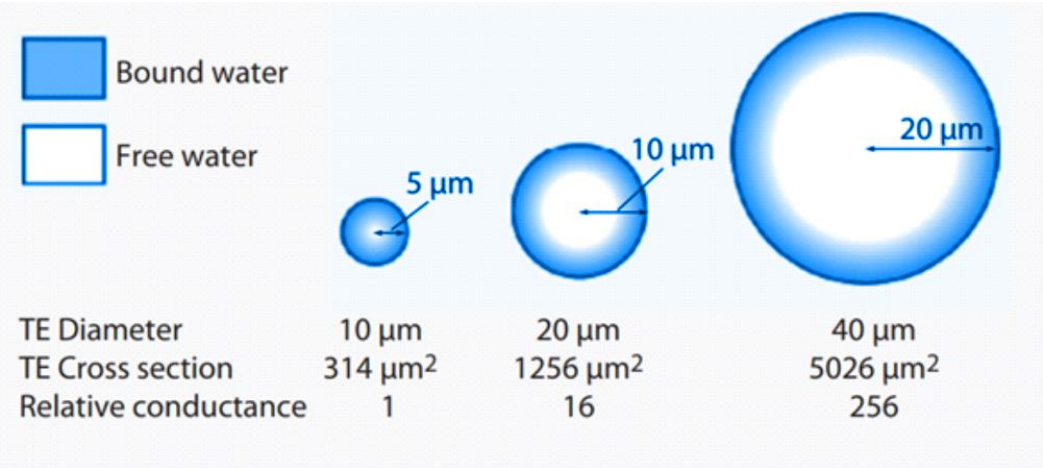


Figure 1-2. Illustration showing the relationship between tracheary element (TE) diameter and relative water conductance. (Redrawn from Mauseth (1988) and Crang et al., (2018))

Within the monocot root system, xylem are split into three groups describing their development, form and function. Protoxylem are the first differentiated xylem, they are the developmental cornerstone of xylem production but have limited water transport capacity. The early metaxylem matures after the establishment of protoxylem and are derived from protoxylem, are larger in size and have a higher capacity for water transport. Metaxylem, (late metaxylem), arise later developmentally than early metaxylem, and are larger in size. Metaxylem are the most significant contributor to hydraulic conductance (Crang et al., 2018).

Phloem

Phloem can present as proto-phloem, phloem element, and phloem companion cells, they transport sugars and hormones down from shoots to roots.

Pericycle

The pericycle is a layer of pluripotent cells, located at the outermost area of the stele, from which lateral roots may develop.

Cortex

The cortex is the layer of tissues between the stele and epidermis. In many roots it functions as storage tissue for starch, water and minerals. It is also the site of gas exchange within the root, and forms part of the system that transports water from the soil to the stele.

Endodermis

The cortex is bounded to the interior by the endodermis, this is a layer of cortical cells that possess a secondary thickened layer between the cells called the casparian strip. This forces water into cells and onto the symplastic pathway. This also serves to waterproof the stele, regulating the flow of water into it, and limiting water losses.

Cortical cell

Cortical cells may serve a range of functions, they are generally unspecialized, but adaptable to a range of environmental circumstances. It is in these cells that much of the root storage takes place, starch deposits (amyloplasts) are common, and mineral crystals such as raphides are often found. Water passage between these cells walls is the symplastic pathway, and within the cells is the apoplastic pathway.

Aerenchyma

Aerenchyma are not so much a tissue type, but a deliberate void within the cortex, and are (typically air filled) spaces between cells. These present in a variety of patterns depending on the process giving rise to them. They are often either constitutive or inducible, and form through schizogony, or lysogeny (Evans, 2004).

Exodermis-Hypodermis

The hypodermis is a cortical tissue layer, generally the radially outermost layer/layers of the cortex underlying the epidermis. It is not found in all plant

species and can be present to a greater or lesser extent depending on environmental circumstances. It can be a more heavily secondary thickened region, or with a larger number of smaller and tightly packed cells with thicker cell walls (multi-serrate cortical sclerenchyma (Schneider et al., 2021). The Hypodermis can also include an exodermis, a layer similar to the endodermis with a band of hydrophobically secondarily thickened cell walls. This has a range of functions, such as providing additional mechanical support to the root, a greater degree of waterproofing to prevent water loss, and protecting the root from pathogens.

Epidermis

The epidermis is the outermost layer of cells in the root (or any organ). It is the site of water uptake, root hair production, and biotic interaction.

1.2.3 Significance and control of root anatomy

Development of the anatomical ideotype

Root anatomy has been shown to affect plant performance in a wide range of ways, as it directly impacts the effectiveness of the root as a transport and uptake system, and also the metabolic cost to the plant of producing and maintaining its root system. Recent extensive investigations of root anatomical traits beneficial to plant growth and stress tolerance has shown that roots with fewer, larger cortical cells, with a high proportion or cortical aerenchyma are parts of root systems well suited to surviving drought stress (Zhu et al., 2010; Chimungu et al., 2014a, 2014b). This may be a combination of an initially cheaper to produce root increasing soil exploration to build resilience, and or that during periods of stress the root system requires less resources to maintain. Large xylem has been linked to increased water transport capacity (Prince et al., 2017; Scoffoni et al., 2017a); however, this can be disadvantageous if the plant is unable to regulate this and water loss effectively in

arial tissue. This can also lead to an increased incidence of xylem embolism if the flow of water is not maintained, which the chances of may also be higher if water is drawn from the soil too rapidly (Saito et al., 2020; Lens et al., 2022).

Sclerenchyma has also been shown to be an agronomically important root anatomical trait. Increased cortical sclerenchyma improves root growth through compacted soil, increases root tensile and bending strength, and enhances plant growth in mechanically impeded soil conditions (Schneider et al., 2021; Vanhees et al., 2022).

Genetic control of root anatomy

Many root anatomical traits have been shown to be heritable and under genetic control in a number of systems. Genome wide association studies (GWAS) have been used to identify genetic regulators of root anatomical traits, such as cell size, aerenchyma prevalence, extent of cortical sclerenchyma formation, and cell number. Specific hormone and plant developmental mutants have also been shown to produce anatomical defects or variants (Carland et al., 1999), that can even be differentially induced to affect anatomy (Mellor et al., 2019). There are several demonstrated mechanism for this vascular patterning in *Arabidopsis* roots involving hormonal signaling (De Rybel et al., 2014), transcription factors and miRNA interactions (Mellor et al., 2017). The majority of this anatomy related mechanistic molecular work has been done in the model dicot *Arabidopsis*, however with advances in genetic transformation it is now possible to look at root anatomy of targeted transformation mutant cereal lines, though these may require new or different phenotyping methods to those employed for *Arabidopsis*.

Abiotic effects on root anatomy

Many plants vary their root anatomy in response to external factors. In the past it is suggested that plasticity has been selected against in plant breeding in order to maximize outputs under controlled conditions (Gage et al., 2017), however as

climate and environmental conditions become more unstable and crops face more stresses, this becomes disadvantageous. Crops that are able to adapt to their immediate environment within the growing cycle may be able to tolerate periods of stress better and recover faster, particularly in low input agroecosystems (Kusmec et al., 2018; Schneider and Lynch, 2020; Chen et al., 2022). The level of plasticity itself can be highly varied between lines and traits, and under different treatments, though in many species a plastic response is often seen under drought, though has also been observed under light and nitrogen deficit (Wahl et al., 2001; Song et al., 2019). In addition to the traits themselves, root anatomical plasticity has been shown to be under separate strong genetic control (Schneider et al., 2020). The ability to reduce root diameter, cortex area, or increase aerenchymal proportions under stress can reduce metabolic consumption and improve carbon use efficiency (Chimungu et al., 2015b; Colombi et al., 2022).

1.3 Plant anatomical phenotyping

1.3.1 Techniques for anatomical phenotyping

History of plant anatomical investigation

Observations of plant morphology and speculation of associated function have been made and recorded since antiquity in works such as the Rigveda, Pliny the Elder's "Natural History", and Theophrastus' "Enquiry into Plants"; though it was in the 1600s, shortly after the invention of the compound microscope that the study of plant cellular anatomy really began. In 1675 Marcello Malpighi published a wide spanning investigation of plant anatomy in *Anatomia Plantarum*, and Nehemiah Grew published "The Anatomy of Plants" in 1682 (Figure 1-3). These works shed new light on the variety of anatomical structures present in plants, and following on from the discovery of plant cells, allowed the identification of tissue structures and the beginning of the characterization of their function.

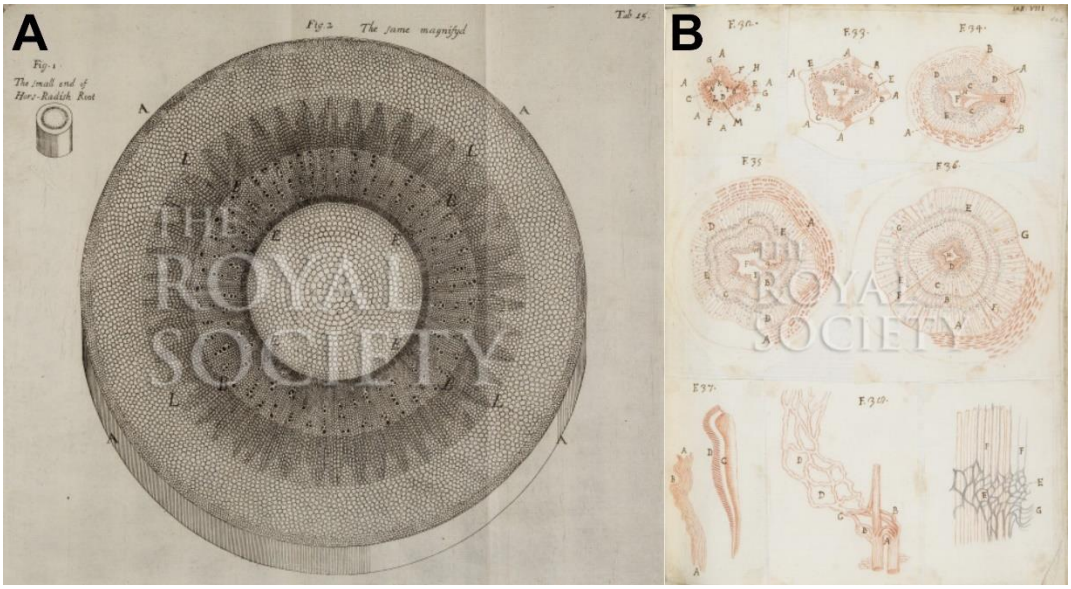


Figure 1-3. Collection of illustrations from early publications on plant anatomy. (A) Horseradish root from "The anatomy of plants" by Nehemiah Grew (1682), (B) Chestnut tree stem from "*Anatome plantarum"* by Marcello Malpighi,(1675).

Important steps towards the development of the field were made throughout the 18th and 19th centuries with the publication of various important texts showcasing the importance of anatomy in plant classification and understanding development (Mierbel, Moldenhauer, Candolle, Meyen, Schleiden, Haberlandt). It was in this time the first early "photographs" of plants were made. Following the development of the heliography process by Nicéphore Niépce, William Henry Fox Talbot developed the calotype process, which he used to capture what is thought to be the earliest plant photomicrograph in 1838 (Figure 1-4).

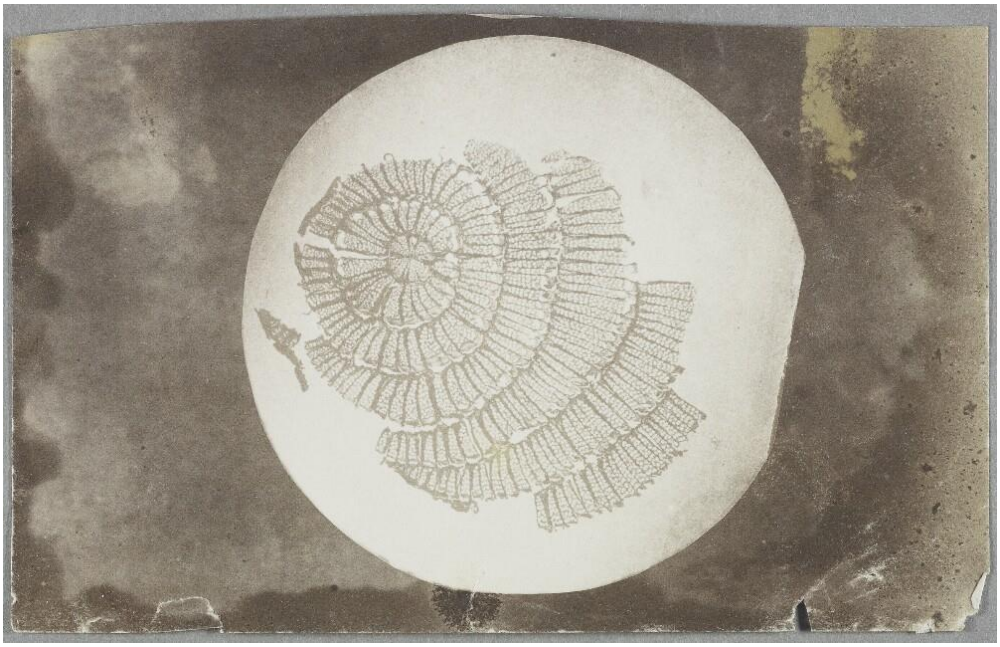


Figure 1-4. Photomicrograph of a section of a plant stem from a solar microscope. Image of possibly either a horsetail or elm stem section, captured on salted paper using a solar microscope by William Henry Fox Talbot in 1838 (The William Henry Fox Talbot Catalogue Raisonné)**.**

While not microscopy (or plants), Anna Atkins shortly thereafter published her cyanotype photography book "Photographs of British Algae" in 1843. This was hugely significant, and shortly followed by several other books of her photography, with collected work including images of ferns and other plants.

In the early 20th century, investigation of plant comparative anatomy was driven by Agnes Arber with several notable publications on aquatic angiosperms, monocot anatomy and Gramineae anatomy. This was followed by Katherine Esau's definitive textbook on plant anatomy in the 1950s, that has been in press since (Simpson, 2019).

Modern techniques of anatomical analysis of plant traits

The advent of digital photography in the late 1950s, and its subsequent integration with microscopy, rapidly advanced the field of plant anatomical phenotyping. Developments of new types of digital sensors has led to a range of imaging techniques that have found applications in plant anatomical phenotyping, including confocal microscopy, X-ray computed micro-tomography, electron microscopy, thermal imaging, magnetic resonance imaging, positron emission tomography, and many types of brightfield imaging (Costa et al., 2019; Pieruschka and Schurr, 2019; Fasoula et al., 2020).

A recent development in plant anatomical phenotyping is the use of laser ablation tomography to rapidly section and image plant samples using a powerful laser to ablate and induce fluorescence in samples for rapid high-quality imaging. Depending on the sample handling and choice of 2D or 3D scanning, this can generate hundreds of individual sample images a day or multiple images a second.(Chimungu et al., 2015b; Walter et al., 2015; Hall and Lanba, 2019; Strock et al., 2019; Neto et al., 2022; Laser Ablation Tomography 2.0, n.d.)

Advances in technique and technology have enabled massive increases in resolution and speed of image acquisition of these techniques, resulting in extremely large image datasets (Atkinson *et al.*, 2019). However, many image analysis techniques remain largely manual, and this is especially the case in anatomical phenotyping. This creates a bottleneck in the potential throughput of any phenotyping pipeline (Minervini et al., 2015). Some systems speed this up through the use of custom designed tools (Lartaud et al., 2015), semi-automatic segmentation systems (Pound et al., 2012a), or fully automatic systems (Burton et al., 2012). These help with this issue, but with high throughput and high resolution image capture, image analysis often fails to keep pace. The advent of deep machine learning has been suggested as a solution to this bottleneck, and bring it at least in line with the other steps in the process (Yasrab *et al.*, 2019).

1.3.2 Previous studies of root anatomy in monocots

Root anatomy has been previously investigated in a range of species using several varied methods. This started with early descriptive work surveying the different types of plant roots and the structures within and has evolved into investigation of how roots interact with their environment, diversity within species and between different organs, and genetic control of root anatomy.

Pearl millet

Pearl millet root anatomy has been investigated in several studies (Brück et al., 2003; Maiti et al., 2012a; Purushothaman et al., 2013; Passot et al., 2016), and quite comprehensively by Passot et al (2016), which showed that pearl millet shared the common cereal root anatomy patterns as described previously in Section 1.2.2. This was followed up with investigation of lateral root anatomy, which showed three distinct anatomical configurations, shared between lateral and crown roots. These classes are largely based on root diameter, and the presence and size of metaxylem in the lateral root stele. These lateral root classes correspond to assigned classes of lateral root in a follow up study, comparing lateral root prevalence and growth in pearl millet and maize. This showed that the majority of lateral roots (62%) are the smallest variety lacking metaxylem, and these had a continuously high growth rate compared to the other classes which slowed and ceased sooner(Passot et al., 2018). Root hair length and abundance has also been found to be related to rhizosheath (the soil region closely associated with and adhered to root systems) formation and soil adhesion in pearl millet (Cantó et al., 2021). While the primary root has been investigated, research tends to focus on crown root anatomy, as the primary root is typically the only seminal root produced and it often dies off after 4-6 weeks of growth. It has been observed that between lines and growth conditions, pearl millet root anatomy is variable in

the amount of sclerenchyma in the exodermis, thickness of endodermal cell walls, and level of lignification in different cell types(Maiti et al., 2012a)

Maize

Maize has become a sort of model organism in investigation of root anatomy (York et al., 2015; Bray and Topp, 2018; Sidhu et al., 2018), as its large roots with well-spaced nodes/whorls make it well suited for root anatomical analysis. The majority of large field trials investigating root anatomy, especially those using LAT scanning have involved use of maize. The maize root system comprises multiple seminal roots as well as adventitious roots at varied positions at the stem. There is a less clear divide between seminal and adventitious roots in their anatomy, as later developed seminals may also have a polyarch arrangement of a large number of metaxylem. Adventitious roots will however generally be larger and may have a more heavily sclerenchymatous hypodermis.

Extensive investigation of maize root anatomy using LAT has shown numerous benefits to root cortical aerenchyma, such as improved drought tolerance (Zhu et al., 2010), enhanced nitrogen acquisition in nitrogen poor soils (Saengwilai et al., 2014), and enhanced soil exploration (Vanhees et al., 2020). Similar benefits have been shown to be conferred by cortical cells being larger(Chimungu et al., 2014a), and having a reduced number of cortical cell files (Chimungu et al., 2014b). Breaking down these constitutive traits has allowed for enhanced genetic discovery and the development of predictive models that facilitate prediction of biomechanical properties and the design of roots for specific environments (Chimungu et al., 2015a; Klein et al., 2020; Schäfer et al., 2022).

Rice

Rice is one of the most important food crops in the world for human consumption. It has similar stele patterning in its different root classes to other cereals. however has different cortical and epidermal patterns (Rebouillat et al., 2009).

Rice is a semi-aquatic plant species, and therefore has several anatomic adaptations to its environment such as a more regular suberized hypodermis and a high proportion of aerenchyma (Clark and Harris, 1981). Investigation of rice root anatomy in response to drought has revealed that anatomy is highly plastic, and that plasticity affects drought tolerance (Fonta et al., 2022). In response to low phosphorus, root area was significantly decreased and a higher percentage area of aerenchyma was observed, however there were limited to few responses to phosphorus treatment in the stele or in vascular traits (Vejchasarn et al., 2016). In a panel of Egyptian rice varieties there was significant variation in traits plasticity levels, and under drought stress lignin deposition was reduced in the cortex and enhanced in the stele, cortical diameters were reduced and meta-xylem number decreased (Hazman and Brown, 2018). Anatomical traits are diverse in rice and investigation has shown variation in xylem and stele size between and within different populations indicating these traits are diverse (Uga et al., 2009) and under the control of specific genetic regions (Uga et al., 2008).

Similar to the earlier work on pearl millet lateral root anatomy, analysis of rice lateral roots found three classes of lateral roots (Watanabe et al., 2020), and further to this found an additional difference between the two large classes of an additional sclerified layer that had a distinct immuno-profile.

Duckweed and close relatives

Duckweed are a family of free floating aquatic angiosperms with an interesting evolutionary history of moving from land back to water, posing interesting anatomical and developmental questions (Jones et al., 2021). Duckweed root anatomy has not been studied extensively or at all in the majority of varieties, despite its on- and off history as a model species (Acosta et al., 2021). There are select research articles with images that make observations on different aspects

(Melaragno and Walsh, 1976; Kim, 2007; Jung et al., 2008; An et al., 2019) of the root and frond anatomy, but not in a high throughput or comparative manner, and it has been described and illustrated in various texts by Elias Landolt, Agnes Arber, and F. Hegelmaier. *Pistia*, a related outgroup that is often included for comparative analysis, has seen some investigation of root anatomy and how this is affected by abiotic stress, but not across the root system (Akapo et al., 2011; Silva et al., 2013).

1.3.3 Monocot leaf anatomy

Leaf anatomy has been shown to be under strong genetic and developmental control for the optimization of gas exchange for photosynthesis (Baillie and Fleming, 2020). Monocot leaf anatomy varies significantly between C3 and C4 plants but can still broadly be broken down into morphological parameters such as length and width, coupled with vascular patterning, porosity and stomatal distribution, and abundance of different cell types. Similar to optimization of root anatomy for water capture, leaf anatomy can be optimized for photosynthetic and water use traits (Galmés et al., 2013; Xiao et al., 2023). Several anatomical traits have been linked to or are suggested to be related to important physiological features that relate to plant growth and performance, such as the stomatal density (Dunn et al., 2019), porosity (Mathers et al., 2018), vascular bundle structure (Warner and Edwards, 1988), vessel diameter (Scoffoni et al., 2017b), and bulliform cell patterning (Mader et al., 2020; Matschi et al., 2020).

1.3.4 Drought and Anatomy

Drought and plant function

Drought is complicated to define and can be used describe either dryer than normal conditions, a lack of rainfall or precipitation, or a shortage of water (Seleiman et al., 2021). For plants this often refers to stress due to insufficient water. As the majority of global agricultural systems are rain fed, drought through lack of rainfall is a major threat/limiting factor to global crop production (Molden

et al., 2011; Fekete, 2013). As the climate changes towards a more unpredictable and unstable system, the trend is for regions already receiving unstable rainfall levels for the instability to become exacerbated. The rising global temperature also causes an increased level of water loss, both from plants and from the environment.

Plants need water to function, it is required for several main reasons; as part of photosynthetic reactions to acquire energy and to facilitate metabolic reactions, to enable transport of nutrients and minerals around the plant, and to provide strength and structure (McElrone et al., 2013). Insufficient water availability results in a range of issues in these areas, and a period of drought can cause serious permanent damage to the plants vascular system resulting from xylem embolisms (Scoffoni et al., 2017b; Lens et al., 2022).

Anatomical traits relating to drought tolerance

A number of plant root anatomical traits have been shown to help plants survive drought and be resistant to potential damage. These include reduced root diameter, increased root cortical aerenchyma, reduced cortical cell layers, large cortical cell size, reduced cortical cell number, and xylem diameter and number (Chimungu et al., 2014a, 2014b, 2015b; Hazman and Brown, 2018; Burridge et al., 2022; Lens et al., 2022).

Conceptually, the benefit these cortical traits offer include reducing root metabolic and water cost, while increasing the volume of soil that can be explored by the root system for the same resource expenditure (Lynch, 2013). In the vasculature there is potentially more to consider with regard to the target environment; as there are tradeoffs between conservation of available water, maximum hydraulic flow, and embolism avoidance, that will be specific to the temperature, soil environment, rainfall, and water availability.

1.4 Studied species I: Pearl Millet Exemplar species for water stress studies

1.4.1 Biology

Description

Pennisetum glaucum (*Cenchrus americanus*), or pearl millet, is a seed crop, which grow on a dense panicle, typically 10-20cm long. It is a monocot, member of the Poaceae, and a C4 plant (Huang et al., 2016) (Figure 1-5). Dwarfed and non-dwarf varieties are both common, as the large leaf stalks are a common fodder crop for animals. It is grown around the world and is the most popular millet variety globally. It is genetically and phenotypically diverse and many different varieties are grown to suit different climate conditions and consumer preferences (McDonough and Rooney, 1989; Hu et al., 2015; Satyavathi et al., 2021).

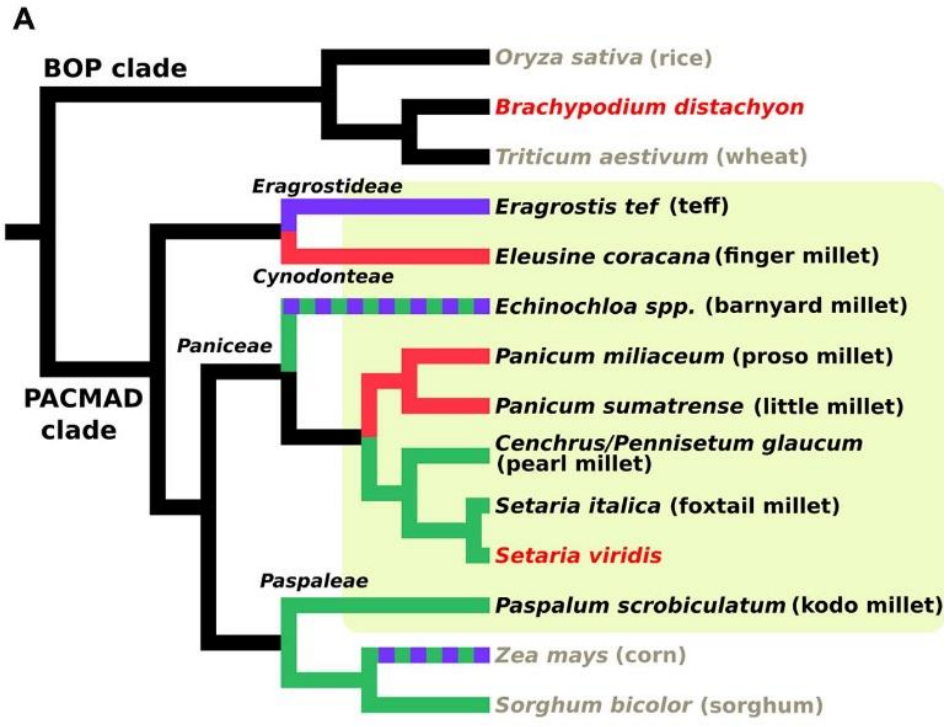


Figure 1-5. Cladogram showing phylogenetic relationships and photosynthetic subtypes of millets and other Poaceae species. Black, gray and red taxa names represent millets, major crops and model grasses, respectively. Millet lineages are also highlighted in yellow. Green, red, purple, and black branch colors represent

three subtypes of C4 (NADP-malic enzyme, NAD-malic enzyme and phosphoenolpyruvate phosphatase) and C3 photosynthesis respectively. Dashed colors represents mixed subtypes of C4. Reproduced from Huang et al., (2016), using phylogeny from Grass Phylogeny Working Group II (2012).

Origins and domestication

Pearl millet is thought to have its center of domestication in the Sahel in western Africa (Figure 1-6) and have been domesticated around 2800 BCE (Manning et al., 2011). This is an extremely arid region, and as a result, pearl millet is well adapted to low water conditions and poor soil and can grow in areas where other major crops cannot (Satyavathi et al., 2021). Around 1500 BCE, it appears to have spread east, possibly along the Indus valley civilizations trade networks, from east Africa to the Indian subcontinent (Haaland, 2011). This spread has resulted in a large genetic diversity of pearl millet, and it readily outcrosses and hybridizes (Sattler et al., 2019).

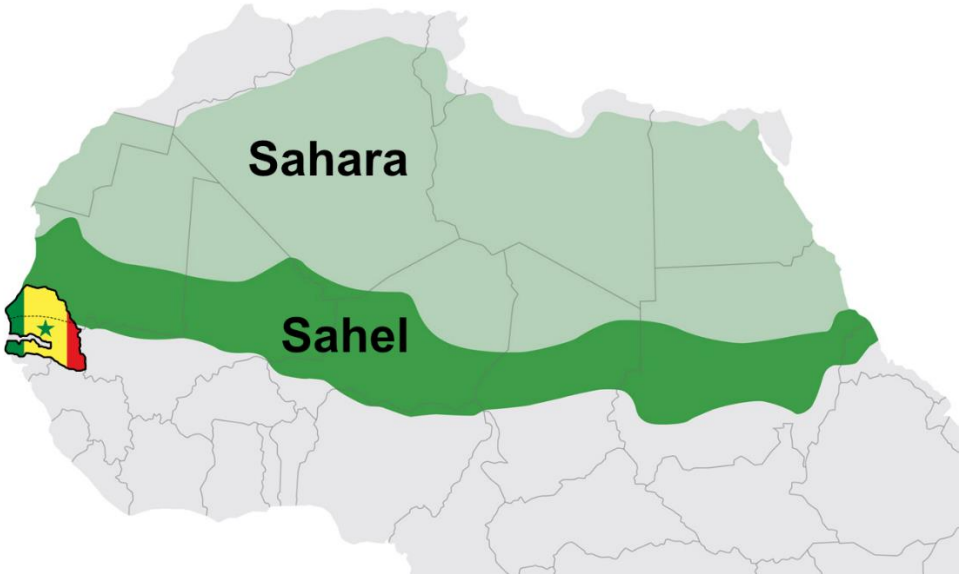


Figure 1-6. Map of North Africa. Map of North Africa showing the Sahara desert (pale green) the Sahel region (dark green), and Senegal (Senegalese flag coloured), with a dashed line denoting the are of the country considered to be in the Sahel.

Genetic resources

There are several pearl millet diversity panels held by different research organizations around the world, including ISRA (Senegal), ICRISAT (Niger), and GRIN (USA) (Hu et al., 2015; Sehgal et al., 2015).

Leveraging these resources through the use of genome wide studies has enabled the identification of candidate genes responsible for agronomically relevant physiological traits, such as grain yield (Sehgal et al., 2015), rooting depth (de la Fuente et al., 2023), and rhizosheath formation (de la Fuente Cantó et al., 2022).

1.4.2 Pearl millet as a crop

Uses

Pearl millet is the sixth most important cereal crop in the world based on harvested area and is the most widely grown form of millet globally and is of particularly high importance in (West) Africa, and in India. Industrially India is the largest producer of pearl millet, however it is hard to estimate the extent to which it is grown in the

Sahel due to the smallholder and subsistence nature. In India it is largely consumed as a flatbread, or in Tamil Nadu, as a porridge. In the Sahel, pearl millet is largely consumed as porridge, as a pearl millet couscous like food, or as a porridge like drink made from the couscous. This is similar across other parts of Africa, including Namibia where it is a staple food in the northern, more drought prone region. Here is it eaten in a porridge, or as a fermented drink.

It is not used as much as a flour due to the need for more processing, or mechanical processes where the infrastructure does not exist or the cost is too high, therefore much of the processing is what can be done domestically, so is typically pounded.

Senegal

Senegal is a west African country with its northern region in the Sahel (a sub-Saharan steppe biome). The earliest evidence of pearl millet domestication is in bordering Mali, along the Senegal river, and Senegal hosts the Institut Sénégalais de Recherches Agricoles (ISRA), one of the leading pearl millet research organizations in the region.

Pearl millet is a staple crop for Senegalese smallholder farmers, and is grown on approximately 800,000 hectares of land, with a national production of 600,000 tons a year (Kane et al., 2022). Senegal and the Sahel is an extremely vulnerable region to climate change and desertification, and is projected to undergo significant population growth in the coming decades (Dembitzer, 2018). These factors combine to make food security a severe regional issue, meaning developing more drought resilient and productive crops is vitally important.

1.5 Studied Species II: Duckweed

1.5.1 Description

The duckweeds are a subfamily of aquatic free-floating angiosperms in the family Araceae consisting of five genera: *Spirodela*, *Landoltia*, *Lemna*, *Wolffia*, and Wolfiella. Phylogenetic studies have shown that *Wolffia* and *Wolffiella* are the most derived genera, with *Spirodela* being the ancestral (Les et al., 2002). Their evolutionary trajectory correlates to a general reduction in both size and morphological complexity, as observed by Landolt (1986), and as shown in Figure 1-7.

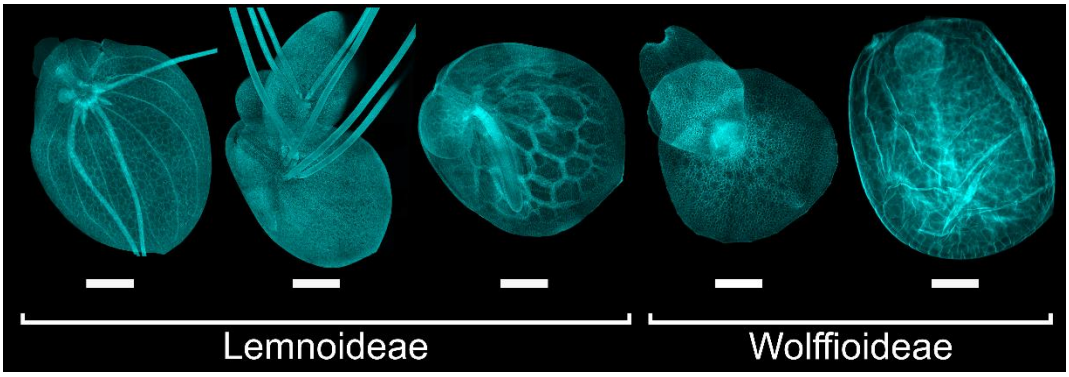


Figure 1-7. Morphological variation between duckweed subfamilies Lemnoideae and Wolffoideae. Representative species of each genus within Lemnoideae: *Spirodela*, *Landoltia*, *Lemna* (left to right). Plants were cleared and stained with Fluorescent Brightener 28 (calcofluor) following the protocol described by (Kurihara et al., 2015) and imaged on a Leica TCS SP5 confocal microscope. Scale bars: A, B =1000 µm, C, D= 500 µm, E=100 µm.

All species comprise of a frond or thallus (Hillman, 1961), a leaf-like structure that in most species floats on the water's surface, with one face exposed to the air and one in contact with the water (Laird and Barks, 2018).

Spirodela, have relatively larger fronds (~10 mm diameter), and typically possess 7–21 roots per frond (Les and Crawford, 1999). *Landoltia* punctata, formerly considered part of the genus *Spirodela*, is morphologically similar to *Spirodela*, and usually has 1–7 roots per frond, but slightly smaller fronds (Les and Crawford, 1999). For *Lemna*, all species comprise of a single root per frond that varies in

length between species (Landolt, 1980). Lemma also has significant variation in frond width (~2–8 mm diameter), length, and thicknesses. The genera *Wolffiella* and *Wolffia* contain the smallest plants, members of both genera are rootless, and have fronds (< 3 mm diameter). One *Wolffia* species, *Wolffia* microscopica, forms a psuedo root (Sree et al., 2015). Duckweed fronds contain parenchymatic tissue containing air spaces between the upper and lower epidermal surfaces, with a large variation in the size and morphology of these air spaces between species (Landolt, 1986). A feature of the life cycle in several of the duckweeds is the production of turions. These are frond-like structures, produced vegetatively by a parent frond, that are smaller and lacking roots. They are less buoyant and sink when they become detached. This is understood to be partly as a result of high starch accumulation (Xu et al., 2018). In this state, duckweed colonies can overwinter or survive other short-term stresses, such as surviving under ice in watercourses when frozen, or short term droughts (Kuehdorf et al., 2014). When suitable growth conditions return, turions then rise to the water surface, where they vegetatively produce new individual plants, complete with root and full-size fronds (Appenroth, 2002).

1.5.2 Vestigiality

Vestigiality is the retention of genetically determined structures that have lost their original function. (Prout, 1964, Fong et al., 1995, Müller, 2002). This is a widespread occurrence in plants (Knobloch, 1951), and often appears where there has been a significant developmental change in a different aspect of a plants environment or lifecycle (Walker-Larsen and Harder, 2001; Sherman et al., 2008; Steiner, 1998). Investigations of vestigiality thus far have been largely descriptive and there is limited understanding of the evolutionary and molecular mechanisms behind organ loss in plants.

As the duckweeds morphologically represent multiple points on an evolutionary trajectory towards rootlessness (Figure 1-8), it is suggested that they could be a powerful tool in understanding this phenomenon, and that the recent development of duckweed specific genetic tools may help unlock this understanding (Yang et al., 2018; Vu et al., 2020; Acosta et al., 2021).

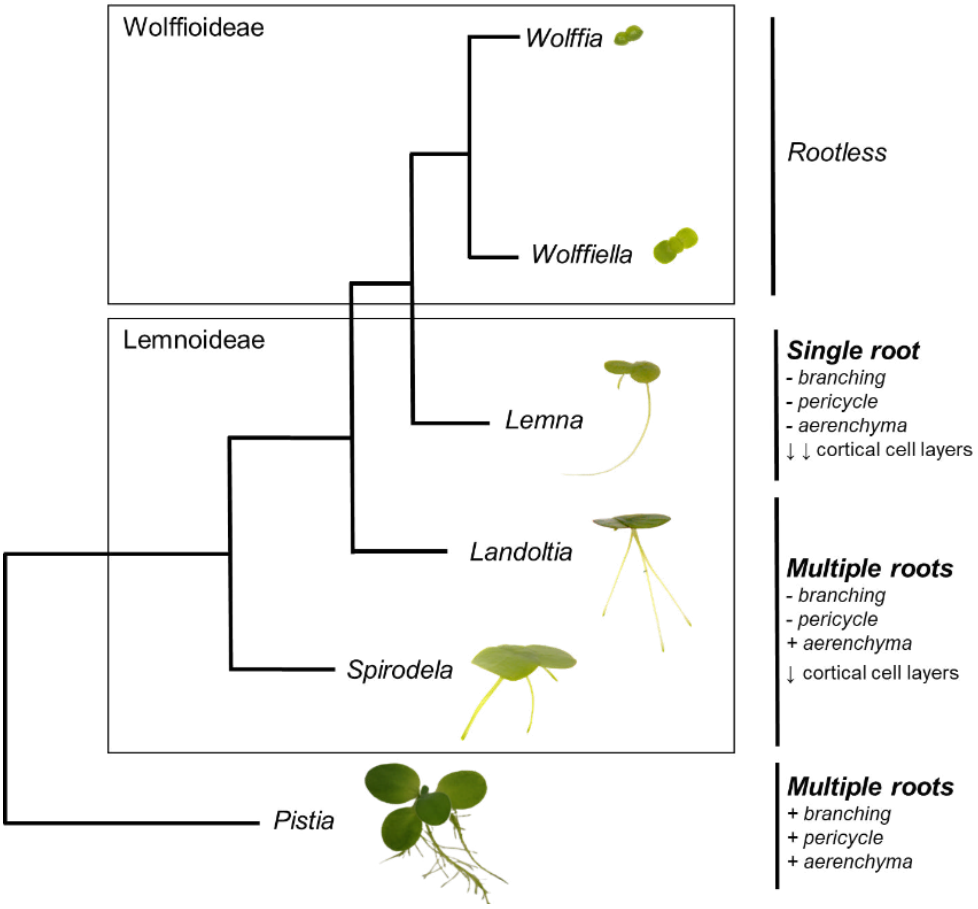


Figure 1-8. Representative phylogeny of the duckweed genera and *Pistia*. Highlighting the progressive loss of roots of roots and loss of individual root traits as genera diverge (indicated by + and -; arrows next to cortical cell layers indicate the progressive reduction in layer number as the genera diverge) (after Tippery and Les, 2020). Representative images (not to scale) of species from each genera are shown for illustrative purposes.

It is suggested that duckweed roots have a limited role in nutrient uptake. For example, *Lemna* gibba individuals without roots have been observed in their natural habitat (Hegelmaier, 1868), and it has been shown that frond contact with

media is required to maintain growth, but roots are not necessarily required (Gorham, 1941; Muhonen et al., 1983). Though these studies don't rule out the possibility that roots still play some role in resource capture, it suggests at least a diminished or shared role.

1.5.3 Anatomy

As mentioned previously, duckweed anatomy, particularly root anatomy, has not received much research attention, and where it has been discusses, it is largely descriptive of a small subset of species, typically *Spirodela polyrhiza* or *Lemna minor*. Since *Landoltia punctata* has been classified as its own monophyletic genus, there has been no description of its root anatomy. What appears consistent is the description of a reduced vascular cylinder, comprising of a single xylem, two or fewer sieve elements, and 5-8 phloem paerenchyma cells. This is surrounded by an endodermis, three cortical cell layers, and an epidermis (Kim, 2007; Echlin, 1981), with a total absence of lateral roots or root hairs (Landolt, 1998). As a primarily asexually reproducing set of plants with a variable lifecycle, it can be challenging to stage duckweed for consistent sampling. In population level studies this is less of an issue but proves challenging when seeking to answer developmental questions.

1.6 Aims and objectives

This study aims to develop approaches for high throughput anatomical phenotyping in order to investigate anatomical traits in monocots and how they relate to water accessibility. These approaches will be applied in investigating root anatomy in several species which span a wide environmental and morphological range (pearl millet, duckweed, maize, brachypodium) in order to survey variation in root traits and how they relate to function.

This will include:

- Investigation of duckweed root anatomy and their potential as a model family to investigate anatomical traits and vestigialization.
- Development of a high throughput laser ablation tomography platform to investigate cereal anatomy and its applicability to other species
- Develop an automated image analysis platform for root anatomical traits.
- Phenotyping a collection of pearl millet lines for drought tolerance, architectural, and anatomical traits.
- Identify root anatomical phenotypes associated with agronomically relevant characteristics and identify genomic associations with these traits in pearl millet.

Chapter Two:
Analysis of Duckweed Root Anatomy and Vestigialization

2.1 Introduction

As aquatic monocots, the duckweeds represent an ideal system for investigating variation in root anatomy in relation to water; particularly as they have previously garnered significant periods of research interest (Hillman, 1961; Landolt, 1986; Les et al., 2002; Laird and Barks, 2018; Acosta et al., 2021), have several species with sequenced genomes, and are well suited for lab cultivation. Especially conducive to this is the successive morphological reduction in the root as species have become more taxonomically divergent, and have moved further away from their terrestrial ancestors. This gives us a unique snapshot of the progression of organ loss over evolutionary time. Studies as far back as Hegelmaier's of 1868, have shown that duckweed roots may be dispensable or have minimal function, there is little experimental validation of whether or not duckweed roots can be considered vestigial. Furthermore, despite the many benefits of duckweed as a model species, high throughput methods for duckweed phenotyping are not particularly well-developed, especially for anatomical traits.

This Chapter presents the work of two papers, investigating anatomy in duckweeds. The first being a methods paper, describing current approaches in anatomical phenotyping techniques in duckweed, and what that has shown, and expanding on these with the development of novel methods for duckweed phenotyping, focussing particularly on the utilisation of µCT scanning, and how to best use this for duckweed and similar aquatic plants. The second, uses the developed techniques to investigate anatomical structural reduction in duckweed and how they accompany the loss of functions of the root system.

2.2 Aims

2.2.1 Phenotyping methods development

The first aim of this work is to develop phenotyping tools for growth, morphology and anatomy to bring what is achievable in duckweed phenotyping up to par with other model species. While research into duckweed is a growing field, this has largely focused on large scale “field” like experiments, ion content, or molecular investigation, with relatively few tools available to address developmental biology. Techniques developed include growth imaging, anatomical analysis via sectioning and µCT X-Ray imaging, uptake studies, and transcriptomics.

2.2.2 Root vestigialization

It is challenging to definitively characterize a feature as vestigial as there may be many ancillary roles or benefits an organ provides, however in order to determine if the salient function of the organ is lost, a range of techniques are used. For almost all angiosperms, a primary function of roots is to supply water and nutrients to the growing plant, sustaining growth of the aboveground tissues (Boyce, 2005). Typically, where salient function has been lost, organs undergo accompanying reductions in size and complexity. Therefore, duckweed root anatomy will be investigated alongside function.

Anatomy

Once validated, these tools will be used to conduct a survey of rooted duckweed species and close relatives in order to characterise the variation present in root anatomical traits in our collection and develop an understanding of whether anatomical traits are part of the trajectory of vestigialization seen in the morphology. With this data it will then be possible to identify correlations between traits present in roots and indicators of root function.

Root Function

Past experiments have shown that the roots and fronds of duckweed have acquired different function roles to those of their land-based relatives. For example, Gorham (1941) demonstrated that in *Lemna minor* frond contact with water was required for normal growth, and Muhonen et al (1983) found that *Spirodela polyrhiza* was still capable of growth following removal of roots. Though these studies imply that roots may not be required for normal growth, they do not explicitly test the capacity of duckweed roots for resource capture. Furthermore, recent studies show that both roots and fronds have the capacity to acquire nitrogen in both *Lemna minor* and *Landoltia punctata*, complicating the picture (Cedergreen and Madsen, 2002; Fang et al., 2007). To better resolve this, systematic approaches testing the effect of root excision on growth and nutrient uptake are required.

Nutrient transporter expression

In *Arabidopsis thaliana*, a land-based plant with a root system that has well characterised functionality, the expression levels of transporters such as phosphate transporter 1 (PHT1;1) increases under low phosphate conditions (Muchhal et al., 1996). Investigating whether or not duckweed shows a similar transcriptomic response to this treatment will add a molecular perspective to duckweed root vestigialization. This will be further supported by investigating the level of tissue specificity of nutrient transporter expression across the whole plant, and comparing this to plants with well characterised root function.

Model for vestigiality

Each of the experimental approaches outlined above, using the developed phenotyping methods, will go towards addressing whether or not duckweed roots fit the hallmarks of vestigiality. This characterisation will be novel and interesting

as and of itself, though will also validate the use of duckweed as a toolkit to investigate loss of root traits, root function, aquatic adaptation, and vestigiality as a whole.

2.3 Materials and methods

2.3.1 Duckweed growth and culture

Plant Material

All duckweed stocks used in this experiment were obtained from the Landolt collection, ETH Zurich (http://www.duckweed.ch), except for *Spirodela polyrhiza* lines 9509 and 7498 which were provided by Klaus Appenroth, Friedrich Schiller University, Jena. Four-digit numerical codes following species names refer to their Landolt accession number. *Pistia stratiotes* was obtained from JAM Aquatics, Wrexham, UK.

List of Lines

Table 2-1 List of duckweed and *Pistia* lines used and provenance

Supplied By	ETH no	Country	Region	Genus	Species
ETH	7760	Australia	South Australia	*Landoltia*	*punctata*
ETH	0049	China	Sichuan	*Landoltia*	*punctata*
ETH	7339	Burundi		*Lemna*	*aequinoctialis*
ETH	7922	Argentina	Buenos Aires	*Lemna*	*gibba*
ETH	9250	Finland	Etela-Suomi	*Lemna*	*japonica*
ETH	7123	Canada	Saskatchewan	*Lemna*	*minor*
ETH	7123	Canada	Saskatchewan	*Lemna*	*minor*
ETH	8389	South Africa	Transvaal	*Lemna*	*minor*
ETH	9260	Italy	Trentino-Alto Adige	*Lemna*	*minuta*
ETH	8539	USA	Virginia	*Lemna*	*perpusilla*
ETH	9243	Vietnam	Cà Mau	*Lemna*	*tenera*
ETH	7192	Uganda	Kigezi	*Lemna*	*trisulca*
ETH	9109	Poland	Podlaskie	*Lemna*	*turionifera*
ETH	7005	USA	Florida	*Lemna*	*valdiviana*

ETH	9208	Bolivia	La Paz	*Lemna*	*yungensis*
ETH	7820	Paraguay	Formosa	*Spirodela*	*intermedia*
KA	9227			*Spirodela*	*intermedia*
KA	9509	Mozambique	Maputo	*Spirodela*	*polyrhiza*
ETH	9192	Colombia	Cordoba	*Spirodela*	*polyrhiza*
KA	5543			*Spirodela*	*polyrhiza*
KA	7498			*Spirodela*	*polyrhiza*
	5684			*Wolffia*	*arrhiza*
	8324			*Wolffiella*	*lingulata*
JAM				*Pistia*	*stratiodes*

Stock Cultivation

Stocks of all lines used were maintained on various size flasks of liquid N-media or Schenk & Hildebrandt media (SH-media; Appenroth et al., 1996) at 120 µmol/m^2/s^1 light intensity and 16/8 h light/dark cycle in a Conviron growth chamber, set to 22 °C with 70% RH.

N media: KH_2PO_4 (60µM), $Ca(NO_3)_2$ (1 µM), KNO_3 (8 mM), $MgSO_4$ (1 mM), H_3BO_3 (5 µM), $MnCl_2$ (13 µM), Na_2MoO_4 (0.4 µM), FeEDTA (25 µM)

SH Media: Ammonium phosphate monobasic (2.6 mM), Calcium chloride (anhydrous) (1.4 mM), Magnesium sulphate (anhydrous) (1.6 mM) , Potassium nitrate (24.8 mM), Boric acid (80 µM), Cobalt chloride·6 H_2O (0.4 µM), Cupric sulfate·5 H_2O (0.8 µM), EDTA acid, Na_2·2 H_2O (54 µM), Ferrous sulfate·7 H_2O (54 µM), Manganese sulphate· H_2O (59 µM), Molybdic acid (sodium salt)·2 H_2O (0.4 µM), Potassium iodide (6 µM), Zinc sulfate·7 H_2O (3.5 µM), Sucrose (58.4 mM).

Cultivation for Anatomical analysis and phenotyping development

Plants were grown in 250 ml conical flasks containing 150 ml of liquid N-media in the same conditions as stocks. Flasks were inoculated with 5-10 colonies from the stock collections and grown for 1-5 weeks.

Cultivation for root removal

Plants were grown on 100 ml of SH media in 500 ml flasks, seeded initially with 3 colonies per flask grown under same condition as stocks. For *Pistia stratiotes*, each flask was seeded with a young individual plant with 3 emerged leaves visible to the naked eye.

Cultivation for low P treatment

Three fronds of *Spirodela polyrhiza 9509* per flask were seeded into six 250ml flasks containing 100 ml N-media. After 7 days of growth media was removed and replaced with fresh media to ensure replete conditions. After 10 days of growth media was replaced, in 3 flasks with regular N-media and in 3 N-media made

without KH_2PO_4 and plants and flasks were rinsed three times with this media. Plants were then grown for an additional 24 hours.

Cultivation for RNA extraction

Spirodela polyrhiza 9509 was seeded into 500ml flasks containing 150 ml N-media and grown for 14 days. After 7 days of growth media was removed and replaced with fresh media to ensure replete conditions.

2.3.2 µCT anatomical protocol development

Embedding methods comparison

Petrolatum embedding was compared to three alternate methods for suitability in maintaining frond stability during µCT scanning. Previously, many small plant µCT

methods have used a small, sealed chamber (Furuya et al., 2019; Kunishima et al., 2020) in order to reduce desiccation of the samples during scanning. This established method, along with keeping duckweed in N-media, and embedding them in N-media solidified with agarose, was tested.

To determine sample stability, fronds were imaged with a digital camera at 0 h, 1 h, and 6 h after preparation (so as to ensure stability exceeded the typical scan time of 1–2 h), with the area of each frond measured at each time point, and observations were made of changes in position and condition of frond over time.

For each treatment, two 24 well trays containing 16 individual plants were prepared according to the different methods and stored under conditions similar to those used in the CT scanner, between imaging intervals.

For plants in air (sealed chambers), plants were removed from media, dried gently on blotting paper, placed individually in wells, imaged, and then covered with laboratory film (Parafilm, Bemis) and stored in darkness until further imaging; Parafilm was removed before and reapplied after imaging.

For liquid media, 2.5 ml of N-media was pipetted into each well, and an individual frond was transferred into each well. Plants were immediately imaged, covered with Parafilm and stored in darkness until further imaging at 1 and 6 h, when Parafilm was removed before and reapplied after imaging.

For embedding in solidified media, agarose (1% w/v) was added to N-media, autoclaved, and allowed to cool to 55°C in an incubating oven. 2.5 ml of this molten agarose-media was transferred to each of 32 wells, and individual plants were then added to each well. Wells were surrounded with ice water, then an additional layer of 0.5 ml of agarose was applied to each well to cover the plants. Trays were imaged, then stored un-covered in darkness until further imaging at 1 and 6 h.

For petrolatum embedding, plants were dried, rinsed in mineral oil, dried again, then transferred to wells filled with 2.5 ml of molten petrolatum, wells were surrounded with ice water, and a minimal amount of petrolatum (~0.2 ml) was then applied to the surface of each frond to cover them completely. Trays were imaged, then stored un-covered in darkness until further imaging at 1 and 6 h.

Frond area at each time point was measured using the magic threshold wand tool in FIJI (Schindelin et al., 2012), and percentage change in area was calculated in Microsoft Excel. Observations were also made at each time interval of relative position of frond in well, and any changes in condition or appearance of fronds. The frond area at each time point was analyzed in Prism 8 (GraphPad) using a two-way analysis of variance (ANOVA) with a Tukeys multiple comparison test, with an n = 32 and a p value of 0.05. Percentage area change of fronds over time was calculated in Excel and graphed in Prism 8.

Optimisation of petrolatum embedding

To prepare samples for X-ray µCT scanning, plants were embedded in a core of petrolatum inside of modified syringes (**Figure 2-1**). This is a novel method developed specifically for µCT scanning duckweed, so thorough validation was performed, and the functionality tested by assaying a range of anatomical features in duckweed.

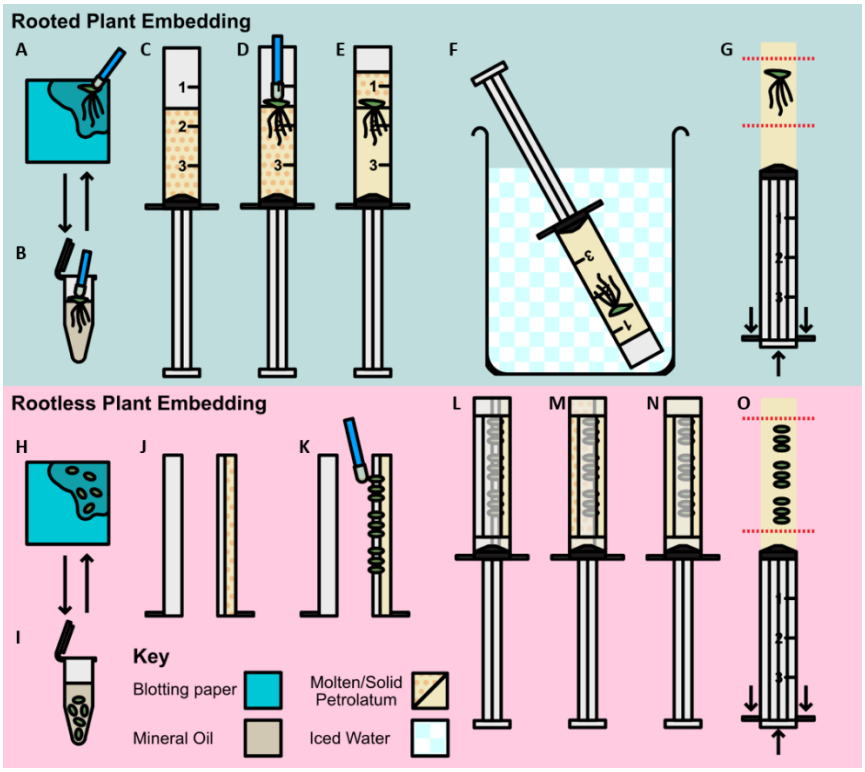


Figure 2-1. Preparation and embedding of plant material for µCT scanning. (A–G) Rooted plant preparation and embedding; (A, B) Pre-preparation of plant material; (A) Plant transferred by petrolatum coated inoculating loop to blotting paper. (B) Plant rinsed in mineral oil then transferred to blotting. (C–G) Rooted plant embedding (C) Syringe barrel cap cut and removed, and barrel two thirds filled with molten petrolatum. (D) Plant transferred to syringe with loop and allowed to partially solidify. (E) Additional molten petrolatum added to barrel, covering plant. (F) Syringe transferred to ice bath. (G) Syringe plunged, and petrolatum core trimmed to region of interest (ROI). (H–O) Rootless plant embedding and preparation; (H, I) Pre-preparation of plant material; (H) Plants removed from media and transferred to blotting paper, (I) Plants rinsed in mineral oil and decanted to blotting paper. (J–O) Rootless plant embedding (J) Syringe barrel cap cut and removed and cut in half along barrel length, two thirds filled with molten petrolatum and allowed to cool. (K) Small plants pressed gently into petrolatum with inoculating loop. (L) Plunger replaced and barrel resealed with microporous tape. (M) Remainder of syringe filled with molten petrolatum. (N) Petrolatum allowed to solidify, cooling in ice bath. (O) Syringe plunged and petrolatum core trimmed to ROI.

Two different approaches were used depending on whether embedding rooted or rootless plants(without roots, more plants could be embedded in a smaller volume of petrolatum and imaged together, increasing throughput).

The following protocol, once components have been prepared, took approximately 3–5 min to prepare a core with a rooted sample embedded, and 5–8 min to prepare a core with between three and nine rootless plants embedded. Unless specified, all steps were carried out at room temperature.

Plant preparation

Different embedding methods were used depending on the size of the sample and the presence or absence of roots, however, the pre-preparation method used was the same for all sized plants; plants were removed from media using a petrolatum coated inoculating loop (to avoid physical damage to the frond), and dried of excess media by placing on blotting paper and patted lightly (Figure 2-1). Samples were then transferred to mineral oil, and shaken gently, to remove any remaining media and reduce cohesion between roots (where applicable; Figure 2-1B). Rooted samples were transferred to blotting paper using an inoculating loop (Figure 2-1A), and rootless samples were decanted with the oil directly onto the blotting paper.

Rooted Plant Embedding

A total of 50 ml of petrolatum was decanted into a 100 ml glass beaker, and placed in a 55°C incubation oven until molten this was then stored at the same temperature until use. Syringes (3 ml Soft-Ject HSW) were prepared by raising the plunger and cutting the barrel tip off with a razor blade at the shoulder thus leaving just the uncovered open barrel cylinder. Petrolatum was then poured from the beaker into the syringe until two thirds full of molten petrolatum (Figure 2-1C). Until use, filled syringes were stored at 55°C. Pre-prepared plants, were then transferred to the molten petrolatum and agitated lightly to separate the roots and dislodge any trapped air (Figure 2 1D). When the petrolatum had solidified enough to hold the frond in place (approximately 30 s), the remaining third of the syringe barrel was filled with molten petrolatum (Figure 2-1E). The syringe was then placed in an iced water bath until the petrolatum core containing the embedded duckweed was fully solidified (∼3 min; Figure 2-1F). Once the core was solid, the plunger was depressed, expelling the core which was then trimmed using a razor blade to minimize the regions without sample included for ease of alignment when scanning (Figure 2-1G). The prepared core was then stored in an ice bath until ready for use.

Rootless Plant Embedding

Petrolatum was prepared as in the previous section. The tip of the syringe was removed, and the barrel bisected along the vertical axis and then taped (microporous tape) along the end of the half barrel. One half of the barrel was then filled to two thirds full of molten petrolatum and allowed to solidify (Figure 2-1J). Pre-prepared samples were then partially embedded by gently pressing the fronds horizontally with an inoculating loop into the soft petrolatum (Figure 2-1K). This should only be done enough to secure the frond in place, while ensuring the frond is not pressed hard enough to push the frond through the petrolatum and in

contact with the plastic of the syringe. The syringe was then reassembled around the plunger and fastened with micropore tape to seal the seams (Figure 2-1L). The remaining volume of the syringe barrel was then filled with molten petrolatum by pouring down the unfilled side of the barrel (Figure 2-1M). Once the petrolatum was partially set (Figure 2-1N), the syringe was cooled in an iced water bath as in Figure 2-1F until the petrolatum core had fully solidified. The plunger was then depressed expelling the core; this was then trimmed by hand to the region of interest (Figure 2-1O). The prepared core was then stored in an ice bath until used. In the case of samples < 3 mm the same process was applied using Falcon Sterological Pipettes (1 ml) instead of the syringes, this allowed for less petrolatum interference during scanning and the ability to achieve higher scanning resolution due to smaller sample width.

µCT Scanning protocol

Each specimen was scanned on a Phoenix Nanotom 180 high resolution X-ray CT system, (Baker Hughes Digital Solutions GmbH, Wunstorf, Germany) at the Hounsfield Facility, University of Nottingham, United Kingdom. Cores extruded from syringes samples (Figure 2-2B) were mounted on a 10 mm diameter rod using the petrolatum drawn from the edge of the core to hold it in place during the scan on the rotation stage (Figure 2-2C).

Figure 2-2 Duckweed embedded in petrolatum core mounted in µCT scanner. (A) X-ray detector panel Hamamatsu CMOS Flat Panel (C7942SK-05). (B) Petrolatum core, (C) Rotation stage, (D) X-ray tube (Source).

Cores prepared in the serological pipettes were scanned directly by placing the tube within the rotation stage. The scan parameters were optimized to allow a

balance between a large field of view and a high resolution (which was dependent on the genera) with the aim to also provide good contrast between petrolatum, plant material, and gas air filled pores. Each sample was imaged using a fast scan procedure with a voltage and current of 70 kV and 100 µA, respectively at a voxel size resolution of between 6–0.8 µm (depending on the genera and sample preparation size), with the specimen stage rotating through 360 degrees at a rotation step increment of 0.25 degrees over a period of 39 min, producing a total of 1,440 projection images by averaging three frames with an exposure of 1,500 ms each, at every rotation step. These settings were optimal in providing the data for high throughput analysis, longer settings can also be used should there be a requirements for better image quality by changing the scan settings to include more projections, increase image timing and increase the number of images captured (average/skip) for each projection to reduce movement in the sample during the scan examples of such setting are shown in Figure 2-2.

Table 2-2 Standard scan settings used for embedded duckweed cores (of different genera) used at high throughput and an example of high image quality settings.

	X-Ray energy (kV)	X-Ray current (µA)	Projection images	Detector timing (ms)	Image averaging	Image skip	Resolution (µm)	Scan time (min)
Standard settings	70	100	1440	1500	1	0	0.8–6	39
Long scan example	75	120	2440	750	3	2	0.8–6	120

Each scan was then reconstructed using DatosRec software (Baker Hughes Digital Solutions GmbH, Wunstorf, Germany). Radiographs were visually assessed for sample movement before being reconstructed in 16-bit depth volumes with a beam hardening correction of 3. An inline median filter was applied to reduce noise in the image. Reconstructed volumes were then post processed in VG Studio MAX (version 2.2.0; Volume Graphics GmbH, Heidelberg, Germany) see Image Processing.

2D image data analysis: ImageJ

Two-dimensional (2D) image stacks were exported in three different projections, XY, ZX, and YX from VGStudioMAX (version 2.2.0; Volume Graphics GmbH, Heidelberg, Germany) from the raw CT data. Image stacks created from VGStudioMAX were exported at resolution thickness of 0.8-6 µm depending upon the genera. Different traits within the duckweed were easier to visualize depending on the image plane XY (top down) was best for visualizing gas space interconnectivity and root structure. Whilst ZX (front on) or YX (side on) are best to visualize cross sections along the length of the frond such as **Figure 2-3.**F and that shown in Figure 2-3.

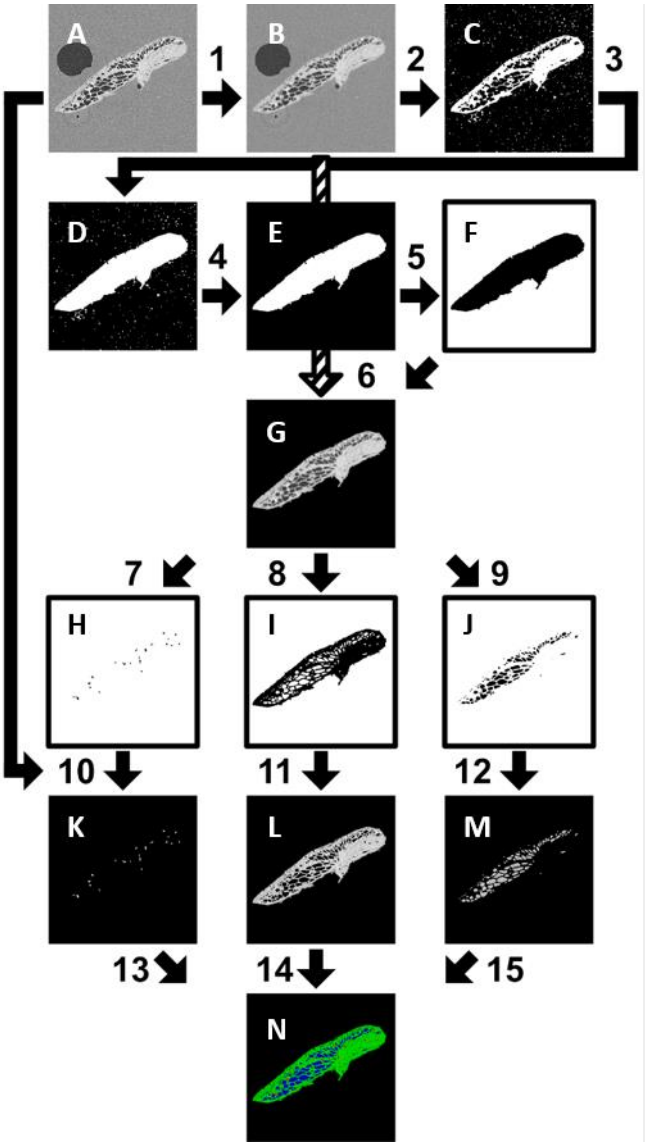


Figure 2-3. Two-dimensional (2D) slice Image segmentation procedure. Carried out in ImageJ, step instructions using ImageJ process commands. The starting point (A) is an 8-bit image, or image stack (referred to interchangeably as image). (1) Gaussian Blur 2.5 pixel sigma radius (2) Threshold 0-155, Invert (3) Fill Holes, Open (4) Analyze Particles (Pixel size:1000-∞, Circularity 0–1, Show Mask) (5) Invert, Dilate, Close, Fill Holes, Erode (6) [((B)Add 1)-F] (7) Threshold 225–255; Analyze Particles 30-Infinity, Invert (8) Threshold 126–224, Invert (9) Threshold 1–125, Invert (10) A–H (11) A–I (12) (A: Invert)-J (13) Merge Channels: C4 (gray) = 'K' (14) Merge Channels: C2(green) = 'L'; (15) Merge Channels:C3(blue) = 'M'. All values given are suggested for described scan settings.

As within VGStudioMAX, the image stacks were segmented using the greyscale distributions (linked to X-ray attenuation and thus relating to the density of the material) into different categories: plant tissue, gas, petrolatum, and high density regions (thought to be starch deposits based on measurement of particle size (Pankey et al., 1965), following the procedure in Figure 2 3. The image stacks (referred to interchangeably with image) were loaded into FIJI; then smoothed with a Gaussian Blur (2.5 pixel sigma radius) to reduce noise (Figure 2 3,1), thresholded (0–155) and processed using ImageJ binary processing tools (Invert, Fill Holes, Open, Analyze Particles (Pixel size:1000-∞, Circularity 0–1, Show Mask, Invert, Dilate, Close, Fill Holes, Erode) to create an overlay mask containing all plant material and minimal petrolatum or gas outside the plant (Figure 2 3,A-F). This was then inverted and removed from the blurred image, leaving only the features of interest (Figure 2 3, 2-6).

The features of interest (Figure 2 3G) were then manually thresholded, using eight-bit image stacks, to different levels to create masks for the desired categories, for example applying a threshold of 1–125 created a mask for enclosed gas spaces, 126–224 for regular plant tissue, and 225–255 for the high density tissue (believed to be the starch deposits). These values can be adjusted to suit the specific image parameters and better align with observed features as required. Full automated thresholds could be applied when processing multiple samples of a similar size. Full set up of this procedure took approximately 10 min, to adjust for variation in threshold values, then subsequent use took under a minute to run for each scan image stack.

3D image data analysis: VG Studio Max

Reconstructed volumes were post processed in Volume Graphics Studio MAX (version 2.2.0; Volume Graphics GmbH, Heidelberg, Germany). Samples were initially assessed to determine if further filtering was required to reduce image noise. An adaptive gauss filter (smoothing = 1.2, Edge Threshold = 1, Iterations = 1,

multiplier = 1) was applied to the data set to reduce the noise and help with image segmentation if this was required. Segmentation was then performed using surface determination and region growing tools. By selecting greyscale tolerances (determined by sample density and X-ray attenuation) a selection of just plant material could be achieved. This selection could then be saved as a region of interest (ROI), and then following the same procedure, be added to using the region grower tool until the whole plant was selected. The ROI smoothing function of 1 was used to reduce noise artifacts before rendering as a 3D model which rotated and clipped to visualize specific regions and structures within the specimen. While largely dependent on processing power of the hardware used, the manual steps of this method took under 5 min to segment a single region of interest.

Validation of CT scanning & Turion composition analysis

All sunken turions were collected from a colony of S. polyrhiza 9509, 2 weeks after inoculation. Of the turions at the bottom of the flask, half were transferred to 50 ml fresh media in a 50 ml falcon tube and stored at 4°C in constant darkness for 8 weeks. The remaining half were transferred to fresh media in a new flask under standard described growth conditions for the same time period. From the new flask, three turions that were floating at the surface of the media, and three that remained sunken at the bottom of the flask were collected. Additionally, three turions from the cold treated set that were not floating were also collected.

All plants were prepared following the rootless plant protocol and scanned using the fast scan µCT settings described. Image stacks were then processed using the described 2D pipeline in FIJI. Post segmentation, analysis was carried out to determine the percentage composition of each turion based on the three categories of plant tissue, gas, and high-density tissue. Total area of each group of

was measured for each image stack in FIJI. Based on the known high accumulation of starch in *Spirodela* turions, the size of starch granules in turions, (Xu et al., 2011), the high density of starch, and comparison with iodine stained turions, the high-density regions on the scans are likely to be starch deposits. However, other structures have been identified in duckweed fronds that may cause a similarly increased level of X-ray attenuation, such as calcium oxalate or tannin deposits (Mazen et al., 2004; Xu et al., 2018). While iodine staining for a greater duration of time shows that there is starch present throughout the turion, measuring these larger presupposed starch deposits may be a useful proxy for total starch content. To determine turion composition, following measurement of image stacks (Figure 2-3H-J) in FIJI, total area of each measured component of turions was calculated in Excel, and percentage composition was calculated and graphed in Prism 8, statistical analysis was not performed due to small sample size.

2.3.3 Histological anatomical protocol development

Root embedding for sectioning

The sectioning method presented by Atkinson and Wells (2017) was adapted to better suit the specifics of duckweed anatomy. Polypropylene 15 ml conical centrifuge tubes (Fisher Scientific) were cut perpendicular to the length of the tube into 5 cm lengths of uniform cross section. Micropore tape was used to seal one end of each of the lengths of tube, which were then filled with 5 ml of molten agarose (5% w/v), and allowed to cool to 39°C. Plants were then removed from media with an inoculating loop, dried of excess media on filter paper, and then submerged in the agarose.

When embedding plants for root sectioning, for blocks with multiple roots it is desirable for these to be parallel to each other so they can be sectioned in the same plane. To achieve this, it was best to hold plants with forceps by the frond, submerge them fully in the agarose to the bottom of the tube, and slowly pull the fronds back toward the surface, which aligned the roots beneath the frond.

Blocks were trimmed by hand at the base prior to mounting to position the sample perpendicular to plane of the desired section. For sectioning a vibrating microtome (7000smz-2, Campden Instruments, Ltd.) was used, with a section thickness of 150 μm, blade speed of 1 mm/s and frequency of 65 Hz.

Imaging

Sections were stained in fluorescent brightener 28 (calcofluor) solution (0.3 mg/ml) for 1 min then rinsed in RO (reverse osmosis, distilled and autoclaved and sterile) water for 1 min before imaging on a confocal laser scanning microscope (Leica SP5). This was done using a 405 nm diode laser at 6% and hybrid detector with a range of 440–450 nm, gain of 15%, and pinhole of 0.5 AU. Basic fuchsin staining was conducted following the same procedure, at a concentration of 0.01% following sectioning prior to calcofluor staining, and imaged using 561-nm excitation and detected at 620–630 nm on a hybrid detector at a gain of 50%, and pinhole of 1 AU.

Frond sectioning

Frond embedding was conducted similarly to the procedure for roots. The number of plants embedded per block was variable and depends on the number of roots per frond. For multi-rooted species (*Spirodela* spp., *Landoltia punctata*), one individual per tube was embedded to prevent sample coalescence. For single rooted (*Lemna* spp.), 3–5 plants were embedded per tube, and for rootless plants (*Wolffiella* spp., *Wolffia* spp., turions), 10-20 plants were embedded in a 5 ml block. Embedding multiple plants per block increases the potential throughput of this method, however, can reduce the stability of the block during sectioning.

To avoid damage to embedded fronds, plants were handled by the root, or Pasteur pipette and inoculating loop for rootless plants. Fronds were submerged in the

agarose, and to prevent fronds resurfacing after embedding, they were embedded as the surface of the agarose was setting and monitored until set.

The same sectioning protocol was used for fronds as roots, however for some samples the section size was increased to 250µm to decrease sample attrition rates. For confocal imaging for anatomy, fronds were stained and imaged using the same protocol as roots.

To image starch content and distribution in fronds and turions, sections were prepared as above, then stained with dilute Lugol's iodine (25% v/v) for 45 s, rinsed for 1 min in RO water, and imaged on a dissecting brightfield microscope (Zeiss).

2.3.4 Whole population area imaging

Imaging

To image whole flasks for population level growth experiments in a high throughput manner, a special imaging chamber was constructed. A watertight box with a transparent base and translucent sides was positioned over a digital camera to enable flasks to be imaged from below. Flasks were transferred to the box, and the box was filled with RO water to meet the water line in the flask so as to correct for the optical distortion of the flask. Two layers of filter paper were placed over the top of the box to provide a neutral backdrop for the flask and diffuse lighting.

Measurement

To analyse images from the imaging chamber, image sequences were loaded into FIJI, cropped to the region of interest and scaled to the reference target in the image. The blue channel was then isolated, subject to a 2 px radius gaussian blur, and thresholded. The threshold was set to isolate just the fronds in the image, and required adjusting for each imaging session due to variation in ambient light level. Images were then measured using the particle analysis tool in FIJI.

For *Pistia*, images were again split into RGB channels, but the red channel was retained. This was then subject to gaussian blur 7 px radius and again only the aerial tissues selected using the threshold tool. In rooted samples where this alone was not sufficient to separate frond and root, the select polygons tool was used to exclude any additional root captured by thresholding.

2.3.5 Clearing

Plants were cleared (Figure 1-7) based on a slight modification of the ClearSee procedure described by Kurihara et al. (2015). As fluorescent markers were not being used, plants were fixed overnight in ethanol and acetic acid (3:1 v/v) rather than paraformaldehyde, as this reduced the toxicity and requirement for vacuum infiltration, which can be damaging to the air spaces. Plants were then rinsed three times in RO water and left for 30 min, then RO water was replaced with ClearSee solution (Kurihara et al., 2015) and left to clear for 2 weeks. Prior to imaging, plants were stained for 1 h with calcofluor in ClearSee (100 μg/ml), and then washed in ClearSee for 1 h. Imaging was carried using a confocal laser scanning microscope (Leica SP5), using a 405 nm diode laser at 12% and hybrid detector with a range of 440–450 nm, gain of 25%, and pinhole of 0.5 AU.

2.3.6 Vestigiality analysis methods

Root anatomical analysis

Plants were sampled between 1-4 weeks of growth. Plants were selected with roots of average or greater length, and fronds of average or greater area based on visual appraisal detailed above. For each line, ten individual plants were embedded and sectioned as per 2.3.3, and 5-10 root sections collected per plant, and sections were stained and imaged as per Section 2.3.3. For a subset of lines, sections were additionally stained with basic fuchsin at a concentration of 0.01%. A

representative image of a single section per plant was selected and measured using FIJI (Schindelin et al., 2012). Cells were classified into layers in concentric rings from the endodermis outwards. The diameter of each layer was measured, as was the number of cells in each layer, along with the diameter of the endodermis, number of endodermal cells, and number of cells in the stele.

A single image section per plant was selected based on quality and representation, then measured using FIJI. Cells were classified into layers in concentric rings from the endodermis outwards. The diameter of each layer was measured, as was the number of cells in each layer, along with the diameter of the endodermis, number of endodermal cells, and number of cells in the stele. Diameters were measured using the ruler tool. At each layer, diameter was measured from 5 points around the circumference of the layer, measuring the maximum distance between points on the layer, then the mean was taken of these 5 points for each layer. Epidermal cells had poor dye penetration, and a reduced fluorescence on the confocal microscope, and so could not be reliably counted.

Root removal treatments and imaging

For the root removal experiment, plants were grown in SH media. For the control treatment, no manipulation was undertaken. In the root removal treatment, all visible roots (typically less than 1mm) were removed from colonies daily using ethanol sterilised surgical scissors. For *Spirodela polyrhiza* and *Lemna minor*, each treatment consisted of five individual flasks, each seeded with 3 colonies onto 100 ml of media. Individual flasks were treated as a replicate and flasks were arranged randomly in the growth cabinet and re-randomized daily. For *Pistia stratiotes*, each flask was seeded with a young individual plant with 3 emerged leaves visible to the naked eye, to a total of 7 plants/treatment. The treatment regimen was conducted for 11 consecutive days. Plants were imaged daily using the described flask area measurement protocol.

Root reduction and wind speed environmental interaction

To investigate the role of the root in affecting the interaction of the plant with its environment roots were trimmed to set lengths and the plants were subjected to an artificial wind treatment. The experiment was setup was in a 40 l x20 w x 15 d cm open top tank, filled to the brim with tap water, with a domestic home fan set to an operation speed and positioned a distance from the tank as to create a continuous air current of 10 m/s (measured with an anemometer), consistent over the area of the tank.

Three representative individual duckweed fronds of average size, without visible daughter fronds, and with roots longer than 40mm were selected from a flask of *Lemna minor* 9505.

Roots were trimmed to a starting length of 40mm, then one at a time plants placed in the "fanotyping" set up, 5 cm away from the edge of the tank nearest the fan. They were held in place with forceps, and then released next to a ruler at the same time as the starting of a stopwatch, the time taken for the plant to travel 15cm was recorded, and this was repeated 5 times for technical replicates, and this was repeated for each of the three selected plants. The roots were then sequentially trimmed by 5mm increments, and the measurements were repeated, down to 0mm of root.

Root removal ionome and nitrogen content analysis

Samples were harvested immediately following the root removal experiment. Prior to harvesting, roots were removed from fronds or aerial tissues and washed 3 times for 2 minutes with MilliQ water. Samples were placed in pre-weighed Pyrex test tubes, and dried at 88°C for 24h. Then, dry weight was recorded, and 1 ml concentrated trace metal grade nitric acid Primar Plus (Fisher Chemicals) spiked

with in internal standard was added to the samples that were further digested in DigiPREP MS dry block heaters (SCP Science; QMX Laboratories) for 4 hours at 115°C following the method adapted from Danku et al.,(2013). After digestion, samples were diluted to 10 mL with 18.2 MΩcm Milli-Q Direct water and elemental analysis was performed using an ICP-MS, PerkinElmer NexION 2000 and twenty-three elements were monitored (Li, B, Na, Mg, P, S, K, Ca, Ti, Cr, Mn, Fe, Co, Ni, Cu, Zn, As, Se, Rb, Sr, Mo, Cd and Pb) but only the 14 elements present in our growth media were subject to downstream analysis. To correct for variation within each ICP-MS analysis run, liquid reference material was prepared using pooled digested samples, and run after every nine samples. Sample concentrations were calculated using external calibration method within the instrument software. Further data processing including calculation of final elements concentrations was performed in Microsoft Excel. For nitrogen content analysis, samples were freeze dried overnight, weighed and packed into tin foil pouches before analysis with a FLASH 2000 CHNS/O analyser.

Low P treatment analysis

After 24 h growth in low P N-media and regular N media, approximately 10 colonies per treatment were collected, washed twice with de-ionised water. Fronds and roots were separated using surgical scissors and flash frozen in liquid nitrogen prior to RNA extraction.

RNA extraction and sequencing

Spirodela polyrhiza 9509 was seeded into 500ml flasks containing 150 ml N-media and grown for 14 days. Media was removed and replaced after 7 days to ensure replete growth conditions. Plants were harvested and divided into 4 tissue types: mature frond, mature root, meristem zone and root tips, with 4 separate biological replicates (grown in different flasks) for each tissue type. Samples were stored in RNAprotect at 4°C until extraction 7 days later. Tissues were ground in liquid

nitrogen and RNA was extracted using TRIZOL followed by binding and washing with Qiagen RNeasy columns. RNA was frozen at -80°C until sequencing.

RNA concentrations were measured using a Qubit Fluorometer and the Qubit RNA BR Assay Kit (ThermoFisher Scientific) and RNA integrity was assessed using an Agilent TapeStation 4200 with an Agilent RNA ScreenTape Assay Kit (Agilent). For each sample, cDNA was generated from 250 ng of total RNA using the QuantSeq 3' mRNA-Seq library prep kit (Lexogen). Indexed sequencing libraries were prepared using a Lexogen i7 6nt Index Set (Lexogen). Libraries were quantified using a Qubit Fluorometer and the Qubit dsDNA HS Kit (ThermoFisher Scientific). Library fragment-length distributions were analyzed using an Agilent TapeStation 4200 and an Agilent High Sensitivity D1000 ScreenTape Assay (Agilent). Libraries were then pooled in equimolar amounts and final library quantification performed using a KAPA Library Quantification Kit for Illumina (Roche). The library pool was sequenced on an Illumina NextSeq 500 using a NextSeq 500 High Output Kit v2.5 75 cycle kit (Illumina), to generate approximately 5 million 75bp single-end reads per sample.

RNA-sequencing data analysis

Reads from each sample were mapped to sorted alignment files against the genome (*Spirodela polyrhiza* 9509 (oxford_v3)) using bwa mem (Li, 2013) and samtools (Li et al., 2009). Alignments were processed with bedtools (Quinlan et al., 2010) to bed format using bamtobed and then using merge into regions, and retained only if the merged region contained more than 5 reads and was more than 1 read long. Bed files were concatenated and sorted and reads were assigned into a genes unannotated 3'UTR using bedtools against the GFF file for the genome with a 150bp (one read) overlap distance, stranded. Read clusters were used to extend GFF CDS features which were extracted into a fasta file, combined with genome

decoys and quantitated with salmon (Patro et al., 2017). Differential expression analysis was performed on the quantitated read counts in Rstudio using the package DESeq2 (Love et al., 2014).

For *Spirodela* tissue specificity calculations, normalized counts from the four biological replicates were exported from DESeq2 and input into the TSPEX calculator set to log-transform input values and calculate tissue-specificity index, TSI (https://tspex.lge.ibi.unicamp.br/). For *Arabidopsis*, count data were extracted from the travadb (Camargo et al., 2020) database as normalized read counts from the DESeq2 data source, using the tissue types L.LAM.y - Leaf blade of the young leaf; M1 - SAM at 7 days after germination; R - Root without apex; R.A - Root apex. For *Zea mays*, normalized counts (FPKM) were obtained from qTeller (https://qteller.maizegdb.org/) using the tissue types Crown Root Node4 V7; CrownRoot_Nodes_1_3_V7 ; V5_Shoot_tip ; V7_Bottom_of_transition_leaf. Data for both species were input into TSI in the same manner as with *S. polyrhiza*. TSI values were then plotted as a heatmap in GraphPad PRISM.

Orthology analysis

For the genome wide identification of N and P transporters in *Spirodela polyrhiza*, the phylogeny construction framework outlined in Mutte et al., (2018) and Mutte et al., (2020) was used. In brief, protein sequences of known low- and high-affinity nitrate and phosphate transporters of plant model *Arabidopsis thaliana* were obtained from TAIR (https://www.*Arabidopsis*.org). This included 9 phosphate and 52 low-affinity and 7 high-affinity nitrate transporters. *Spirodela polyrhiza* protein sequences (version 2; Wang et al., 2014) were downloaded from Phytozome13 (https://phytozome-next.jgi.doe.gov) and *Zea mays* protein sequences (B73 reference NAM-5.0_Zm00001eb.1) were downloaded from MaizeGDB (https://www.maizegdb.org/assembly). BLAST database for *A. thaliana*, *S. polyrhiza* and *Z. mays* were generated using '*makeblastdb*' module in BLAST +v2.9.0 (https://blast.ncbi.nlm.nih.gov). Protein sequences from *Arabidopsis* were

used to query *Spirodela* and Maize blast databases independently for each transporter family using BLASTp. We used 0.01 as E-value cut-off to filter BLAST hits. The protein sequences of filtered BLAST hits were run through the InterproScan database (ver5.52–86.0; http://www.ebi.ac.uk/interpro/) to look for conserved domains. Presence or absence of individual domains and their organization were used as criterion to filter potential orthologous protein sequences. Filtered protein sequences were further tested by BLASTp search against *Arabidopsis* proteome (bi-directional blast analysis) to confirm orthology inferences. Gene IDs (converted between versions 2 and 3 of the *Spirodela polyrhiza* genomes using BLAST) encoding confirmed orthologous proteins were used for further tissue-specific expression analysis.

Statistical analysis

All statistical analyses were conducted in GraphPad Prism version 9.0 (graphpad.com). For the anatomical dataset, principal coordinates analysis was conducted on 19 variables and 210 rows utilising parallel analysis with 1000 simulations and a random seed. For root removal experiments, two-way repeated measures ANOVA was performed, followed with Šidák's multiple comparisons test to establish differences in growth on a per-day basis. For nutrient concentration comparisons generated by ionomic analyses, data were compared with one-way ANOVA followed by Šidák's multiple comparisons test to establish differences in concentration between individual nutrients. Log2 fold changes generated from ionomic data were calculated as Log2(elemental conc. roots removed)-Log2(elemental conc. rooted).

2.4 Results

2.4.1 µCT protocol development

Evaluation of sample embedding methods

Of the four preparation methods tested, only petrolatum embedding produced consistent usable results. When scanning was performed in either growth media or air, the frond or roots were able to move, and in agarose solidified N-media the plants became deformed, and decreased in area, presumably due to loss of turgor within the core (Figure 2-4). These observations were also confirmed in the µCT image data; in addition to a poor contrast between the agarose solidified media and the plant, there appeared to be respiration of the plant, creating a gas pocket around the frond, and significant shrinkage/movement of the frond within resulting in poor or unworkable data.

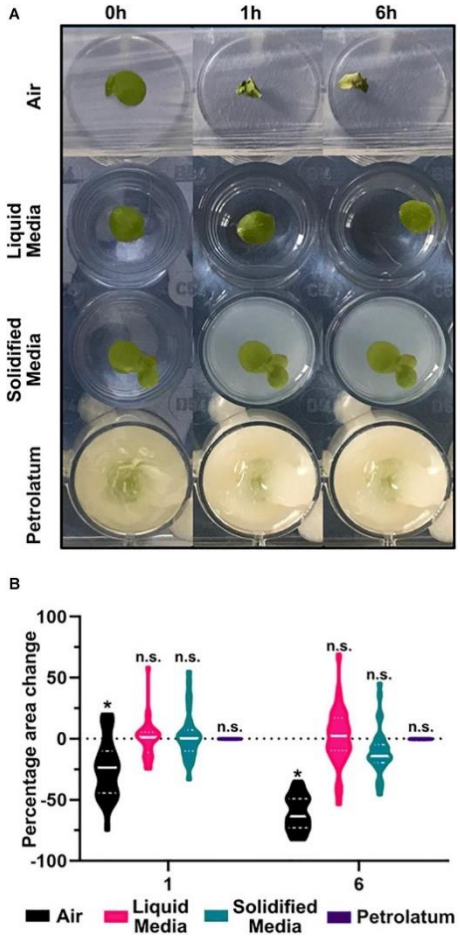


Figure 2-4. Preparation of samples in petrolatum provides the most stable method for CT imaging. (A) Representative images of *Spirodela polyrhiza* condition under different preparation methods over time. (B) Percentage change in frond area after 1 and 6 h under different preparation methods, * significant difference in mean area from start point $p < 0.05$, n.s. = No Significance in mean area change from start, n = 32 ANOVA with a Tukeys multiple comparison test.

µCT scanning quality assessment

Three individuals of one species from each duckweed genus was prepared, scanned, and processed as described in 2.3.2 using the described methods for CT scanning. Representative scans were rendered into 3D to gauge the efficiency of the preparation and scanning method; showing that across the full range of sizes

within the Lemnoideae this method produces high quality images at a relatively high throughput (Figure 2-5).

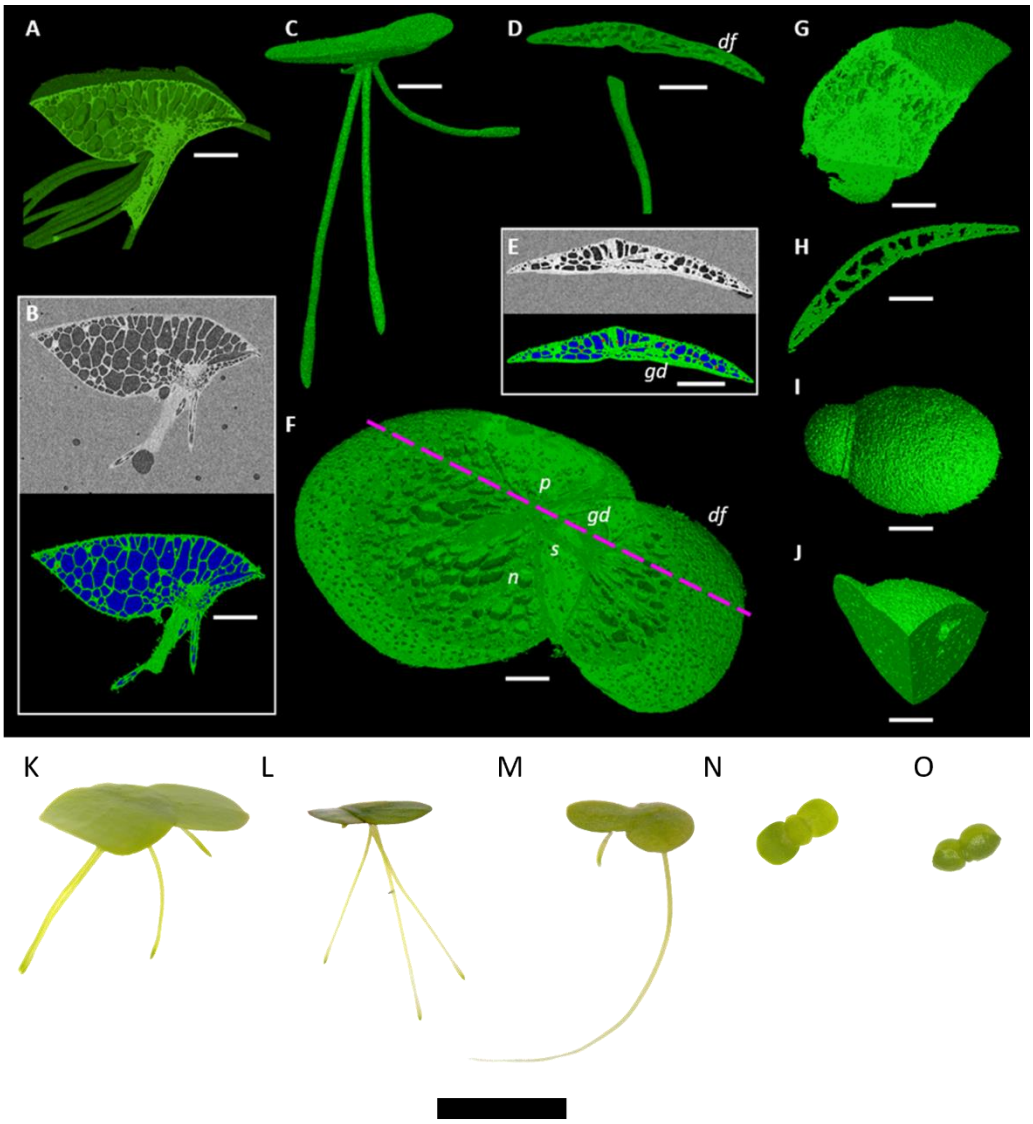


Figure 2-5. Representative images of duckweed genera showing render capabilities and segmentation of micrographs. (A,B) *Spirodela* intermedia, (A) Render clipped to midpoint of frond, (B) Micrograph and segmentation of micrograph of midpoint slice (White: Starch rich tissue Green: Tissue Blue: Gas), (C) Render of *Landoltia* punctata, (D–F) *Lemna* minor, (D) Render clipped to back half of frond, daughter frond (df), granddaughter frond (gd), (E) Micrograph and segmentation of micrograph, (F) Render clipped to partially remove adaxial frond surface revealing stipe (s), nerves (n), and daughter frond pocket (p), mauve dashed line shows clipping plane of (D,E), (G,H) *Wolffiella* lingulata, (G) Render clipped twice, revealing meristem and internal anatomy of daughter frond, (H)

Render clipped to midpoint showing longitudinal section of frond, (I,J) *Wolffia* arrhiza, (I) render of whole plant, (J) Render clipped twice to reveal internal gas spaces. Scale bars (A,B,C): 1 mm, (D,E): 0.75 mm, (F): 0.5 mm, (G–J): 0.3 mm. K *Spirodela intermedia*, L *Landoltia punctata*, M *Lemna minor*, N *Wolffiella lingulata*, O *Wolffia arrhiza*, Scale bar K-O = 1 cm

2D µCT image processing pipeline assessment

The different image processing methods presented provide a range of options for visualization and analysis depending on the desired information. To visualize the internal structures, segmenting and rendering the plant using the 3D method gives the most flexibility and perspective as one is able to view the plant as a whole (Figure 2.5C,I) or clip into the render revealing internal structures (Figure 2.5A,D,F,G,H,J). This can be done aligned to the three projection planes (XY, ZX, ZY), or unaligned, presenting different perspectives to those possible with 2D alone. The plant can also be rotated and clipped to multiple planes to reveal or isolate particular features in the 3D object view (Figure 2.5G,J). Though very rich in information and capable of enabling measurements of internal structures, this method is the most time consuming in segmentation, costly in processing power, and limited in the rate of measurements possible without additional computational measurement add-on packages to the software.

Table 2-3. Results of 3D particle analysis of gas spaces within representative fronds scanned

Line	Number of gas spaces	Vol. (mm^3)				Surface area (SA) (mm^2)			Euler (χ)		Thickness (mm)	
		Min.	Median	Max.	Total	Min.	Median	Max.	Mean	Std. err.	Mean	Std. err.
S. intermedia	2187	4.25E–07	0.00003	0.02853	0.5822	0.00447	0.02763	4.963	0.9186	0.02292	0.08454	0.001251
L. punctata	3167	1.97E–07	1.1E–06	0.001	0.01173	0.000267	0.004	1.261	0.982	0.002526	0.02346	0.000272
L. minor	926	2.76E–07	4.53E–06	0.00105	0.01792	0.00159	0.00795	0.7155	0.9633	0.007848	0.0313	0.000209
W. lingulata	228	1.13E–08	5.65E–07	0.00042	0.00347	0.00019	0.00284	0.5657	0.9167	0.03213	0.03082	0.000523

Analysing this data from the *S. intermedia* scan, the volume distribution of gas spaces can be determined (**Figure 2-6.**C) and thus statistical analysis can be performed on the uniformity of the frequency both at an intra and inter species level when applied to large experimental programs. The recoloured image stack outputs from BoneJ (Doube et al., 2010), allow for visualization of the number of individual gas spaces in 3D (**Figure 2-6.**A), and the distribution of differently sized gas spaces throughout this frond. The volume differences between gas spaces

shown by the graduated colour mapped image (**Figure 2-6.**B), and the thickness of each gas space shown by the heat mapped image (**Figure 2-6.**), show that in this individual, larger and thicker gas spaces are located in the middle of the frond, while smaller and thinner gas spaces are found at the surfaces of the frond. This type of quantification will allow for much better understanding and phenotyping of duckweed species when applied to a whole replicated experimental program.

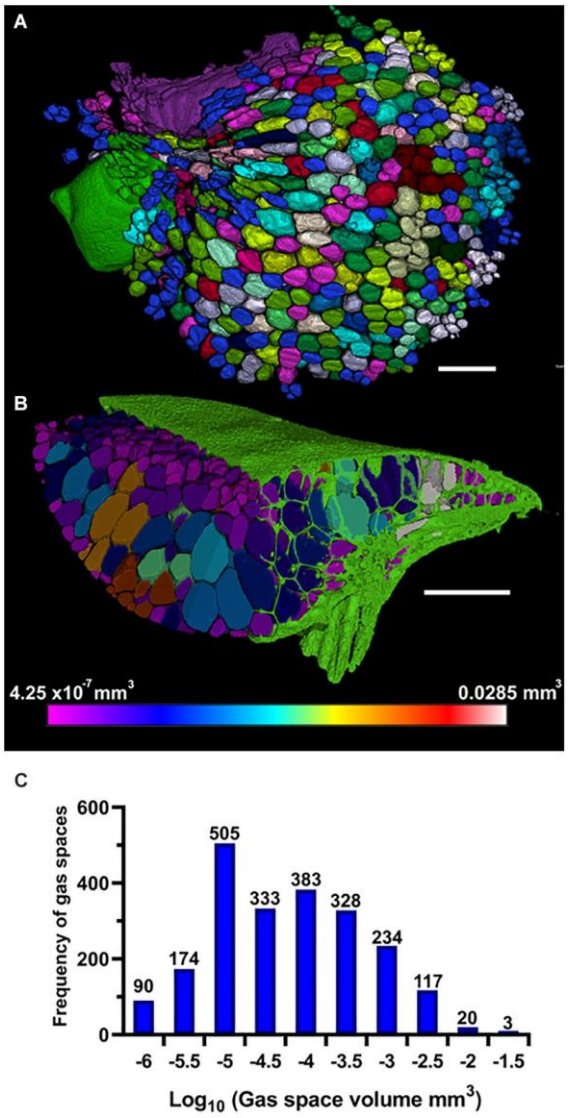


Figure 2-6. Three-dimensional (3D) particle analysis of *Spirodela intermedia* shows number and volume of each gas space within frond. (A) Render showing internal air spaces of *Spirodela intermedia* frond colored by individual gas space. (B) Render showing internal air spaces of *Spirodela intermedia* frond, colored by volume, clipped to reveal variation in volume between inner and outer gas spaces within the frond (green). (C) Frequency histogram showing distribution in volume of gas spaces within *Spirodela intermedia* frond. Scale bars: 1 mm. Graduated color scale from 4.25×10^{-7} mm^3 to 0.0285 mm^3.

3D µCT Data processing pipeline assessment

A combined approach, utilizing the 2D segmentation procedure for 3D trait analysis was carried out using the FIJI plugin BoneJ as previously used for analysis of gas content of plant material (Lundgren et al., 2019). Particle analysis of the binary masked gas space stack (Figure 2 3J), outputs measurement of a range of topological features of each distinct gas space (volume, surface area, Feret diameter, thickness, Euler number), and can generate recoloured image stacks, coloured according to values of particle traits (number, volume, thickness), which can subsequently be visualized in 3D using FIJI 3D viewers or with VGStudioMax. Representative 3D renderings of pore number (Figure 6A) and pore size (Figure 2.6B) as well pore thickness (Figure 2.6) illustrated by heat maps, were constructed in VG StudioMAX (version 2.2.0; Volume Graphics GmbH, Heidelberg, Germany) using Phong rendering tools (Phong, 1975).

Heat map data of the 'Thickness' of pores was produced as a function within FIJI plugin BoneJ (Figure 2 7). After binarization of the image stacks (Figure 2 3K-M), use of this plugin was fully automated. Image processing takes from a few minutes to several hours depending on the scan and processing power of the machine used, with the larger the plant and more numerous and interconnected the gas spaces generally the longer the process. Following the 3D particle analysis of internal gas spaces, results were processed in Prism 8. To confirm presence of gas within fronds and roots, pixel value measurements were taken of air inclusions in the petrolatum core, and of gas spaces within frond and root at 50 points within each area using the point tool in FIJI. These measurements were analyzed in Excel with a Student's t-test.

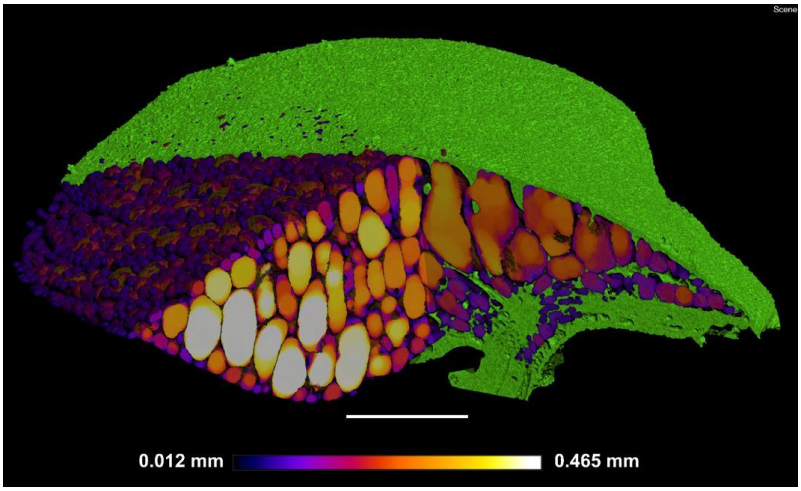


Figure 2-7. Localized thickness of each gas space within *Spirodela intermedia* frond. Frond tissue in green, gas spaces from Blue–White in graduated scale from 0.012 mm to 0.465 mm in thickness at each point within each gas space in the frond. Scale bar: 1 mm.

Root composition determination

In addition to enabling the acquisition of three-dimensional anatomical data, µCT scanning can also support other methods of anatomical phenotyping. Sections of *S. intermedia* roots (Figure 2-8), showed large extracellular voids. Though these were identifiable as aerenchyma based on understanding of root anatomy (Jung et al., 2008), confirming that these are in fact interconnected gas filled channels, was not possible with the vibratome sectioning method described alone. Measurement of the image pixel values for the air bubble inclusions within the petrolatum, and the values observed inside the root channels and frond are similar enough that it can be said with confidence ($p = 0.0154$) that the extra-cellular spaces in the root are gaseous in the samples observed. This agrees with the segmentation method described in Figure 2-3, as shown in Figure 2-8C. Using this information, the extracellular spaces in Figure 2-8B, can be labelled and recoloured as air spaces (Figure 2-8D).

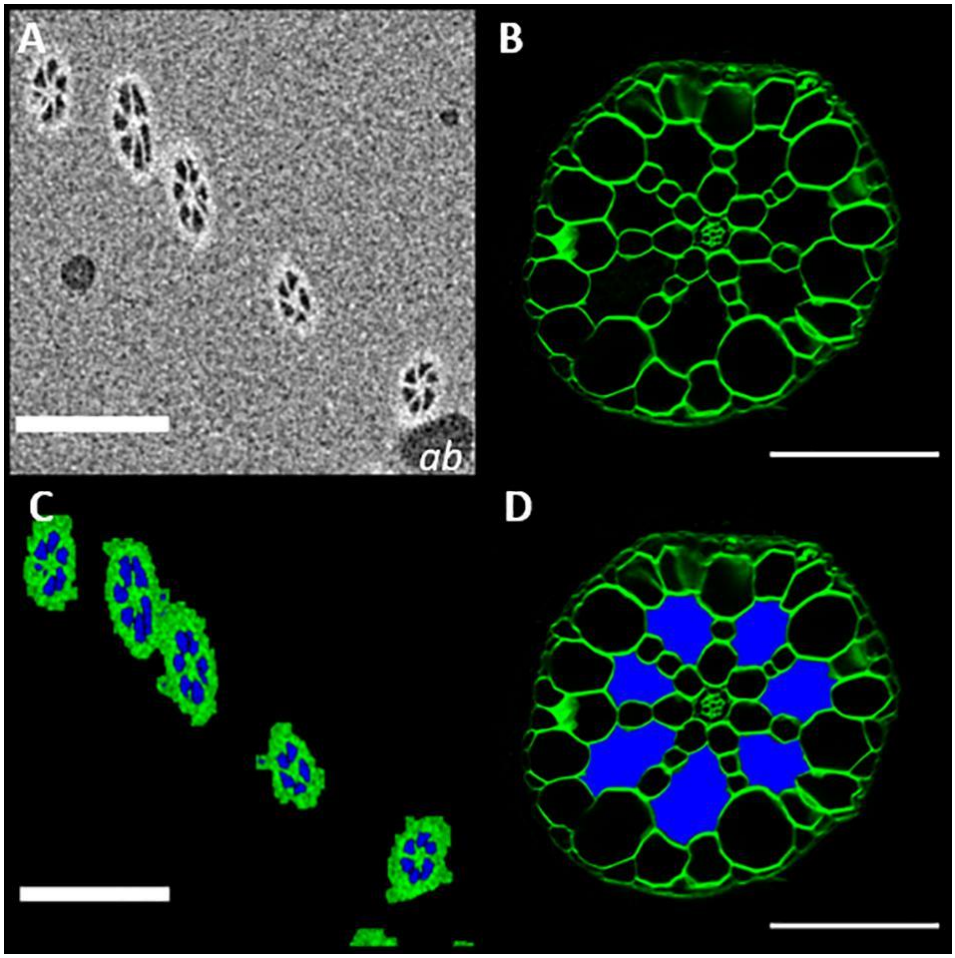


Figure 2-8. MicroCT imaging confirms that the extracellular spaces seen in root sections are filled with gas. (A) µCT micrograph of *Spirodela* intermedia root embedded in petrolatum, with air bubble inclusions (ab), 16bit greyscale micrograph representing xray density from white (high density, to black (low density). (B) Confocal image of a *Spirodela* intermedia root section, 150 µm thick, stained with calcofluor (green) (C) Segmentation of (A) using the method described in Figure 3 Green = tissue, Blue= intra plant gas region, (D) Recolored root section (B) showing the classification of extracellular spaces based on segmentation in (B) green= calcofluor stained cell walls, b= aerenchyma, Scale Bars: (A,C) = 200 µm (C,D) = 50 µm.

Turion composition determination

Further to the confirmation of gas spaces, µCT can be used as a method to evaluate differences in material composition. The imaging and analysis pipeline was shown to be effective in evaluating differences between collection variants of duckweed turions. Figure 2-9A-C show three representative images from the middle slice of XZ image stack of sunken, floating, and cold-treated turions; whilst Figure 2-9D-F shows the segmentation of these slices using the 2D segmentation method described in Figure 2-3. Quantification of turion composition shows a differing range of percentage composition of tissue, gas, and starch between collection variants. Although significance testing was not possible due to the small sample size, the scans showed a lower proportion of tissue and a higher proportion of gas in the floating turions than the sunken or cold treated turions (Figure 2-9I).

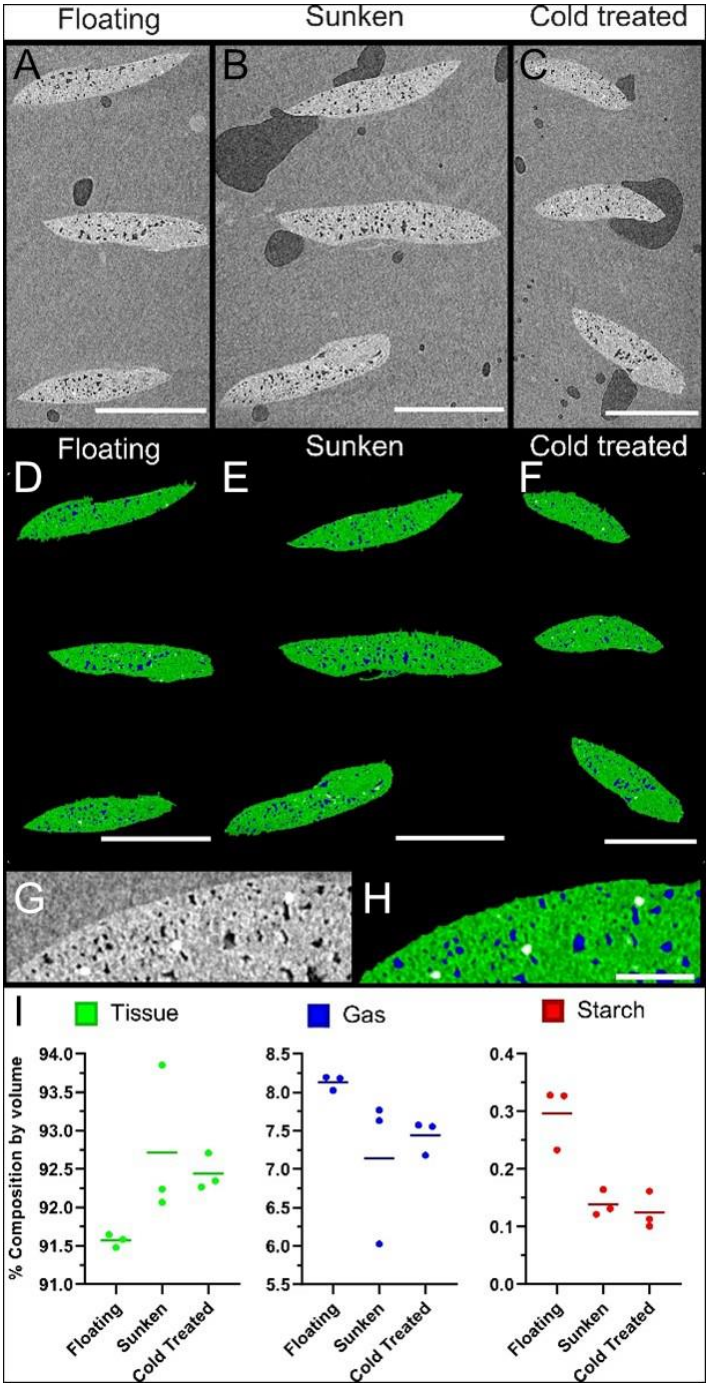


Figure 2-9. Buoyant Spirodela polyrhiza turions contain a higher percentage of gaseous extracellular space than those that are submerged. (A–C) Mid slice of three µCT micrographs of stacks of three turions, collected under differing conditions. (D–F) Segmentation of images from (A) following steps in Figure 3. Green: Tissue, Blue: Gas, White: Starch (A,D) Turions floating at surface, (B,E)

Turions sunk to bottom of flask, (C,F) cold treated turions showing petrolatum (p), Starch (s), Tissue (t), and gas spaces (gs). (G) Expanded micrograph of Cold treated turion. (H) Expanded segmentation of micrograph of Cold treated turion showing petrolatum (p), Starch (s), White, Tissue (t), green, and gas spaces (gs), blue, recolored as determined by segmentation. (I) Composition values of each turion set under each treatment as determined by processing and analysis pipeline. Dots represent data points, horizontal line the mean value. Scale Bars (A–F): 1 mm, (G,H): 0.1 mm.

2.4.2 Root vestigialization

Root anatomy

The root anatomical survey was conducted on a panel of 20 duckweed lines, representing 13 species (Figure 2-10), with all *Spirodela* and *Landoltia* species represented and 10 of the 13 *Lemna* species, alongside *Pistia stratiotes* (**Figure 2-10.**). in line with previous observations (Landolt, 1986), in no instances were lateral roots or root hairs observed in duckweeds.

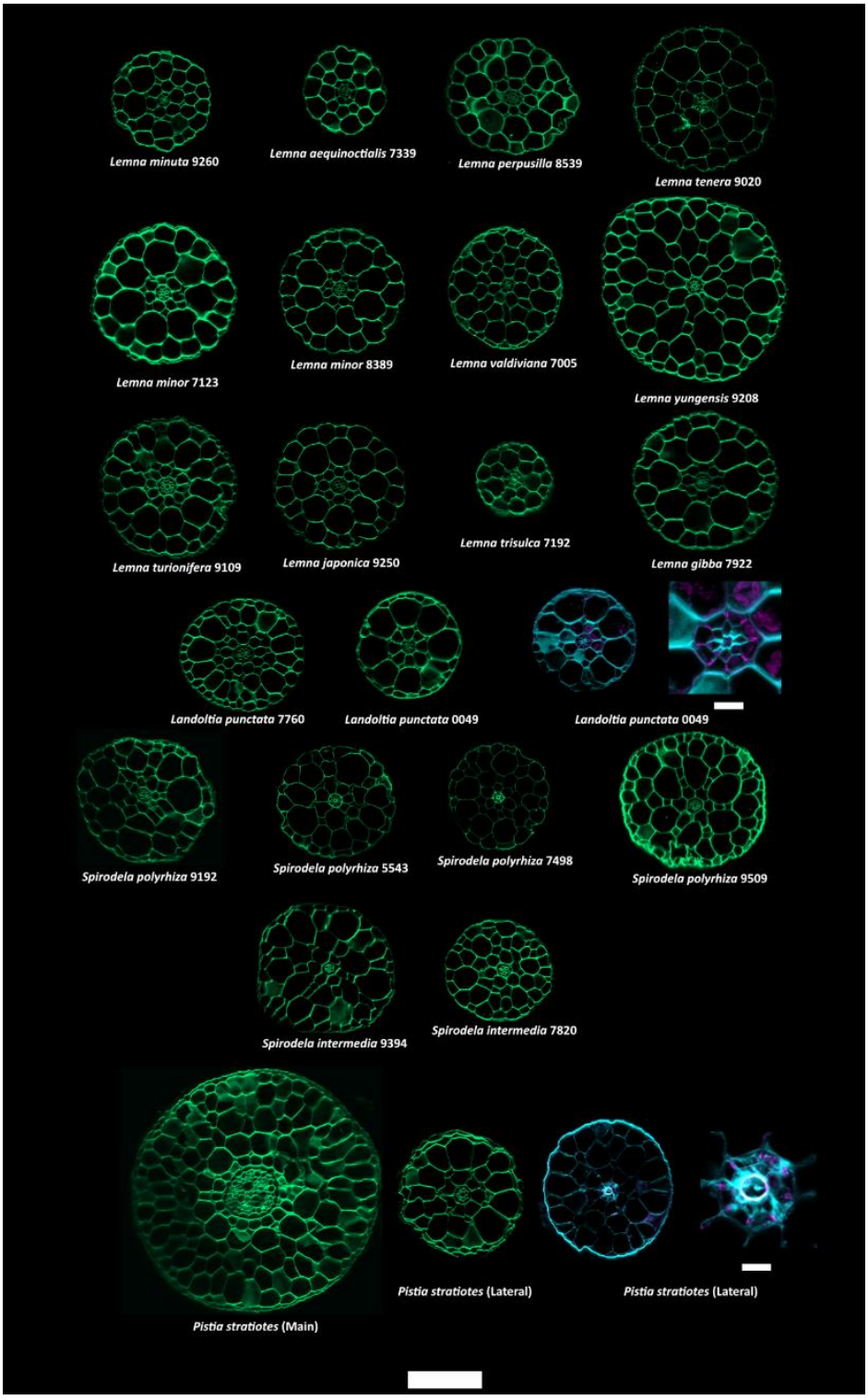


Figure 2-10. Representative root sections from 20 duckweed lines encompassing 13 species, and *Pistia* stratiodes main and lateral roots. Images were obtained via

fresh tissue sectioning and confocal imaging from a representative portion of the mid point of the length of the root. The *Pistia* stratiodes and Landoltia punctata roots are counter-stained with fuschin to highlight lignified tissue, Scale bar for whole roots= 100 µM, Scale bar for magnified stele =10um

Pistia had a considerably larger and more complex root system with lateral roots. 11 out of 12 duckweeds have a mean root diameter between 120-200 µm, with only *Lemna yungensis* falling outside of this range with a mean diameter of 256 µm. No duckweed species possessed a maximum root diameter close to the 325 µm observed in *Pistia*. An average of 212 total cells were counted in *Pistia* cross-sections, while duckweeds display mean total cells values of 28-81 cells. *Spirodela* sp. displayed mean cross section cell numbers ranging from 40 to 81 cells, whereas *Lemna* species typically displayed fewer cells in cross-section than *Spirodela*, averaging between 28 and 45 cells, apart from *Lemna yungensis*, which has a mean total cell count of 73. Morphological analysis of root patterning revealed a highly reduced anatomy common to all duckweed species. This consisted of a 3-5 of cortical cell layers and a consistent and highly reduced vasculature (**Figure 2-11.**) comprising a single central xylem, typically surrounded by a small number (7-10) of what appear to be phloem parenchyma cells (although this identity could not be and has not been explicitly defined).

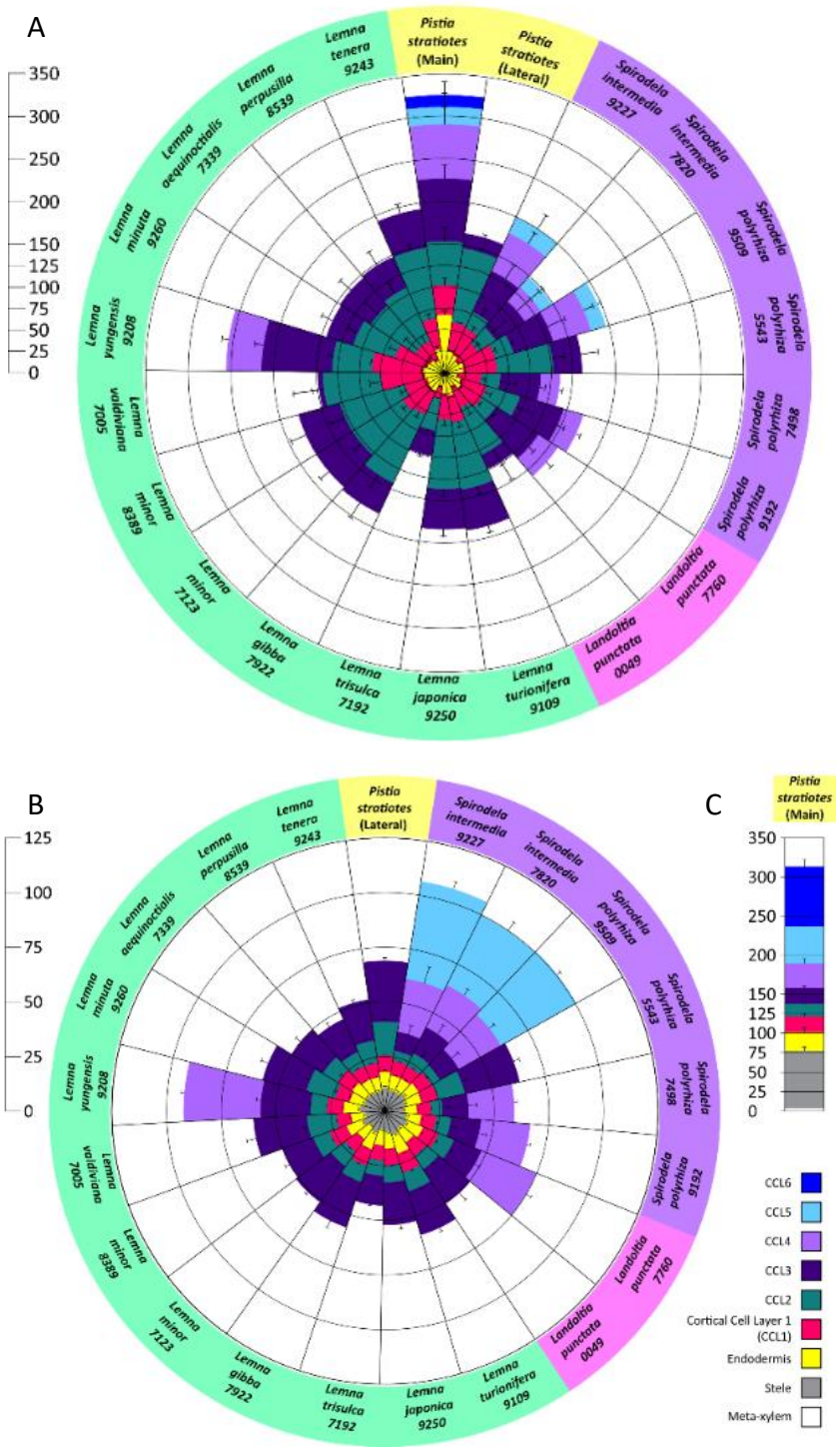


Figure 2-11. Comparison of root anatomical traits across almost all extant duckweeds reveals a highly reduced anatomy. (A) Rose diagram displaying the width of each cell layer (µm) for roots of 20 duckweed lines encompassing 13

species, denoted at the outside of the circle. B) Rose diagram displaying the number of cells in cell layer for roots of the aforementioned lines, denoted at the outside of the circle, with P. stratiotes main roots (C) in a separate bar chart for ease of resolution. Background colour underlying the species labels represents genera; yellow represents *Pistia*, purple *Spirodela*, pink *Landoltia*, and green *Lemna*. E) Colour coded key to the different cell layers displayed on the rose diagrams. CCL stands for cortical cell layer. n = 10 root sections derived from different plants, except for *Pistia* stratiotes (main) and L. trisulca where n = 5 root sections derived from individual plants.

Pistia, conversely, has 3-6 metaxylem in its stele and considerably more phloem and/or parenchyma . It also has a discernible pericycle, which was absent in all duckweeds surveyed here (**Figure 2-12.**). In duckweeds, the stele was enclosed by an endodermis normally comprised of 6-9 cells, with each cell centred over the cleft between the two phloem/parenchyma cells situated beneath. This identity was confirmed with the fuchsin staining, showing the characteristic lignin deposition pattern describing the casparian strip of the endodermis as shown in Figure 2-12.

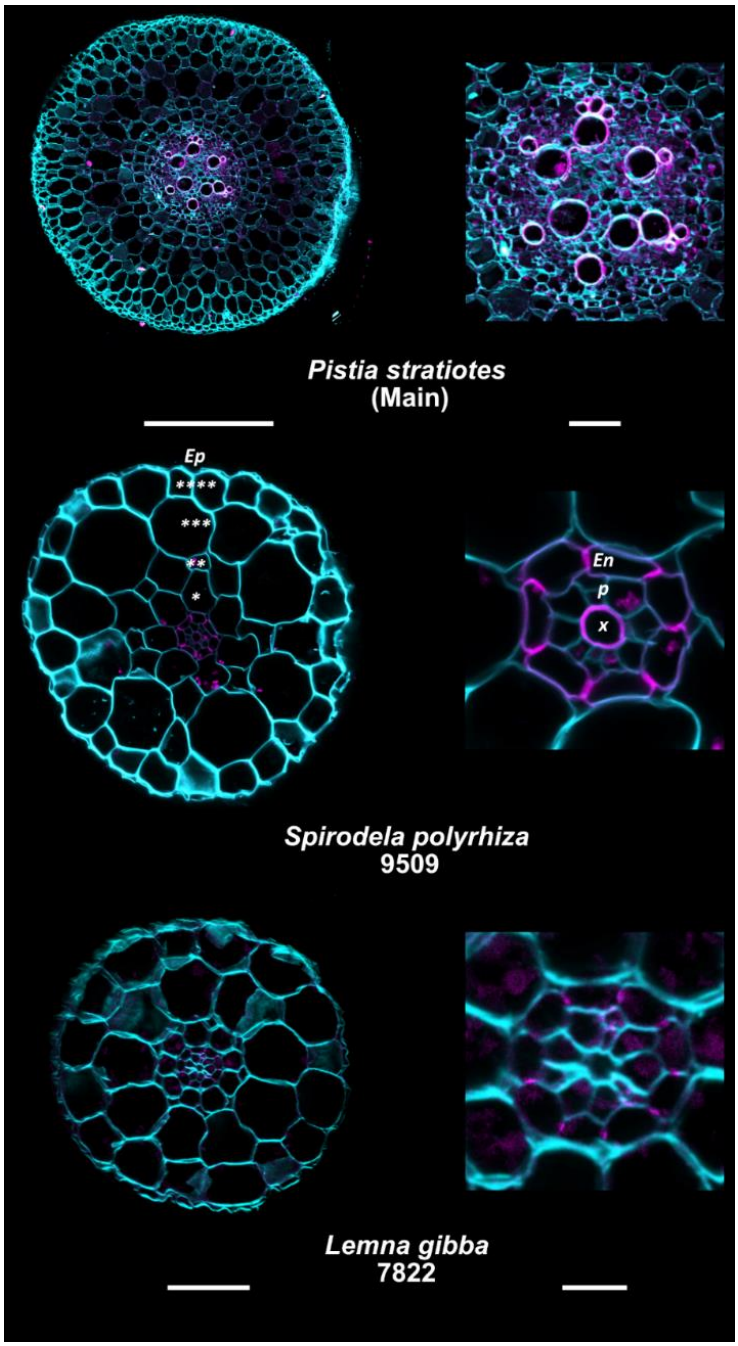


Figure 2-12. Basic fuchsin staining of duckweed vasculature highlights lignification in the endodermis and central xylem. Entire root section and accompanying close up of the vasculature of Spirodela polyrhiza 9509 with cell wall staining (calcofluor white; green) and lignin staining (0.01% Basic Fuchsin; magenta). Scale bar = 50 µM for entire roots; 10 µM for vasculature close-up.

When comparing between duckweed genera, a trend in the reduction of number of cortical cell layers (CCLs) (Figure 2-13C) was observed from the earlier diverging *Spirodela* (3 of 6 accessions display 5 CCLs) to the later diverging *Lemna* (3 CCLs in 11 out of 12 accessions) (Ware et al. 2023). However, this was not the case in root diameter, endodermis diameter, or vascular cell count. Several duckweed species have large extracellular air spaces within the cortex, similar to the schizogenous aerenchyma found in many other aquatic plants (Jung et al., 2008). This feature appears more frequently in *Spirodela* (5 out of 6 lines), in 1 out of 2 of the *Landoltia* lines, and in only 2 out of 12 closely related *Lemna* lines that are currently proposed to represent a single species (*yungensis valdiviana*) (Bog et al., 2020). *Pistia* main roots however were significantly larger in every metric when compared to roots of all other duckweed species.

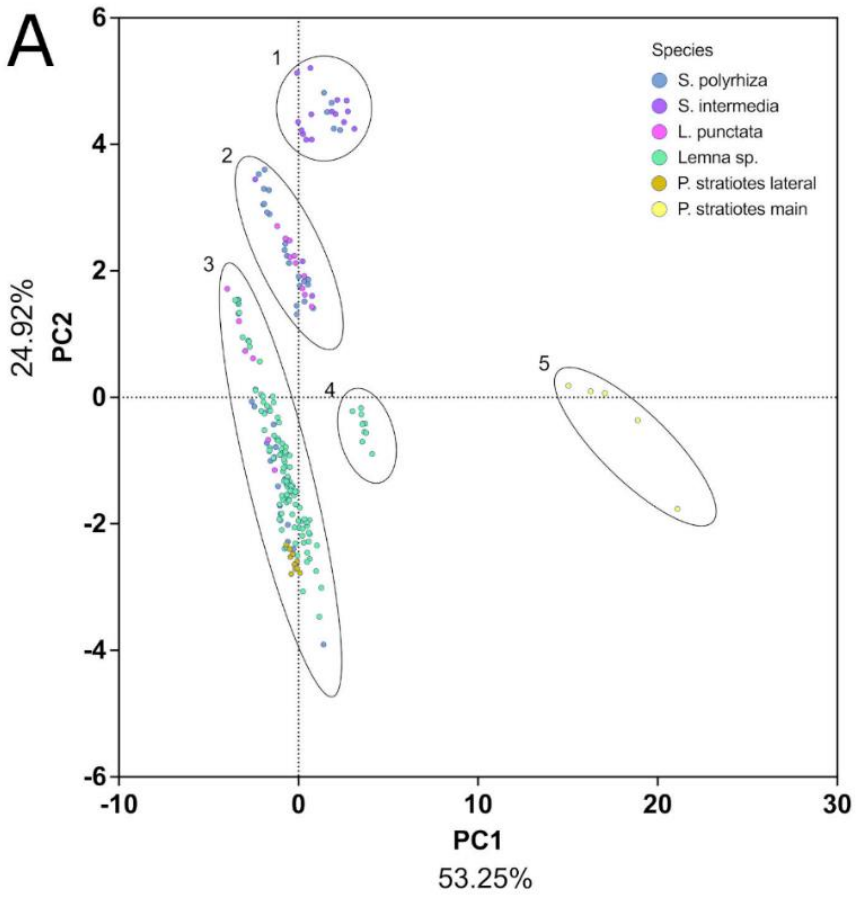


Figure 2-13. Principal coordinates analysis of duckweed anatomical traits highlights interspecies differences and a gradient of reducing root anatomical complexity. A) PCoA based on 21 components, with 210 rows, derived from an anatomical analysis of fresh root sections from 20 duckweed lines, encompassing 13 species, and main and lateral roots of *Pistia* stratiotes. Clusters have been manually highlighted and numbered for ease of further discussion. The percentage of variance explained by each PC is indicated on the relevant axis.

To process the data and visualise its spread and trends, the root anatomical data was subject to a principal component analysis, shown in Figure 2-14A. The PCA shows 5 well separated clusters, consistent with phylogenetic groupings. All *Lemna* species are found in a single cluster (3), apart from *Lemna yungensis*, which forms a distinct unique cluster outside of the larger *Lemna* cluster containing this species alone (4). *Spirodela intermedia* occurs in two distinct clusters (1 and 2), neither of which contain any *Lemna* individuals. The majority of *Spirodela intermedia* individuals cluster together, in a group also consisting of a small number of *Spirodela polyrhiza* samples (cluster 2). *Spirodela polyrhiza* is distributed more broadly and located within clusters 1, 2 and 3, with the majority of individuals falling into cluster 2, which contains only *Spirodela* and *Landoltia* species. A small number of *Spirodela polyrhiza* samples also fall into the *Lemna* cluster. *Landoltia* data points are mostly located in cluster 2 with *Spirodela polyrhiza* and *intermedia* data points, and a few individuals occur in the *Lemna* cluster. *Pistia* main roots group distant from all duckweeds driving the main axis, PC1. Notably, all *Pistia* lateral roots fall within the *Lemna* cluster.

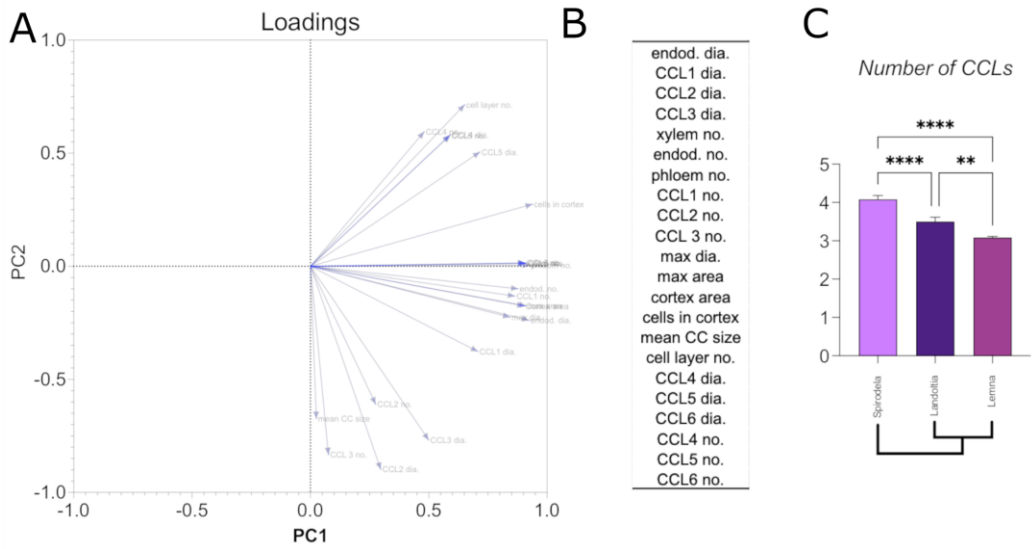


Figure 2-14. PCA details and cortical cell layer number analysis. A) Loadings plot of PCA in 2-13 B) Summary of the 22 variables used to generate the PCA. *n* = 10 root sections derived from different plants, except for *Pistia stratiotes* (main) and *L. trisulca* where *n* = 5 root sections derived from individual plants. C) Mean number of cortical cell layers for representative species of each genus.

Effect of root removal on plant growth

Frond (or aerial tissue) area was measured daily following root removal and normalized to the initial area value (Figure 2-15A). Considerable increases in frond area for all duckweed species with intact root systems were observed. For all duckweed species, apart from *L. turionifera*, final percentage growth did not differ significantly between control and plants treated by daily root removal. In contrast, root removal markedly and significantly reduced the growth rate of *Pistia stratiotes* (Figure 2-15). Dry weight measurements showed the same results pattern, with only *P. stratiotes* and *L. turionifera* exhibiting a significant reduction in dry weight in the root-excised condition (Figure 2-15B).

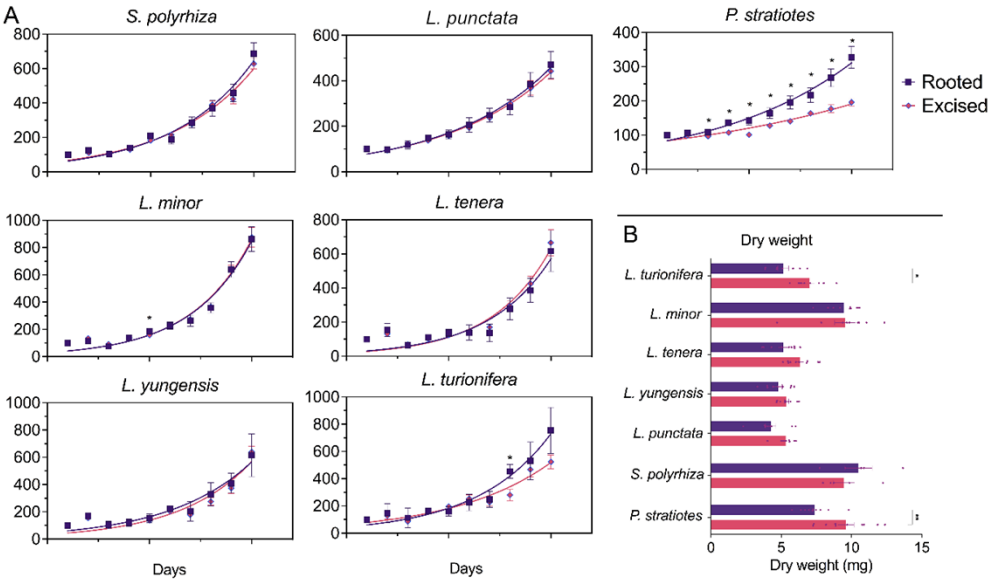


Figure 2-15. Growth and nutrient uptake of six duckweed species is not impacted by continual root removal, unlike the aroid *Pistia* stratiotes. Plants were subjected to continuous root removal and growth and elemental ionomic composition of fronds was compared to untreated controls. A) Growth measured as area of fronds (or aerial tissues for *Pistia*), derived from daily imaging from beneath, and plotted as a percentage increase relative to the initial (day 1) area value. Species are indicated on the graphs. n = 10 flasks, each initially seeded with 3 colonies for duckweed and 1 plant for *Pistia*. Asterisks show statistically significant ($P < 0.05$) differences as assessed by two-way repeated measures ANOVA followed by Šidák's multiple comparisons. Error bars = 95% CI. Lines show the best fit of an exponential (Malthusian) growth curve. B) Dry weights of frond or aerial tissue harvested from the final timepoint of the growth series shown in A. Asterisks show statistically significant ($P < 0.05$) differences as assessed by one-way ANOVA followed by Šidák's multiple comparisons. Error bars = SEM.

Effect of root length on movement in response to wind

The length of duckweed roots was shown to significantly affect the speed duckweeds travelled in a response to an artificial wind treatment. For all three biological replicates, as the root length was reduced the time taken to travel 15 cm decreased and the speed of travel increased. This happened exponentially, with negligible changes in movement speed between plants with 30-40 mm of root, and small insignificant changes between 20-30 mm, though reducing the root length below 20 mm caused major increases in movement speed with each removal increment (Figure 2-16).

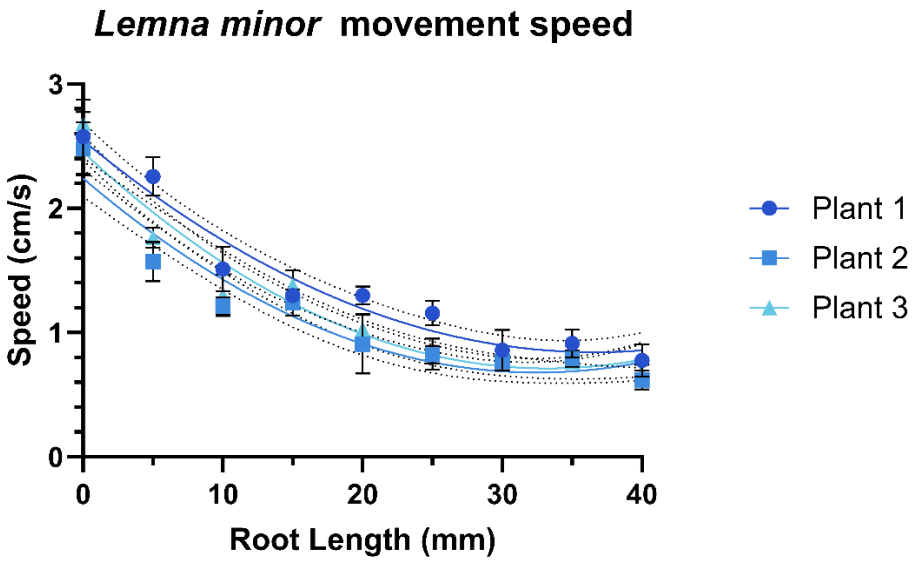


Figure 2-16 Reduction in Lemna minor root length causes an increase in movement speed under wind stimulus Measurement of time taken for each duckweed plant to travel 15 cm was expressed as speed in cm/s, measured 5 times per trimmed root length

Effect of root removal on plant nutrient uptake

To investigate root function with regard to ion uptake, the fronds and aerial tissues of duckweed and *Pistia* produced by the previous experiment were analysed to

determine their ionomic and nitrogen and phosphorus content. For ionomic analysis, though some rare elements such as Li and Cd were detected, only the 13 elements present in the growth media B, Na, Mg, P, S, K, Ca, Fe, Mn, Co, Cu, Zn, and Mo, were considered.

In no instances did root removal in duckweed impact N or P levels in the frond, whilst both elements were significantly reduced in by root excision in *Pistia* (Figure 2-17). Additionally, no other elements included in our analysis (0 out of 13) exhibited reduced accumulation in *Spirodela polyrhiza, Landoltia punctata* or *Lemna yungensis* under root removal treatment. *Lemna tenera* and *turionifera* both exhibited reduced accumulation of a single element - K and Na respectively – after root removal, while *Lemna minor* showed reduced accumulation of 2 elements, B and Cu. Surprisingly, a higher accumulation of B, S, Mg, Ca, Fe, Mn, Co and Mo was found in several species following root excision (Figure 2-17). In *Pistia*, 7 of the 14 elements quantified exhibited reduced accumulation in shoot tissues following root removal, with N, P, S, K, Fe, Mn and Zn all being significantly reduced (Figure 2-17).

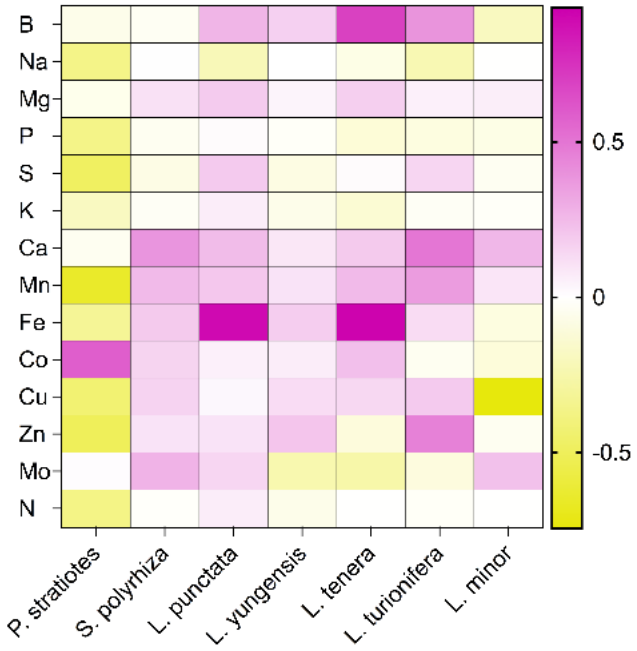


Figure 2-17. Effect of root removal on duckweed ionome. Heatmap showing the log2 fold change of elemental concentrations in the frond for rooted versus rootless treatments for each species. Significance ($P < 0.05$) was determined by one-way ANOVA followed by Šidák's multiple comparisons test. n = 5 flasks, each initially seeded with 3 colonies for duckweeds; n = 7 flasks, each initially seeded with 1 plant for *Pistia*.

Expression of nutrient transporters in different tissue types

As part of this investigation, gene expression of nutrient transporters in different tissue types and in response to contrasting nutrient exposure was analyzed. Plant growth and sampling was conducted by Dylan Jones and Alex Ware, and expression analysis was run by Alex Ware. Expression of tissue specific nutrient transporters was analysed using a bulk RNA-sequencing dataset using tissue from the mature frond, frond meristematic zone, root tip and mature root of *Spirodela polyrhiza* (9509). In order to compare this to land plants with functional roots a selection of nutrient transporter gene families (NRT1, NRT2 and PHT) were investigated and used to calculate tissue specificity indices (TSI) to then be compared to the TSI of the same transporter families in *Arabidopsis* and *Zea mays* in comparable tissues, obtained from publicly available datasets (Klepikova et al., 2016; Stepflug et al.,

2015) (Figure 2-19). A gene-family level approach was taken to identify all members of each gene family in duckweed, ensuring no potential root-uptake members were missed. Protein domain structure based ortholog identification revealed a substantial contraction in the quantity of members of these families in *Spirodela polyrhiza*, consistent with a previous report In *Arabidopsis thaliana* and *Zea mays*, there is a clear bias towards root specificity in all 3 gene families (Michaels et al., 2017).

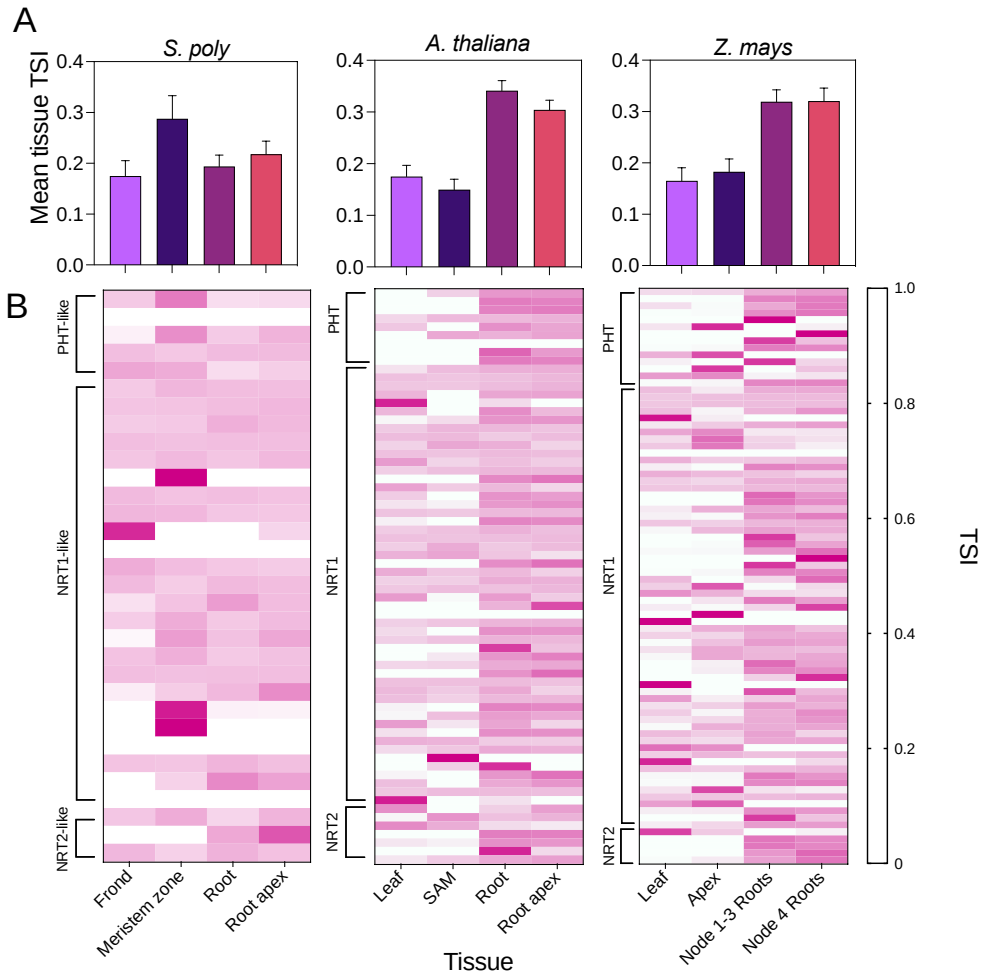


Figure 2-18. Expression of the NRT1, NRT2 and PHT nutrient transporter gene families shows root bias in A. thaliana and Z. mays, but not S. polyrhiza. A) Mean TSI (tissue-specificity index) was calculated as per Julien et al. (2012) and Brawand et al. (2011) for all members of the PHT, NRT1 and NRT2 family as identified by

orthology analysis across 4 tissues encompassing root, root tip, shoot apical meristem (SAM) and leaf in each species. For each gene, expression levels per tissue type were normalized against total expression across all tissues. For Z. mays, data for root tip and mature root was unavailable so instead 2 separate root types of differing maturity level were used. B) Corresponding heatmap of the individual gene TSI values for each tissue type in the three species.

Averaging the tissue specificity index of all transporters allows for concise evaluation of this trend (Figure 2-19), and shows elevated average TSI for root tissues in both species relative to non-root tissues for these nutrient transporters. This expression pattern is lost in *S. polyrhiza*; none of these transporters exhibit any level of root specificity in their expression (Figure 4A). This could be due in part to the loss of root hairs and/or lateral roots, as both organs have been shown to have high expression of many transporters including the PHTs (Mudge et al., 2002).

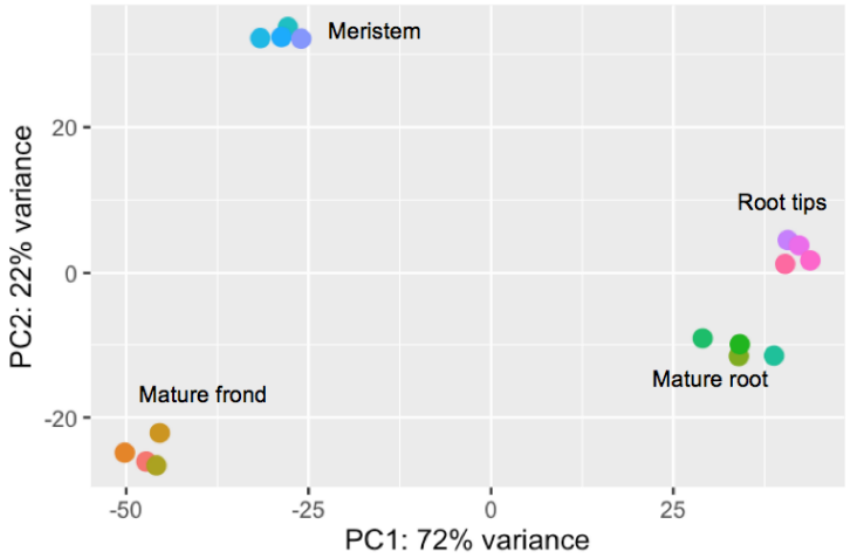


Figure 2-19. PCA showing clustering of replicates of the four tissue types sampled in the *S. polyrhiza* bulk RNA-sequencing experiment.

RNA expression in response to low P treatment

Transcriptomic analysis of *S. polyrhiza* (9509) in response to low P treatment revealed a stronger response in the root than the frond, where following low P

treatment, the *PHO1* and *PHO2* orthologues were the only PHT and PHO family genes to be differentially expressed, and both showed higher induction in the frond than root (Figure 2-20A). Following transfer to low phosphate media, a higher number of differentially expressed genes in the frond with a specific enrichment for transporters was also observed (Figure 2-20C). Collectively these data suggest that alongside root vestigialization, there has been both a contraction in the number of members in N and P transporter families, and a shift in the expression patterns so that these transporters are no longer predominantly expressed in roots.

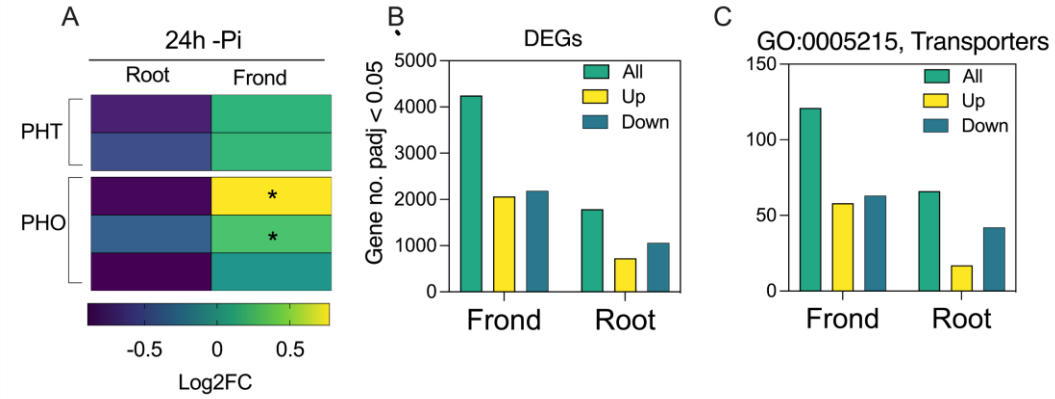


Figure 2-20. Transcriptomic response of *S. polyrhiza* 9509 to 24 hours phosphate starvation. A) Heatmap showing Log2 fold change of PHT and PHO genes in *Spirodela* fronds and roots subjected to 24 hours of phosphate starvation versus control groups grown with phosphate. Stars indicate genes with a Bonferroni corrected p value < 0.05 as per DESeq2. B) Total number of DEGs for the same groups, showing the total number alongside those up and down regulated. C) Genes enriched with the GO term 'transporters' for the same groups, ag their regulation is up or down.

2.5 Discussion

The work presented in this chapter addresses the stated aims, and has generated several novel findings and results. The development of new tools for duckweed phenotyping was successful, and using these has facilitated an investigation of duckweed root anatomy, function, and root vestigialization.

2.5.1 Phenotyping methods development

Several methods have been developed and implemented over the course of this research for aquatic plant phenotyping. The biggest advancement in technological application has been in the use of µCT scanning for duckweed.

µCT scanning preparation and imaging

The described method for embedding duckweed for µCT scanning has a number of advantages. When looking at root morphology and position relative to the frond, this method allows the roots to spread and position themselves relative to the frond as they would in media. This makes it easier to segment and measure individual roots, as well as to accurately visualize the morphology of the plant as a whole, in a way more similar to how it would appear 'in aqua'.

While the process of embedding plants in this way can be quite time consuming to set up and perfect, preparing multiple plants concurrently becomes very quick, and not then having to section or stain the samples speeds the process greatly. Ultimately the determining factor of scan resolution was the distance of the sample from the detector; the smaller it was possible to make the sample, the closer the stage could be to the detector and the higher the resolution. The scan quality was affected by whether or not the sample was extruded from the syringe or not, as the additional material layer caused additional x-ray beam attenuation and if the sample touched the walls segmentation was made more difficult. However, if unextruded, it is easier to position the core closer to the detector. This trade off can be optimised for different sample types.

µCT image processing

The 2D freeware analysis pipeline presented provides a higher throughput analysis method that is largely automatable and has a much lower requirement of processing power. It is well suited for analysis of plant composition (tissue/gas), and rapid measurement of segmented features. If properly embedded, specific measurements can be manually taken such as organ length, width, and thickness. Of the scans taken, segmentation of the micrographs agrees with visual assessment of ROIs with a high degree of accuracy. To observe specific traits such as gas space interconnectivity, distribution of nerves, and root anatomy, it is easier to do so by parsing through 2D stacks than clipping through the 3D model as the 2D images are of a single plane (depending on the data set size), and can be done without the need for segmentation.

The method of 3D trait analysis of gas spaces using the 2D segmentation worked well for analysis of the representative scans of S. *intermedia*, *L. punctata*, *L. minor*, and *W. lingulata* included in Figure 2-5, however, the process ran poorly on the W. arrhiza and S. polyrhiza turions due to the resolution of the scan and the small size of the gas spaces.

Of the image processing and analysis methods, a combined approach of 2D and 3D visualization, segmentation and analysis tools was most effective. The most dynamic and illustrative visualization possible was in using the designated 3D software, though manual measurements were easiest to obtain from 2D image stacks. For segmentation, there were a variety of tools in the 3D software package that enabled the most accurate segmentation of anatomical features, however, this can be time consuming and required a high degree of skill. The 2D method was also highly accurate but took less time, is amenable to automation, and can be optimized to specific scans and sample sizes with simple adjustments. For post-

segmentation analysis, all measurements presented of 2D and 3D features used ImageJ, though it would have been possible to do this using add-on packages for the 3D software. At any point in the 2D processing, images could be rendered in the 3D software for visualisation of analysis.

Future work using µCT scanning

The analysis of turion anatomy shown presents a promising avenue for future research. The results from turion composition analysis suggest that position in the water column may be moderated through variation in anatomical structure and composition. The observed proportion of gas space was comparable to previous investigations putting the aerenchyma volume in turions in *S. polyrhiza* at between 9–15% using a combination of sectioning and TEM (Kim, 2013). Using µCT scanning has several advantages. Firstly, µCT allows the full 3D turion to be investigated and so composition does not need to be inferred from a few slices. Secondly, as this technique is non-destructive, it could be applied to the same turion at multiple stages during dormancy to observe changes over time. Further work is needed to test whether the increased volume of gas filled space within the turion is causal for its rise from the bottom of the water, and µCT would enable multiple rounds of scanning the same turion to establish this. It may be possible to more definitively identify the high-density regions in the turion as starch which would also add to the understanding of buoyancy regulation possible as part of CT scanning. Previous analysis of turions through sectioning have reported the presence of starch granules (Appenroth et al., 2011). Through isolation of these starch grains, scanning electron microscopy (SEM) has been used to show that these start to reduce in size under exposure to high light (Appenroth et al., 2011). Imaging of turion anatomy using light microscopy is challenging due to their small size, waxy coating, high starch content, and heavy pigmentation, so µCT scanning may be the best method for this.

Other duckweed phenotyping

Duckweed worked well as a subject for the majority of phenotyping techniques used, though often required specific adjustments to be made. Growth phenotyping was initially challenging due to the reflectiveness and distortion that comes with imaging on or through water. This was overcome using the imaging chamber set up described previously, and enabled high throughput imaging of large duckweed colonies while maintaining aseptic conditions. Other solutions have been developed, using large open containers, Petri dishes, or other growing set ups, though these required either manual measurement or much more tailored image analysis pipelines. These have a number of drawbacks around time requirements for image analysis and or the experimental growth conditions, that the system presented here largely avoids.

Duckweeds have been shown to be highly amenable to ionomic analysis, and their small body plan and lack of secondary growth and thickening makes them easy to break down for analysis. However, conversely, their small size makes subsampling for any sort of analysis challenging.

While duckweed roots appear similar to *Arabidopsis* in size, and cortex and stele configuration, unless sectioned they take up dye much more poorly, and even when sectioned the epidermis does not stain well. This is challenging for confocal imaging of vasculature and imaging of the root tip, though using the adaptations to established sectioning and clearing methods presented above, high quality images can still be taken.

Evaluation of developed methods

Of the methods investigated for the anatomical phenotyping of duckweed, the only technique that allowed live whole plant imaging with the capability to

visualize internal anatomical features was µCT scanning. To enable µCT imaging of duckweed requires maintenance of turgor, limiting of unwanted movement, and images of sufficient contrast. The method of plant preparation tested that met all of these needs was embedding in petrolatum. Other workable techniques may exist; but the method described in **Figure 2-6.** is quick, inexpensive, easy to use, and produces high quality results.

Other phenotyping methods may be better suited to the measurement of specific traits, given the limited availability and potential high cost associated with µCT. Much of the phenotypic data gathered from a µCT scan, can also be collected with other methods, albeit in a much slower and time-consuming manner. 3D geometry of the plant can be obtained without the use of tomography scanning, especially due to the simplified body plan of the majority of species, and internal anatomical data can be collected through sectioning and microscopy. Clearing and mounting whole plants can give gross anatomical and cellular data in tandem, with either confocal microscopy or lightsheet scanning. Where higher resolution may be required, various techniques utilizing electron microscopy may be used (Melaragno and Walsh, 1976). Of the methods investigated, identification and quantification of all the gaseous spaces and tissue within the plant is only currently possible with µCT scanning, and the richness of the data coupled with the high throughput imaging and analysis methods presented make this the best method for structural anatomical phenotyping of duckweed of the methods investigated. As shown in Figure 2.11, this is particularly effective to gain anatomical insight on a structural and cellular level when combining µCT scanning and confocal microscopy.

Several of these developed techniques were then used to great effect in the investigation of duckweed root vestigialization which was also informed by data generated during their development.

2.5.2 Root vestigialization

Anatomical reduction

The results from the duckweed and *Pistia* root anatomical survey show that along with a reduction in frond size and number of roots there is a loss of anatomical traits along duckweeds evolutionary trajectory. The PCA of anatomical traits shows that duckweed roots cluster differently to *Pistia*, and that within the duckweeds, genera tend to fall into their own clusters. This indicates that there is a strong link between these phylogenetic groups and their anatomical traits.

The significant reduction in stele size in duckweeds when compared to *Pistia*, may suggest a reduction in their active nutrient transport function. Between duckweed genera, from *Spirodela* spp. to *Lemna* spp., there is a significant reduction in cortical cell layers, as well as the loss of aerenchyma in most species.

The anatomy of the duckweed root is also highly similar to *Pistia* lateral roots, which again is similar to the anatomy of fine lateral roots of other monocot species (Watanabe et al., 2020). This similarity is affirmed by the PCA placing *Pistia* lateral roots within the *Lemna* cluster. It is conceivable that this convergent anatomy, seen in *Lemna* represents or is approaching an anatomical 'minimum' without which it would not be possible to form a root.

Root function

Through the perspective of what is normally considered to be the salient function of the root, it appears that the roots of all species of duckweeds surveyed have ceased to perform their raison d'être, however *Pistia* have not. This is evidenced by the lack of impact root removal has on the panel of duckweed species investigated in both growth and ionome. The root removal experiments show that the *Pistia* with roots left intact have a significantly higher growth rate than with

roots excised, however this is not the case for almost all duckweed species and timepoints, implying for duckweed roots are not required for normal growth. Furthermore, the ionomic analysis showed a significantly diminished ionomic profile in *Pistia* with excised roots (6 out of 13 elements reduced and reduced nitrogen content), and no elements (0 out of 13) exhibited reduced accumulation in *Spirodela polyrhiza* grown without roots, and only 2 out of 13, (B and Cu), did in *Lemna minor*. Interestingly, in both *Spirodela* and *Lemna* there was actually a small significant increase in certain nutrients following root excision, included Ca, Fe, Zn, and Mn, with Ca increased in both genera. This may be suggestive of stress, or degree of sequestration of certain elements to the root under normal condition, for example, raphides (pinnate crystalline calcium oxalate) have been found in the roots of *Lemna minor* (Franceschi 1987, 1989).

Evaluation of Vestigiality

In *Spirodela polyrhiza*, the reduced tissue specificity of normally primarily root expressed transporters lends further credence to the hypothesis that duckweed roots are vestigial. With the perspective of the outgroup of *Pistia* with an apparently fully functional root system, it is interesting to see the ordering of the loss of molecular, physiological, and anatomical traits across the duckweeds, and the steps that have happened in tandem and separately. At some point prior to the evolution of *Spirodela polyrhiza*, the duckweeds lost the ability to produce lateral roots or root hairs (it is less uncommon for there to be an absence of root hairs in aquatic plants than terrestrial(Shannon, 1953)), and tissues specificity in transporter expression was also lost, though at this point they still maintained the ability to produce multiple adventitious roots. It also appears that at this point, duckweed roots had already lost their function with regard to supporting growth and nutrient uptake. It is interesting then that post this loss of function, there is still a gradual loss of morphological and anatomical traits as the duckweed genera diverge further. This suggests that in these species natural environments there may

still be a benefit to possessing a root, beyond those normally considered as part of normal root function, that can still be fulfilled by a single root with limited potential for transport.

As described previously, exactly when a feature becomes vestigial is somewhat abstract, and relies on evaluation of its ancestral or salient function. When comparing the function of duckweed roots to those of their terrestrial forbears, with regards to supporting growth through water and nutrient uptake (and mechanical support), the data presented here clearly supports classifying duckweed roots as vestigial, though as observed the roots do function in a manner when considering a potential role in reducing movement in their environment. This shows the potential for duckweeds to serve as a unique model system for plant root vestigialization. The presentation of a spectrum and trajectory of trait loss as opposed to a binary presence/absence is somewhat unique, and the wide range of germplasm and growing toolkit for duckweed phenotyping and molecular work makes this a promising avenue for future research.

2.5.3 Future work

The work presented here, while complete in its initial aims, has presented several promising areas of research for future work.

The initial screen of turion anatomy and differences under cold treatment and lifecycle illustrates well that the techniques developed can be used to identify differences in anatomical structure but does not ultimately resolve the question of buoyancy regulation in duckweed and turions. A more in-depth study of this, using a greater sample number, range in treatments, more specific developmental staging, and use of multiple timepoints may resolve this. Furthermore, the identification of starch granules in the CT images could be better resolved, either through more comparative microscopy of the same samples stained for starch as

scanned, or establishment of a correlation between high density CT regions and starch content using direct analysis of starch content.

The μCT scans, while high resolution, are not sufficiently high to definitively determine whether or not there are any connections between the air spaces within the frond or the root, or between airspaces. These large voids can be seen forming as early as at the grand-daughter stage frond within the mother, however their internal composition at this stage could not be determined using clearing and were too small for μCT. How gas is exchanged within the plant, given that some species have many internal chambers that appear sealed and insulated from their surroundings, and that the majority of the plant is submerged, is unknown and may be illuminated by use of higher magnification techniques such as serial block face scanning electron microscopy (He et al., 2018).

These newly developed phenotyping techniques present several new opportunities for increased eco-physiological investigation in how duckweed has become adapted to different environments as it has lost root traits and become reduced in size.

In the area of root development, there is much that could be done. Firstly, although initial screens of root anatomical plasticity under nutrient/osmotic stress were conducted and found to be non-impactful, it may be naïve to assume that under no environmental circumstance does root anatomy vary in the duckweeds surveyed. There is some reported architectural variation, with roots growing to variable lengths under varied nutrient conditions.

Chapter Three:

Novel Approaches to Anatomical Phenotyping

3.1 Introduction

Plant anatomical phenotyping has grown as a field from providing useful descriptive data that informs our understanding of tissue function, to a powerful "-omic" tool, facilitating genetic association analysis.

Anatomical traits have a significant effect on plant growth and performance and can be an important factor in stress tolerance and response. They can affect a plant's metabolic expenditure, resource acquisition, and transport systems.

Many anatomical analysis techniques are labour intensive or time consuming, and can involve protracted or low throughput sample preparation, sectioning, staining, and imaging steps, followed by limited manual measurement.

A significant development in the field of plant anatomical phenotyping is the process of using laser ablation tomography (LAT) scanning. This method uses a high-power laser in combination with highly accurate positioning stages and semi-automated image capture to sequentially remove layers of material from a sample, and image the freshly exposed face. This technique can be very high throughput but has seen limited application in the range of species and tissues investigated, and there still exists a large disparity between the potential LAT image quality and throughput, and the quality and rate of image analysis of LAT images.

3.2 Aims

Overview of aims

This Chapter describes the development of novel methods for plant anatomical phenotyping. It aims to do this by developing new high throughput equipment and techniques for sample preparation, scanning and imaging, as well as new image analysis tools. This will be done and validated with three different biological use cases; preparing for investigation of pearl millet anatomy, investigating the effect

of soil microbiome on maize and gamagrass root anatomy, and characterizing root anatomy of brachypodium mutants.

3.2.1 Anatomical imaging

Quantification of anatomical traits, in particular root anatomy, is a growing field of popularity for research, and recent technological advancements have enabled generation of anatomical data that can be used alongside other high throughput phenotypic or genomic datasets. The University of Nottingham has recently acquired a laser ablation tomograph (LAT), the first of its kind outside the US. This technique was developed for root anatomical analysis (see 1.3.2) but has only quantitively been used on roots and in a relatively small number of species, with few methods for sampling and sample preparation given.

The LAT unit at Nottingham has been provided in a semi-open-source configuration, meaning hardware and software changes can be made to optimize the LAT workflow. Protocols for sampling, sample preparation, ablation, and imaging, require development; either universally or in a sample-specific basis.

3.2.2 Anatomy image analysis

The development of high-throughput image acquisition approaches such as LAT exacerbates the existing bottleneck of the image analysis stage (Minervini et al., 2015; Depending on the level of data looking to be extracted from the image, this can be a very time consuming and normally manual task. A number of analysis options for anatomical images will be evaluated for their suitability when designing the LAT workflow. Where there are not appropriate extant image analysis solutions, new ones will be developed through collaboration with computer scientists.

3.2.3 Use cases

Pearl millet

The first case study involving the use of LAT to investigate monocot anatomy under water stress involves pearl millet. Pearl millet root anatomy is of significant research interest as this is an extremely important crop globally and especially in regions and communities afflicted by food insecurity and drought. Root anatomy and drought tolerance is being investigated in a large multi-year study, comprising Chapter 4. Part of the pilot year of this is to develop the anatomical phenotyping techniques that will be used in the subsequent years and determine strategies for anatomical sampling. Tandem to this, several smaller experiments were performed locally to optimize methods for the field trial and provide sample material.

Gamagrass and Maize

The second LAT use case study used root samples from a study investigating the effect of microbiome and water stress on gamagrass and maize.

Eastern gamagrass (*Tripsacum dactyloides*) is a monocotyledonous grass variety native to the eastern United states and south America. It is noted for its drought tolerance, deeply penetrating aerenchymous roots (Clark et al., 1998), and ability to hybridize with maize (de Wet and Harlan, 1974).

Root associated microbes can greatly impact plant physiology and health of their plant hosts, and this relationship has been shown to be influenced by both plant and microbiome genetic factors. This investigation aims to determine how microbial communities adapt to drought and their host, the benefit this confers to the plant, and how this is reflected by plant physiology and anatomy.

The thesis aims relating to this investigation are to develop suitable LAT based methods for each sample type provided, investigate root anatomical differences

between treatment groups, and determine whether or not the microbiome can affect root anatomy in these species.

Brachypodium

The third case study is *Brachypodium distachyon*, a relatively new model species for cereal and grass functional genetics (Draper et al., 2001; Hasterok et al., 2022). It is well suited to this role due to its relatively small genome, morphological simplicity, and proximality to wheat and other major food crops (Kellogg, 2015). Apart from a small number descriptive studies, brachypodium anatomy has not featured strongly in recent work (Watt et al., 2009; Pacheco-Villalobos and Hardtke, 2012).

PIN1 is an auxin transporter with an important role in vascular patterning, common to monocots and dicots (Li et al., 2015; Omelyanchuk et al., 2016; O'Connor et al., 2017; Y et al., 2019), and has been shown to have an important role in regulating development under drought conditions (Bawa et al., 2022; Borrell et al., 2022). *PIN1a* mutants have recently been developed in brachypodium (O'Connor et al., 2017).

The role of PIN1 in the water stress response in *Brachypodium* will be investigated by growing control and mutant lines under drought stress and investigating their anatomical differences. This will be done using LAT, which will first require development of LAT preparation and scanning protocols tailored to *Brachypodium*.

3.3 Biological material

3.3.1 Pearl millet (Senegal)

Pearl millet seeds were provided by ICRISAT to research partners, and seed stocks are maintained by IRD (Montpellier) and CERRAS (Senegal).

Field trial pilot year

Pearl Millet root samples were provided by collaborators in Senegal. These were crown and tiller roots, taken from a selection of 20 lines grown under well-watered and droughted conditions. Full experimental details are given in 4.3.2.

Sampling

The roots provided were segments of second, third and fourth whorl roots from the primary stem, and crown roots produced by tillers. These were sampled from 4cm away from the stem.

These roots had been sampled in Senegal and were stored in 2ml Eppendorf tubes containing 50% v/v ethanol upon sampling and kept in a cool dark place for 2-4 weeks until shipping. Ethanol was then removed from each tube for shipping. Upon receipt of samples in Nottingham, tubes were refilled with 50% ethanol and stored at 4°C.

3.3.2 Pearl millet (Nottingham)

Line selection

Five pearl millet lines, provided by Ndjido Kane (CERRAS) were surveyed for suitability for growth in Nottingham facilities. Seeds were sieved in calibrated sieves, and seeds between 1mm and 1.2mm were kept. Per line, 20 seeds were taken and used to assess the suitability of each line. Seeds were surface sterilized by immersion in 5% v/v sodium hypochlorite solution for two minutes, rinsed three times in sterile RO water, then immersing in 70% v/v ethanol solution for a further two minutes. Seeds were then rinsed three times in sterile RO water, and then left in water for ten minutes. Seeds were transferred to petri dishes containing sterile water-soaked filter paper, sealed with micropore tape, and stored in the dark at 28°C for 24 hours.

After incubation, the number of germinated seeds were counted, and at this point the lines that had a <70% germination rate were discarded.

The remaining seedlings were planted out on 6 well potting trays containing Levington M3 potting compost mix, one seedling per well. The trays were placed in a growth room with 14h of daylight (400µm/s/light radiance-Check bright growth room with all lights on), at a daytime/nighttime temperature of 28/24°C.

After 7 days, lines which showed less than <80% continued growth were discarded. From the remaining lines, the twelve largest plants were selected and transferred to 3l pots containing the same compost mixture. Pots were kept well-watered by filling the propagation tray they were based in with 5cm of water twice a week. 21 days after germination, watering for half the pots was stopped, and the plants were exposed to drought stress. Plants were then grown for another 4 weeks under drought and well-watered conditions.

At the end of this period, the number of surviving plants of each line/treatment were counted and sampled. Root crowns were excavated and trimmed to within 10 cm of the base of the stem. Root crowns were then washed, and the number of whorls present were counted. A single line was selected on the criteria of having produced at least 4 whorls of crown roots under well-watered conditions and drought stress in >3 plants, and then the line with the highest surviving number of plants was selected. The selected line was then used going forward in further experiments.

Growth

Seeds of the selected line were sterilized and germinated using the protocol described above. 36 seedlings were then planted into 18 soil columns of diameter 30 cm and height 100 cm , 5cm apart at 2cm depth.

The soil composition was ½ bulk soil and ½ sharp sand, and columns were prepared at field water capacity 2 days prior to planting. Plants were kept well-watered on a drip system, delivering 15ml of water twice a day.

After 21 days after germination (DAG) watering was switched off, for ½ the plants and growth was continued until day 48. Supplementary ad hoc watering was given to all plants throughout according to need when visual inspection appeared that plants were overstressed. This occurred on 32 and 41 DAG, and all plants were given 200ml of water, and plants were harvested on day 48 DAG.

Sampling

Flag leaves were removed from plants and placed in a sealed plastic bag with 10ml of water. Stems were cut 10cm above soil, and root crowns were excavated by hand, and to loosen soil all columns received 1l of water. Root crowns were dug out and rinsed in water to remove loose soil, then trimmed to 10cm of root material, and were then rinsed again and gently massaged to remove loose soil from the root ball. The stem was then trimmed to 5 cm and the root crowns were then stored in plastic bags containing 20ml of RO water.

Roots were sampled from the crown. Each root crown was transversely bisected to reveal the inner whorls, and the crown halves were then washed again to remove any remaining soil. Starting from the innermost whorl working outwards each root was sequentially removed and grouped according to its whorl. For each whorl per plant, two to three median size roots were subsampled, taking the top 2 cm from each root. These were then stored in 2ml Eppendorf tubes in 50% v/v ethanol solution.

The flag leaves were also subsampled and from the widest portion of the leaf, typically ¼ of the leaf length away from the leaf base, a 2cm region was taken and stored in an 2ml microcentrifuge tube (Eppendorf) with 50% ethanol v/v solution.

3.3.3 Maize and gamagrass

The maize and gamagrass samples were provided by Gabriel Castrillo and Maggie Kennedy from a BBSRC and NRF funded research project "A holistic approach to understand drought adaptation in plants, their symbionts, and free-living microbiomes". The full experimental design and rationale is given in Appendix 2.

Experimental Summary

Soil was collected from six sites across Kansas, contrasting in precipitation and irrigation (Figure 3-1 Obj. 1, Appendix 3). In controlled conditions, these soils were either planted with or without gamagrass, and either subjected to water stress or well-watered conditions, then harvested after 4 months (Figure 3-1 Obj. 2). This will result in four microbiome treatment groups for each of the six original soil sources.

Maize and gamagrass with then be grown in sand that has been inoculated with colonies obtained from each of these 24 treatment groups and subjected to either water stress or well-watered conditions for one month (Figure 3-1 Obj. 3).

From both objectives, the most recently developed crown root was sampled at the base of the stem. Roots were harvested and stored in 70% v/v ethanol and shipped to Nottingham from Kansas, following the same protocol as with the Senegalese pearl millet samples.

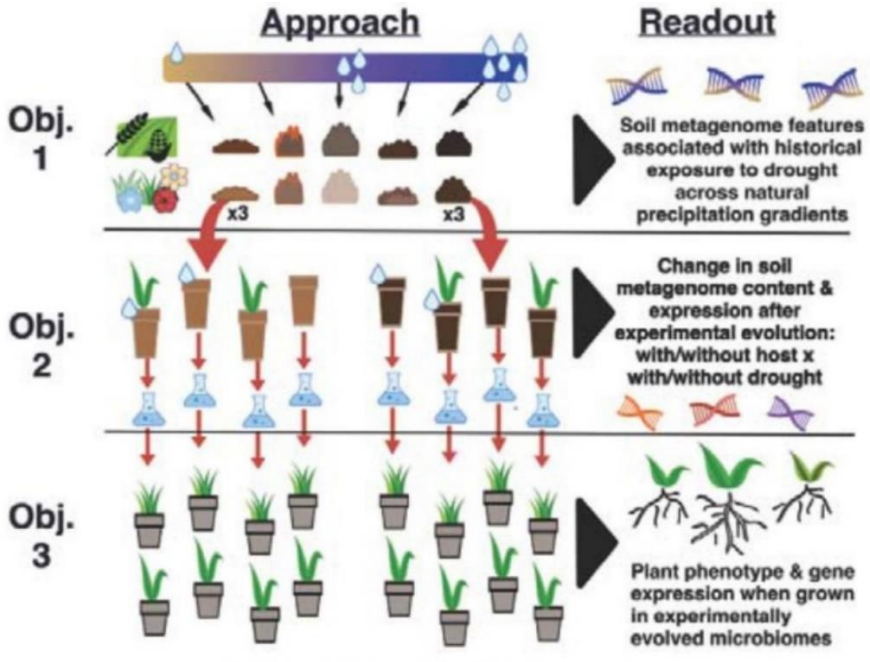


Figure 3-1. Illustration of maize and gamagrass experimental design. provided by Valeria Custodio

3.3.4 Brachypodium

Plant material

Root, leaf, and stem samples from an experiment investigating the effect of drought stress on wild type and PIN1a *Brachypodium distachyon* mutants were provided by Riccardo Fusi for anatomical analysis. These plants were grown in 15cm diameter, 50cm long, soil mesocosm cylindrical columns in a controlled environment chamber, under controlled and water deficit conditions for a period of four weeks.

Sampling

After four weeks of growth, the whole root system was washed out of the column, the arial tissue was separated from the root. A 2cm portion of stem was sampled from immediately below the first leaf, and a 2cm portion of leaf was sampled from the widest region of the youngest fully ligulated leaf. A crown root sample was

taken from whorl two, the oldest available whorl. Samples were stored in 70% ethanol v/v solution until preparation for scanning.

3.4 Sample preparation

The power of LAT scanning comes partially from its ability to scan samples without the need for staining or lengthy sample preparation processes, and indeed the majority of published uses of LAT scan samples when freshly removed from the ethanol solution they have been stored in.

While this technique has been shown to work well with mature maize roots, this was not the case for the majority of plant tissue used during this thesis.

3.4.1 Wet sectioning

Initial testing of scanning samples without any prior processing produced mixed results from species to species. While in most cases, timing the evaporation of solution with sample progression and imaging, with careful laser application, could produce images of acceptable quality, this was highly inconsistent.

Pearl millet crown roots

Pearl millet crown roots of various classes were imaged straight after removal from 70% ethanol solution. Rapid collapse of the cortex was observed in whorl 3 and 4 roots, and cortex was largely indistinguishable in W2 roots, however tiller roots were less affected. Using this method, however it was near impossible to confidently classify cortical aerenchyma. The ethanol in the cortex either clouded the entire tissue, forming a homogenous light reflective surface, or as it evaporated caused the cortex to collapse, creating numerous aerenchyma like voids. In all root classes, the stele seemed reasonably impervious to artifact generation as a result of wet scanning, however vascular bundles often appeared noisy or hazy.

Metaxylem could contain larger volumes of trapped ethanol that erupted from the root, causing bright flashes or obscuring the vessel.

Pearl millet leaves

Pearl millet leaves collapsed extremely quickly once removed from ethanol for scanning, all cell types became rapidly distorted and the leaf as a whole tended to curl, making consistent ablation difficult and imaging infeasible. Freshly harvested unpreserved leaves faired marginally better, however the waxy cuticle often caused leaf samples to burn or reflect the laser in a way that made anatomical visualization impossible.

Maize

Two different sets of maize roots were tested on the LAT, one from the microbiome soil history experiment, and a second set of mature brace roots from harvest age plants provided by Amanda Rasmussen (Nottingham).

The brace roots were able to be ablated wet to a similar standard of quality as that published in previous LAT studies (Schneider et al., 2023). Stele and cortical cells were clearly visible, and major traits count easily be identified and would be able to be quantified. This could be done without significant care to balance ablation rate with sample drying. Prolonged exposure to the laser beam for cutting or illumination did cause gradual shrinkage and eventual collapse, but this was at a slow rate and quality images could easily be captured.

The younger and smaller roots provided as part of the soil history experiment did not fare well when scanned wet. The cortex rapidly collapsed, even when not illuminated by the laser, and even within the stele it was not possible to differentiate cell types.

Gamagrass

Contrasting with the maize from the same experiment, gamagrass roots scanned very well directly from ethanol solution, there was no evidence of cortical damage (noting that there were extremely high proportions of aerenchyma, meaning there were minimal cortical paerenchyma cells to damage), even under extended periods of laser exposure. Stele cells were clearly visible, with even endodermal cells readily distinguishable from their surroundings.

Other

A number of other species and organs (including duckweed root and fronds, brachypodium primary and crown roots, rice root tips, barley primary root, rice and wheat cotyledons) were tested fresh and directly from ethanol with very poor results. An observed trend was that the younger the tissue, or the lesser degree of secondary thickening the organ had experienced, as well as the higher the original water content of the tissue, the worse the sample withstood laser ablation and the worse quality the images would be.

3.4.2 Critical point drying

Critical point drying is a technique of sample preparation that preserves biological material by completely removing any liquid in the sample and exchanging it with CO_2. Supercritical fluids are materials where under a certain combination of pressure and temperature conditions, they pass between liquid and gas phases without crossing a phase boundary. For CO_2, this supercritical phase is at (and above) the reasonably accessible 304.1 Kelvin (30.95 °C) and 72.8 atm. Between this temperature and the triple point temperature (-56.6 °C), and at a pressure above 5.1 atm, CO_2 exists purely in its liquid state (Figure 3-2). Under these conditions, a dehydrated sample stored in a medium of ethanol or methanol has

all of its liquid contents exchanged with liquid CO_2 in a pressurized and temperature-controlled chamber. The liquid CO_2 is then further pressurized and heated, bringing it into the supercritical state. In the supercritical state, fluids lose all of their stiction and surface tension meaning there is no mechanical effect on a sample as its liquid components evaporate, unlike with non-supercritical fluids. The pressure in this system can then be reduced, bringing the CO_2 into its gas phase, leaving a completely dehydrated and dry sample. Samples can then be stored on desiccated silica gel beads to keep them moisture free.

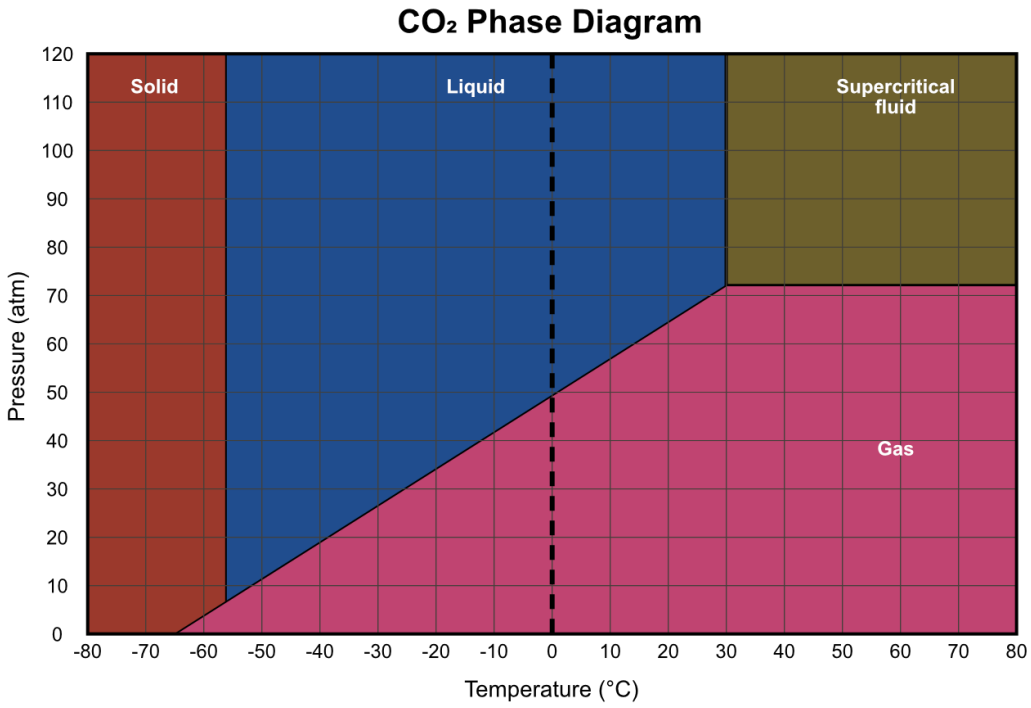


Figure 3-2. CO_2 Phase diagram. Showing the temperature and pressure conditions required for CO_2 to exist in its different states

Dehydration process optimization

In order for samples to be critically point dried, they need to be completely dehydrated as alcohols have a higher miscibility with liquid CO_2 than H_2O. For sample dehydration, initially a series of dehydration steps were used, individually aspirating and refilling each Eppendorf for an ethanol dehydration series from

70%-80%-90%-95%-100%-100%, each stage filled with fresh ethanol solution for 4 hours. This process was time consuming and resulted in higher occurrences of mechanical sample damage, so a new method of transferring samples directly from their storage ethanol level to pure methanol for 24 hours, then pure ethanol for 24 hours was tested. Reducing the number of dehydration steps saved a significant amount of time and reduced the incidence of mechanical damage to the sample, without any decrease in sample quality.

Sample holder design

The critical point drier model used (Leica CPD300) is provided with several differently sized sample holders, offering between 6-12 unique sample positions (big enough for plant roots) in holders with a volume of one third or half the capacity of the drier chamber. At maximum use this gives the CPD capacity for 24 samples in a processing run, lasting between 1-5 hours.

To improve on this throughput new holders custom made to fit the CPD chamber were designed. Additionally, by using the new CPD sample holders during the dehydration process to move batches of samples between solutions, throughput here could be significantly increased. By using 3D printing these holders can be made cheaply, quickly, and tailored to the specific dimensions of different samples. With these goals in mind, the holders must withstand every stage of the sample preparation process including submersion in water, ethanol, methanol and high pressure and temperature CO_2. Several 3D printing materials were tested for this purpose including a variety of Formlabs SLA resins (Tough 2000, Clear, Grey-Pro, and Flexible 80A), and Ultimaker FDM filaments (Tough PLA, PLA, ABS, Nylon). All materials were visibly affected by the process, either cracking, becoming brittle, shrinking, becoming discoloured, or partially dissolving. The least affected were the holders made from PLA with only ~5-10 % shrinkage and light discolouration, so

this material was used for holder fabrication (specifically white PLA to avoid colourant leeching).

Several designs of sample holder optimized for different tissue types and sampling methods were developed, noting that to ensure liquid exchange the base is printed with a lattice mesh, large enough to allow unimpeded fluid exchange even when shrunken, but fine enough to securely hold samples. These holders must be loaded with samples positionally as no labeling system survives the CPD process. It was found most efficient to do this by creating a schematic representing the possible sample positions in a numbered holder and a map to a correspondingly numbered Eppendorf freezer box with the original labeled sample tube in the equivalent holder position.

Settings optimization

For the model of critical point dryer used, there are 10 primary settings that can be changed to configure the drying process. Iterative alteration of the drying settings, testing the range of available settings revealed optimal configuration for preservation of anatomical features for LAT scanning for different plant tissues.

3.4.3 Optimal sample preparation methods

These protocols were found to be optimal for throughput and sample quality and were used to prepare all further samples for LAT scanning.

Roots (≤8 mm diameter)

Root samples under 8 mm in diameter (tested in millet, maize, wheat, barley, rice, pea, brachypodium, gamagrass) can be prepared for scanning fairly simply. Roots are removed from their storage medium (normally 50% or 70% v/v ethanol solution, trimmed to the length of the sample holder slot, and placed in the holder, sat in a shallow bath of ethanol solution at the same concentration as for sample storage. Once the holder is filled it is sealed either with the stainless-steel mesh lid

provided with the CPD, or with parafilm that is then perforated. The holder is then drained and blotted and transferred to and fully submerged in 100% methanol and stored at 4 °C for 24 hours. After this period, it is then drained and blotted dry again and transferred to 100% ethanol solution and stored at 4 °C for 48 hours. After this the samples are ready for critical point drying. Holders are transferred to the CPD chamber, filling up any unused chamber volume with filler pucks and then filling the chamber with 100% ethanol solution. The CPD is then run with settings in Table 3-1.

Table 3-1 Critical Point Dryer settings optimized for smaller root samples

Step	Setting	Value
Cooling	15	
Co2 In	Slow	
Exchanges	20	40
Heat	Slow	
CO2 Out	Fast	
Mixing	Slow	

After the process is completed, samples are then stored in their holder until scanning in a sealed container containing desiccated silica gel.

Roots (>8 mm diameter)

Roots of greater than 8mm diameter were handled similarly, though placed in a holder with larger and horizontal sample sub-trays. Roots were also cut transversely into lengths no longer than 1cm.

At the methanol stage, holders were placed in a vacuum infiltrator, slowly starting and increasing the strength of the vacuum until bubbles stop being released, then left on high vacuum for 30 minutes. Samples are then treated as above then the CPD is then run with settings in Table 3-2.

Table 3-2 Critical Point Dryer settings optimized for larger root samples

Step	Setting	Value
Cooling	15	
Co2 In	Slow	
Exchanges	20	40
Heat	Slow	
CO2 Out	Slow	
Mixing	Slow	

Leaf

Leaf samples require a significantly different holder configuration to roots but have the advantage of being stackable without the risk of moving position. Leaves were ordered, trimmed to 2cm lengths, and stacked horizontally for loading into the leaf holder and positioned between the holder posts. Leaf samples only needed 4 hours in each methanol and ethanol solution, then could be dried using the settings in Table 3-3.

Table 3-3 Critical Point Dryer settings optimized for leaf samples

Step	Setting	Value
Cooling	15	
Co2 In	Slow	
Exchanges	16	40
Heat	Fast	
CO2 Out	Slow	
Mixing	Slow	

Stem/ Cotyledon

Stems of up to ~6mm could be prepared using either the smaller root or leaf methods in either of the root holders using the faster methanol-ethanol steps as with leaves. They could then be critically point dried very rapidly compared to the other tissue scanned (Table 3-4).

Table 3-4 Critical Point Dryer settings optimized for stem and cotyledon samples

Step	Setting	Value
Cooling	15	
Co2 In	Slow	
Exchanges	20	40
Heat	Fast	
CO2 Out	Fast	
Mixing	Slow	

Stems thicker than this begin to encounter issues with critical point drying. Leafy stems, with many layers of furled leaves contained within, often showed mechanical damage to internal leaf layers as a result of CPD. Hollow stems larger than this dried well with minimal issue if sampling an area not connected to a node, or between two nodes; otherwise, these tissue types had differential shrinkage rates and mechanical stress developed. Finally, mature fibrous stems were challenging to critically point dry and frequently collapsed or were crushed by the process. Dissecting the samples into volumes of less than $1cm^3$ and treating similarly to the large root samples mostly produced undamaged samples.

3.5 Laser ablation tomography

Laser ablation tomography is a powerful technique for rapid root sectioning and imaging. In 2018 the University of Nottingham purchased a LAT unit from L4IS, a spin out company of the Pennsylvania State University, Lynch lab. When purchased it was more similar to the configuration used in Pennsylvania State University, however in order to better suit its intended applications, significant alterations were made to the contents and configuration.

3.5.1 LAT set up

The changes to the Nottingham LAT set up include addition of sample positioning actuators with a custom 3D printed sample mounting clip system, sample

positioning alignment lasers, brightfield illumination, and the replacement of a DSLR camera imaging system with a machine vision camera attached to microscope objectives (**Figure 3-3**). Custom image capture software was developed alongside the hardware changes. These alterations were made over time and protocol development was done with differing hardware configurations, though the described configuration was used for the majority of work conducted and all methods given are for this set up.

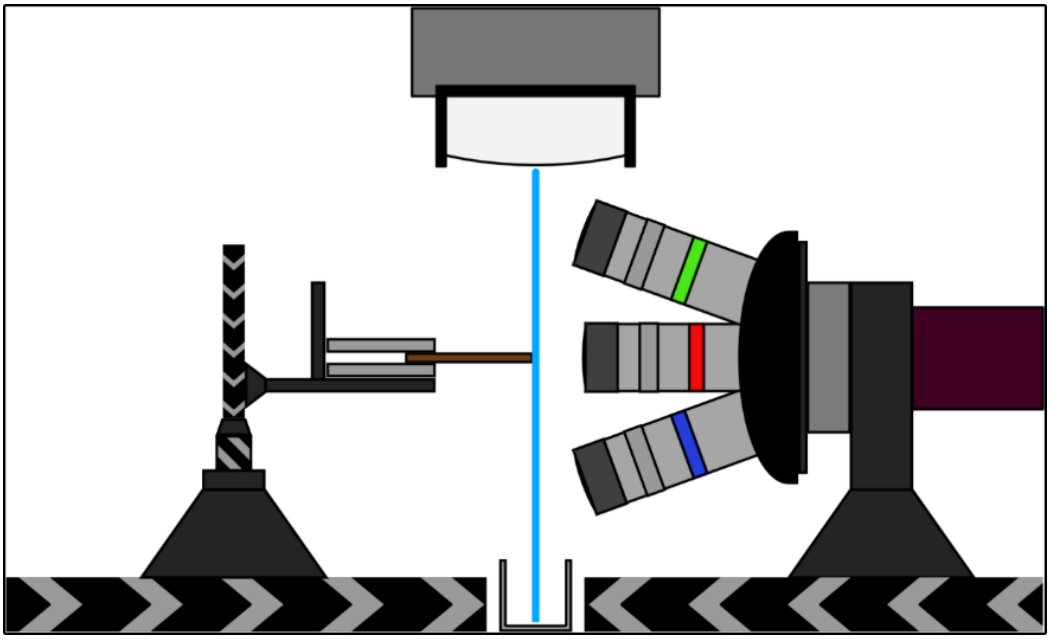


Figure 3-3. Schematic showing simplified layout of Nottingham Laser Ablation Tomograph Unit. A: Laser galvanometer, B Z-axis Linear actuator for sample (nanometer precision PI stage), C: X axis linear actuator, D: Y axis linear actuator, E:Sample stage F: Magnetic sample holder F: Root sample G: Laser sheet H: Heat sink and debris collector I:Microscope turret and objectives J: Microscope body, K: machine vision camera K: camera focusing stage.

Laser

The laser ablation tomograph consists of a 355 nm UV laser (q-switched, pulsed UV Laser, 150µJ @ 100KHz 12ps pulse (Edgewave Model PX100-3-GF) and a galvanometer (Scanlab Model RTC4) used to produce a laser sheet (**Figure 3-3**). The laser hardware settings are given in Table 3-5.

Table 3-5 LAT Laser hardware settings

Laser 1	2.6 A
Laser 2	5.5 A
Laser 3	60 A
Pulse Rate	99.84 Hz
Internal Gate Pulse Rate	1M Hz
Power Regulator	100%

For all scanning, the laser is shaped by the galvanometer as a rectangular sheet at the focal distance. The dimensions of this rectangle and the pattern used to draw this rectangle are set by the user, however the thickness of the beam (the dimension parallel to the Z movement plane) was kept constant at 5 µm and the scan speed was maintained at 1500 mm/s.

Stage

There are 4 sets of stage movement motors used in the LAT setup, three lead screw driven linear actuators for the sample *X-Y* movement and for fine focusing of the

camera, and a high precision Physik Instrumente (PI) Piglide air bearing linear stage for sample movement in the *Z* plane. The three lead screw actuators are controlled by the image capture software, and the PI stage is controlled by the task manager.

Camera and objectives

The camera is a FLIR Grasshopper 3 model camera, with 12.3 MP (4096*3000), capable of 30 FPS capture, and a SONY IMX253 full colour sensor. This is connected to a C-mount microscope adaptor fitted with a 4-position turret, holding four out of five available Mitutoyo infinity corrected long working distance objective lenses. The available objectives are 1X, 2X, 5X, 10X, and 20X (Appendix 1). This camera-microscope unit is mounted on a ZABER Technologies Inc., stage to enable fine focusing of the objectives.

Software

The laser is controlled using software provided by the manufacturer. The galvanometer is controlled using SPiiPlusSPC software (ACS Motion Control) that also allows user-defined operation of the laser, galvanometer and x, y and z-stages via scripts termed “recipes”. The camera is controlled by a program written in the LABVIEW development environment (National Instruments) that allows user-control of camera focus and acquisition parameters and connects to the SPiiPlusSPC software to trigger sample movement and laser firing after each image is taken Figure 3-4.

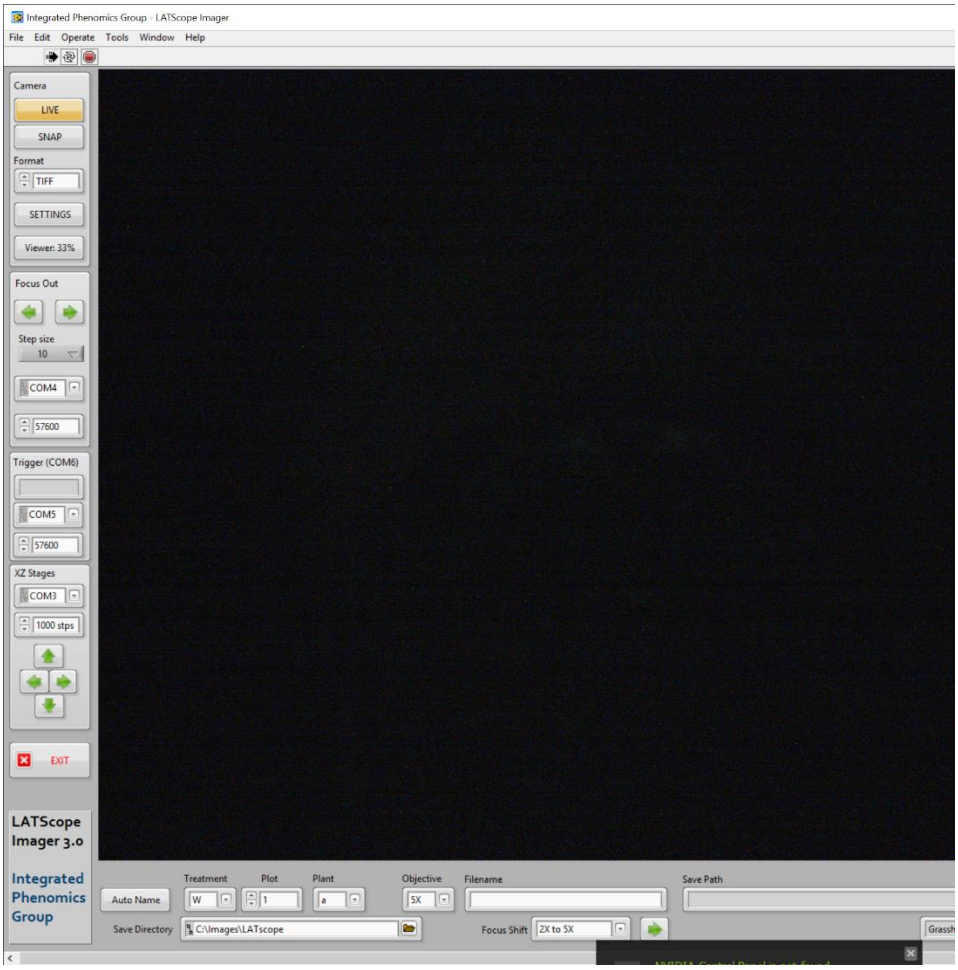


Figure 3-4. Image of the user interface of the LAT image control software.

Camera settings were varied between sample types and changed ad-hoc to best image individual samples rather than being kept constant.

Sample handling

The sample stage is positioned by the *X*-*Y* motors sat on top of the *Z* stage. Samples are held by magnetic clips that sandwich a portion of the sample, that then magnetically locate to the sample stage. Multiple sized holders were designed with different size channels to avoid excessive squashing of the root when holding. Oversized samples were either glued to the front of the stage or mounted on a pin or scalpel blade to suspend them in place.

Scan settings

Scan settings were thoroughly optimized for each sample type and research goal. Specific settings and workflows for each sample type are outlined below.

3.5.2 Pearl millet roots

To section and image pearl millet roots a multi-step workflow was developed. This formed the template for all further sample imaging.

Preparation of pearl millet roots for LAT

Samples were mounted in the sample clips and placed on the stage. Using the alignment laser and the brightfield light source the sample was positioned in the field of view of the camera and in with the path of the ablation laser. The 5X objective was used initially and to focus for all root samples. If the sample exceeded the field of view, the 5X was used first and the process was repeated using a larger lens size.

Having selected the most appropriate size objective lens, using recipe "Slow_Focus" shown in Figure 3-5, the ablation beam is fired in a 16 mm wide sheet (beam width) 50 times (Reps), then the beam is fired again though for 30 reps, this time not intersecting the sample having ablated or cut it, therefore illuminating it. During this time the camera can be focused by adjusting its *Z* position relative to the sample in the imager window. To keep the surface from shrinking away from the laser due to the heat, after each illumination run the sample is moved forwards (towards the path of the laser beam) by 2 µm, and the process of ablation and

illumination is repeated until the camera is in its most focused position for the sample.

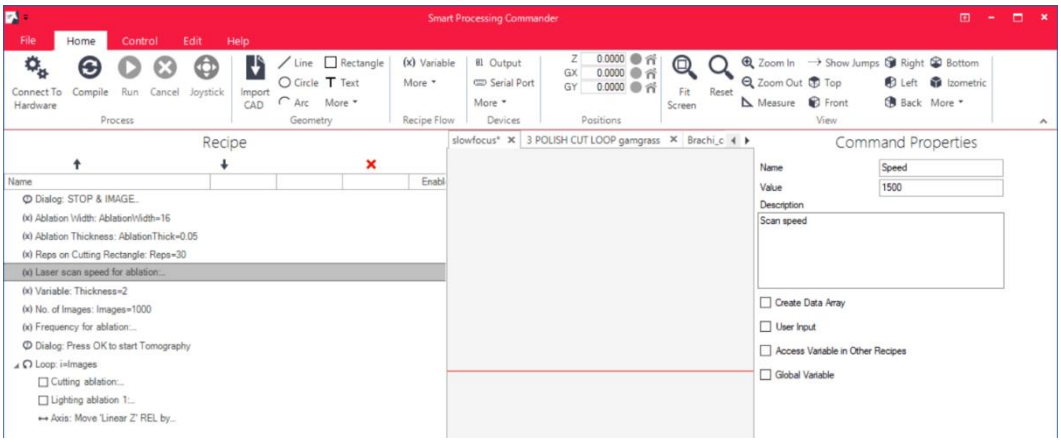


Figure 3-5 LAT Recipe "Slow_focus", SPC recipe for small step ablation and sample progression to focus the sample

A distinction is made between the use of terms ablation and cutting. When referring purely to sample ablation it is meant that the surface of the sample progressed forwards does not exceed the thickness of the laser's focal rectangle and that the entirety of the sample region progressed forwards is destroyed, in practice this was ~ 10µm, though could be as low as 0.1µm. Cutting is still an ablative process, but the distinction is made where there is a significant portion of sample on either side of the laser focus area (so much so that the sample is bisected rather than just reduced).

Imaging of pearl millet roots using LAT

Once samples were correctly positioned, as many images as required could be captured, spaced at any interval from one another using either the 2D or 3D imaging sequences.

Initially, following alignment, a single image was captured, reviewed, and either repeated at a different position or accepted. This process was slow and relied on the users "on the spot" appraisal of image quality; additionally, observation

showed that the first cut into a new root region often caused the generation of various artifacts and areas of sample damage.

To overcome this and to speed up the process of locating and imaging a good quality representative region, a partially automated recipe was developed.

Starting with a cut into a fresh region, 10 sets of 10 µm "polishing" ablations are performed, followed by 5 sets of ablation and illumination 10 µm apart, with images captured in sync with the illumination steps. The sample is then moved forward 500 µm, and this process is repeated three times, giving a total of 20 images across 2.65mm of root, using the "Polish_Cut_Loop" recipe shown in Figure 3-6.

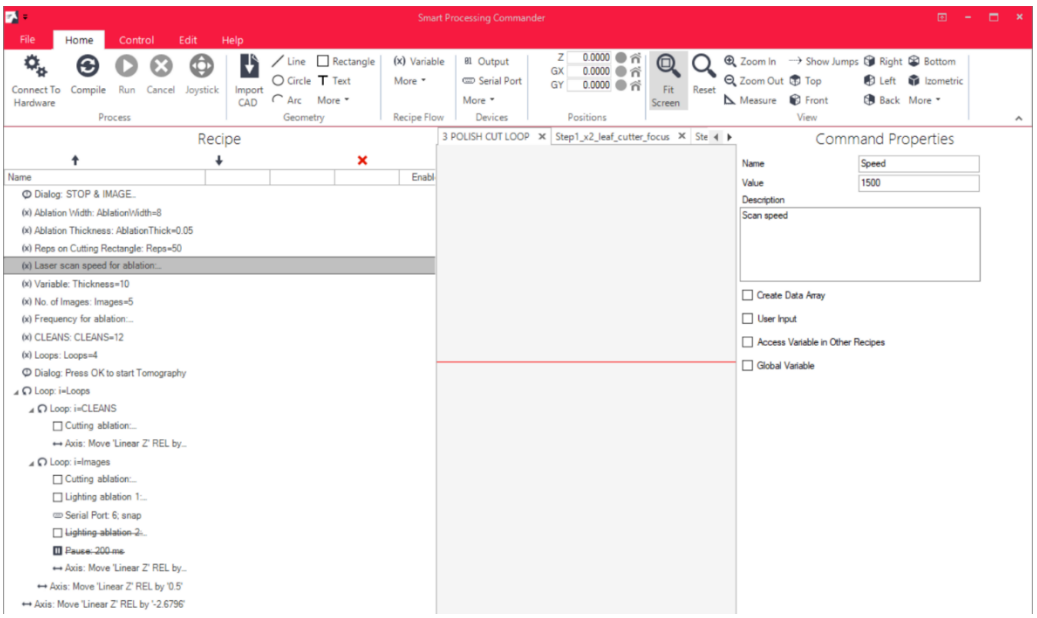


Figure 3-6. LAT Recipe "Polish_Cut_Loop", SPC recipe for sequential ablation, imaging and sample progressing, repeated three times for imaging coverage

A standard laser width of 8 mm and 50 reps were used for the majority of samples, though this was altered to improve image quality for specific samples if needed.

This automatic replicate system meant that rather than a single image potentially containing image artifacts such as lateral roots or soil remnants, 20 images are obtained quickly, many hopefully avoiding problematic or non-representative regions and image features such as fluctuations in brightness, laser artifacts such as burning or striped patterns, or biological artifacts such as lateral roots). The 500 µm gap between imaging sets was found to be sufficient to move past the majority of regions containing mechanical or laser inflicted damage. A representative image could be picked from the image set at a later time.

3.5.3 Pearl Millet leaves

Preparation of leaf samples for LAT

Pearl millet leaves were prepared similarly to the roots, with the same initial camera and alignment settings, however in addition to the leaf sample being mounted in the holders, a sacrificial leaf sample (normally the previously scanned leaf) was positioned above the sample in a second tier of holders. The 1X lens was used as a start point rather than the 5X, and a beam width of 18 mm was also used. As many leaf samples exceeded this width, the “Slow_Focus” recipe was altered to increase the number of cutting replicates so that the whole width of the sample could be moved under the path of the beam to cut it (Figure 3-7)

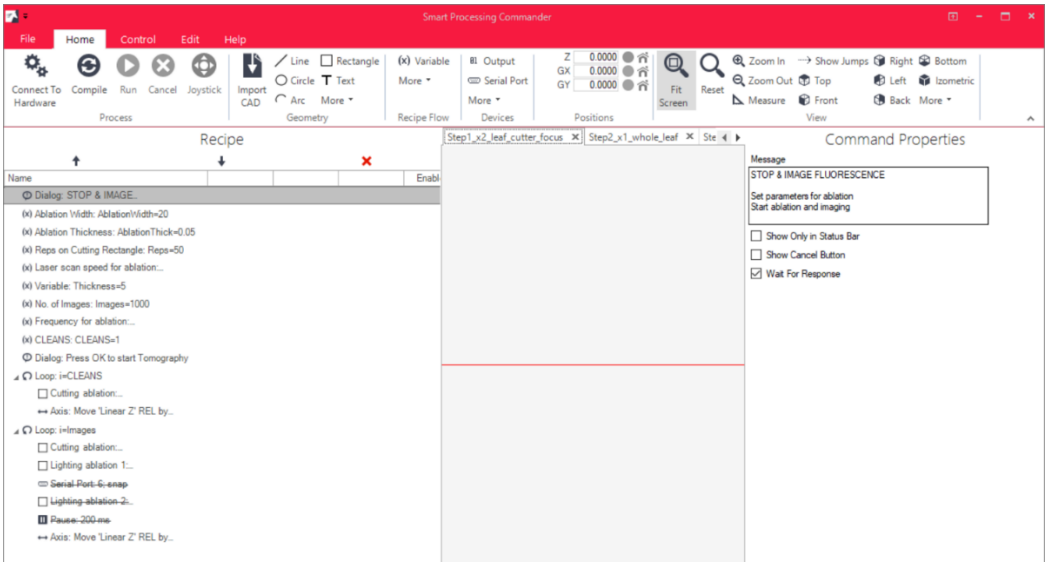


Figure 3-7. LAT Recipe "Leaf_Cutter", SPC recipe for sequential ablation, imaging and sample progressing, repeated three times for imaging coverage

LAT scanning of pearl millet leaves

Leaves were scanned at three magnification levels, 1X to image the whole leaf, 5X for the midrib, and 10x for a portion of lamina, as shown in Figure 3-8. Each region had its own imaging protocol.

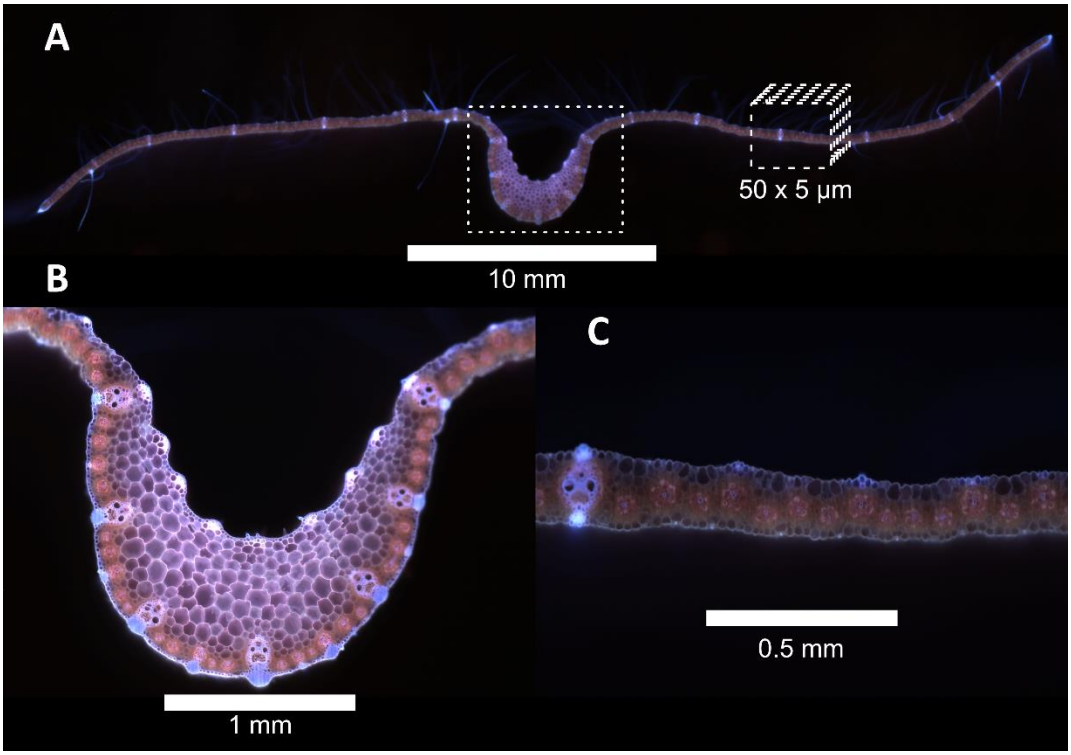


Figure 3-8. Leaf imaging regions. (A) Composite whole leaf image stitched from multiple frames captured using 1X magnification, with boxes showing regions imaged in B (left) and C (Right), (B) Midrib leaf image captured using 5X magnification, (C) Lamina portion of leaf imaged using 10X magnification (50 images captured at 5 µm *Z*-intervals, Scale Bar A=10 mm, B=1 mm, C=0.5mm

Whole leaf cross sections were scanned by tile scanning over the width of the leaf with the 1X lens. Having cut the leaf using the laser to expose a clean surface, the leaf was positioned so that the left edge of the leaf was in the left edge of the frame, Using leaf recipe 2 (Figure 3-9), the leaf was imaged, then the sample was moved 20000 steps (giving a ~15% overlap on the 1X), to the left (as well as up and down if needed), and the recipe was run again. This was repeated until an imaging run had been completed on every part of the leaf from left to right.

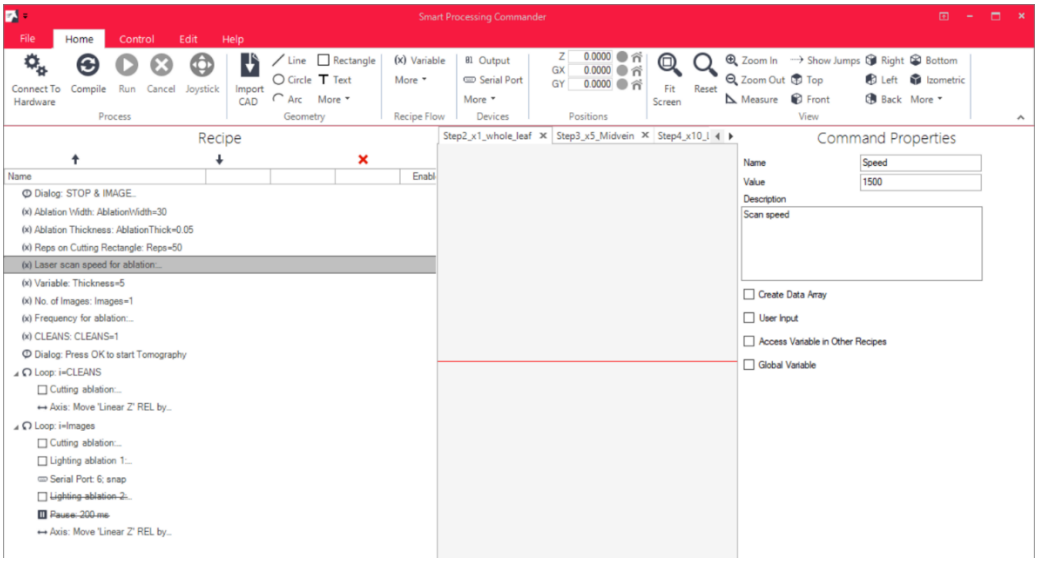


Figure 3-9. Whole leaf imager 1X recipe

The magnification was then increased to 5X, and refocused using “Slow_Focus” on the central midvein. Leaf recipe 3 was then used to take three polishing ablations of 10 µm, and five images with 10 µm ablations in between (Figure 3-10.

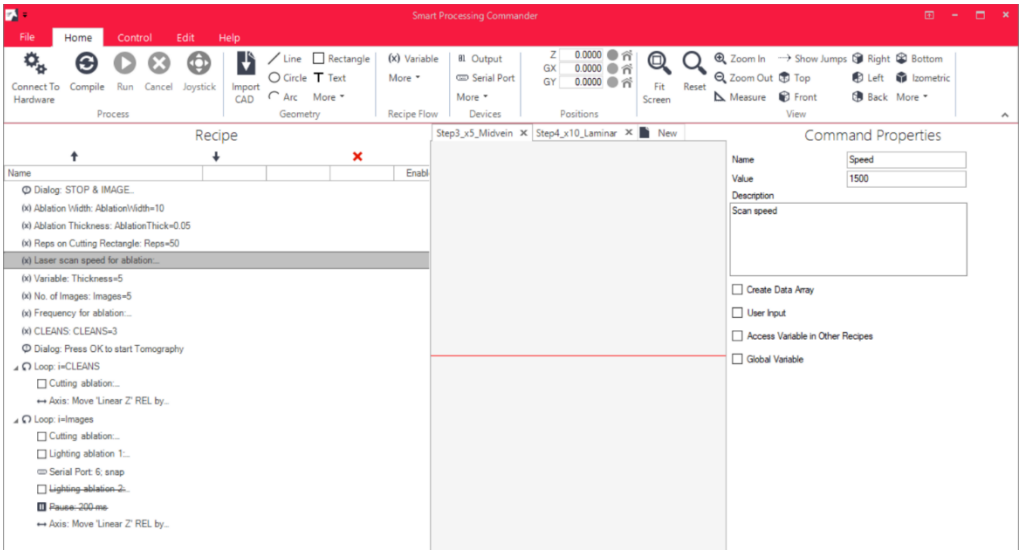


Figure 3-10. Leaf midrib imager 5X recipe

From these five images a single representative image was later selected.

For the lamina section, the magnification was increased to 10X, and the third major vascular bundle to the right of the midrib was positioned in the left of the image frame. The camera settings were changed for the lens, then three 5 µm polishing ablations were made, then a series of 50 images with 5µm *Z* intervals were captured using the recipe shown in Figure 3-11.

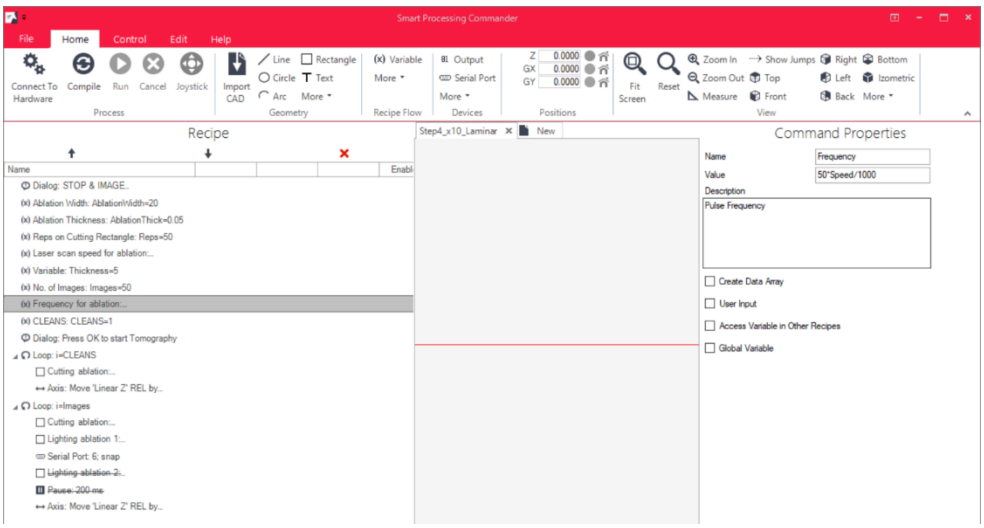


Figure 3-11. Leaf lamina portion 10X recipe

3.5.4 Gamagrass and maize roots

Gamagrass roots and maize roots were imaged using the same looped 20 image approach as pearl millet roots using the 5X lens, though with optimized camera, and laser width, slice thickness, and laser repetition settings (8 mm, 20 µm 50 repetitions).

3.5.5 Brachypodium

The brachypodium root, leaf, and stem samples all required specific adaptation of the methods used previously.

Brachypodium root imaging

Samples were prepared and scanned in the same manner as pearl millet roots, though using the 10X lens, adjusting the camera settings, and adapting the method to use a beam width of 12 mm, 2 µm thickness ablations, and 20 laser repetitions.

Brachypodium leaf imaging

Leaves were stacked and scanned 3 samples at a time, with an additional later of sacrificial leaf added above. The 2X lens was used for these samples to image whole leaf anatomy, with the recipe in Figure 3-10, capturing a set of five images. If any portions of the leaf were out of frame this was run multiple times until all areas were thoroughly imaged. This process was repeated using the 10X lens, focusing on the midrib of each sample.

Brachypodium stem imaging

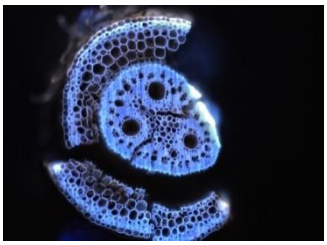
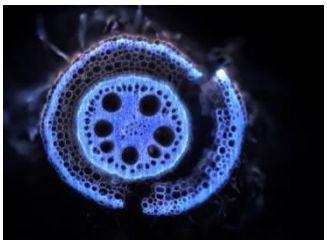
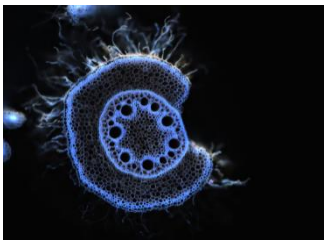
Stems were imaged with the 5X objective, using a layer of leaf positioned above each sample and ablated and imaged using the pearl millet leaf 3 recipe to capture 5 images of each sample.

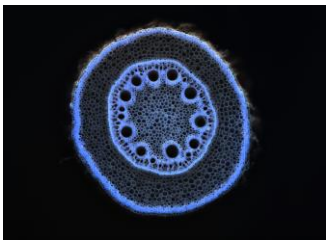
3.6 Image analysis

3.6.1 Pearl millet root quality assessment

The quality of the different whorl samples received from the pilot year field trial was assessed to determine future sampling strategies. A subset of 30 images from each whorl/treatment combination were scored from 1-5 based on the level of damage sustained during the harvesting, sampling, preparation, and imaging processes in order to determine the suitability of the methods. This was done using the scoring system described in Table 3-6.

Table 3-6 Root quality scoring scheme

Score	Reason	Example
1	Significant voids, damage or artifacts within cortex and stele	
2	Significant voids, damage, or artifacts only in the cortex	
3	Moderate voids, damage, or artifacts, limited to <1/3rd of the cortex	
4	Minor voids, damage, or artifacts	

5	Undamaged root	

This was replicated with the Nottingham grown plants using 12 images from each whorl/treatment and compared to the results from the Senegalese samples.

3.6.2 Pearl millet leaf image processing and measurement

Whole leaf measurement

The whole leaf images were stitched automatically per directory using Fiji's image stitching plugin developed by Preibisch et al. (2009), using grid stitching with unknown position. This was incorporated into a macro to automatically stitch every image set, set the image scale, and enhance the image contrast.

For measurement, the image was cropped to half the leaf width including the full midrib, for whichever half of the leaf was better preserved. Using FIJIs multi-point tool, the midpoint of each major vascular bundle from the central vascular bundle of the midrib to the leaf tip, and the very end of the leaf tip, was annotated, and the X-Y position was recorded. From this, leaf half width, number of major vascular bundles (MVBs), and distance between MVBs was calculated trigonometrically in excel.

Midrib image measurement

Of the 5 midrib images captured, a single representative image was selected based on appraisal of image quality, this was then processed using CLAHE to improve contrast. In FIJI, the thickness of the midrib was measured with the line tool, and

area and diameter of the large metaxylem in major vascular bundles was measured using the magic wand tool.

Lamina image processing and measurement

From the 50 lamina images, the 26th image was selected to represent the set, unless the image quality or fluorescence was poor then an alternate image from nearby in the stack was used.

Several traits were measured in FIJI from the representative lamina image; leaf thickness at major, secondary, and tertiary vascular bundles was measured, as well as height of 3 central bulliform cells from the adaxial surface, 3 peripheral bulliform/adaxial epidermis cells, and of three abaxial epidermal cells. The width of every vascular bundle in the imaged portion of the leaf was also measured, which also provided the midpoint of each vascular bundle, giving the distance between vascular bundles.

To count and measure stomatal files a macro was used to compress each sample image stack into a representative median image of the whole 250 µm scanned region. From the median projection image, stomatal files were made more visible (Figure 3-12), and every stomatal file was counted using the multi point tool on the adaxial and abaxial surface, giving a count of stomatal files for each surface, and the distance between each file.

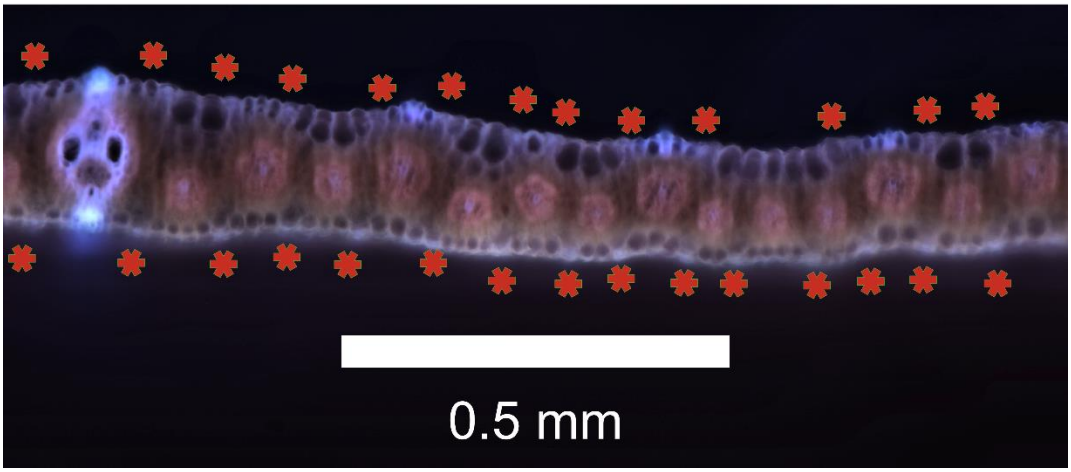


Figure 3-12. Median projection of 50 pearl millet leaf lamina images. Taken 5 µm apart in the *Z* plane, with asterisk marking more prominently highlighted stomatal files

3.6.3 Gamagrass and maize root image analysis

Gamagrass and maize images were measured manually in FIJI, following CLAHE processing using default settings. The whole root, cortex and stele were measured using the polygon selection tool, giving measurements of area, perimeter, and min and max diameter. Number, total and mean area of metaxylem and aerenchyma were measured using the magic wand tool. The number of cortical cell layers were counted from the first layer radially outwards from the endodermis to the epidermis.

3.6.4 *Brachypodium* image analysis

Roots were measured manually using FIJI following default CLAHE adjustment. The whole root and stele area, perimeter, diameter and centroid were measured using the ellipse tool. Metaxylem size, number, and centroid were measured using the magic wand tool. The distance between individual metaxylem centroids and the

stele centroid for each sample was calculated trigonometrically in excel. Leaves and stems were not measured.

3.7 Development of root anatomical analysis software

3.7.1 Training set generation

Training set images

Whorl four roots from the 2018 Senegal field trial were imaged using the described LAT methods above. Following image acquisition, a single image was selected per replicate, based on the described curation procedure. This provided 348 images, 193 from the well-watered treatment plants, and 155 from the drought stress treatment plants. Of these, 100 from each treatment were selected; first by excluding any images that had damage clearly caused by the sample preparation or scanning methods, secondly by removing images of roots too large for the image size, images taken using other than the 5x objective, and images of insufficient quality, and finally selecting images at random for removal if a large number of highly similar images were already present until a set of 100 images was reached.

These images were then processed using Fiji's (Schindelin et al., 2012) "enhance local contrast" (CLAHE) tool using default settings (Blocksize: 127, Histogram Bins: 256, Maximum slope: 3.00, Mask: *None*, Fast), to create a second set with more clearly visible cortical cell walls.

Training set segmentation and annotation

To produce annotated root images a semi-automatic software tool, CellSeT (Pound et al., 2012b), was used. For segmentation the CLAHE processed images were used. Images were loaded in CellSeT in the blue channel option, then default filters were applied. At the automated segmentation stage default segmentation was tested, and if an appropriate amount of cell walls were detected, this was then used as a starting point. However, in the majority of cases, default segmentation significantly

under detected cell walls, especially within the stele and endodermis. To address this, global manual watershed thresholding was used. The lower the threshold used, the more predicted cells were found, and vice versa, adjusting the threshold between 1-10 for most images allowed for identification of the most accurate threshold value approach to minimize manual correction time. In most cases, a threshold value of 3 was found to be most suitable. This resulted in a significant overestimation of cells, but the correctly identified cell walls were often segmented accurately and removing extraneous cell wall segmentation manually was faster than adding in unsegmented walls.

At the network refinement stage cell walls were manually removed or drawn into the segmentation to better represent the root anatomy.

In order to do this, several compromises had to be made in how the root is represented in the segmentation:

- Root hairs were excluded from epidermal segmentation.
- Individual stele cells could not be segmented so large vascular cells were drawn around, and supporting stele cells were drawn in as borders.
- Artificial subdivisions of aerenchyma had to be added for software size and number of cell borders limits, remnants of lysed cells also often remained in aerenchyma.
- Endodermis was not always clearly depicted, so was segmented as accurately as possible, or drawn in cell by cell at the correct position.

Once the manual refinement was completed, snake refinement parameters were set, for most images these were Node spacing: 8, Curvature: 1, Continuity: 8, and Image Weight: 5, though on occasions this failed, snake refinement was skipped.

Once the segmentation was complete, each segmented cell could then be annotated. This was done by assigning each cell to one of nine classes: meta-xylem, stele cell, vascular bundle, endodermis, cortical cell, void, aerenchyma, cortical sclerenchyma, and epidermis. Once each cell was annotated, measurements, cell maps and masks were exported. In CellSeT, by enabling a modified version of the nuclei plugin and outputting the thresholded images without suppressing walls, a simple recoloured mask of the annotation without the underlying original image is produced, this is the final output for deep learning training.

Training set expansion

Upon generation of the training set, the original images can be augmented, artificially increasing the size of the training set. This was done through rotation, contrast enhancement and degradation, addition of noise, rotation and reflection. These processes increased the size of the training set from 200 to 1200.

Post model deployment (Model version Epoch44Cortex), and processing of a selection of 2021 field images, areas of poor performance were identified. 10 images that performed badly and had common problematic features were identified. These included a large number of aerenchyma, voids and damage, scattered laser reflection, burning, laser shadow, lateral root emergence, high presence of cellular contents and cell end wall reflection. These supplemental images were annotated as described previously and added to the training set.

3.7.2 Model development

Network training

A deep learned neural network was trained to recognize the 9 tagged cell types in the pearl millet root images. The segmentation masks and the original and augmented LAT images were provided to the model for it to learn how to recognize

the different cell types. The high-resolution images (4096*3000 px) acquired by the LAT however make this challenging as processing large images is highly computationally demanding. To address this, images were tiled and subsampled into 4x4 1024*750 px regions. This significantly reduces the VRAM requirement for model training without a significant decrease in accuracy, however the smaller the tile, the greater the loss of context for specific cell annotation and the introduction of additional edge effects. To address this, cross talk (XT) is to the network, allowing for a global perception of tile context, enabling greater accuracy in cell identify prediction. Through testing of the optimal network tiling and crosstalk configuration in order to optimize accuracy with regard to VRAM usage was conducted.

Due to the high image quality and the level of resolution being largely superfluous to the level of trait quantification, images were also downscaled to 0.5 of the capture image size.

During training the input images were augmented to artificially increase the size of the training set. These augmentations include brightness, random pixel value modulation, contrast adjustment, CLAHE, brightening and dimming of image sections, cortex darkening and brightening, flipping and rotation.

The network was created using the PyTorch machine learning framework using a combination of Python and C++. Unsupervised training and model generation was run using the University of Nottingham Augusta High Performance Cluster.

Model testing

As a highly iterative process, and by nature of being unsupervised, specific adjustments could not be readily made to models, however supplementation and

adjustment of the training sets, and rules imposed on classification methods could be added.

As a result of this, objective assessment of model quality and accuracy is challenging. Sørensen–Dice coefficient values could be calculated for the model based on the similarity of outputs to the holdout or training set, however this may not be a representative assessment, as accuracy on certain cell types can weigh the calculation more heavily than others and or the training sets may provide an imperfect yardstick for quantification.

At various stages, additional rules were imposed on the networks classification system based on knowledge of root anatomy in an attempt to limit erroneous annotations. These told the network that the stele was inside a ring of endodermis, that metaxylem and vascular bundles, were within the stele and of a certain range of sizes, that aerenchyma was within the cortex, and all cells sat within the epidermis. However, adding these constraints to the model caused accuracy to decrease and for the model to crash frequently so they were removed, relying instead on improving the quality of the training set.

The ability to retrain models was added to the final deployable version of root scan. The inputs for model training, being a folder of images, a folder of files of annotations of the image set, and a validation/hold out set of images and annotations.

The model trains in epochs, reviewing each image in the training set each epoch, and runs 600 epoch iterations. Every 5^{th} epoch, the model compares its segmentation and annotation accuracy to the holdout set, reports its DICE score, and records the best current model.

Model implementation

The final version of the model ("DarkCortexTraining53Dataset-Epoch334"), was trained on 6/3/23, using a training set of 206 images. This was trained on a RTX G-force 4090 graphics card with 36 GB of VRAM.

3.7.3 Software deployment

Image output measurement

Measurement of the segmented output of the model was conducted by the software. Traits of interest were cell type areas and topology, and metaxylem and vascular bundle count.

Initial versions of the measurement provided a greater list of metrics than the final output, however a large number were removed due to redundancy or for simplicity.

Various measurements were tested for reliability, utility, and representativeness of the original image, and the final measurements to be used by the software are given and generated as described in Table 3-7.

Table 3-7 Example measurements exported by ROOTSCAN, and the method of measurement

Measurement	Method of generation
Xylem Total Area	Sum of total area tagged as metaxylem
Xylem Number	Count of metaxylem tagged pixel areas, greater than 900 and less than 200000

Vascular bundle mean area	Mean area of all vascular bundles
Cortex Circle Area	Bounding circle based on mean radius of outermost centroids of cortical cells
Stele area	Convex hull of centroids of the 80% (User defined) of stele cells closest to the stele centroid
Root Pixel Area	Sum of area of all pixels in the image annotated as root and aerenchyma

Data generation

To process input images in the software an input folder of images and an output folder is selected. The images are then processed in batch, running through each image in the folder individually, exporting a segmented annotated cell mask, two sets of overlay images showing the fitted circle and the convex hulls of the cell layers, and the measurement sheets.

These measurements are exported as CSV files by ROOTSCAN, each root image generates a file of metaxylem measurements, vascular bundle measurements, and whole root measurements. Additionally, a running list is produced with a summary row for each image processed in the run.

3.8 Results

3.8.1 Pearl millet

Nottingham line selection

Screening of the five pearl millet varieties available showed that the most suitable line for use in further Nottingham experiments was GB-8735. This line provided usable material for method development and served to validate the methods developed for pearl millet anatomical investigation.

These methods produced consistently analyzable images, of roots and leaves, though occasionally struggled to perfectly preserve and capture the anatomy of thicker stem samples, as seen in Figure 3-13

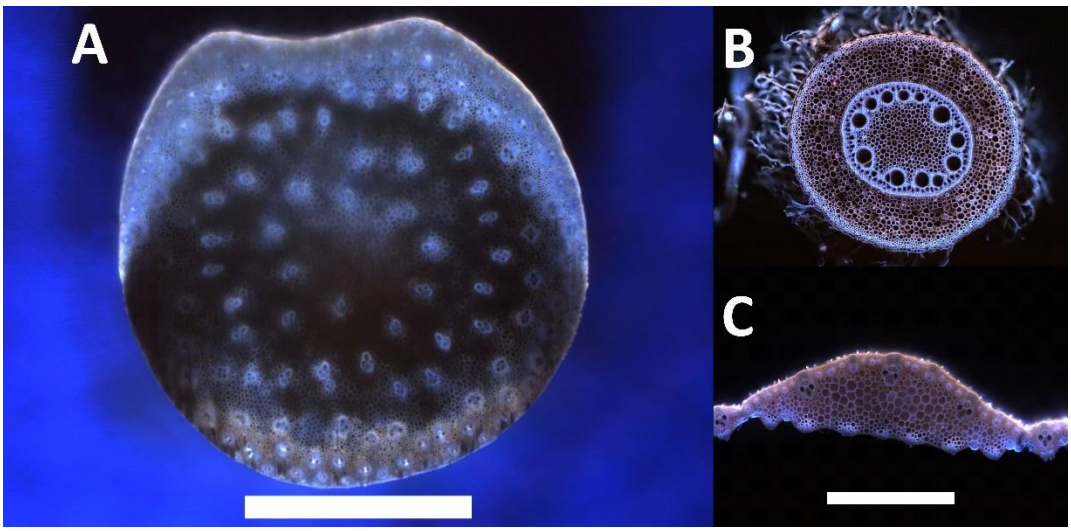


Figure 3-13. Representative images of pearl millet organs. Scanned using the methods developed in 3.5.2, and 3.5.3. (A), Pearl millet stem from internode

immediately beneath panicle, (B) Fourth whorl crown root, (C) Flag leaf midrib, Scale bars: A=5 mm, B&C= 1 mm

Using the root images from the Nottingham trial, ROOTSCAN was tested in its ability to accurately segment, measure and annotate images of plants grown in different conditions, and in how well it handled roots of different whorls and magnifications. The outputs of Figure 3-14, show that ROOTSCAN was accurate in its annotations in a range of conditions and that it could be used transferrable.

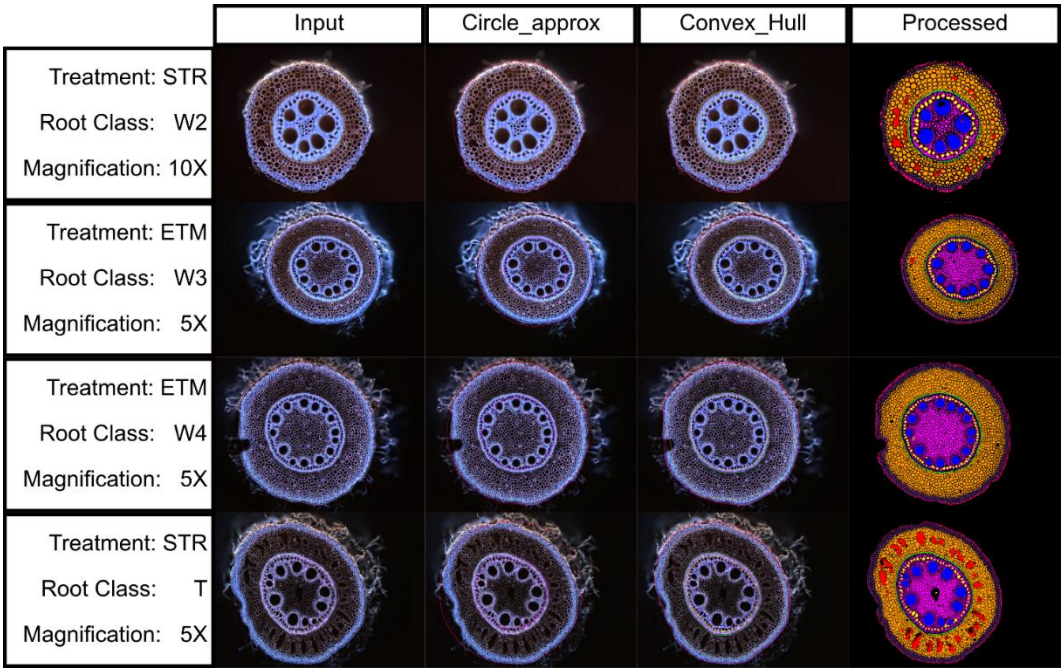


Figure 3-14. Paneled image showing the Outputs from ROOTSCAN's measurements of different whorls from the Nottingham grown samples, Images organized into table showing the input images and three types of output from ROOTSCAN for four different adventitious root classifications under two different treatment groups. STR: Water stressed, ETM: Well-watered, Magnification: Mitutoyo lens used on LAT camera, Circle_approx: circle approximated by ROOTSCAN based on mean distance from outermost cell layers cell centroids to root centroid, Convex_Hull: polygon outlining the outermost cell layer of each cell type, Processed: Segmented and recolored image produced by ROOTSCAN representing the identified cells in the sample image.

Scoring the Nottingham grown pearl millet roots of different whorls showed that the preparation methods were largely suitable for all root classes, with the highest range of samples with scanning issues being well watered tiller roots Figure 3-15).

These issues arose primarily as a result of soil adhesion or sample size limitations at the drying stage.

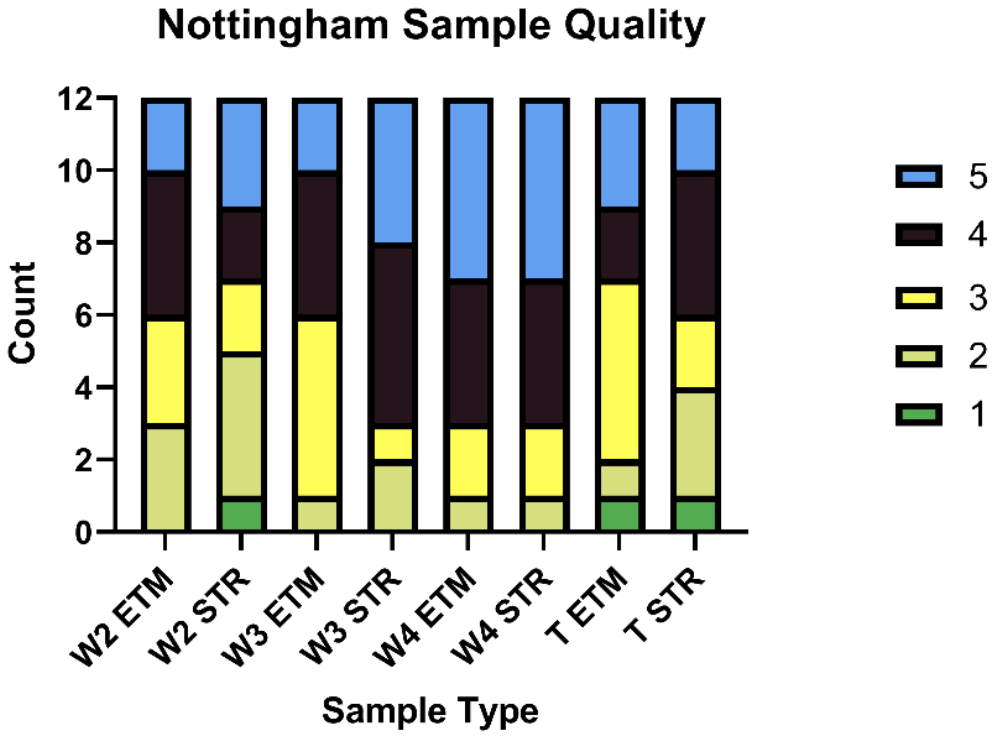


Figure 3-15. Nottingham grown root image quality scores. Stacked Bar chart showing the distribution of sample quality image scores for the different whorls and treatments of pearl millet crown roots obtained from the Nottingham grown plants, scoring system described in Table 3-6 (1: Totally damaged unusable root – 5: Perfectly preserved root), ETM = Well watered, STR = Water stressed

Senegal field trial whorl selection

Screening of the Senegalese pilot year pearl millet root sample images for sample integrity and quality showed that the most consistently high-quality root sample class was whorl four (Figure 3-16). The majority of water stressed whorl two and three roots had sustained at least large regions of damage to the cortex, and many had sizeable stele artifacts. The tiller roots often also showed significant damage

to the whole root sample, in both the stele and the cortex. Whorl 4 roots were very infrequently damaged in a region larger than 1/3rd of the cortex, and in the well-watered and water stressed individuals had the first and second largest number of completely undamaged samples respectively.

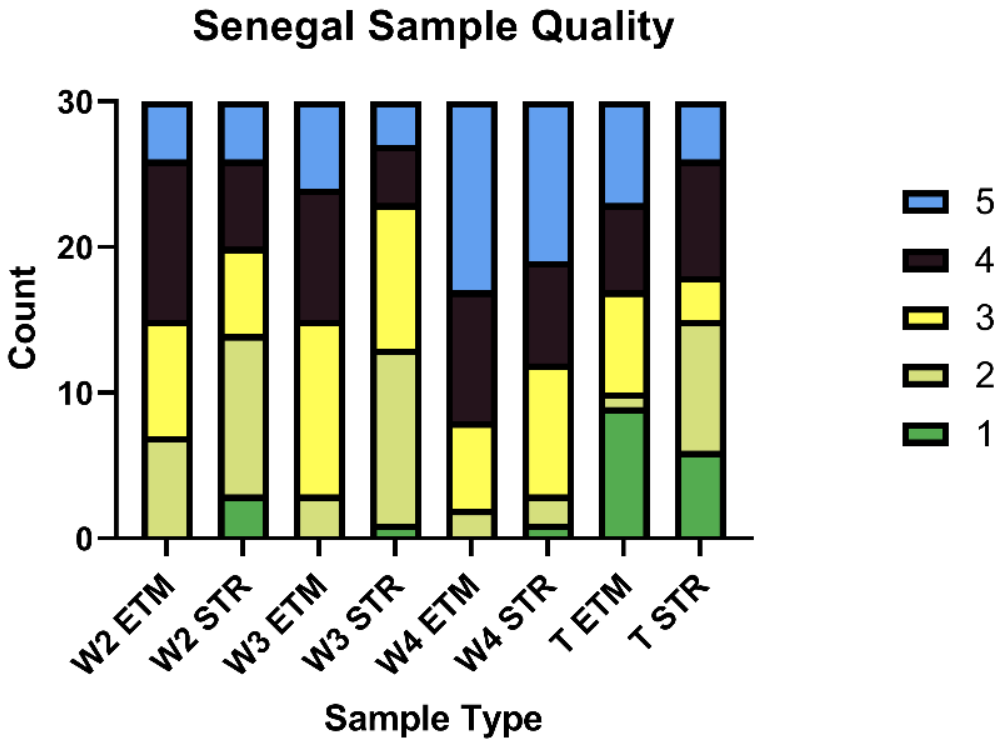


Figure 3-16. Senegal grown root image quality score. Stacked Bar chart showing the distribution of sample quality image scores for the different whorls and treatments of pearl millet crown roots obtained from the Senegal field trial pilot year, Scoring system described in Table 3-6 (1: Totally damaged unusable root – 5: Perfectly preserved root), ETM = Well watered, STR = Water stressed

3.8.2 Gamagrass and Maize

Of the 683 gamagrass and maize samples provided, a total of 13660 LAT images were captured using the methods described in 3.6.3, and a single image was selected and measured for each sample. These were 97 gamagrass root images

from objective two, 298 gamagrass images from objective three, and 288 maize images from objective three.

Effect of drought on gamagrass root anatomy

The gamagrass samples obtained from objective two showed that there were very few (3/60) significant anatomical differences between the different water treatments, across most of the different soil mesocosms (Figure 3-17). There was a slightly higher number of significant differences when comparing anatomic differences between mesocosm within treatment (13/300), but at a lower occurrence when considering the number of tests. Metaxylem number and cortical cell layer number were the most significantly variable traits. Where there were significant trait differences, roots from the WEL (soil from highest rainfall level) mesocosms tended to have smaller area, diameter, and number values.

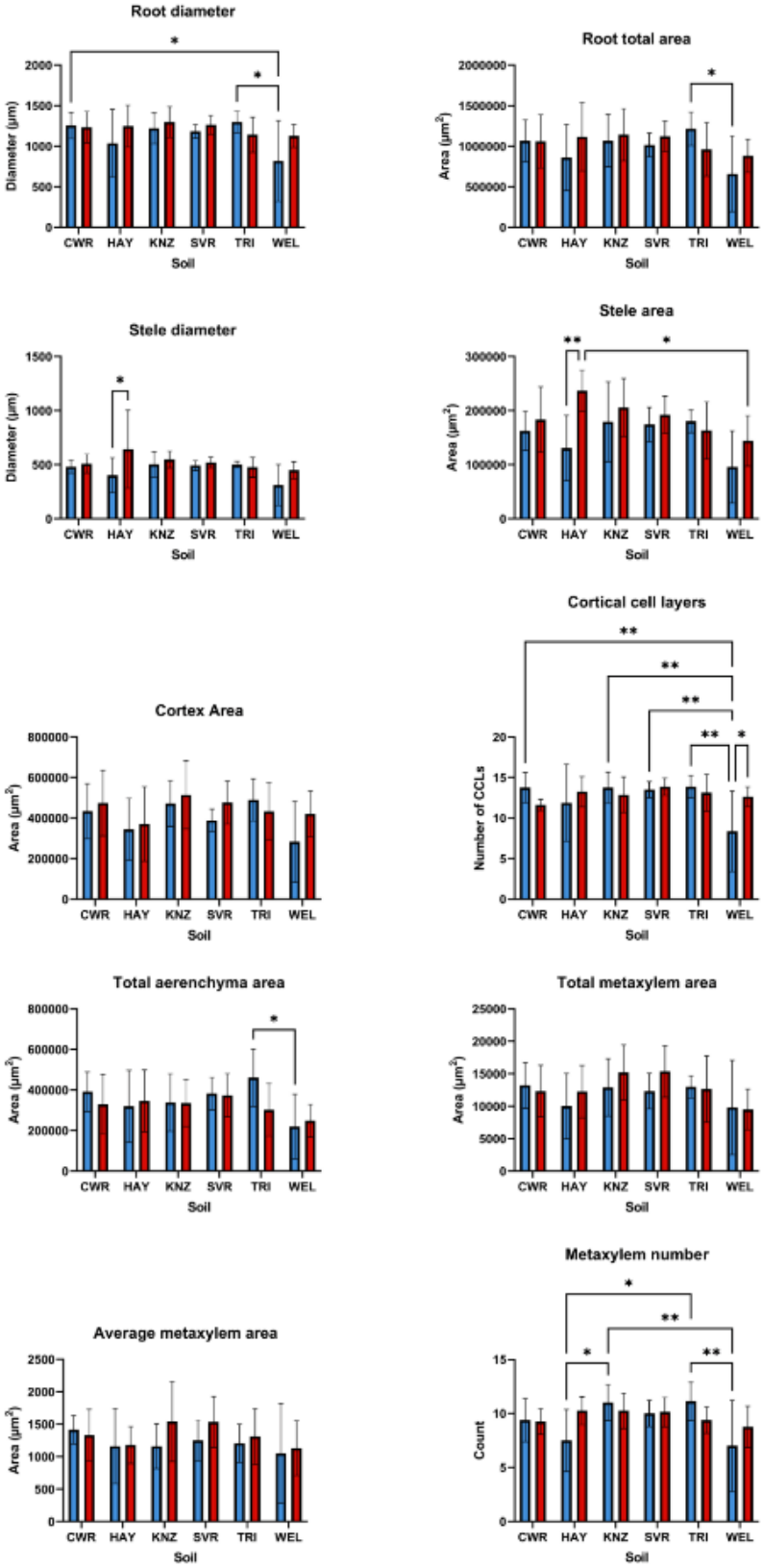

Root diameter
Diameter (µm)
Soil
CWR HAY KNZ SVR TRI WEL
Root total area
Area (µm²)
Stele diameter
Stele area
Cortex Area
Cortical cell layers
Number of CCLs
Total aerenchyma area
Total metaxylem area
Average metaxylem area
Metaxylem number
Count

Figure 3-17. Effects of water stress and mesocosm source on gamagrass crown root anatomical traits Gamagrass grown in 6 different mesocosms containing soil from sources contrasting in annual rainfall (TRI=18 in, SVR=19 in, HAY=24 in, KNX=33 in, CWR=37 in, WEL= 40 in), grown under well-watered and water stressed conditions, Blue bars = control well-watered conditions, Red bars = Water stress treatment, Mean values shown, *n*= 8, Error bars = Standard deviation, Comparisons given are 2-way ANOVA with Tukey's multiple comparison test correction, calculated in Prism 9 (GraphPad), reporting differences only either between different soils of the same water treatment or between water treatments in the same soil, Significant differences; *=P<0.05, **=P<0.01, ***=P<0.001

In the gamagrass objective three data (Figure 3-18), there is also a very low number of significant differences in anatomical traits when comparing between water treatments within the same microbiome treatment (14/240), though in four of ten of the trait comparisons there is a significant anatomical difference in plants grown with a WEL derived community.

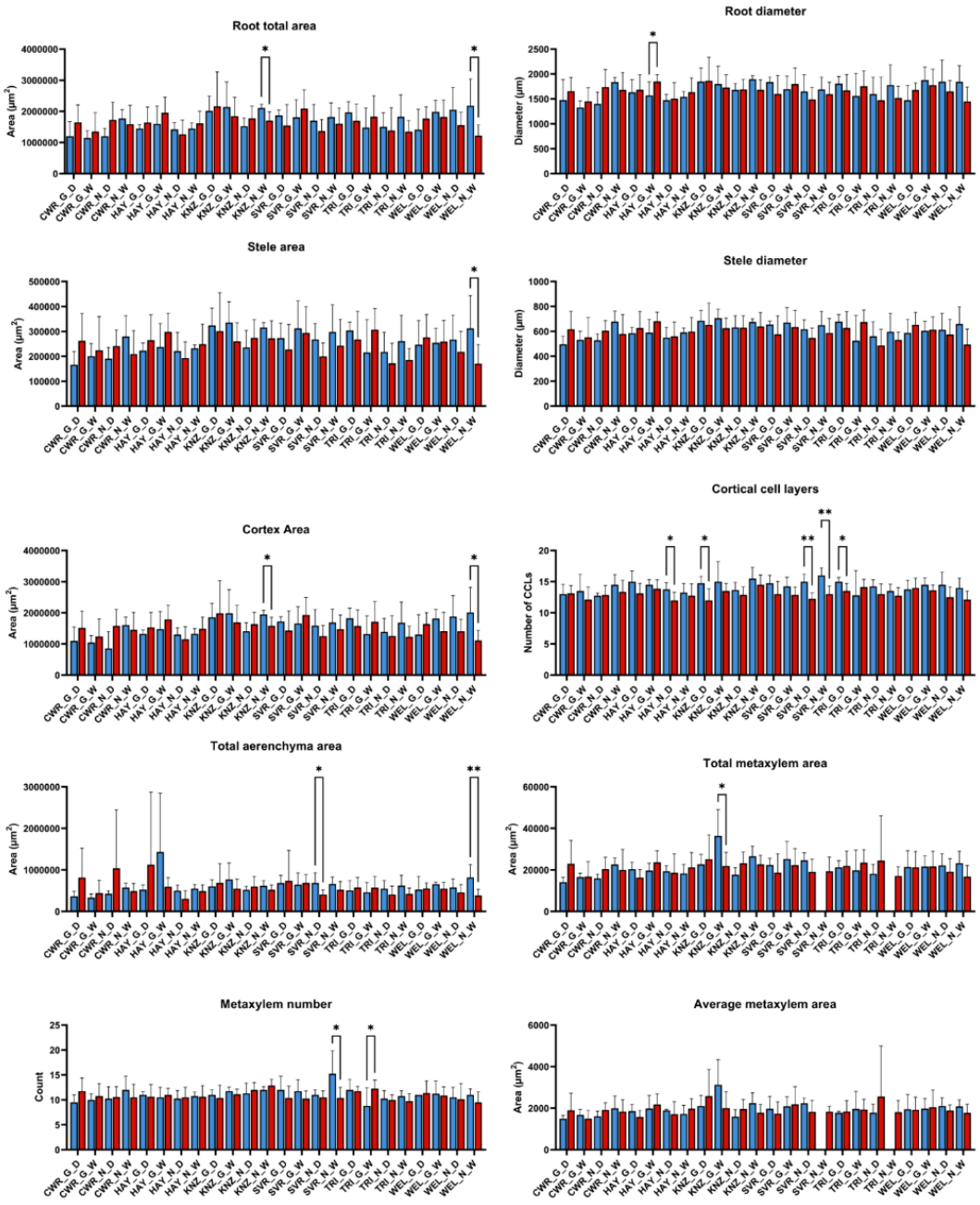


Figure 3-18 Effects of water stress and microbiome on gamagrass root anatomical traits, Gamagrass root anatomy of plants grown in sand inoculated with 24 different microbe communities (derived from soil collected from 6 different locations contrasting in rainfall (TRI=18 in, SVR=19 in, HAY=24 in, KNX=33 in, CWR=37 in, WEL= 40 in) following a period of gamagrass host (G) or free living adaptation (N) in combination with well-watered (W), or water stressed (D) adaptation), grown under well-watered and water stressed conditions, Blue bars = control well-watered conditions, Red bars = Water stress treatment, Mean values

shown, *n*= 8, Error bars = Standard deviation, Pairwise comparisons given are multiple T-tests comparing water treatments for the same microbiome inoculations, with multiple comparison corrections using the Holm-Šidák method (Šidák, 1967) calculated in Prism 9 (GraphPad), Significant differences; *=P<0.05, **=P<0.01, ***=P<0.001

Effect of microbiome adaptation on gamagrass root anatomy

When comparing within water treatment groups and looking at the effect of microbiome derived from contrasting previous water treatments there is little significant effect on anatomy. In two (out of 72) comparisons there are significant differences in number of cortical cell layers and in total metaxylem area (Figure 3-19), and no prevalent trends in difference between the two groups.

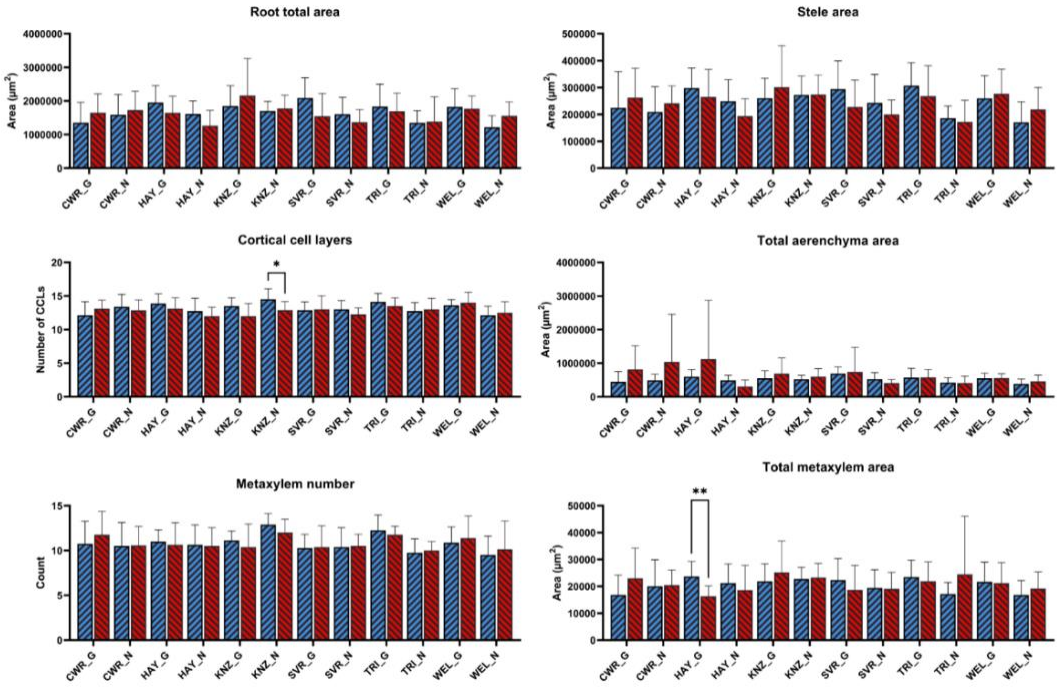


Figure 3-19. Subset of gamagrass root anatomy data presented in Figure 3-18 presenting only measurements of drought stressed plants. Blue ascending striped bars = microbiome history of well-watered conditions, Red descending striped bars = microbiome history of water stress treatment, Mean values shown, *n*= 8, Error bars = Standard deviation, Pairwise comparisons given are multiple T-tests

comparing difference between traits when grown with microbiome adapted to contrasting water levels, with multiple comparison corrections using the Holm-Šidák method (Šidák, 1967) calculated in Prism 9 (GraphPad), Significant differences; *=P<0.05, **=P<0.01, ***=P<0.001

Similarly, when comparing trait values between gamagrass grown under well-watered conditions but contrasting in microbiome water treatment history there are scant significant differences (4/72) (Figure 3-20). There is a slight visual trend of traits being larger in the plants grown with communities adapted to well-watered conditions (but no difference in watering), and all significant differences are in this direction, however as mentioned, the preponderance of these differences are not statistically significant.

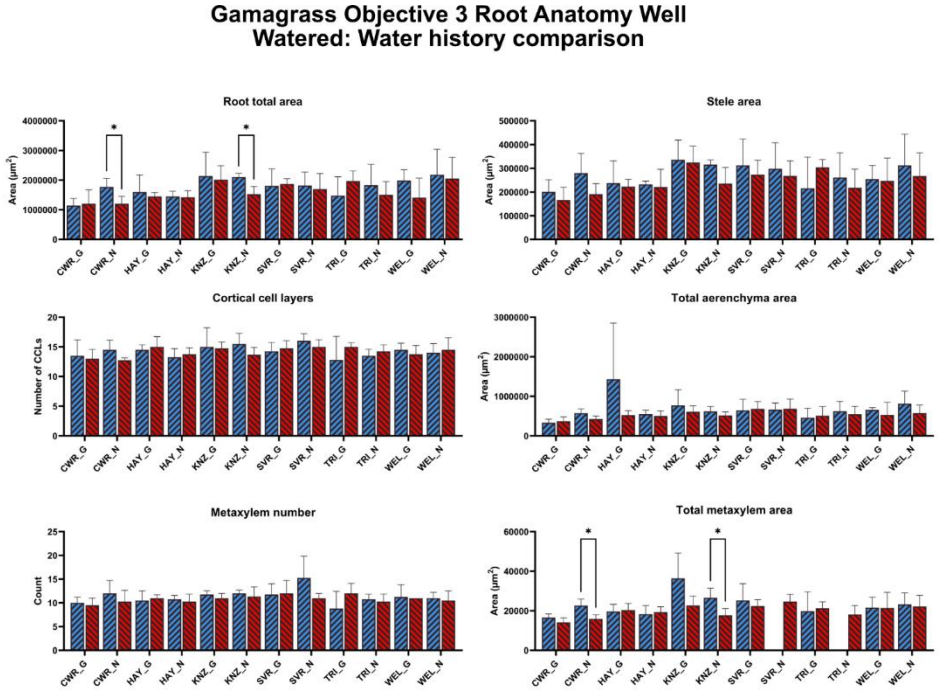


Figure 3-20. Subset of gamagrass root anatomy data presented in Figure 3-18 presenting only measurements of well-watered plants. Blue ascending striped bars = microbiome history of well-watered conditions, Red descending striped bars = microbiome history of water stress treatment, Mean values shown, *n*= 8, Error bars = Standard deviation, Pairwise comparisons given are multiple T-tests comparing difference between traits when grown with microbiome adapted to contrasting **Figure 3-19. Cont.** water levels, with multiple comparison corrections

using the Holm-Šidák method (Šidák, 1967) calculated in Prism 9 (GraphPad), Significant differences; *=P<0.05, **=P<0.01, ***=P<0.001

Effect of drought on maize root anatomy

In maize, between water treatment groups 30 out of 240 trait/microbiome combinations showed significant differences (Figure 3-21). In particular, mean aerenchyma total area showed a high level of plasticity, and its area was significantly decreased by drought stress in 10 out of 24 treatment groups. Plants grown with the KNZ_N_D microbiome community (Microbiome from soil from location KNZ with 33 inches of annual rainfall, adapted to a free-living water stressed environment) showed significant variability under drought for eight out of ten traits analysed. Beyond the significant effects, there was a general trend in reduction in size, number and area of most traits analysed.

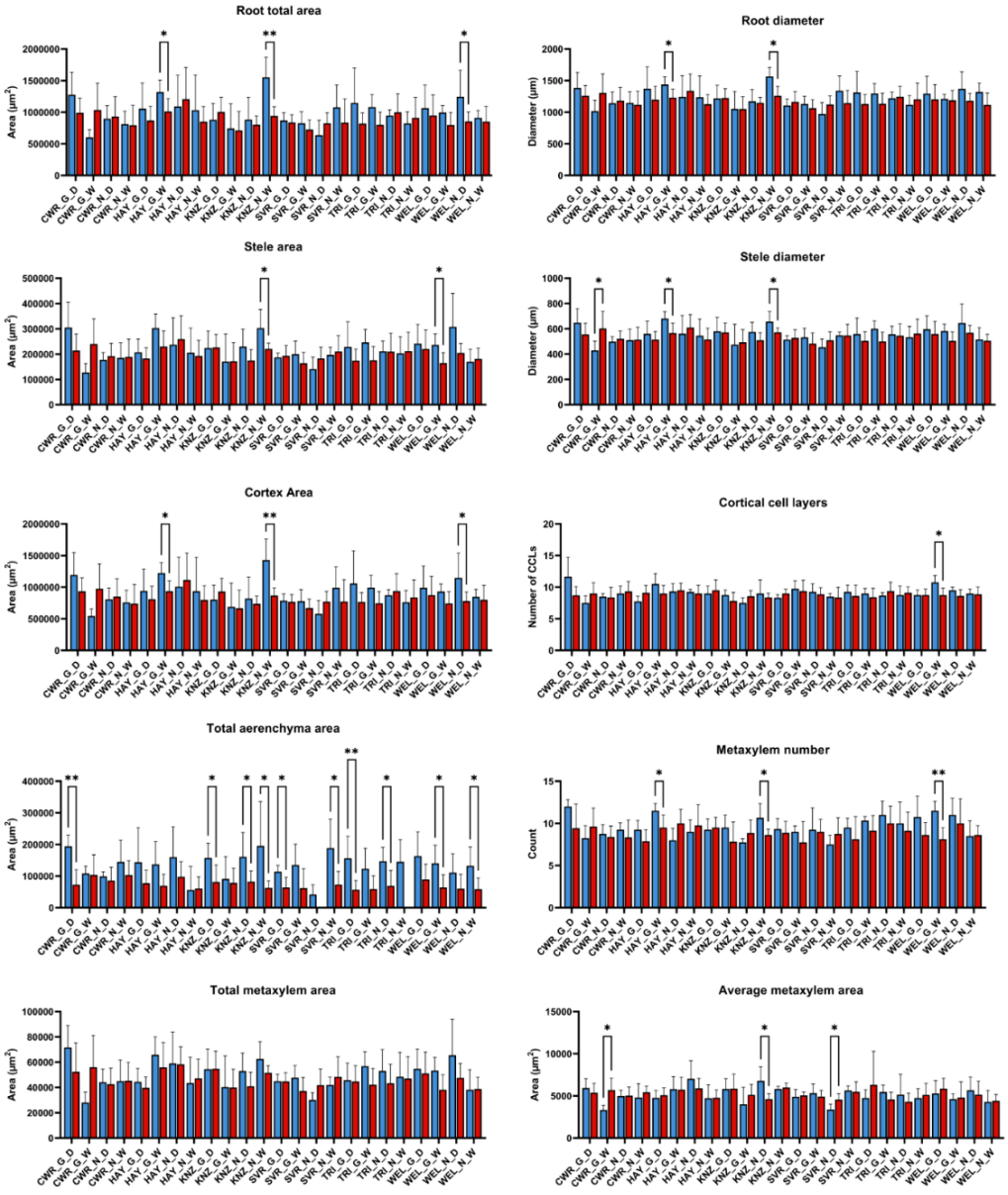


Figure 3-21. Effects of water stress and microbiome on maize root anatomical traits, Maize root anatomy of plants grown in sand inoculated with 24 different microbe communities (derived from soil collected from 6 different locations contrasting in rainfall (TRI=18 in, SVR=19 in, HAY=24 in, KNX=33 in, CWR=37 in, WEL= 40 in) following a period of gamagrass host (G) or free living adaptation (N) in combination with well-watered (W), or water stressed (D) adaptation), grown under well-watered and water stressed conditions, Blue bars = control well-watered conditions, Red bars = Water stress treatment, Mean values shown, *n*= 8, Error bars = Standard deviation, Pairwise comparisons given are multiple T-tests comparing water treatments for the same microbiome inoculations, with multiple

comparison corrections using the Holm-Šidák method (Šidák, 1967) calculated in Prism 9 (GraphPad), Significant differences; *=P<0.05, **=P<0.01, ***=P<0.001

Effect of soil history on maize root anatomy

Within water treatment groups there were significant differences in maize root anatomy between plants grown with different microbiome communities (Figure 3-22). Subsampling and analyzing for contrasting microbiome prior treatment of water stress, showed that within the water stressed plants, aerenchyma area was significantly larger in plants grown with a microbiome history of water stress than with well-watered conditions, for five of twelve pairs of treatment groups. The only other significantly affected traits were decreases in stele and metaxylem area for KNZ_N in plants grown with a microbiome history of water stress. This was representative of a general trend in these traits.

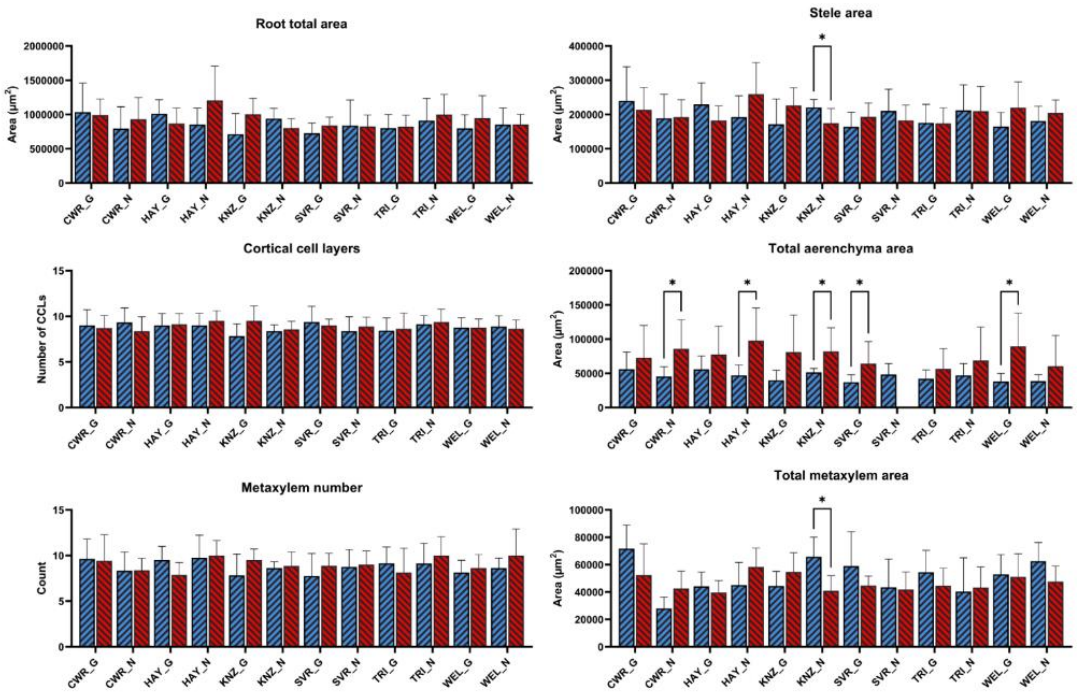


Figure 3-22. Subset of maize root anatomy data presented in Figure 3-21 presenting only measurements of water stressed plants. Blue ascending striped bars = microbiome history of well-watered conditions, Red descending striped bars = microbiome history of water stress treatment, Mean values shown, *n*= 8, Error bars = Standard deviation, Pairwise comparisons given are multiple T-tests comparing difference between traits when grown with microbiome adapted to contrasting water levels, with multiple comparison corrections using the Holm-Šidák method (Šidák, 1967) calculated in Prism 9 (GraphPad), Significant differences; *=P<0.05, **=P<0.01, ***=P<0.001

A less strong pattern of effect was seen when comparing the effect of microbiome history within maize grown under well-watered conditions. There were 13 significant differences out of 60 pairs of traits compared (Figure 3-23), however

there was no consistent direction to the difference between plants grown with a microbiome with a history of well-watered or drought stress.

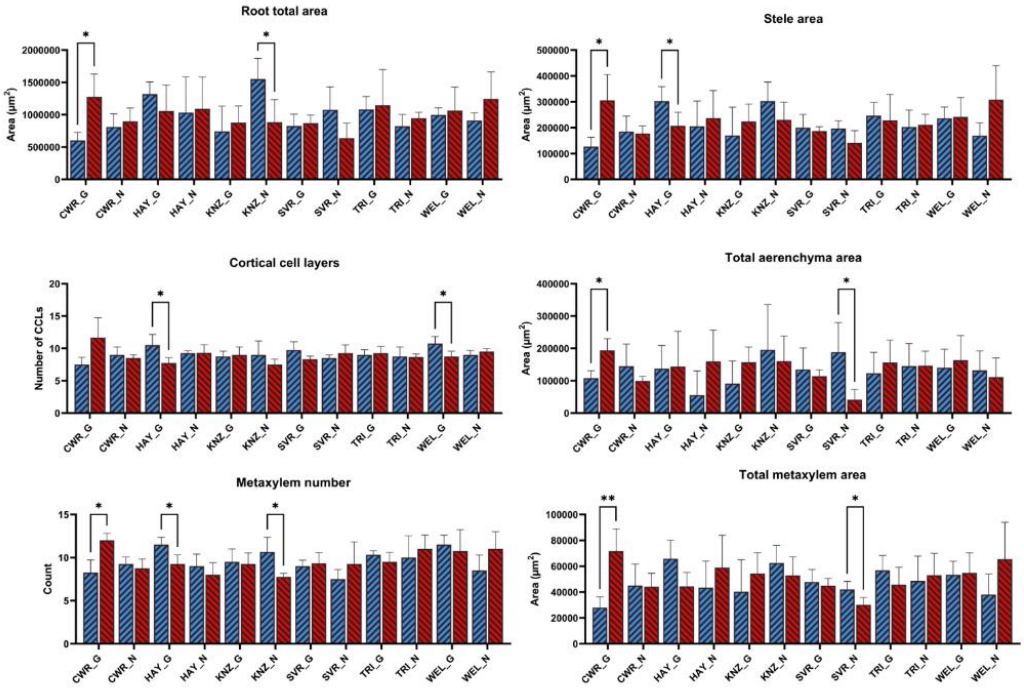


Figure 3-23. Subset of maize root anatomy data presented in Figure 3-21 presenting only measurements of well-watered plants. Blue ascending striped bars = microbiome history of well-watered conditions, Red descending striped bars = microbiome history of water stress treatment, Mean values shown, *n*= 8, Error bars = Standard deviation, Pairwise comparisons given are multiple T-tests comparing difference between traits when grown with microbiome adapted to contrasting water levels, with multiple comparison corrections using the Holm-Šidák method (Šidák, 1967) calculated in Prism 9 (GraphPad), Significant differences; *=P<0.05, **=P<0.01, ***=P<0.001

3.8.3 Brachypodium

Brachypodium root anatomy varied between the wild type and PIN1a lines (Figure 3-24) and was also significantly affected by water stress in the PIN1a mutants.

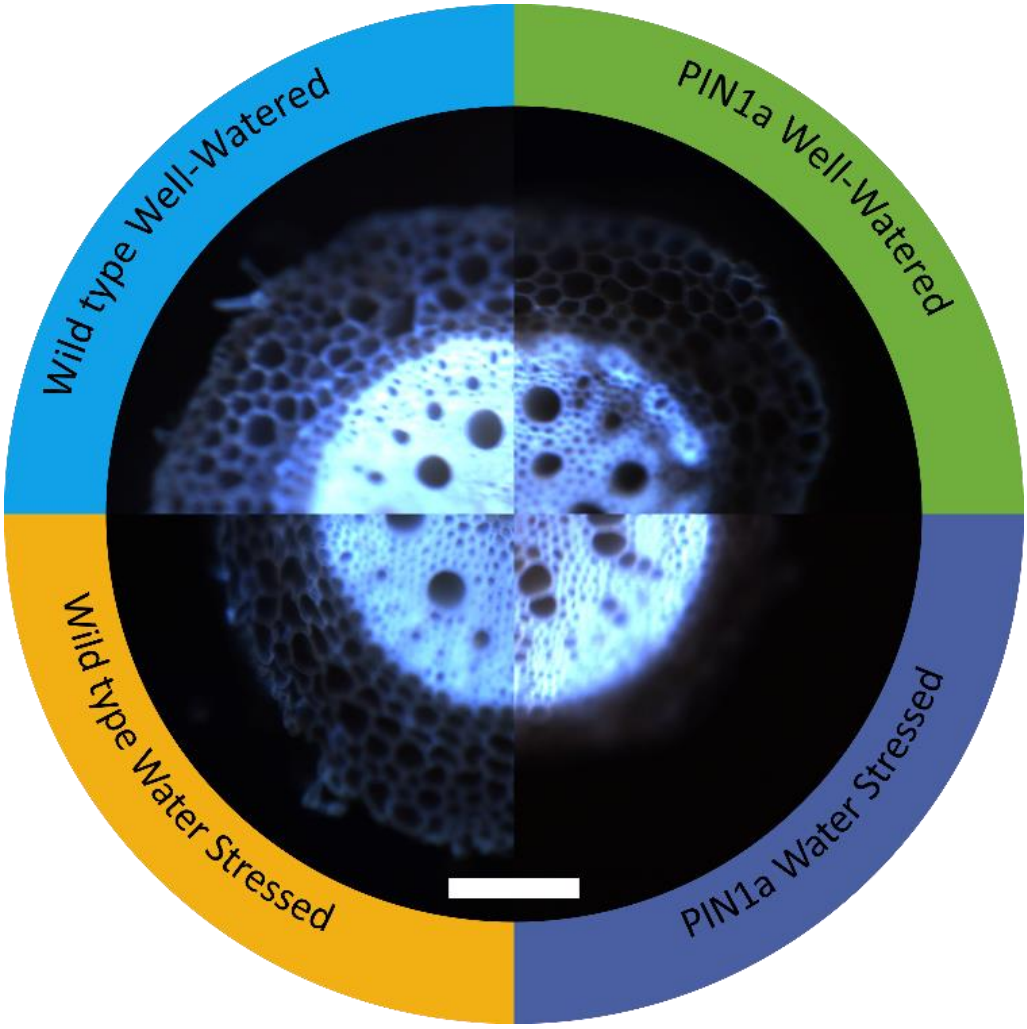


Figure 3-24. Composite root image comprised of quadrants from images of well-watered and water stressed, wild type and PIN1a mutant *Brachypodium distachyon*. Scale bar= 100 µm

There were no significant differences in the measured anatomical traits between the well-watered (WW) and water stressed wild type (WT) *Brachypodium* root samples (Figure 3-25). The only significant trait differences between well-watered wild type and PIN1a knock out mutants were in metaxylem distribution, though there were no significant differences in total metaxylem area for any of the line and treatment combinations. Root diameter, root area, and metaxylem number, were significantly decreased in water stressed PIN1a mutants compared to WT, and in water stressed PIN1a mutants compared to well-watered. Water stressed PIN1a mutants mean metaxylem area was significantly higher than in well-watered WT and PIN1a plants.

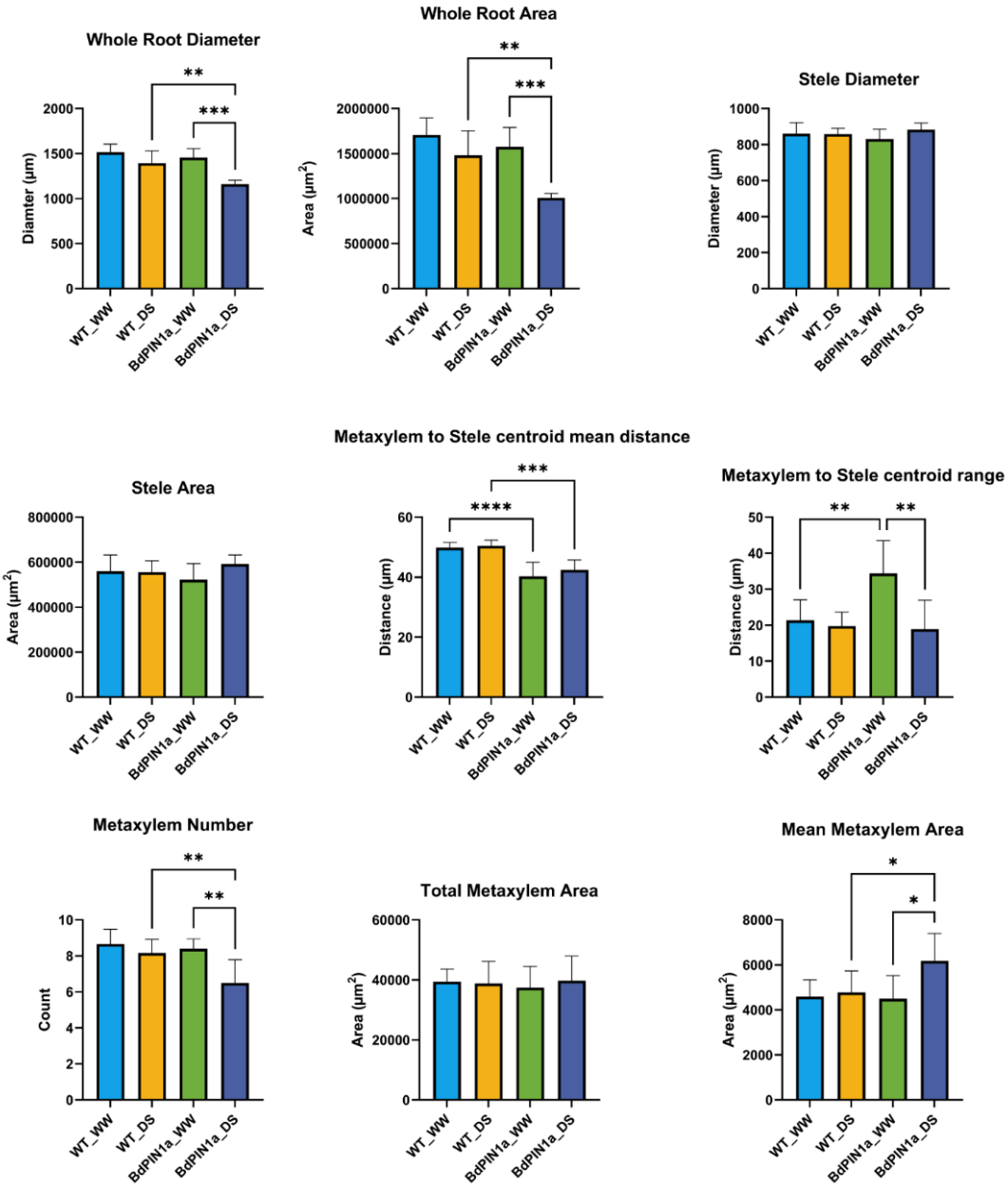


Figure 3-25. Root anatomical traits of wild type and *PIN1a Brachypodium distachyon* under well- watered and water stressed conditions. WW= Well watered plants, DS= Water stressed plants, Mean values shown, WT_WW&DS *n*= 6, PIN1a_WW *n*= 5, PIN1a_DS *n*= 4 Error bars = Standard deviation, Comparisons given are one-way ANOVA with Tukey's multiple comparison test correction, calculated in Prism 9 (GraphPad), reporting differences only either between the

same ecotype or water treatment, Significant differences; *=P<0.05, **=P<0.01, ***=P<0.001, ****=P<0.0001

3.9 Discussion

3.9.1 Evaluation of developed methods

Evaluation of developed methods of sample preparation for LAT scanning

Critical point drying was found to be an essential preparatory process for the majority of sample types scanned as part of this study. With careful handling, fast ablation and imaging, and a rapid sample progression rate, it was possible to stay ahead of sample desiccation and collapse when scanning without excess ethanol obscuring the image. This was extremely inconsistent however, as well as overly time consuming, and requiring high number of images to be taken (~200) to be later sorted through, and often resulted with no suitable images. However, this was not the case with large maize root samples, gamagrass roots, or with samples of arial plant tissue with a naturally low water content (wheat stem, seed heads, woody stems) (J Atkinson, Pers. Comm., 2021), as these could be readily scanned either freshly harvested or following storage in 30-70% ethanol solution with no need for CPD.

With the appropriate, sized holder and correct CPD settings, most samples tested could be dried using the described method without causing damage, regardless of length, provided they were <~8mm in diameter at their thickest point. Larger than this and issues started to arise with the process as samples often collapsed in the CPD or sustained damage to cell regions. This could be overcome by slicing samples into shorter lengths and mounting them differently, but this reduces throughput and makes it more likely to damage samples in handling.

Viewing the time taken for dehydration and solution exchange steps as a sunk time cost (as these could be done in batch and required minimal manual intervention), this additional sampling step only added 30-60 seconds to the workflow per sample and significantly increased the output quality.

Overall, these methods were highly suitable and advantageous to the quality of images. Using the custom designed sample holders maximized throughput of this step, minimizing the overall detriment of CPD to the throughput of the pipeline.

Suitability of LAT for different sample types

As LAT relies mostly on inducing fluorescence in the sample for imaging, the composition of the sample is a significant determining factor in suitability for LAT imaging. With the current set up, and not using staining as part of the workflow, secondary thickened tissues are largely required in a sample for good imaging due to their increased autofluorescence compared to primary cell walls. Testing of a range of additional samples showed that LAT was poorly suited to root tips, *Arabidopsis*, cereal coleoptiles, duckweed (roots and fronds of all species surveyed in 2.3.1), and that the cortex of plants grown hydroponically or on plates had poor visibility compared to the stele or to soil grown plants. The sample types scanned as part of the case studies all performed well, some issues arose with the larger tiller millet roots, and the smaller *Brachypodium* roots were harder to image due to their small size and system vibration, but measurable images were consistently achievable with all samples scanned.

Although theoretically the power and speed of the LAT laser is sufficient to cause athermal ablation, certain samples still appeared to burn or char when being LAT scanned. This was first noted with leaf samples and duckweed; it appeared that the waxy cuticle was more flammable or caused greater heat transfer to surrounding sample than other sample types, though this was also seen with the upper surface of some root samples too. Where possible, forming the laser sheet with a wider beam tended to reduce these issues, but did not remove them entirely. Alternatively, it was seen that positioning a sacrificial material aloft of the target sample, and ablating both simultaneously, this could reduce the effects of

the burning seen. A similar issue was seen where there was any adhesion of sand or soil to the samples, these particles absorbed a large amount of heat from the laser and burnt any surrounding sample in contact with it, as well as creating bright image artifacts. This showed the importance of very thorough sample cleaning when sampling or preparing samples. Extremely thick samples, such as the base of maize or millet stems also proved difficult to cut.

With the built in oversampling rate for security in the imaging recipes, these programs still only took 30-180 seconds to run, and approximately 30 seconds per image folder to curate if done manually.

Assessment of image analysis pipelines

The developed automatic image analysis software, *ROOTSCAN*, was shown to be suitable for its intended purpose of segmenting, annotating, and measuring LAT images of whorl four pearl millet crown roots. The running time of this depended on the hardware used, though is recommended to be run on a computer using an NVIDIA graphics card. On a GeForce RTX3070 Laptop, ROOTSCAN could fully process an image in approximately 100 seconds, and on a computer using an RTX4090, in approximately 30 seconds. Crucially, this process is automatic and could be run fully unsupervised, so even on slower performing machines taking 5-10 minutes an image, images could be processed without taking user time. However, quality could be varied, and problematic images for the network could only be identified post processing, which would then need manual exclusion or correction in the dataset.

The fully manual methods used to measure gamagrass, maize, and *Brachypodium* roots (Section 3.6.3, 3.6.4), and the pearl millet leaf images took large amounts of user time (5-10 minutes per root image, 10-20 per leaf sample image set). While more time consuming than an automated process, apart from in instances of user error it is much less likely to have an inaccurate measurement. If only a specific

trait is required, or a set of traits that can be easily measured in tandem (area, diameter, and other shape descriptors, or number and size of metaxylem), this can be done very quickly (~30 seconds an image) in FIJI when making use of macros and or keyboard shortcuts.

All methods developed and described worked well in their use cases. Whether it is worth developing or retraining ROOTSCAN for different LAT datasets, or using manual methods would be dependent on sample number and the desired image output measurements.

3.9.2 Pearl millet whorl selection

When comparing sample quality in LAT images, from the range of whorls provided from the Senegal field trial and the Nottingham trial, it became apparent that whorl four was the most suitable root class to use going forward. To compare the effect of water stress on anatomy, samples from both treatments needed to be of sufficient quality to accurately measure traits of interest. Whorl four was the only class where over half of samples from both treatments were either perfect or near perfect in condition (score of 4 or above) (Figure 3-16). This was confirmed with the Nottingham grown samples, where again, whorl 4 roots were the only class to meet this target. Whorl three was close, having 6/12 and 9/12 roots meeting this target in this experiment.

There are some explanations for this variation, firstly, the samples obtained for Senegal faced much harsher conditions than the samples grown in Nottingham and due to large sample numbers were likely harvested in a more hasty manner. The W2 roots were likely grown prior to the imposition of water stress, W3 during the early stages of imposition, and W4 while experiencing water stress (Maiti and Bidinger, 1981; Passot et al., 2016). As W4 likely developed during water stress there may have been a developmental response in the root rather than a shock cell

death response as seen in the cortex of the older whorls. Tiller roots were large and in some cases their size meant they did not dry well with the CPD and scanning pipeline and suffered damage in those steps. There were also a number that did not suffer any cell collapse issues, but did seem to crack or fracture, unlike any other class of root. This may be as a result of the high lignin deposition in these samples and a high level of secondary thickening, which can enhance the toughness of plant cells but increase the chance of non-plastic deformation or fracture (Lucas et al., 1995).

3.9.3 Effect of combination of microbiome and water stress treatments on maize and gamagrass root anatomy

Effect of water stress on gamagrass root anatomy

Gamagrass roots were largely anatomically insensitive to the effects of the water stress impositions in this experiment and showed very little plasticity in any trait. Gamagrass is known for its water stress tolerance, as well as its resistance to a suite of other abiotic stresses (Clark et al., 1998; Gilker et al., 2002; USDA ARS, 2023), so it is perhaps unsurprising that its anatomy was not significantly affected by the treatments imposed in many cases.

Effect of microbiome on gamagrass root anatomy

The gamagrass grown with the WEL_N_W community (Derived from a high-water environment, well-watered and not cultivated with gamagrass in Obj. 2), did seem anatomically plastic as it showed significant decreases in several size related traits under water stress. In this more stratified phase of the experiment, there was a trend toward a reduction in cortical cell layers under water stress, validated by several of the treatment pairs having significant differences in this direction. When looking purely at the differences in microbiome treatment within the same watering regime there are very few points of distinction between whether plants were grown with a water stress or well-watered adapted microbiome community.

Across the whole panel of treatments and traits there are very few significant differences in the comparison between treatment groups. However within the well-watered plants there appears a slight perceptible trend in a reduction of trait values in plants grown with a microbiome that has a history of water stress exposure. These reductions are significant in total root area and metaxylem total area in plants grown with CRN and KWZ free living derived communities. The microbiome can have a significant impact on plant water stress tolerance (Naylor and Coleman-Derr, 2018), and it is possible that from these backgrounds there is a feature in the composition of the microbiome that is beneficial to plants that is lost when the community is adapted to not having a plant host. Even though the plant is not experiencing a water stress, the water stress adapted microbes may still be inducing a water stress response in the plant through the production of volatile organic compounds (Poudel et al., 2021).

Effect of water stress on maize root anatomy

Maize root anatomy appeared far more susceptible to the effects of water stress than gamagrass. In particular, aerenchyma area was significantly decreased under water stress in many of the treatment groups, with only a small number of treatment groups experiencing a decrease in root area. This is somewhat surprising given previous studies noting an increase in aerenchyma area under drought in several species and benefit thereof (Evans, 2004; Zhu et al., 2010; Basu et al., 2021). This may be explained by a difference in sampling, or it may be a magnified impact of the general size reduction seen in most other traits under water stress.

Effect of microbiome on maize root anatomy

Comparing root anatomy between microbiome treatments and within water treatment groups showed more significant effects for maize than in gamagrass. In the well-watered plants, there was not a clear pattern of the effect of prior

microbiome water stress exposure, with some traits increasing and some decreasing significantly. There was however a significant increase in size or number of almost all traits in the plants grown with the CWR_G (High-precipitation, host adapted) (Figure 3-22) water stressed community as opposed to the well-watered, why this may be is unclear. Within the water-stress treatment there was a clear pattern of enlarged aerenchyma when plants were grown with a water-stress adapted community compared with a well-watered adapted community (Figure 3-23). This is interesting given that the direct impact of water stress was a reduction in aerenchyma (Figure 3-21), and this data seems to show that a prior microbiome exposure to water stress buffers against the direct effect of water stress on aerenchyma area.

Variation in root anatomy in Brachypodium distachyon auxin transporter mutant and under water stress

The anatomy of the wildtype *Brachypodium distachyon* roots was not significantly affected by water stress in any of the traits measured, however anatomy was affected by water stress in the PIN1a mutants, and there were anatomical differences between the lines for both treatments.

Water stress significantly reduced root area in the PIN1a mutants relative to both the water stressed wild type and the well-watered PIN1a mutants. Given that this effect was not present in the wilt type, it is clear that the PIN1a mutants are either more sensitive, or more plastically responsive to water stress than the wild type. This is affirmed by similar findings of altered water stress response of PIN1 mutants in *Arabidopsis* (Bawa et al., 2022), and in improved water stress tolerance in over-expressors of other PIN family members in rice (Zhang et al., 2012), potentially due to altered xylem physiology reducing cavitation risk, though PIN1 also affects many other developmental factors that affect water stress response, such as epidermal and guard cell patterning (Bawa et al., 2022).

There were no significant differences in stele diameter, stele area, or total metaxylem area across any of the lines or treatments, which made the differences in metaxylem arrangement, number and mean area especially interesting. There were clear differences in vascular arrangement between the PIN1a mutants and the wild type on visual comparison. In order to assess this, in addition to count, total area and mean area of metaxylem, the distance of individual metaxylem centroids from the stele centroid was calculated, both as an absolute micron distance and as a percentage of stele radius, along with the mean range in these values (Figure 3-25). This gave a thorough quantitative overview of the metaxylem arrangement and revealed statistically significant variation between the lines and treatments. The mean position of metaxylem in PIN1a mutants was closer to the stele centroid for both water treatment levels, though had a significantly higher range in distances from the stele centroid under well-watered conditions. The water stressed PIN1a mutants also had a significantly smaller number, of significantly larger metaxylem than the well-watered PIN1a plants or the water stressed wild type plants. With the same total metaxylem area as the other plants, this would give the water stressed PIN1a plants the highest theoretical hydraulic conductance (Heymans et al., 2021). It could potentially be beneficial to have the metaxylem positioned “deeper” within the stele (as seen in the PIN1a mutants), this would create additional barriers of stele cells around the metaxylem, potentially limiting water loss from these vessels.

3.9.4 Conclusions

This Chapter described the development of improved methods for sample preparation, LAT imaging, and image analysis, and validate them with a range of case studies investigating the impacts of water stress on monocot anatomy.

These aims were all met by the work presented in this Chapter, and the range of tissue and sample types that can be used with LAT scanning has been significantly increased.

For LAT images of pearl millet, a novel, fully automated, image analysis platform has been developed, which has shown to be applicable to sample types beyond those used in the training set. This is a good indicator that this software and the developed neural network may be applied successfully to other species and sample types, and even possibly to other imaging methods with the right training set.

Pearl millet sampling, preparation, imaging, and analysis methods were optimized, which will facilitate future work. Anatomical differences were found between the microbiome and water treatment groups tested in maize and gamagrass, and *Brachypodium* root anatomy was found to be different in auxin transporter mutants to the wild type, and that these mutant lines were affected differently by water stress treatment.

Chapter Four:

The Anatomical Basis of Drought Tolerance in Pearl Millet

4.1 Introduction

Pearl millet

Pearl millet is a cereal crop native to west Africa, where it is grown extensively, in part due to its high drought tolerance. It has received relatively little research or development interest in the past and has great potential for improvement, which will be necessary due to climate change (See Section 1.4).

Senegal

The center of domestication of pearl millet is in or around modern-day Senegal, likely around the Senegal river. Bordering the Sahara, the north of the country has a desert climate, and crop production in the region is threatened by desertification, especially in the inland regions. A largely agricultural economy, combined with rising temperatures and sea levels, reduced rainfall, and an increasing population all contribute to food insecurity and the country's high vulnerability to the effects of climate change.

Project

To attempt to address this, a large-scale research project has been conducted, investigating water stress tolerance in pearl millet. This Royal Society International Collaboration Award project links the University of Nottingham (UK), IRD Montpellier (France), and ISRA (Senegal), to carry this out.

The project uses 160 genotypes from the Pearl Millet inbred Germplasm Association Panel (PMiGAP) (Sehgal et al., 2015) in a multi-year study investigating the effect of water stress treatment on a range of physiological and agro-morphological traits measured in field and at harvest, including root architecture, leaf and soil ionomic profiling, seed proteomics, ionomics, and hyperspectral imaging, and anatomical analysis.

4.2 Aims

There are several far reaching aims to this project, the end goal benefits being able to promote economic growth and development in Senegal and the wider Sahel region through improving yield stability and food security of a major dietary staple. It will be possible to use the data produced by this study to look at genetic control and correlation between every trait measured and how they are affected by water stress, however in this Chapter the focus will be on anatomical traits, their relationships, and their genetic control.

Characterization of pearl millet root anatomy and development of anatomical analysis methods

The first project target was to develop an understanding of pearl millet root anatomy across the whorls and to understand the variation within the root system. Necessitating development of a series of high throughput root phenotyping and analysis methods as described in Chapter 3.

These approaches would then be used in screening a large population of pearl millet lines, grown under well-watered and water stressed conditions.

Identification of beneficial traits for water stress tolerance

The root anatomy of the selected panel of pearl millet lines will be phenotyped, as well as a suite of other morphological, ionomic, agronomic, and physiological traits. This will be done in both the well-watered and water stressed grown plants, and the plasticity of these traits will be calculated. The correlations between these traits will be investigated for both treatments, as well as the benefit of plasticity in maintenance of yield under water stress.

Identification of genetic control of anatomical traits

Following the quantification of these traits under the two conditions and their plasticity, genomic association studied will be carried out for the two main field trial years in order to attempt to identify genetic regulators of these features.

4.3 Materials and Methods

4.3.1 Germplasm

The 160 pearl millet lines used during the experiments are from the PMiGAP population, representing the diversity of lines found across the world. This panel is made up of 250 lines, and is a representative spread of the germplasm cultivated in Africa and Asia, including elite cultivars, hybrid parental inbreds, and inbred mapping populations (Sehgal et al., 2015). Within this panel there are 6 subpopulations which are all well represented by the 160 lines selected (Appendix 5). In Senegal there are two main pearl millet morphotypes, early flowering Souna varieties, and late flowering Sario (Diack et al., 2020), these are also represented in the panel.

These fully sequenced lines allow for the identification of 29,542,173 Single-Nucleotide Polymorphisms (SNPs), which can then be used in genomic association studies (Varshney et al., 2017).

4.3.2 Plant Growth

These lines were grown under well-watered, and water stressed conditions over two full years of field trials and a pilot study (as referenced in Chapter 3). This was carried out at the Centre National de la Recherche Agronomique (CNRA) of Institut Sénégalais des Recherches Agricoles (ISRA) in Bambey, Senegal (14.42°N, 16.28°W).

Plants were grown in the dry season (March-June), under well-watered or water stressed conditions. The soil was prepared with light plowing and harrowing before sowing with a fertilization of 150 kg ha $^{-1}$ of 15N-10P-10K, then 5-6 seeds, treated with "GRANOX®NM" fungicide seed treatment, were sown per hill. 15 Days after sowing, plants were thinned to one plant per hill, and an additional 50 kg ha $^{-1}$ of the same fertilizer was applied. Under watered conditions, plants received 30 mm of water twice a week continuously, and under water-stress, watering was paused between 21 and 41 days after sowing.

The lines in the field were arranged in a randomized alpha-lattice (CITATION NEEDED), and the field was arranged in experimental units of plots of 3 m by 2.4m, with 10 rows of plants (spaced at 30 cm), arranged in 3 columns (spaced at 80cm). Each plot contained a single genotype and was replicated four times per treatment in different experimental blocks. One meter spacing was left between blocks, and 10 m was left between the water stress stressed and well-watered blocks.

Experimental design and all work carried out in field was managed by Alexandre Grodin (IRD) and Awa Faye (ISRA) and performed by ISRA staff. In year three after the relaxation of travel restrictions imposed due to the Covid-19 pandemic, I was able to travel to Senegal to assist with sampling and work as part of the field trial team.

Year 0

The pilot year experiment was conducted in 2019 using a subset of 20 lines (Appendix 5). These were sown on the 15th of May, water stress was imposed on the 5th of June, roots were harvested on the 26th and 27th of June, then watering was resumed, and the remainder of the plants were harvested at maturity.

Year 1

In 2020, the full panel of 160 lines were sown on March 3rd and 4th, and water stress was imposed on March 31st (one week later than planned due to slow growth). Harvest for root anatomy was planned for the 21st of April, however; due to a state of emergency being imposed in Senegal in response to the novel coronavirus pandemic, total curfew was imposed, and it was impossible to proceed with the experiment as planned, and the experiment was abandoned with regard to anatomical sampling.

Year 2

Year 2 of the project was run in 2021, using 160 pearl millet lines, planted as described on the 1st and 2nd of March in a randomized alpha-lattice design. Water stress was imposed on the 22nd and 23rd (21 DAS), and due to colder weather than expected and in the pilot year, water stress was imposed for an additional week, until April 23rd (49 DAS) when plants were sampled, and the remainder of plants were harvested at maturity.

It was observed during this growing period that there were large empty patches within the water stress treatment plots, and that many of the plants were too stressed to be able to measure.

Year 3

The final field trial year was run in 2022. 160 lines were sown in the same randomized configuration as the previous year on the 28th of March. Water stress was imposed on the 18th of April (21 DAS) and roots were harvested from the 9th to 12th of May (42-44 DAS), and the remainder of plants were harvested at maturity. There were some empty patches in the water stressed (STR) plots where plants did not grow well, as seen in Figure 4-1, but less so than in the previous year.



Figure 4-1. Images of field trial site. Images of the Year 3 (2022) field sites at the ISRA Bambey field station, showing the water stressed (STR) field on the left, and the well-watered field (ETM) on the right

4.3.3 Plant Anatomy Sampling

From each plot, three plants were sampled at the end of the water stress treatment period in order to see the effect of maximal water stress. Representative plants were taken from the center of each plot to avoid edge effects. Once collected according to the protocols below, plant samples were stored in individually labeled 2ml Eppendorf tubes, in 2ml of 50% ethanol v/v, and stored out of direct sunlight in the coolest available area. Prior to shipping to the UK, the ethanol was poured off, leaving the sample wet, but with minimal residual ethanol, and the tubes were quickly resealed. Upon delivery, the tubes were immediately refilled with 2ml of 50% ethanol v/v and stored at 4 °C.

Year 0

In the pilot year roots were sampled from each whorl present on the main stem (Whorls 2-4), as well as tiller roots. Root sampling was done on the 26th and 27th of June (42 DAS) in the field, 21 days after stress imposition. Root architecture was phenotyped in field using established “Shovelomics” approaches; root crowns were carefully excavated, cleaned, then bisected along the sagittal plane (The midpoint of the stem at its widest plane when considering tillers). Half of the crown

was used for architectural imaging, and half was sampled for anatomy. Root samples were taken from the second, third, and fourth root whorl, as well as a tiller adventitious root. Samples were an approximately 2 cm length of root, 2 cm away from the stem (where present), and if possible, a second root from the same whorl was also collected. With three plant replicates in four plot replicates of twenty lines, under two treatments, and harvesting four root types, this provided a projected 1920 samples.

Year 1

In Year 1, due to COVID19 related local restrictions in place at the time, no samples could be collected.

Year 2

In Year 2, samples were collected on April 18-23rd (48-49 DAS), 28 days after stress imposition. Root sampling was done in the same way as the pilot year but using 160 lines and only sampling from the fourth whorl. This gave a projected total of 3840 samples.

From a subset of 20 lines selected for diversity based on a prior screen of water use efficiency by J. Burridge, leaf samples were also collected at the same time as root harvesting (48 DAS). These were taken from one plant per plot by selecting the median sized plant on visual appraisal. The youngest fully ligulated leaf was removed and a 2cm portion from the widest point of the leaf was subsampled. This provided 160 leaf samples.

Year 3

In Year 3 root samples were collected, processed and partially phenotyped in field (Figure 4-2) on the 9th-12th of May (42-44 DAS). This was done using the same methodology as the previous year, though with some improvements to the methodology. watering was resumed the day before each plot was harvested in

order to loosen the soil and facilitate excavation. Roots were also sampled immediately next to the stem, not leaving a 2cm gap. This increased the consistency of the root region sampled and made handling easier. Leaf samples were collected in the same manner as the previous year on the 8th of May (41 DAS).



Figure 4-2 Sample harvesting, subsampling, and root architecture phenotyping stations for the Year 3 (2022) field trials in Bambey, Senegal

4.3.4 Anatomy Sample Preparation, Imaging, and Measurement

Full details of how samples were prepared, scanned, and images analysed, and how these methods were developed, are given in Chapter 3 Section 3.5.

Sample Preparation

After samples were transported to the UK and the ethanol solution in the tubes was replaced, samples were stored at 4 °C until sample preparation. Samples were loaded into custom designed holders and dehydrated, first with 100% methanol, then 100% ethanol. They were then critically point dried.

Imaging

Samples were imaged using LAT scanning, using a picosecond pulsed UV laser to ablate and then illuminate samples. They were imaged in sync with the laser illumination, utilizing the plants autofluorescence resulting of UV exposure in combination with brightfield illumination. This was done using a machine vision camera connected to a turret of infinity corrected microscope objective lenses.

Measurement

Root images were analysed using bespoke image analysis software, ROOTSCAN. This has been developed to automatically segment, annotate, and measure eight cell and tissue types, quantifying their size, number, and arrangement. Leaf images were measured manually using FIJI. Post ROOTSCAN, the image outputs were checked for quality, and on visual appraisal, any that had a low agreement with the input image were discarded.

4.3.5 Root Architecture

Imaging

In the field, half of the root system removed and not sampled for anatomical analysis was used for root systems architectural analysis.

Root crowns were imaged using a specially constructed imaging booth, where each half root system was positioned on a mounting nail protruding from a painted black board (in Year 3 this was changed to a blue felt mat), with the cut face towards the camera. The sample label was placed next to the sample, and a target 10 cm white circle was included for scale and white balance, these were then imaged using a DSLR camera.



Figure 4-3. Root Architecture Phenotyping Setup. (Left) Image of setup of root architecture phenotyping station used in Year 3 of field trials, DSLR camera mounted in wooden frame facing a blue felt board with a mounting nail, scale reference, and sample labels attached, (Right), image of bisected root crown used for architecture imaging and representative of anatomy sampling material

Analysis

Images were measured using a combination of DIRT (reference), an automatic root crown image analysis system, and manually using FIJI plugin ObjectJ. In the pilot year, DIRT was found to be only partially capable of measuring these pictures due to a reflection from the paint streaks presenting similarly to roots and confusing the system, so FIJI was used for all years. In FIJI, total root angle width was measured using the angle tool, selecting the leftmost point of the top root whorl, the stem midpoint at the top whorl, and the rightmost point of the same whorl. In ObjectJ, Stem diameter and root crown diameter was measured, along with root crown diameter.

4.3.6 Leaf Ionome

Ionome was measured as part of the year 2 and 3 field experiments.

Sampling for ionomic profiling

The flag leaf of each plant harvested during root architecture imaging and anatomy sampling was removed and collected in a paper bag and set aside for drying. When dry, 1cm leaf disks were punched from the leaf, around the widest point of the leaf, but avoiding the midrib or the edge where possible.

Ionomic analysis

After harvesting, leaves are placed in an oven at 60°C for 3 days. The three sachets containing leaves from the same plot are grouped together. A disc of leaf 5mm in diameter is taken 5cm from the base of the stem, avoiding the midrib. The three discs from the three leaves of the same plot are grouped together in a labeled 2ml Eppendorf tube. The entire sample constitutes approximately 5-10mg of dry tissue. The tubes are then sent to the University of Nottingham, where analysis was conducted using the same method as in 2.3.6.

4.3.7 Soil ionomic profiling

Sampling for soil ionome

Soil ionomic profiling was done for years 2 and 3. Soil cores were taken at 20 points across the fields, at depths of 0-20, 20-60, 60-100, 100-140 cm. In year 2 this was done on April 6th and 7th 2021 (35-36 DAS), and on May 5th and 6th 2022 (35-36 DAS). This was done in a random distribution, between plots. Samples were placed in plastic bags and dried in the sun for 2/3 weeks. The dry soil is then homogenized and 5g of soil is taken and placed in a labeled 50ml Falcon tube for ionomic analysis at Nottingham.

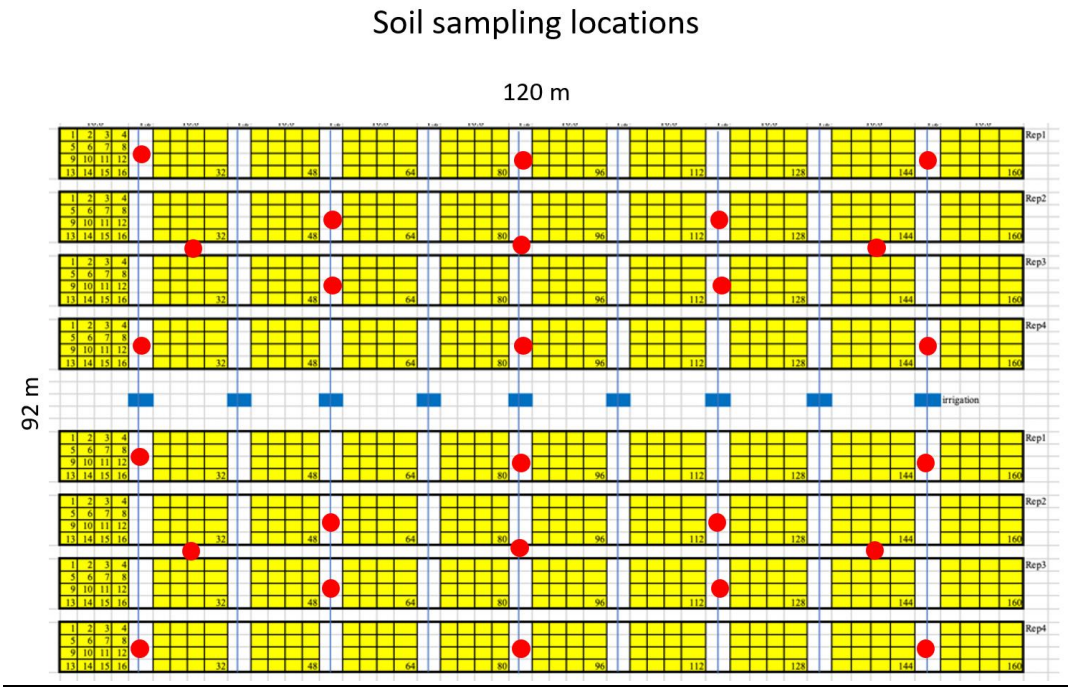


Figure 4-4. Plot map showing field layout from pearl millet field trials. Top block ETM (Well-watered), Bottom STR (Water stressed) soil sampling locations shown by red dots

4.3.8 Physiological Measurements

UAV canopy phenotyping

In years 2 and 3 drone flights were conducted throughout the field experiment to image the field and provide spectral vegetative indices (SVIs) for each plot for leaf area and canopy temperature. These flights were at 21, 28, 35, and 42 DAS in the morning (~ 9 am, local time). On the final two days, an additional afternoon flight was flown in the afternoon, around 4 pm.

Agro-morphological traits

Biomass was recorded twice, first using the shoot biomass of the plants harvested at 42 DAS for root anatomy, and again at maturity on three different plants. At final harvest, height at top of panicle and height of base of flag leaf was recorded, along with the number of panicles and of tillers. The seed heads of the three plants were collected to measure 1000-grain weight, and total grain weight.

4.3.9 Genotyping

All lines were re-genotyped each year by sequencing (GBS). 35 days after sowing, tissue was collected from one leaf per plot in block 1 of the well-watered treatment plants. Samples were then placed in the lyophilizer for 2 days, prior to shipping to Freedom Markers (USA) for GBS.

4.3.10 Statistical analysis

Pilot Year Data

Data from the pilot year as a standalone, and without genetic analysis. Correlations between traits, differences between lines, effect of water stress, and variation in plasticity were analysed. Correlations between each trait were calculated and plotted in Prism 9, and mean trait values for each line/treatment were calculated in excel and graphed in Prism 9. Trait plasticity was calculated in excel, these were graphed, and plasticity correlations were calculated and graphed in excel.

Heritability

Heritability was calculated for a subset of traits across years 2 and 3, spanning the breadth of measurement. All traits investigated showed high heritability between years and treatment groups (Pers. Comm., Alex Grondin).

Spatial Field Correction

For each trait from that was measured from all plots, an R script was used to assess the spatial distribution of variation in the field. This calculated a plot specific adjustment value that estimated the field effects within the treatment group. This was then applied to the mean plot values, which were then used to generate a single best linear unbiassed estimate of each mean trait value for each line and treatment. Full R script and workflow given in Appendix 6.

Genome Wide Association Studies

Genome wide association studies were conducted in R, using the GAPiT plugins (Lipka et al., 2012; Wang and Zhang, 2021). All available models were tested and appraisal of the QQ plots showed that FarmCPU was the best suited for the datasets. Due to field heterogeneity and the likelihood of genetic variation between years, this was run separately for years 2 and 3.

Leaf anatomy analysis

Leaf anatomy data was analysed using Microsoft Excel and GraphPad Prism 9. Due to limited sample numbers providing a less detailed map of field spatial trends, spatial correction was not run. 2-way ANOVAs were used to check for block effects, year effects and treatment effect. When multiples of the same feature were measured in a single image, the median of each trait was used in further analysis. To compare lines and treatment differences, multiple unpaired T-tests were run in excel and prism, comparing the mean value for the line/treatment combination.

Correlation matrices were generated in prism using multivariate data analysis, using both the mean values for each trait per line/treatment combination, and the individual replicate values per rep (horizontal block), for both years. Plasticity was calculated in excel and graphed in Prism 9.

4.4 Results

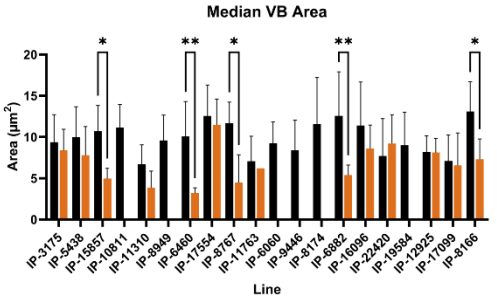
4.4.1 Year 0

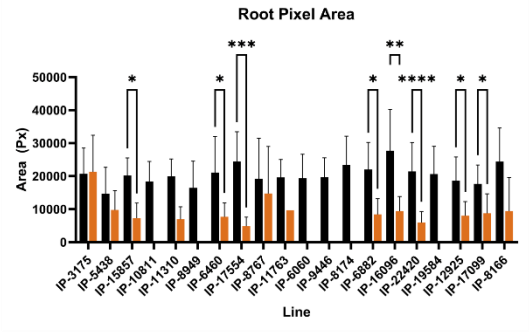
Pilot year outcomes were discussed in part in Chapter 3 Section in the methods development and whorl selection results. The primary aims of this year were to develop the methods to be used in the following years and identify and implement necessary changes. The material was also used to investigate the effect of water stress on this subset of lines under these different conditions and use this to look for correlations between traits.

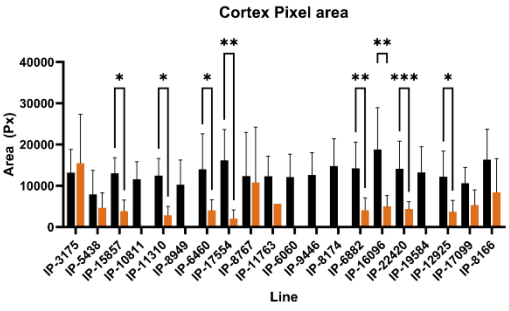
Root anatomy

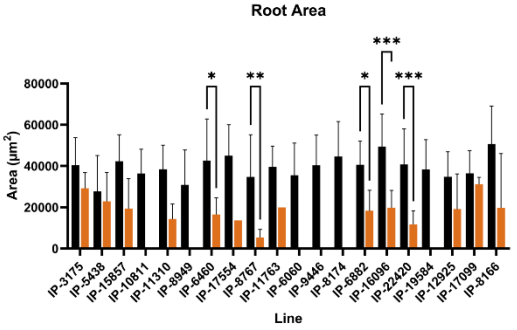
Due to the quality of samples being very varied and poor for whorl 2, whorl 3 and tiller roots, only whorl 4 samples were used for analysis. After filtering for quality, 186 W4 (120 well-watered and 66 water-stressed) individual sample image were analysed.

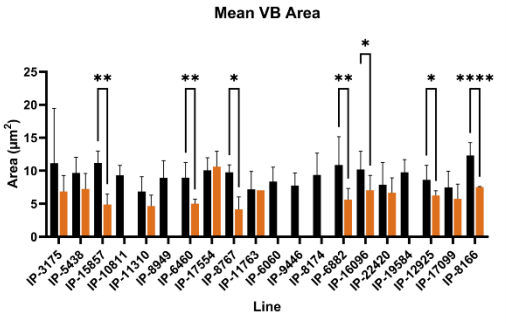
Nineteen root anatomical measurements produced by ROOTSCAN were analysed to assess the effect of water stress on the set of lines used in the pilot study (Figure 4-5.

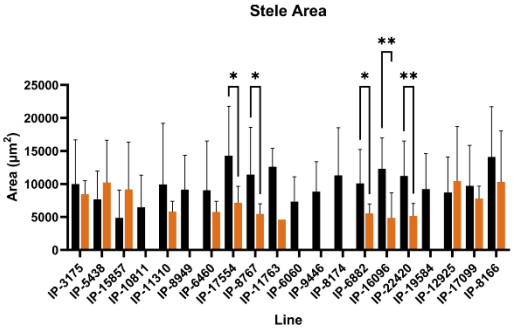

Median VB Area
Area (μm²)
Line
IP-3175
IP-5438
IP-15857
IP-10811
IP-11310
IP-8949
IP-6460
IP-17554
IP-8767
IP-11763
IP-6060
IP-9446
IP-8174
IP-6882
IP-16096
IP-22420
IP-19584
IP-12925
IP-17099
IP-8166

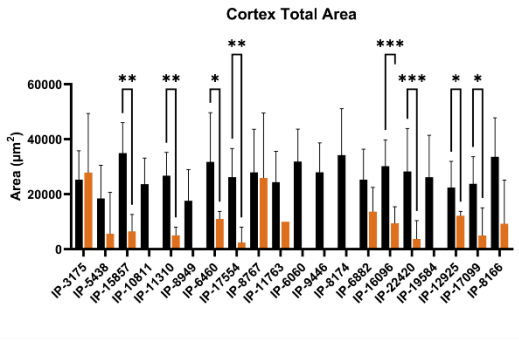

Root Pixel Area
Area (Px)
Line

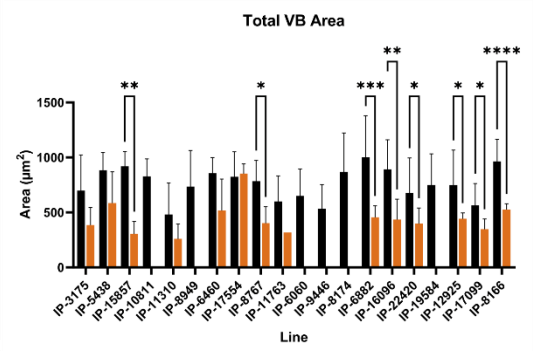

Cortex Pixel area
Area (Px)
Line

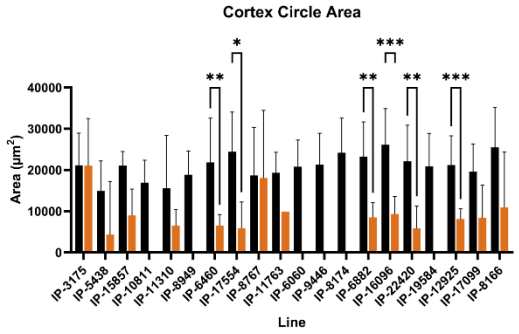

Root Area
Area (μm²)
Line

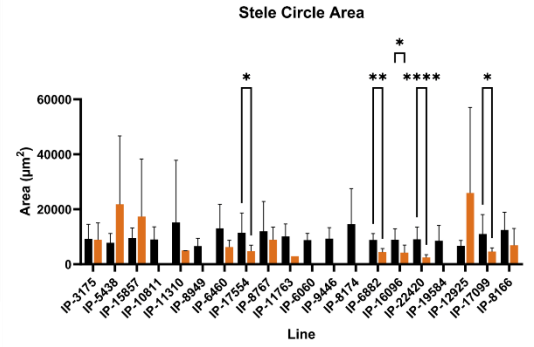

Mean VB Area
Area (μm²)
Line

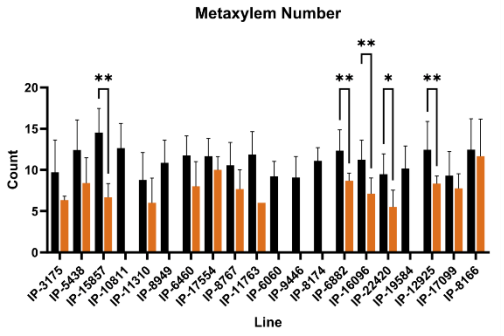

Stele Area
Area (μm²)
Line

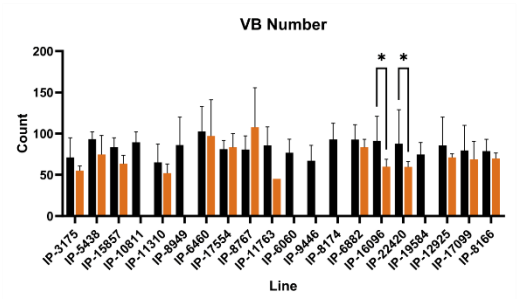

Cortex Total Area
Area (µm²)
60000
40000
20000
0
IP-3175
IP-5438
IP-15857
IP-10811
IP-11310
IP-8949
IP-6460
IP-17554
IP-8767
IP-11763
IP-6060
IP-9446
IP-8174
IP-6882
IP-16096
IP-22420
IP-19584
IP-12925
IP-17099
IP-8166


Total VB Area
Area (µm²)
1500
1000
500
0
Line


Cortex Circle Area
Area (µm²)
40000
30000
20000
10000
0
Line


Stele Circle Area
Area (µm²)
60000
40000
20000
0
Line


Metaxylem Number
Count
20
15
10
5
0
Line


VB Number
Count
200
150
100
50
0
Line

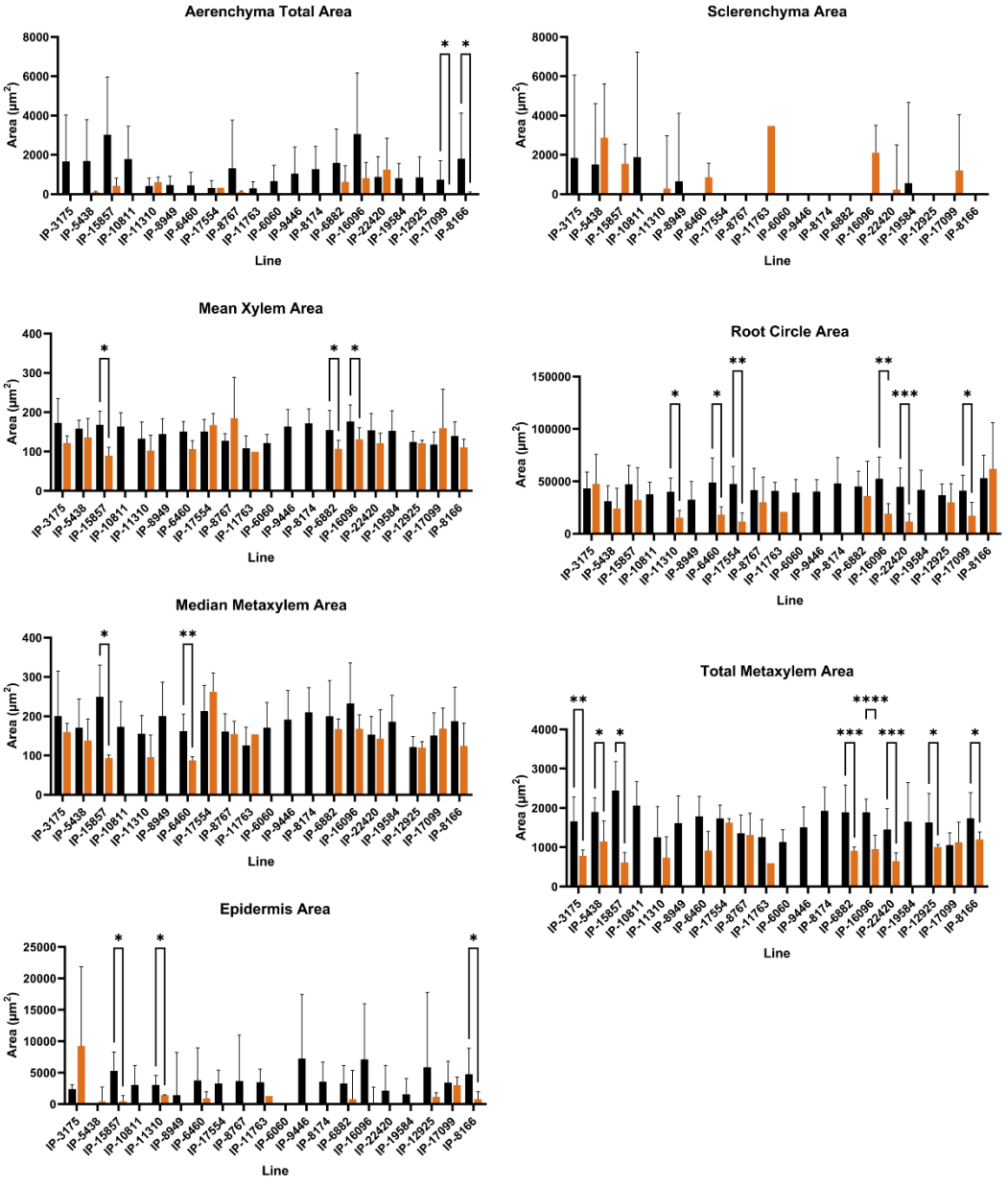


Figure 4-5. Root anatomical traits of pearl millet pilot year subset lines grown under well-watered, and water stressed conditions. Traits defined in table 3.7 as given by ROOTSCAN, Mean values shown, n between 1- 12 dependent on presence or absence of traits in sample, Error bars = Standard deviation, black = control well-watered conditions, Orange = Water stress treatment, Pairwise comparisons given are multiple T-tests comparing water treatments for the same line, with multiple comparison corrections using the Holm-Šidák method (Šidák, 1967) calculated in

Prism 9 (GraphPad), Significant differences; *=P<0.05, **=P<0.01, ***=P<0.001, ****=P<0.001

Analysis of the root anatomical data in combination with agromorphological and root architectural data via principal component analysis showed clear separation between treatment groups (

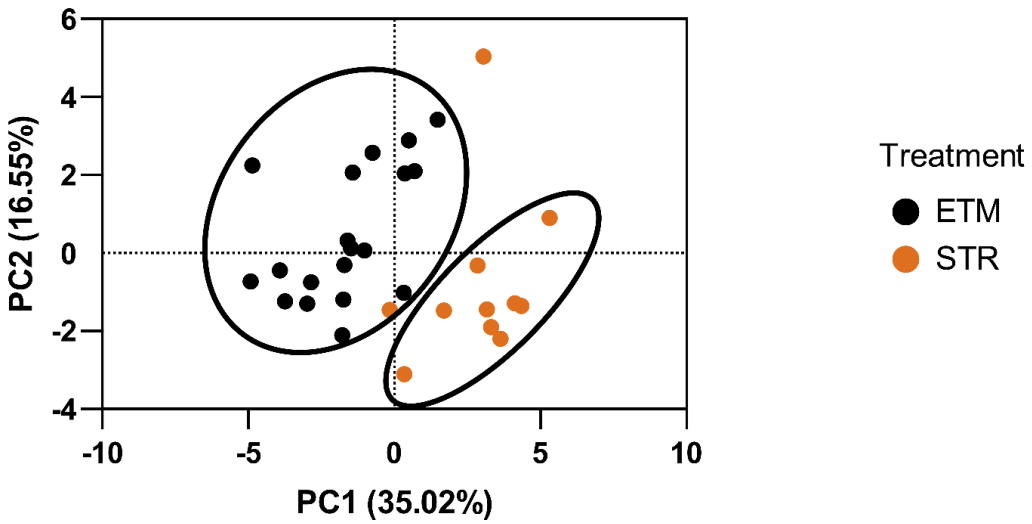


Figure 4-6).

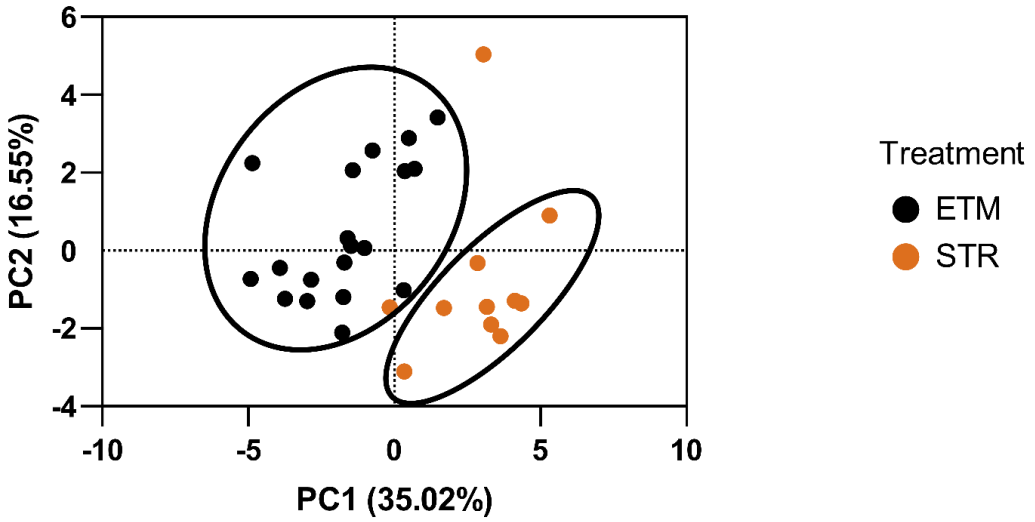


Figure 4-6. Principal component analysis of pilot year root anatomical data. Principal component analysis showing two clusters, one largely containing the ETM/Well-watered datapoints (left, black) and the other containing the STR/Water stressed datapoints (right, orange), separated by PC1 of 35.02%, and PC2 of 16.55%.

Trait correlation

The multivariate root anatomy, architecture, and agromorphological data used in the principal component analysis (Figure 4-6), was analysed to identify correlations between these traits. This showed that the various root anatomical traits frequently correlated strongly with each other, and identified several significant positive and negative correlations between anatomical, architectural, and agromorphological traits (Figure 4-7). Root area correlated strongly with biomass, root system width, and length of root system excavated, most likely due to the thicker roots being more able to withstand excavation. These largely follow the trend of larger root anatomical traits correlating with greater biomass, though specifically mostly larger and greater number of metaxylem and vascular bundles correlated with an increase in plant height.

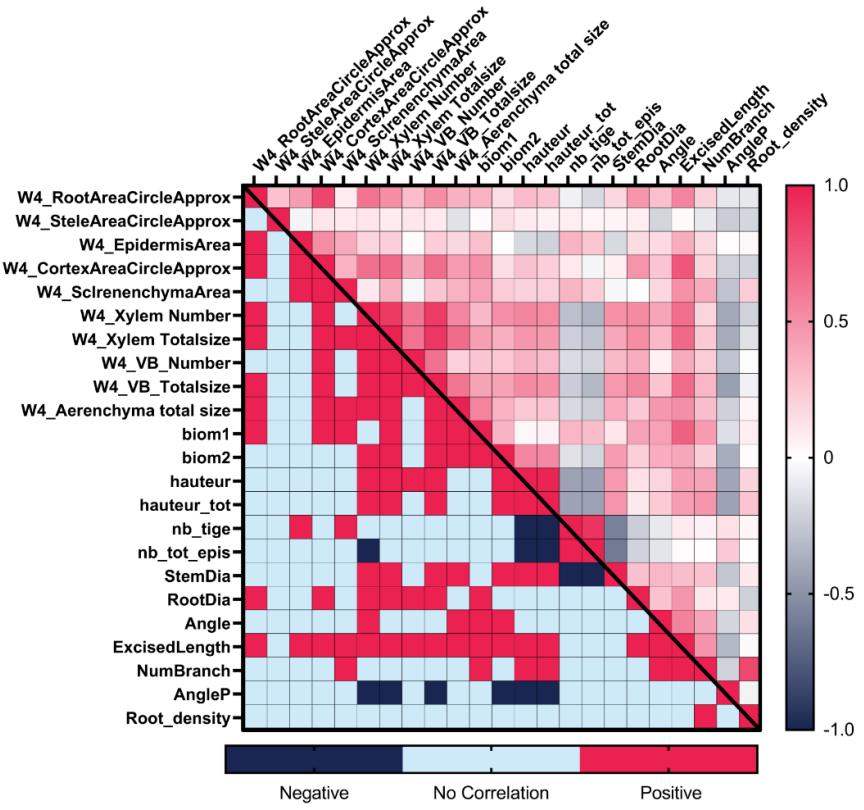


Figure 4-7 Correlation matrix of root anatomical traits with agro-morphological and root architectural traits. Pearson's correlation matrix showing correlation of traits measured, Details of measurements given in Table 3.7 and Appendix 8. Separated to show full correlation data, and significance level. Bottom-left triangle shows significance level: Dark Blue=Significant negative correlation at P<0.05, Light blue= No significant correlation, Pink= Significant positive correlation at P<0.05. Top-Right triangle shows Pearson correlation R value, graduated colour scale shown.

4.4.2 Year 2

Root anatomy survey

Root anatomy was surveyed in the 160 lines selected from the PMiGAP panel used in the field trial (Appendix 5) in plants grown under water stressed and well-watered conditions. 1644 samples were measured from the ETM (well-watered) treatment, and 1280 samples from the STR (water stressed) treatment. In the nine root anatomical traits measured there was a large amount of diversity in the panel,

under both treatments, and in the percentage change between treatments. In most traits the majority of lines showed a significant decrease in value under water stress, though root and cortex circle area showed an increase under water stress in a similar number of lines to those that showed a decrease. The most highly plastic traits were aerenchyma total area and sclerenchyma total area, with ranges in percentage change under water stress from -98%-687% and -78%-190% respectively (Figure 4-8).

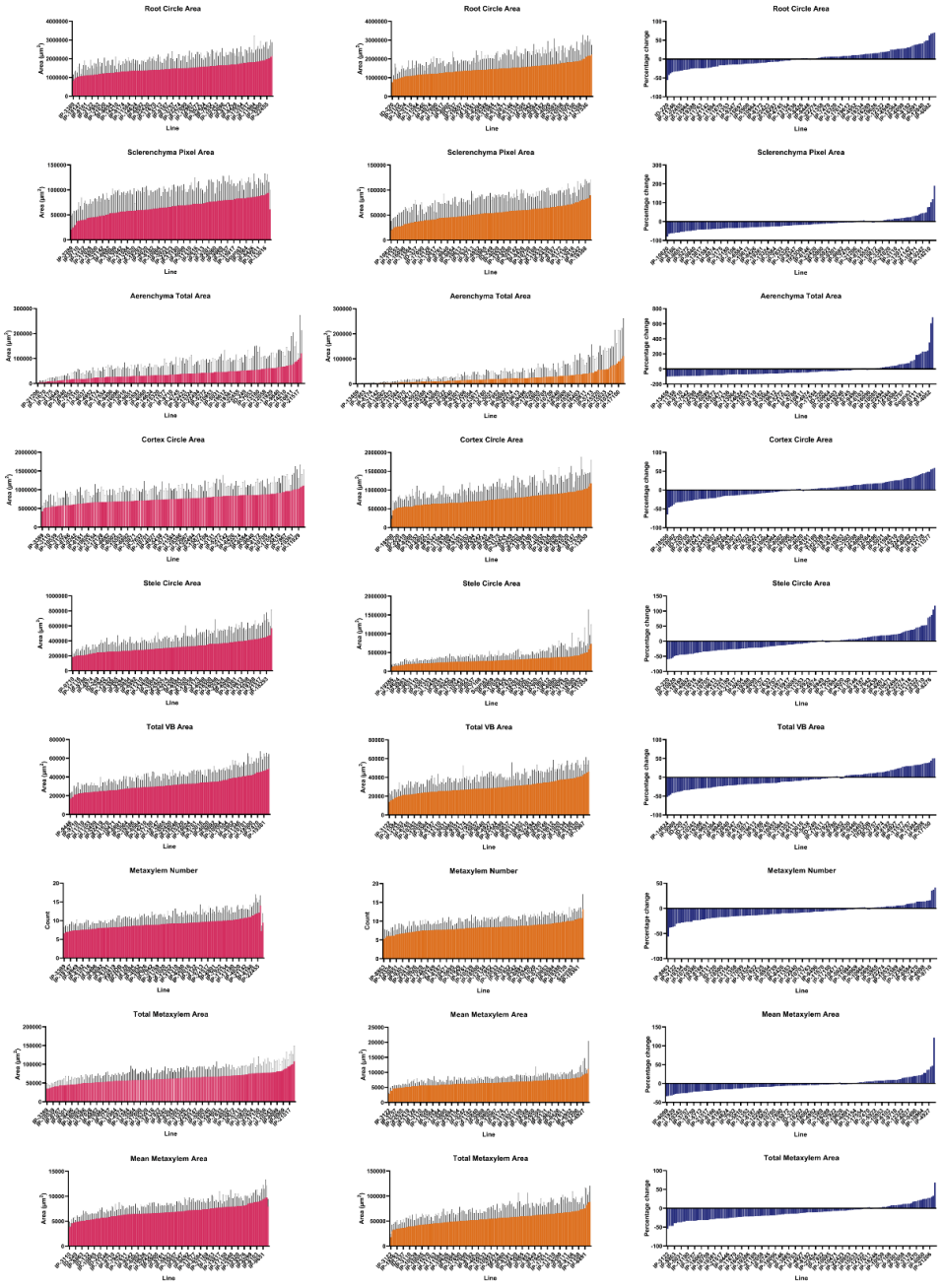


Figure 4-8. Anatomical diversity of pearl millet roots in Year 2. Column chart showing the mean trait value of nine root anatomical traits, from plants grown under well-watered conditions (Pink), water stressed conditions (Orange), and the percentage change in each trait between well-watered and water stressed (Plasticity) (Blue), for each line. Error bars = Standard Deviation

Correlation of root anatomical traits with other field measurements

Analysis of the correlations between root anatomical traits and agronomic and root architectural traits showed several significant correlations. Sclerenchyma area correlated negatively with days to heading and flowering. Stele area correlated positively with biomass (at root phenotyping date), ear weight, and grain weight, as did total metaxylem area, which also correlated with 1000 grain weight. Vascular bundle area correlated positively with biomass (at harvest), height at panicle and flag leaf, root angle, and the harvest stress tolerance index. Aerenchyma correlated positively with flag leaf and panicle height, biomass at root phenotyping and harvest, and ear and grain weight. There were no significant correlations between root anatomical plasticity and either agronomic or root architectural traits, or the plasticity of either of these sets of traits. There was a significant negative correlation between root area and plasticity in biomass at root phenotyping under water stress (Figure 4-9).

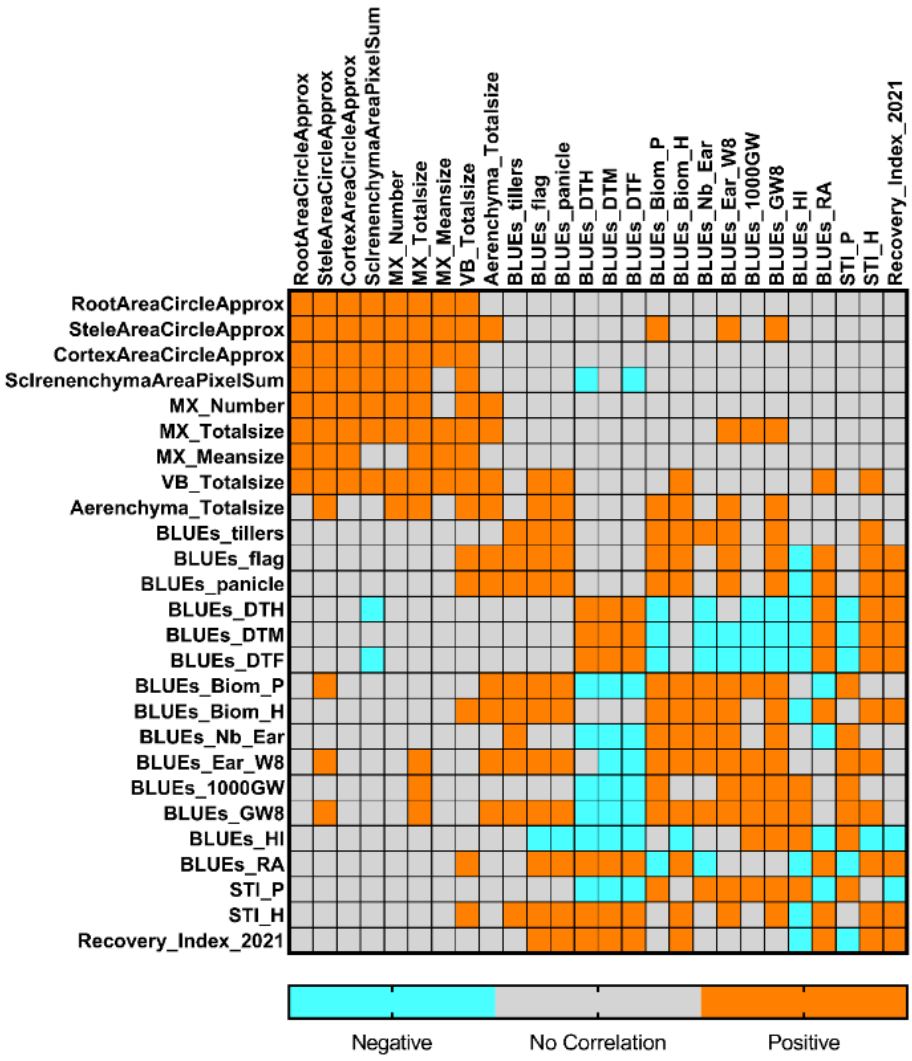


Figure 4-9. Correlation matrices of Year 2 phenotypic data and plasticity. Pearson correlation matrices showing the relationship between root anatomical traits, agromorphological traits, root architecture, and the plasticity (Pla) of these traits under water stress from Year 2 field data. Details of measurements given in Table 3.7 and Appendix 8, Matrix split to four quadrants for clarity. Recoloured to show significant positive or correlation at P<0.05 level, Cyan =Significant negative correlation at P<0.05, Light blue = No significant correlation, Orange = Significant positive correlation at P<0.05

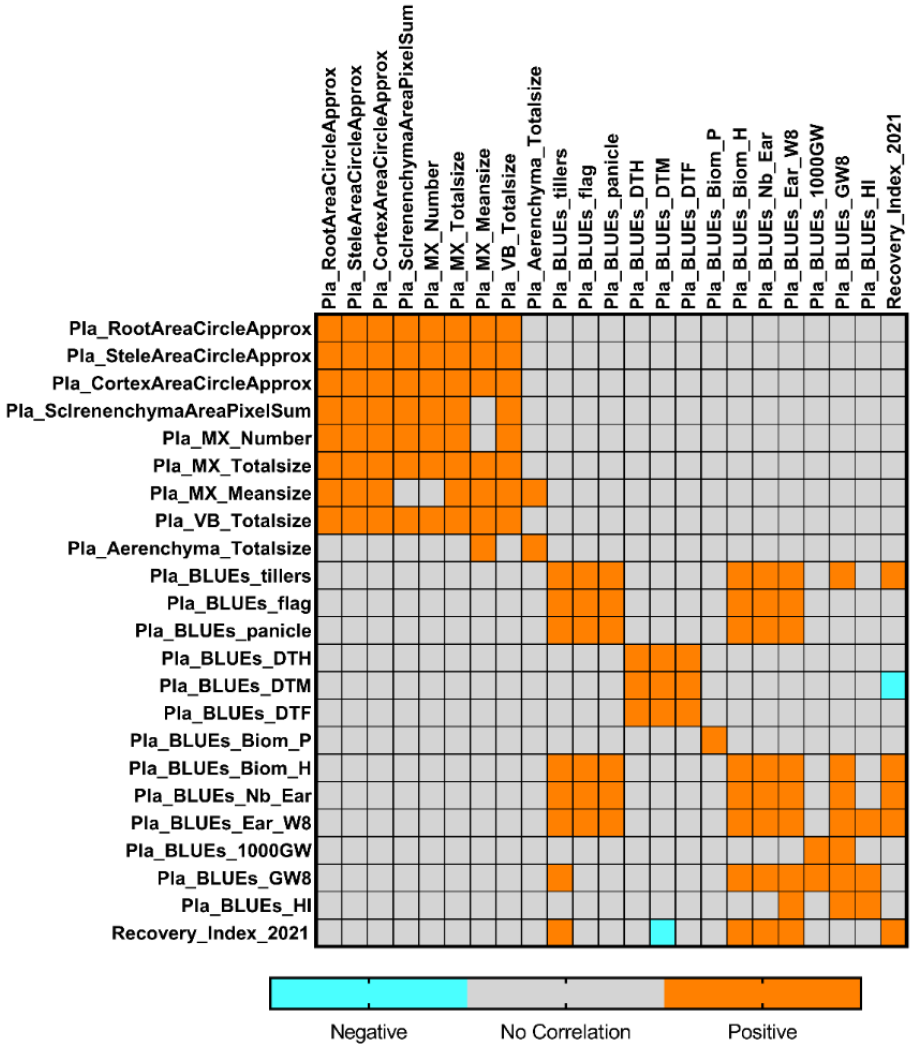


Figure 4-9. Cont.

Genome Wide Association Studies

Genome wide association studies (GWAS) were carried out to identify associations between anatomical traits and single nucleotide polymorphisms (SNPs), that had been identified during genotyping (GBS performed by Freedom Markers, USA, data provided by Alexandre Grondin). These were run in R, using the script given in Appendix 7. This analysis used spatially corrected, best linear unbiassed prediction values generated from the field data using the scripts given in Appendices 6. These studies identified significant associations of SNPs with the total area of aerenchyma in the roots of plants grown under well-watered conditions (Figure 4-10), and with the plasticity of total sclerenchyma area.

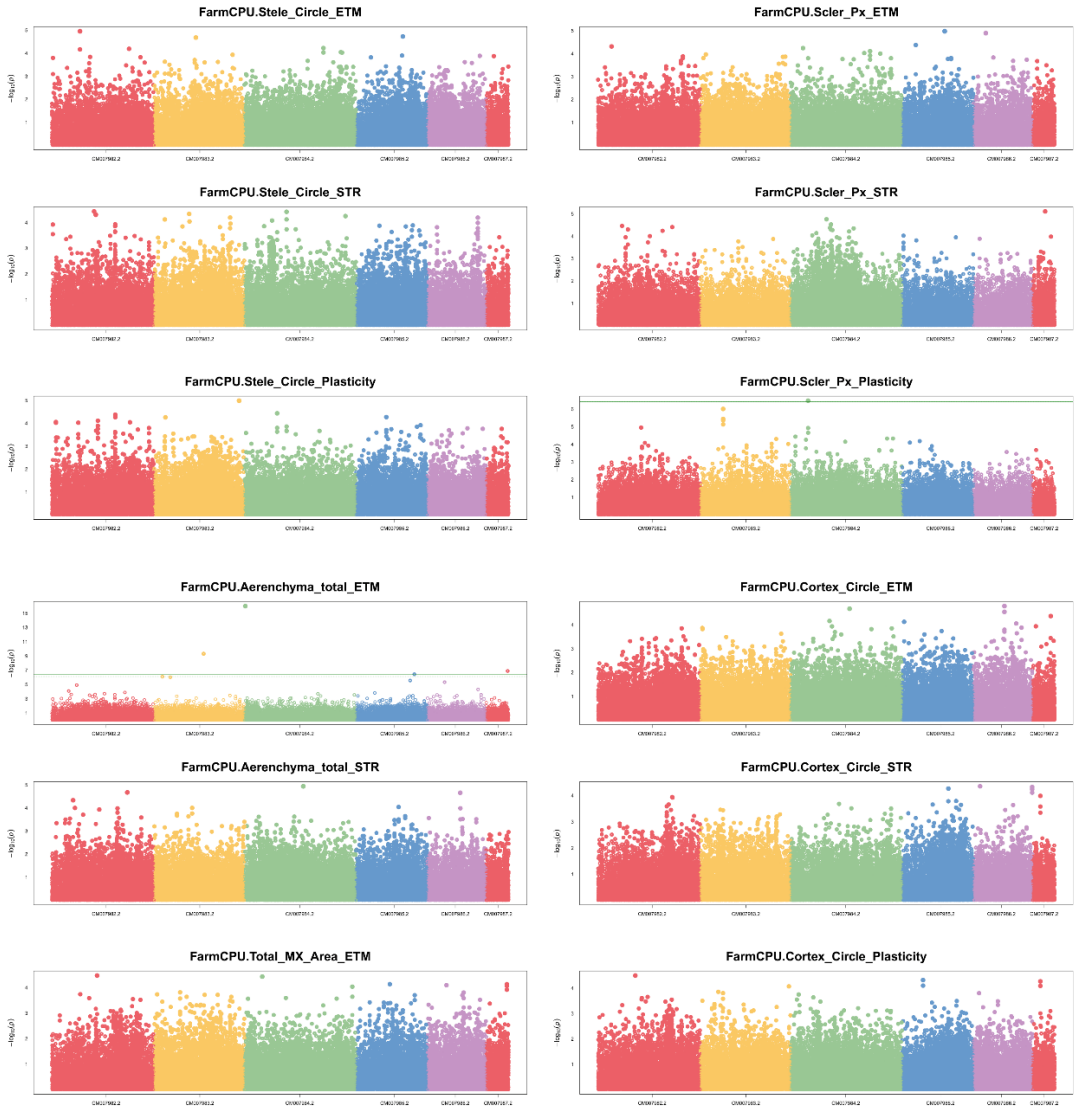


Figure 4-10. Manhattan plots of GWAS of root anatomical traits from Year 2. Manhattan plots showing genome wide association study results from analysis of root anatomy of pearl millet panel lines grown under well-watered conditions, water stress, and trait plasticity Traits investigated: Stele bounding circle area, Sclerenchyma area pixel area, cortex bounding circle, aerenchyma area, count, total and mean metaxylem and vascular bundle area, and total root bounding circle area. Produced in R using GAPiT, FarmCPU model.



Figure 4.10. Cont.

Leaf Anatomy

Analysis of the anatomy of the 20 lines selected for contrasting water use efficiency showed there was anatomical diversity within this subset, and that the leaf anatomy of particular lines was significantly affected by water stress (Figure 4-11).

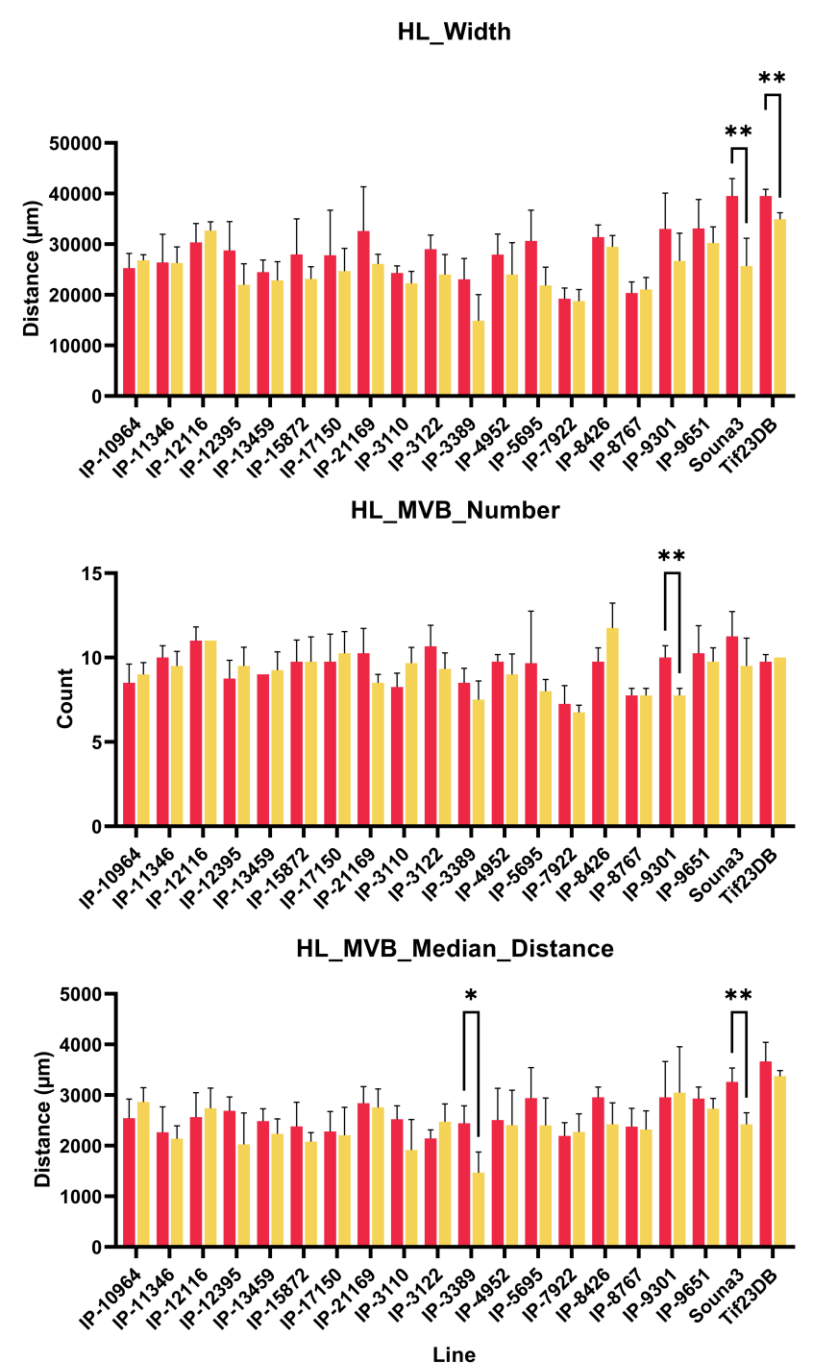


Figure 4-11. Leaf anatomical traits of pearl millet Year 2 water use efficiency lines subset grown under well-watered, and water stressed conditions. Mean values shown, Error bars = Standard deviation, Red = control well-watered conditions, Yellow = Water stress treatment, Pairwise comparisons given are multiple T-tests comparing water treatments for the same line, with multiple comparison

corrections using the Holm-Šidák method (Šidák, 1967) calculated in Prism 9 (GraphPad), Significant differences; *=P<0.05, **=P<0.01, ***=P<0.001, ****=P<0.001

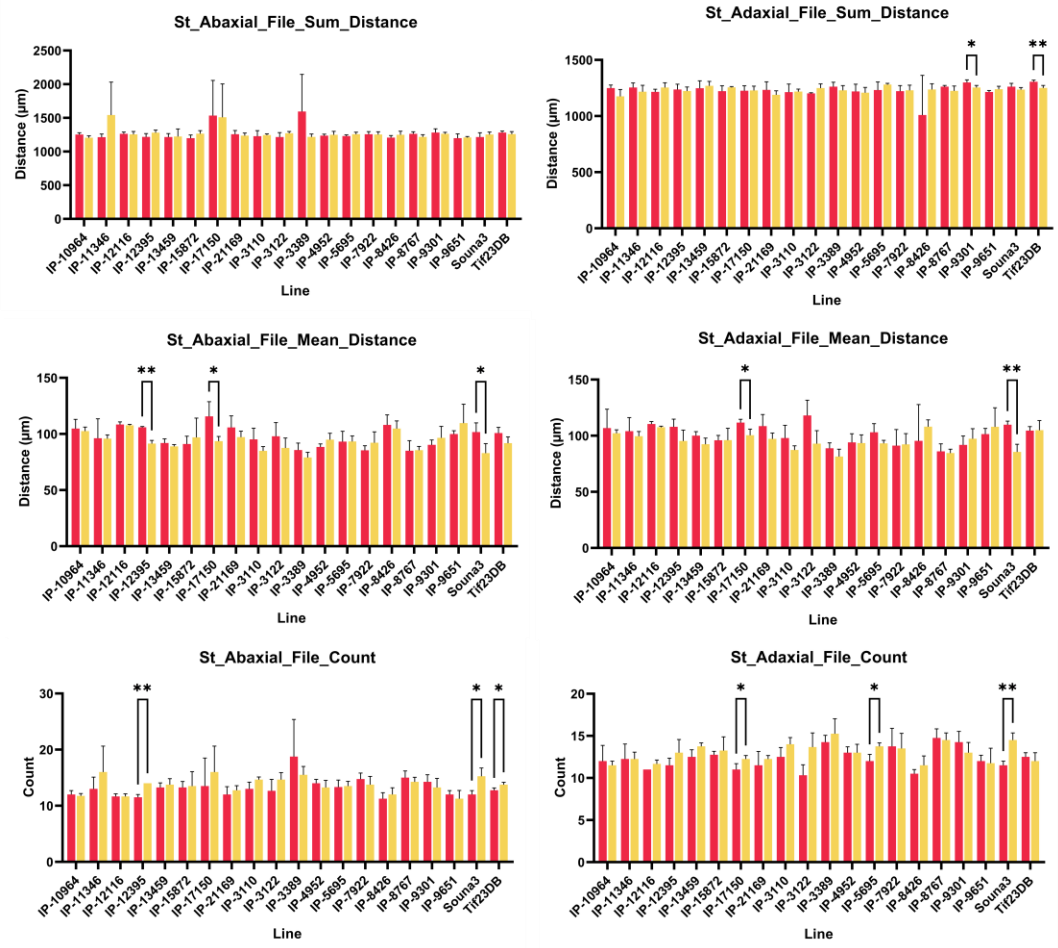


Figure 4-11. Cont.

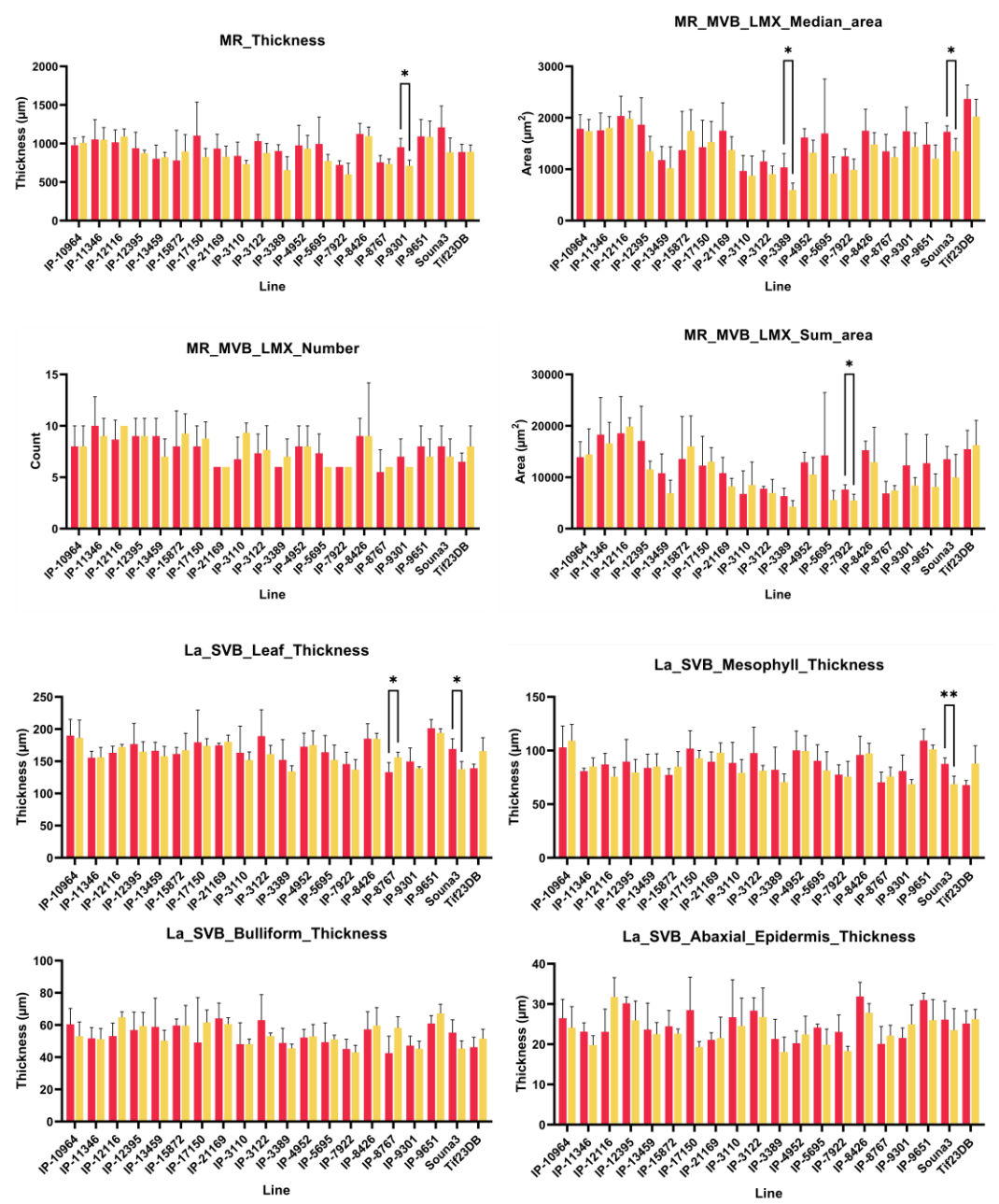


Figure 4-11. Cont.

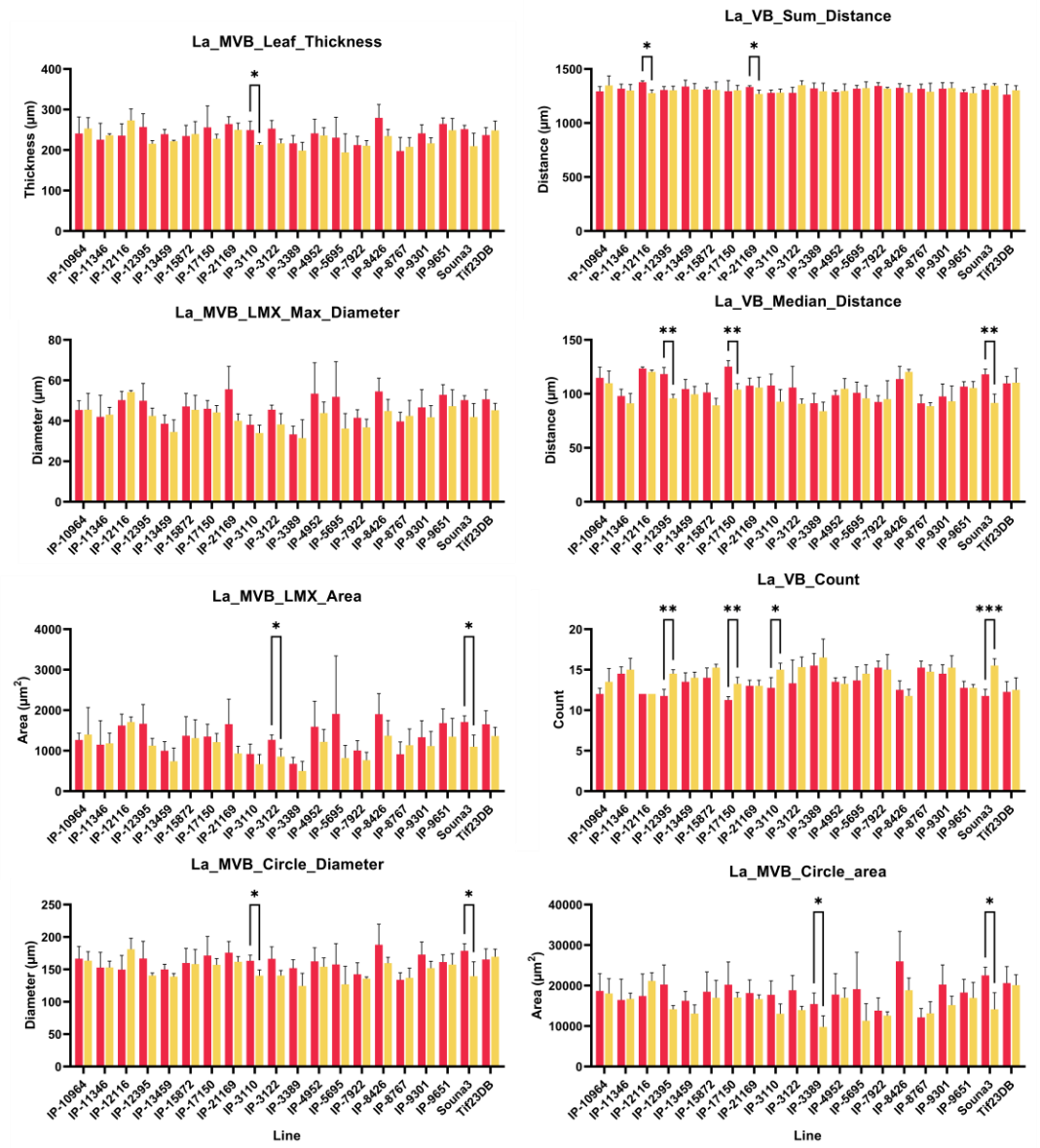


Figure 4-11. Cont.

Correlation analysis of root and leaf anatomical traits showed that the majority of leaf anatomical traits showed strong positive correlations with each other, as did root anatomical traits. There were also many significant correlations between root and leaf anatomy, particularly relating to size (Figure 4-12).

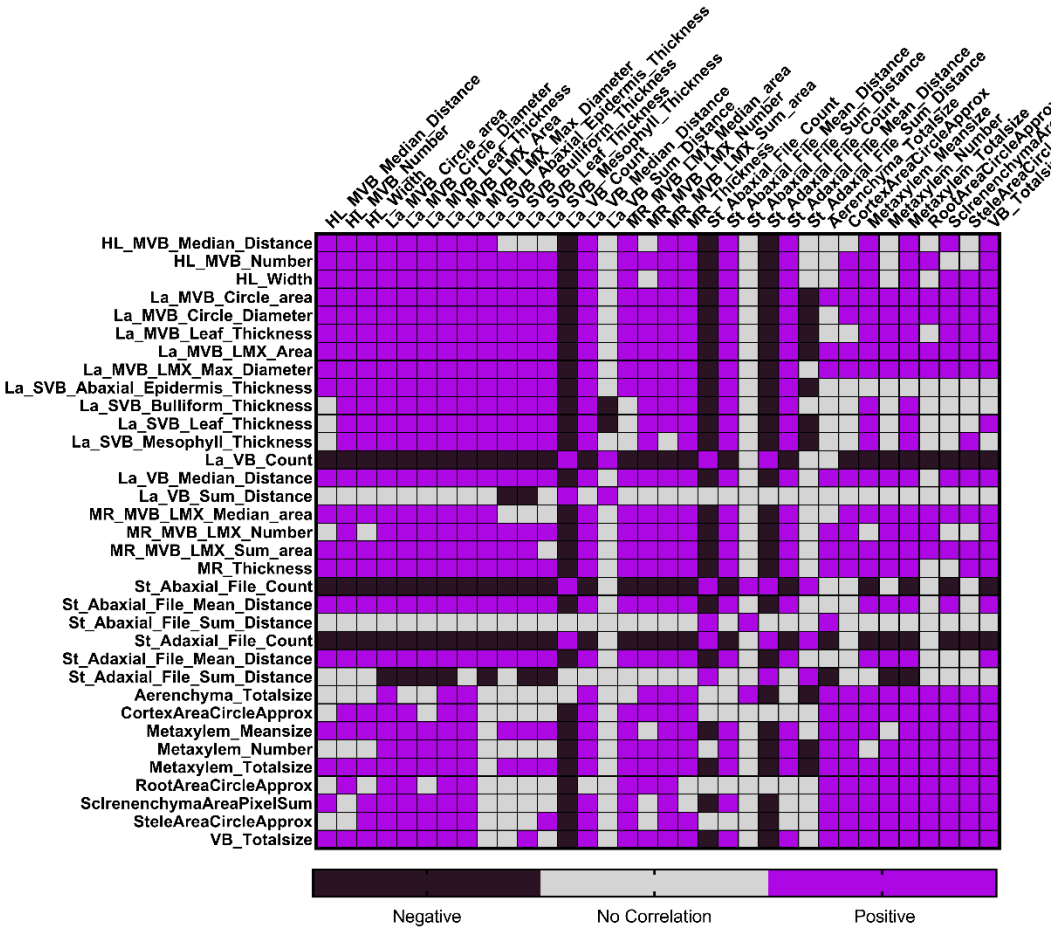


Figure 4-12 Correlation matrix of leaf and root anatomical data from Year 2 field trials. Pearson correlation matrix showing the relationship between root and leaf anatomical traits. Details of measurements given in Table 3.7 and Appendix 9, Recoloured to show significant positive or correlation at P<0.05 level, Black =Significant negative correlation at P<0.05, Grey = No significant correlation, Purple = Significant positive correlation at P<0.05

4.4.3 Year 3

Root anatomy survey

In the Year 3 root anatomy investigation 1611 ETM samples and 1351 STR were scanned and analysed, this showed a similar pattern in diversity to the previous year's data. The largest range in plasticity was again in aerenchyma total area, followed by sclerenchyma pixel area. In contrast a majority of lines showed an increase in root and cortex area under water stress, however this was not seen in stele area, and an even greater proportion of lines than the previous year showed a decrease in area under drought. (Figure 4-13).

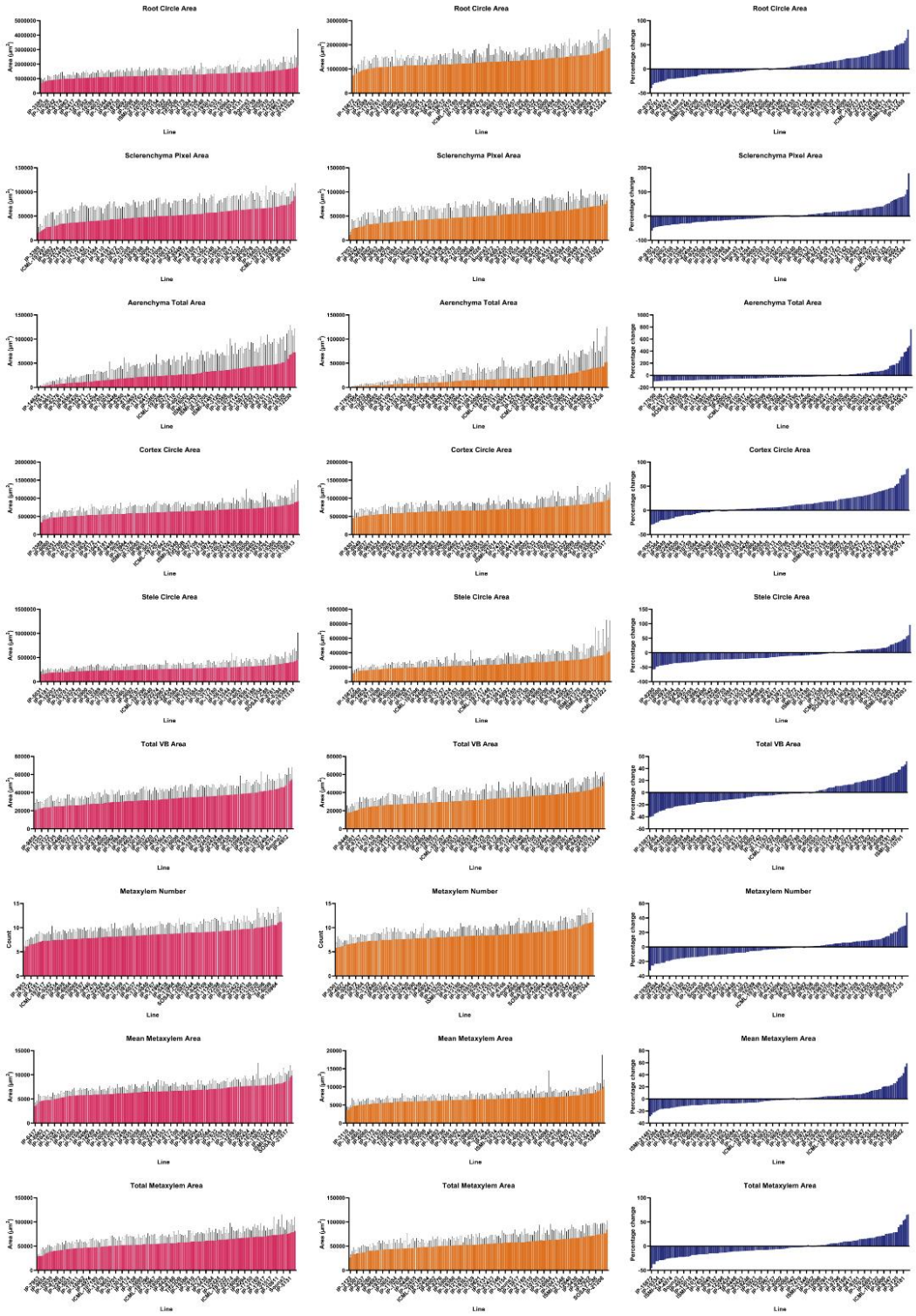


Figure 4-13. Anatomical diversity of pearl millet roots in Year 3. Column chart showing the mean trait value of nine root anatomical traits, from plants grown under well-watered conditions (Pink), water stressed conditions (Orange), and the

percentage change in each trait between well-watered and water stressed (Plasticity) (Blue), for each line. Error bars = Standard Deviation

Correlation of root anatomical traits with other field measurements

In Year 3, correlations between root anatomical and other phenotypic traits were again present, however different relationships appeared compared to the previous years. There were no correlations between root anatomy and plasticity of any other trait under water stress, nor between root anatomical plasticity and any other trait (Figure 4-14).

Unlike the previous year, there were correlations between the plasticity of root anatomical traits and the plasticity of other measured traits. Though these are positive correlations, this simply shows that these traits were both affected by water stress in the same way.

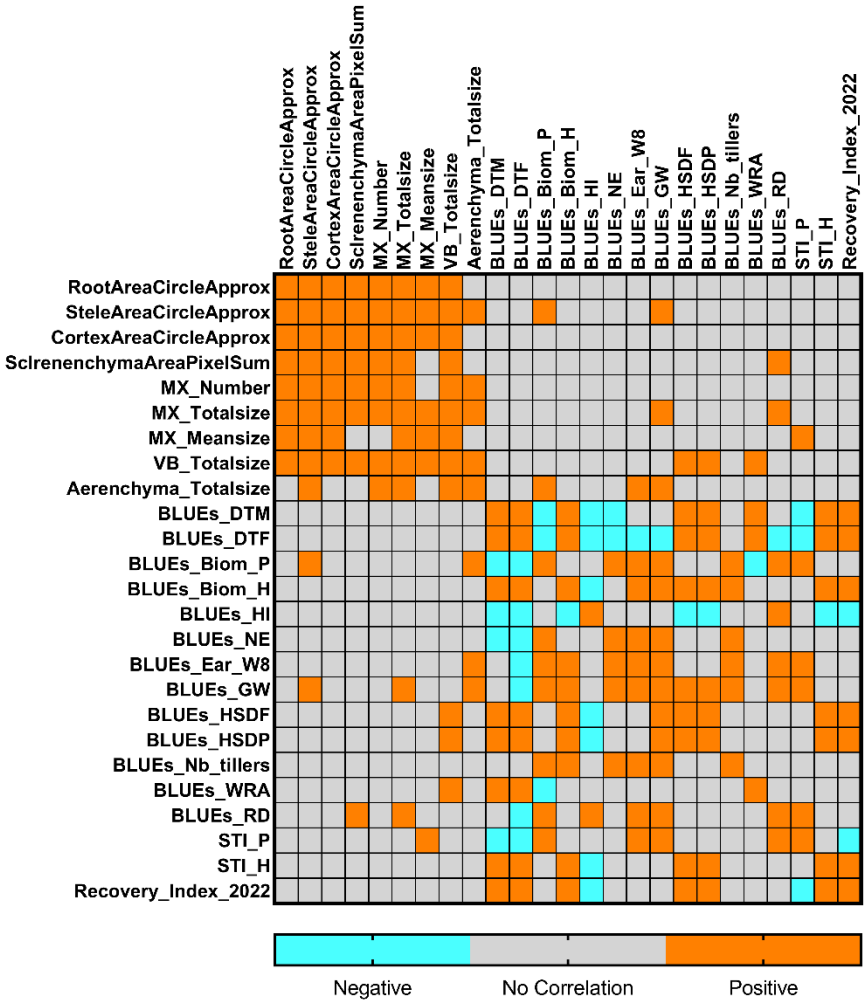


Figure 4-14. Correlation matrices of Year 3 phenotypic data and plasticity. Pearson correlation matrices showing the relationship between root anatomical traits, agromorphological traits, root architecture, and the plasticity (Pla) of these traits under water stress from Year 3 field data. Details of measurements given in Table 3.7 and Appendix 8, Matrix split to four quadrants for clarity. Recoloured to show significant positive or correlation at P<0.05 level, Cyan =Significant negative correlation at P<0.05, Light blue = No significant correlation, Orange = Significant positive correlation at P<0.05

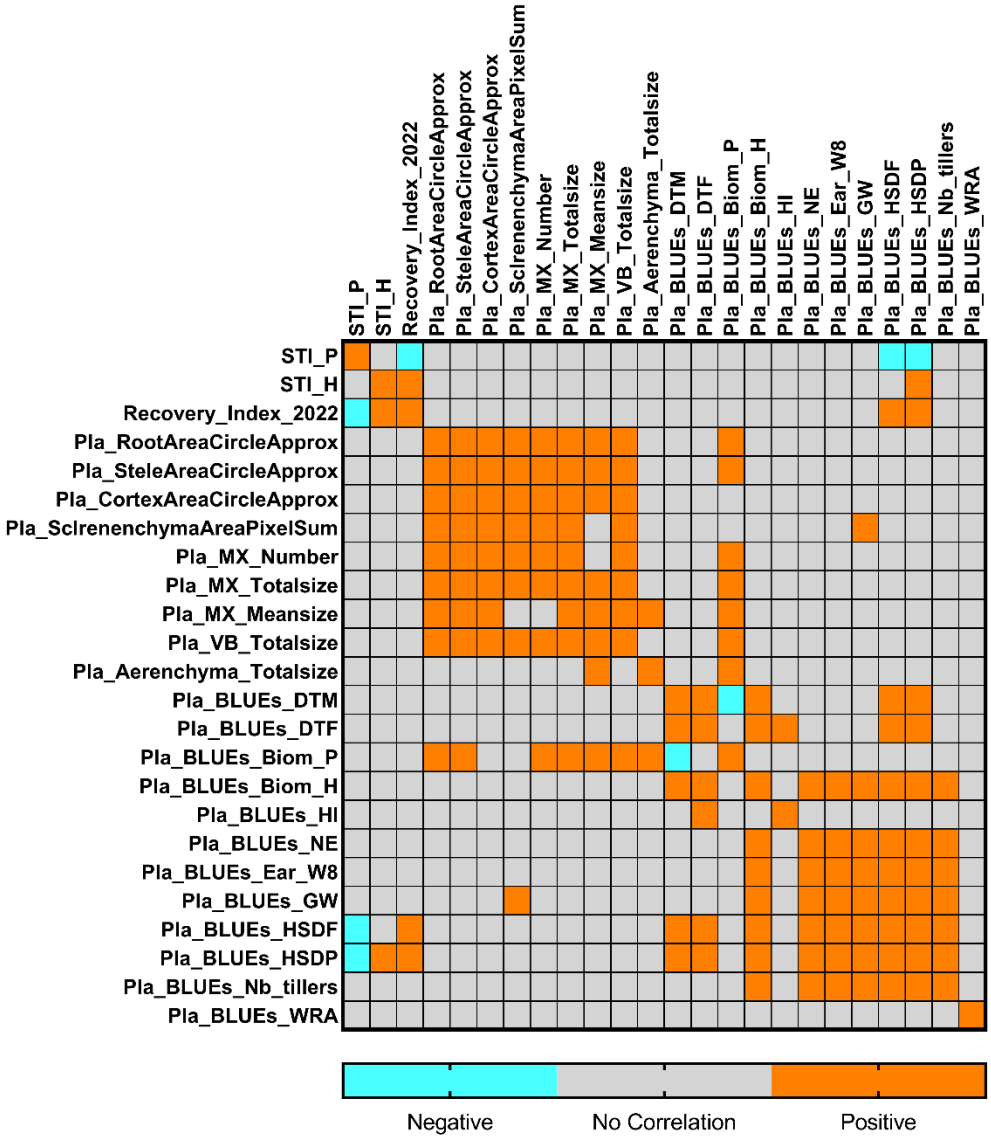


Figure 4-14. Cont.

Leaf Anatomy

Analysis of leaf anatomy in Year three showed a higher incidence of a significant effect of water stress on the measured traits than the previous year. Souna3 was again one of the lines most frequently showing a significant anatomical response to water stress; IP-8426, and Tif23DB among the others (Figure 4-15).

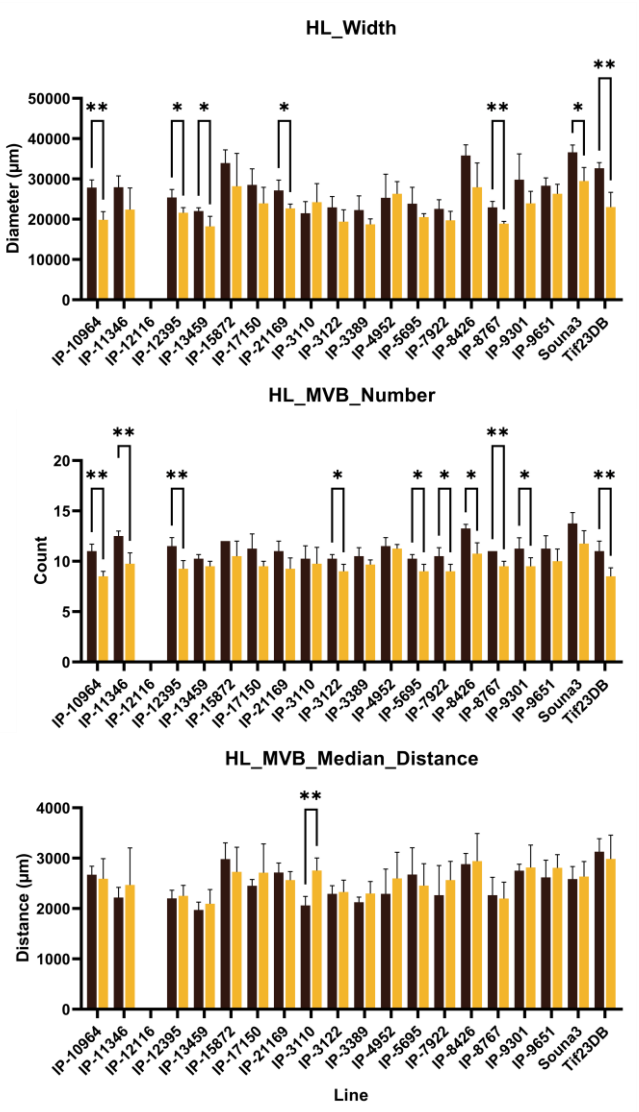


Figure 4-15. Leaf anatomical traits of pearl millet Year 3 water use efficiency lines subset grown under well-watered, and water stressed conditions. Line IP-12116 samples unavailable in Year 3, intentionally included for comparisons to Year 2, Mean values shown, Error bars = Standard deviation, Black = control well-watered conditions, Yellow = Water stress treatment, Pairwise comparisons given are multiple T-tests comparing water treatments for the same line, with multiple comparison corrections using the Holm-Šidák method (Šidák, 1967) calculated in Prism 9 (GraphPad), Significant differences; *=P<0.05, **=P<0.01, ***=P<0.001, ****=P<0.001

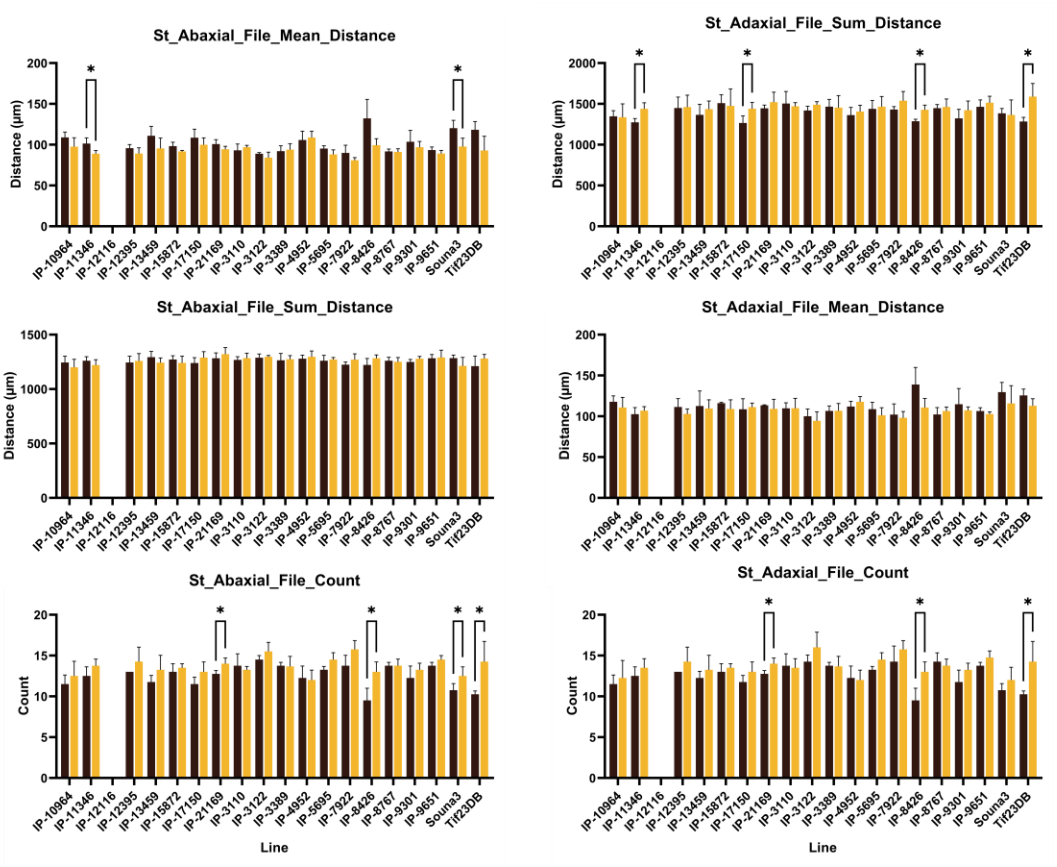


Figure 4-15. Cont.

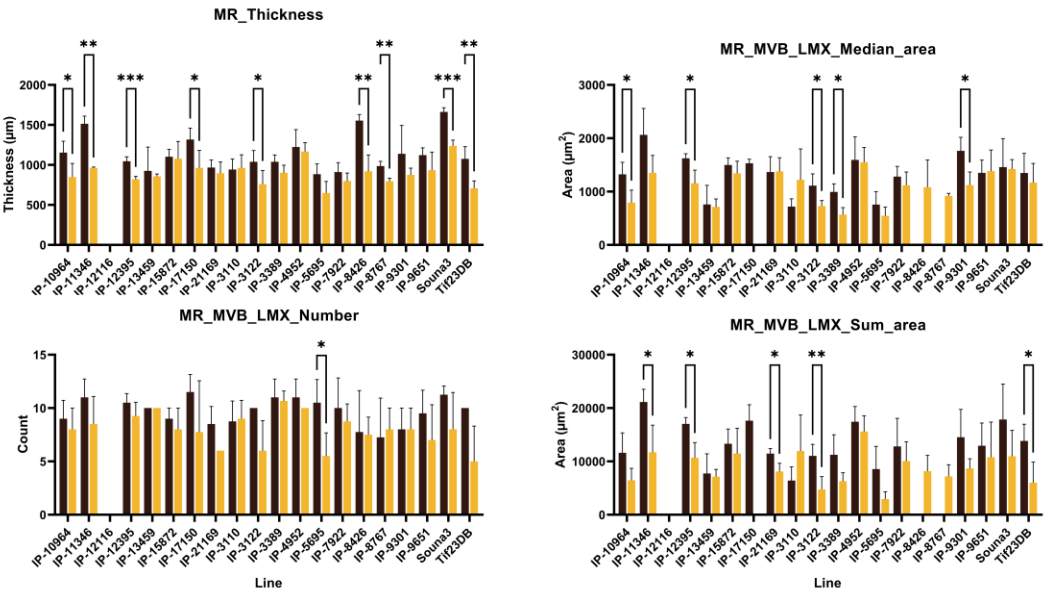


Figure 4-15. Cont.

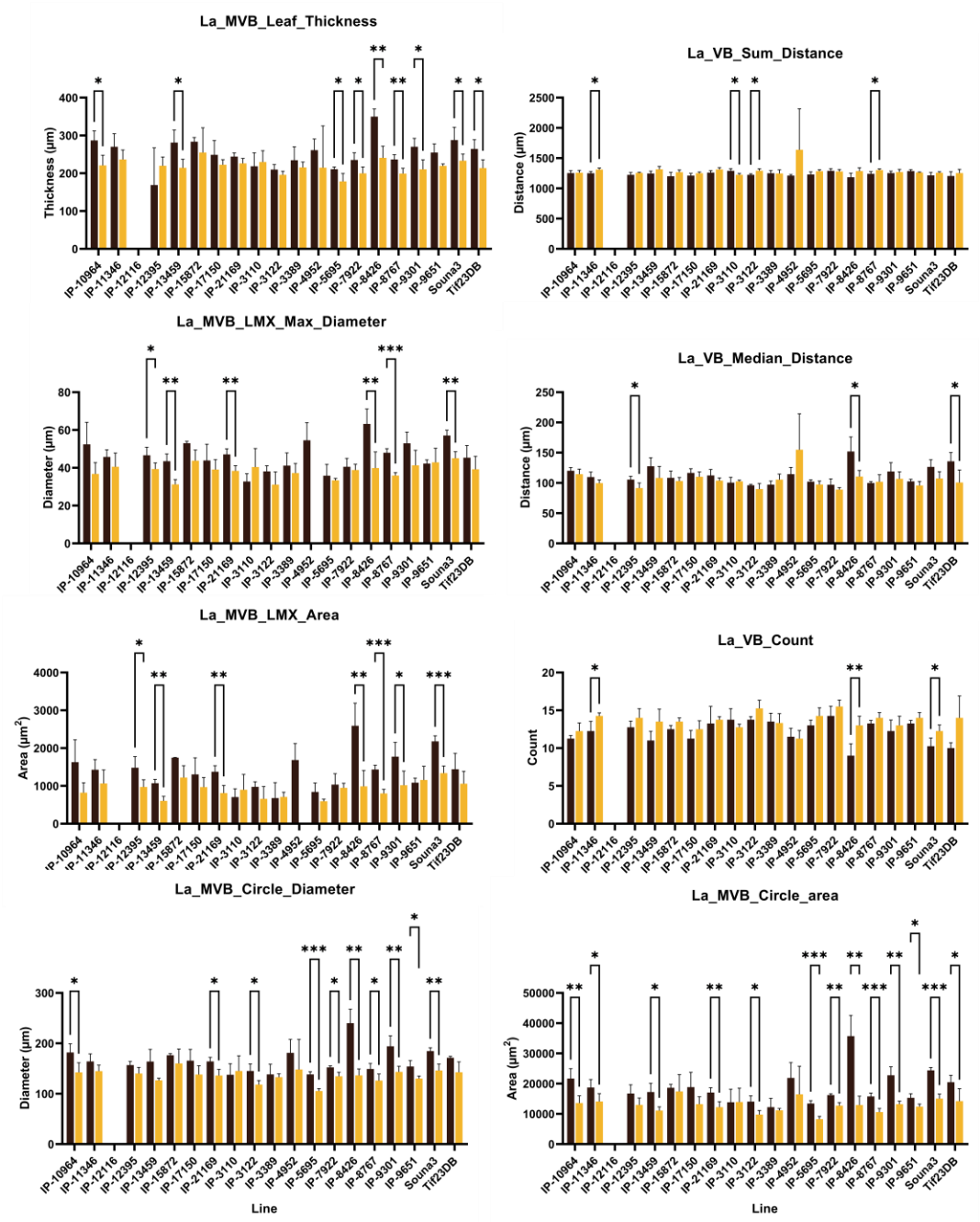


Figure 4-15. Cont.

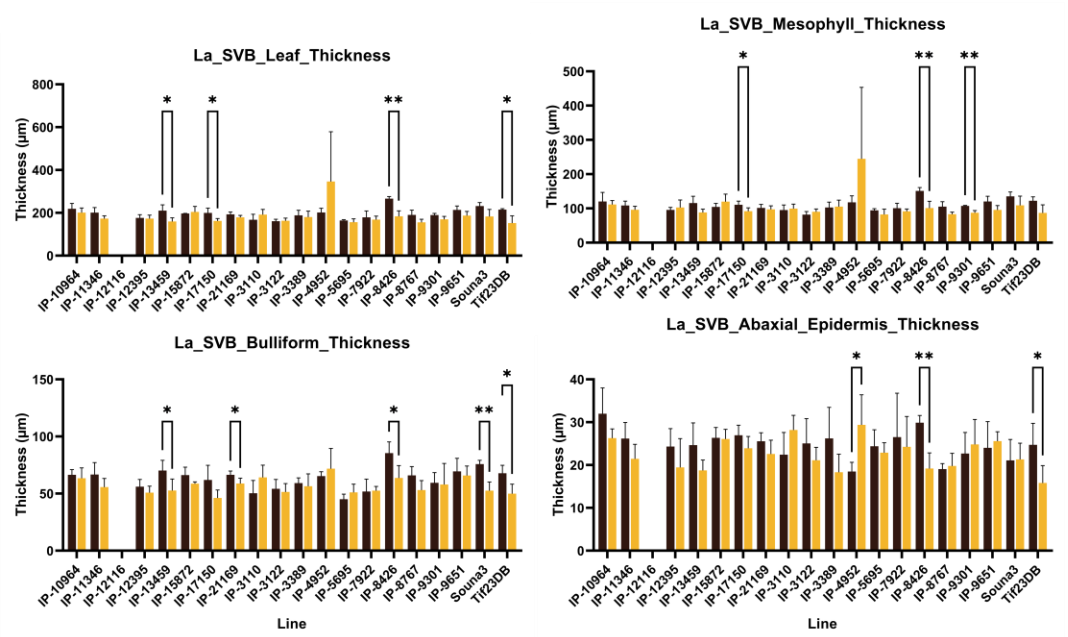


Figure 4-15. Cont.

4.5 Discussion

4.5.1 Discussion of results from pilot year

The pilot year served as a strong baseline in establishing that there was significant plasticity in pearl millet roots in response to water stress. and established which ROOTSCAN outputs were of most value.

There was a strong agreement between the multiple measurement methods of similar traits, and the circle area tissue layer measurements appeared the most resilient to negative effects of image artifacts. With the smaller subset of lines available in the pilot year, the full set of measurements available could be clearly visualized, and redundant measurements could be identified for exclusion in following years. Of the 38 measurements produced, 9 were seen to sufficiently assess the anatomical variation and water stress response in these lines. This was validated by analysis of the PCA loadings.

The principal component analysis discriminated well between the water treatment groups and it was possible to assign the majority of replicates to one of two clusters.

There were several significant correlations between root anatomical traits, and with anatomical traits and the other agronomic and morphological traits measured in the pilot year. Several of the root size related traits (Root circle area, stele circle area, cortex circle area), correlated strongly with biomass at point of root sampling, but this did not hold through to biomass at full harvest. These traits also correlated strongly with the width of the root crown (RootDia), and the length of roots in the crown (ExcisedLength). There were also strong negative correlations between the number of metaxylem in a W4 root, and the number of panicles at harvest, and the side on width of the root crown. This is surprising as for metaxylem number there is also a positive correlation with the root front on angle, unfortunately root side angle was not measured in following years.

The pilot year revealed many technical challenges in the setup of the field experiment, and enabled significant improvements. Positioning of the field plots relative to their surroundings (particularly trees, paths, and culvets) was reconsidered, as was working to ensure homogeneity in field history.

While limiting the experiment to whorl 4 may somewhat reduce the scope of the trials, and risks losing important physiological parameters, th

4.5.2 Discussion of results from year two

Year two root anatomy results showed there was significant root anatomical diversity across the full panel in plants grown under water stressed and well-watered conditions, and in plasticity.

The first year of leaf anatomical data showed that majority of leaf traits were highly susceptible to the effects of water stress, that within this subset of lines there is anatomical diversity, and that there is diversity in the level of plasticity in response to water stress. From this survey there were also clearly lines that were consistently more affected anatomically by the effects of water stress than others, such as Souna3, IP-3389, and IP-3310. The majority of leaf anatomical traits measured showed strong positive correlations with each other, though this is unsurprising as many of the traits are measuring similar size related traits.

Many of the leaf anatomical traits also correlated positively with root anatomical traits, in particular the metaxylem area in the lamina area (LA_MVB_LMX), showed strong positive correlations with all of the root anatomical trait included in the analysis.

Root anatomical traits showed weaker levels of correlations with the agro-morphological and root architectural data than with leaf anatomy, though select traits did stand out. Sclerenchyma area correlated negatively with days till heading and flowering, and stele area correlated positively with biomass at phenotyping (41 DAS), ear weight, and grain weight. Total aerenchyma area also showed these same positive correlations as well as with height of flag leaf and panicle. The total area of vascular bundles also correlated strongly with root angle, and with stress tolerance at harvest (STI_H).

The negative correlation of sclerenchyma area with the maturity rate of above ground traits may suggest an antagonistic relationship between root systems expenditure, particularly with regard to secondary thickening, and pearl millet flowering rate. As there are known to be late and early flowering groups of lines (Souna and Sario), analysis of these subpopulations for root sclerenchyma traits may help further understand this relationship. These may be alternate stress tolerance strategies to the different types of drought (early or late), that occur in the region (de la Fuente et al., 2023).

When looking at root plasticity and agro-morphological plasticity, fewer correlations are present. The only significant correlation between anatomy and agronomic plasticity was a negative correlation between well-watered root area, and percentage change in biomass at point of phenotyping (Pla_BLUEs_Biom_P). This suggests that with a root system with larger diameter roots, there is a negative impact on the plants production of above ground biomass under stress. There was not a strong relationship between stress tolerance index at phenotyping or harvest, or recovery index, with the plasticity of any root anatomical traits.

Genome wide association studies identified several associations with SNPs for anatomical traits. Total area of aerenchyma was found to have three significant SNP associations, cumulatively accounting for approximately 26% of the variation seen in total aerenchyma area. These were on chromosome 2, 3, 4 and 6, and the strongest linkage was the association to position 2572668 on chromosome 3, which accounted for 12% of the variability in aerenchyma (Table 4-1).

Table 4-1 SNPs identified significantly explaining phenotypic variance of total aerenchyma area in well-watered roots

SNP	Chromosome	Position	P.value	maf	nobs	effect	Phenotype_Variance_Explained(%)
CM007983.2-133245230	2	133245230	4.84E-10	0.292857143	140	9626.659508	10.35490134
CM007984.2-2572668	3	2572668	9.99E-17	0.378571429	140	11110.63335	11.98939034
CM007985.2-156784685	4	156784685	3.64E-07	0.257142857	140	7212.242051	0.893411665
CM007987.2-57944143	6	57944143	1.27E-07	0.267857143	140	-8437.081841	3.840722447

Plasticity of total area of root cortical sclerenchyma was also found to have a strong association with a particular QTL. GWAS analysis showed that position 47505820 on chromosome 3 accounted for 41.27% of the variance in this trait (Table 4-2).

Table 4-2 SNPs identified significantly explaining phenotypic variance in sclerenchyma plasticity under water stress

SNP	Chromosome	Position	P.value	maf	nobs	effect	Phenotype_Variance_Explained(%)
CM007984.2-47505820	3	47505820	3.32E-07	0.210714	140	-29.4911	41.26777

As both of these traits also showed strong correlations with important agronomic traits these genomic regions are strong candidates for further analysis.

4.5.3 Discussion of results from year three

Analysis of year three field trial data is ongoing as of submission, preliminary descriptive data is shown Section 4.4.3.

When viewing the trends in plasticity for the various root anatomical traits measured, it is interesting that many of the roots show an increase in overall area under water stress, whereas the majority show a decrease in stele area, and correspondingly, most show an increase in cortex area. Broadly, the vascular cell measurements follow the same trend in number of lines showing similar levels of percentage change.

Interesting measurements to include in future analysis once the measurements generated by the deep learned software have been further validated would be to investigate aerenchyma and sclerenchyma as a proportion of the cortex, and investigate the ratios of different root tissues, and how these are affected by water stress. These ratiometric measures would help in identifying more standout lines that go against the identified trends; for example, seeing a change in the proportion of vascular tissue that doesn't scale with the stele area or root area and relating that to water use would be highly informative. The same would apply for cortex subdomains like the aerenchyma, and sclerenchyma, though this could be

more complex as analysis of the change in proportion of the root or cortex these occupy would be compounded by stele and whole root change.

With the context of both years of leaf anatomical data, It is notable that Souna3 showed high levels of leaf anatomical plasticity under water stress in both years. Souna3 is often included in pearl millet research as a point of reference for its high drought tolerance (Sattler et al., 2019; Diack et al., 2020; Ndiaye et al., 2022); though further work would be needed to confirm the role of leaf anatomical plasticity in this. Further experiments are ongoing focusing on this line subset, and a greater range of leaf focused physiological measurements will be integrated into this analysis.

Chapter Five:

Discussion

5.1 Introduction

Plant anatomy is a key determining feature of organ functionality, particularly with regards to water transport. Furthermore, anatomy can significantly affect the cost of production and maintenance of organs to the plant. Improving our understanding of the impact of anatomy on these characteristics and the genetic regulation of anatomy is key in the effort to improve plant performance and stress tolerance (Maiti et al., 2012b; Strock et al., 2022).

Anatomy is determined by a complex and constitutive set of traits, for example, the size of an organ is determined by the size, number, and arrangement of all its component cell types, and the presence of any airspaces, cavitations, or particular topological features.

This thesis has presented the development of these methods and shows their applications in varied investigations of monocot anatomy, and how this is influenced by the relationship plants have with their water environment.

5.2 Analysis of duckweed root anatomy to determine function and root vestigialization

Duckweed has intermittently been viewed a model species during the history of plant science research, and has had somewhat of a recent resurgence (Acosta et al., 2021). The current wave of research interest has focused primarily either on developing our understanding of duckweed genomics, or on its potential applications, rather than its use as a tool for evolutionary and developmental biology. This may be in part due to its higher amenability to the current toolkits of these fields (Zhao et al., 2019).

Chapter 2 described the development of anatomical phenotyping methods, and analysis of duckweed anatomy with the context of an analysis of root function, in order to determine if duckweed roots are vestigial.

This showed that there has been a dramatic loss of function, and reduction in anatomy, in tandem with the well described trajectory of morphological simplification shown by the three rooted duckweed genera.

Whether or not this makes duckweeds roots vestigial is somewhat subjective and depends on how one defines the function of a root. Discussed extensively in Chapter 2 is the significance of the root in supporting growth, and in acquiring nutrients. It is shown rather conclusively that duckweed roots are not required for these functions, and that on a molecular basis, the specificity of these functions to the root has been lost when compared to terrestrial plants. What is less clear is if there are ancillary benefits to the plant of maintaining a root or root system beyond these functions. In land plants, a key role of the root is mechanical stability, and anchorage of the aerial portion of the plant to the soil. It has been posited that the duckweed root may aid in its dispersal (Cross, 2017), or function as a sort of 'sea anchor', stabilizing the frond in its environment (Landolt, 1986).

This hypothesis was investigated by the experiments subjecting duckweed of different root length to wind treatment, and through a combination of modeling and physical experimentation, it was clear that there was an effect of the root on how duckweed interacted with its physical environment. The greater the volume of the root system, the less the plant moved around its environment in response to simulated wind conditions, and the higher the probability the frond would orient correctly if disturbed. Whether or not this is environmentally relevant, or sufficient to say the root is performing a salient function is unclear but poses an interesting possible future area for research. It may also be the case that the root is partially responsible for orienting the duckweed so the correct surface is facing the air, the loss of roots raises interesting questions about the mechanism by which rootless

duckweed varieties may orient themselves, or whether they have adapted to no longer need to.

When considering the environment the more diverged duckweeds that possess reduced physical characteristics have become adapted to, there does appear to be a trajectory towards adaptation to increasingly tropical, high temperature and high light environments. As the duckweeds have gotten smaller it is also observed that they tend to sit less proud on the water and can be found layered in films on top of each other. It would be expected that it is less likely for these smaller more submerged plants to be affected by wind, so theoretically could have reduced need for the roots in this manner as well. The *Wollfia* and *Wolfiella* are also more commonly found in high light environments, so it may be the case that even if they are susceptible to drift, they are more tolerant of where they may end up.

There are large, genotyped collections of duckweed (In particular *Spirodela polyrhiza*) (Wang et al., 2014), that are suitable for genome wide association studies, so this may present a possible future application for duckweed root anatomical phenotyping studies. As there are a small number of traits, anatomical diversity between accessions of the same species (as seen within the small of *S. polyrhiza* accessions surveyed), this may be a powerful tool to understand genetic control of trait loss.

However potential drawbacks to this could be the throughput of the sectioning methods available. Though facilitating a throughput descriptive overview of root anatomy with a sufficient *n* for comparative analysis, the methods presented may be too low throughput for genomic analysis. At its fastest, it takes approximately 20 minutes for sample preparation, embedding and mounting, 3-5 minutes for sectioning, and 1-5 minutes for imaging depending on sample quality and resolution. While parts of these processes can be handled in batch, sufficiently high

repetitions on a large enough pool of plants for GWAS may be infeasible. Additionally, µCT scanning's high associated cost and limited availability may also limit its potential ability for applications in this field, and it may remain better suited to smaller studies of harder to measure features.

Furthermore, the analysis of root anatomy showed that even within the most ancestral duckweed genus roots, vasculature had already become reduced to an apparent minimum that was not significantly altered in either of the more recently diverged genera. While there was still a significant reduction in cortical traits, duckweed no longer possessing a spectrum of root vascular traits may limit its applicability to research in this area.

5.3 Novel approaches to anatomical phenotyping

5.3.1 LAT methods

The laser ablation tomography pipelines developed for different tissue types presented in Chapter 3 worked well in the use cases presented, and it seemed highly possible to develop LAT based anatomical imaging solutions for the majority of tissues. With the fitted lenses there is an upper focal area limit of 16 mm by 12 mm, and there are associated tradeoffs between field of view and magnification if this were to be increased. While this is true of all microscopy systems, LAT being a destructive process limits the ability to reimage or effectively tile scan a sample at the same point, unlike other techniques.

Sample preparation methods aside, the larger a sample is, the more challenging it is to cut or ablate the whole sample with optimized lighting for the focal area of the camera, without causing damage to the remainder of the sample. This was workable in the leaf samples as they are only particularly large in one dimension, but with stems or exceptionally large roots it was harder to have uniform ablation and image quality across the whole of the sample.

With consistent sample quality and size, LAT imaging is a very high throughput method of sectioning and imaging, especially in acquisition of 3D or image sequences. With the protocols developed, all that is required is manually loading a sample into the scanner with correct positioning and running the recipe for imaging. With fast handling, this can bring the time taken for a sample to be scanned to under a minute, though in practicality this may be quite different. Field grown samples, and those grown in sand for the maize and gamagrass experiment often contained soil and sand particles that were stuck to the root. An unexpected drawback in LAT imaging compared to other methods was that it handled these soil artifacts very poorly. The higher thermal capacity of soil and sand particulates than plant tissue caused any tissue in contact with this to burn (and occasionally ignite), during ablation. Washing samples thoroughly during harvest would be advisable, as once dry samples become very fragile, though anatomical sampling can be overly time consuming without this step even. A possible improvement to the pipeline may be the implementation of a washing or cleaning step prior to dehydration if this can be done while samples are in their holders.

A major advantage of LAT to the sectioning techniques presented in Chapter 2 (in addition to the discussed benefit of throughput and eliminating the need for staining), is that the samples can easily be cut. The field grown millet roots were extremely tough, and very difficult to section without causing significant mechanical damage, and the vibratome was frequently unable to cut the root before pushing it out of the agarose it was embedded in.

While the LAT unit in its current configuration does have a brightfield illumination system, due to the large working distance of the lenses used, the images acquired using are often of much lower clarity than those using autofluorescence. This limits the ability of the system to capture images well of specimens that do not auto-fluoresce reliably. A potential improvement to the system would be to test

alternative illumination systems, tunable in hue and temperature to complement the sample requirements, or to focus the light through a lens to reduce the depth of sample illuminated.

5.3.2 AI image analysis

Developing an automated deep learned artificially intelligent image analysis pipeline was essential for the completion of goals set out in Chapter 4. For the speed of image acquisition possible from LAT scanning, and if 3D or multiple images were to be analysed per sample, manual measurement would not be possible beyond an extremely limited set of traits and sample numbers.

There was a significant time cost involved with generating the material required to develop ROOTSCAN pipeline. Approximately 220 training set images were segmented and annotated, which at a time cost of 120 minutes an image, gives a total time demand of 26400 minutes. With the approximately 8000 total sample images intended to be run using the AI, this gives a time cost of 3.3 minutes of ROOTSCAN development time per final measured image. As a comparative example, the fastest trait to measure manually was metaxylem (Area, number, shape parameters), which could be done in ~40 seconds an image in FIJI fully manually (not including setup time).

The image pipeline involves capturing 20 images for redundancy to avoid capturing image artifacts. Multiple images per sample could be measured as an assessment of intrasample variability, with no additional person-time cost.

There are improvements that can be made to the ROOTSCAN pipeline. Currently, the user can set the upper and lower pixel bounds for classification of metaxylem based on individual size. It would be beneficial to be able to set these thresholds for multiple cell types. The current training set inputs are the outputs from CellSeT. On occasion, ROOTSCAN correctly segments an image, but annotates it poorly, if the training set input range was expanded to be able to include re-annotations of

previous outputs, this could significantly increase users' ability to retrain a model suited to new input data as well as greatly decrease the time cost of this as opposed to starting from scratch with CellSeT.

Overall, this case study demonstrates the benefit of utilization of deep learning and artificial intelligence in developing pipelines for plant phenotyping. This will likely only become easier and less time consuming as this field continues to advance; though this example does highlight the importance of understanding the time expenditure required to develop these methods, knowing what traits are of interest and how long it would take to measure them using other methods for a given number of samples, and analyzing the cost-benefit of the different approaches.

5.3.3 Maize and gamagrass and the microbiome on the LAT and in root anatomy

Maize root anatomy has been well studied, especially on the LAT, though this investigation of anatomical response to the microbiome is highly novel. It is unsurprising that maize root anatomy is affected by water stress given the wealth of literature on the subject, though it is interesting that within a water treatment group the microbiome is able to affect root anatomical traits. From this data it is unclear what the mechanism behind this is, whether these microbiomes affect root signaling in a way that affects anatomy, or if these communities are affecting water or nutrient uptake by the root directly and thus the plant is altering its morphology in response to this increased uptake, and both may occur.

Furthermore, the investigation of gamagrass anatomy under these biotic and abiotic treatments largely showed a very low level of plasticity. It may be that gamagrass roots have very low plasticity compared to maize and the other plants surveyed, or that they are already so well adapted to water deficit, this stress is insufficient to trigger an anatomical response. A contributing factor to this may

also be that the gamagrass samples had a very high proportion of root cortical aerenchyma, making up the significant majority of the cortex. This made them easy to cut with the LAT but makes the cortex difficult to quantify as it is occasionally unclear if cells are lysed or not.

5.3.4 *Brachypodium* root anatomy

The methods developed were suitable for imaging and analysis of *Brachypodium* root anatomy and were used to show that *BdPIN1a* mutants had a significantly altered root anatomy to the wild type and were also anatomically significantly more susceptible to the effects of water stress than the wild type. *Brachypodium* roots were in general, the smallest out of all surveyed, and are probably close to the minimum size that are suitable for LAT scanning before the requirements for sample preparation, alignment, and adjustment of imaging settings to account for system vibration, makes LAT lower throughput than other methods (Atkinson and Wells, 2017). As an emerging model for cereal genetics, *Brachypodium* may also work well as a model for understanding the function and genetic control of anatomical traits

5.4 The anatomical basis of drought tolerance in pearl millet

This field study has been one of the largest and most thorough investigations conducted on drought tolerance in pearl millet to date. The work presented by Chapter 4 of this thesis comprises a relatively small aspect of what may come from an extremely large dataset. That said, there are still meaningful findings that can stand alone as well as support future work.

5.4.1 Discussion of field trials

There are many benefits to field trials compared to glasshouse experiments when investigating crops in particular (Birch et al., 2007; Poorter et al., 2016). Working directly with the crop of interest in the environment where it is grown means

findings may have a higher degree of applicability to real world environments. With the population of lines grown in this study, where many of the lines used are grown commercially or by smallholders, any increased understanding of their physiology or drought tolerance can have immediate benefit.

However, environmental and spatial effects are hard to control for. It was clear in the field trials that water stress effects were not uniform and that there were significant field effects at play. Though these were attempted to be accounted for by spatial correction, this is imperfect, and there were additional biotic and pest factors that may have had further confounding effects that are more difficult to correct for than the broad spatial trends such as field hydrology.

Additionally, much was learned and improved from year to year. While beneficial in some regards, this did cause issues of consistency and meant that each year has to be treated separately. Drought stress was imposed at different points relative to sowing each year (to account for environmental conditions), and field boundaries were shifted each year to avoid previously identified problem areas. Most significantly, the anatomical sampling method was slightly changed (2 cm further towards stem base) between years 2 and 3 to improve anatomical consistency within samples. These factors may all have different or confounding effects on the comparability of the results from one year to the next but were considered necessary.

Root architectural phenotyping methods were also altered over the years, as only after a field trial were issues with the pipeline identified. This resulted in a well optimized final method, but with a smaller pool of architectural measurements than was intended.

5.4.2 Anatomical traits in pearl millet

The work of Chapter 4 shows that pearl millet root and leaf anatomy is significantly altered in response to water stress. In the panel investigated there was a significant range of anatomical diversity present in well-watered and water stressed roots, as well as in the level of plasticity in response to water stress. A negative correlation was found between cortical sclerenchyma area and maturity time, and a highly significant SNP was identified through GWAS to be associated with the change in sclerenchyma area under drought. Aerenchyma area was also found to relate to several agronomic traits, including grain weight and biomass production, and GWAS analysis identified several SNPs that were significantly associated with aerenchyma area. Both of these anatomical traits have been shown to be linked to abiotic stress tolerance in maize, adding to their meriting future work (Zhu et al., 2010; Schneider et al., 2021).

Many of the root anatomical traits observed were significantly affected by water stress in a large number of lines, this was the case for metaxylem size and number which would significantly alter the theoretical hydraulic capacity of these lines in response to drought. Proving definitively whether this is an adaptive response to manage the plants utilization of water, or a result of limited resources to support growth is challenging. This sampling method also overlooks the incidence of totally arrested growth of the sampled whorl, as this was observed to be reasonably frequent in the drought stressed plants. Decoupling these size related traits from simple allometric scaling of the plant in response to limited resources may further the validate the “plasticity” of these vascular traits, but the factors that determine

a plants size are myriad and therefore hard to control for in experimentation and analysis as many of physiological traits will reciprocally affect one another.

The method of analysis of these anatomical traits was well suited to this use case. To obtain anatomical images of the required number of roots with the mechanical properties of these samples using other methods would present many challenges. The preparatory steps for microtome sectioning would be too time consuming and low throughput and testing showed they worked poorly on our samples, vibratome sectioning resulted in torn, fractured, or uncut roots due to the hardness of the sample, as did hand sectioning. A potentially workable alternative method may have been µCT scanning, by taking short (5-10 mm) sections of the root, and critically point drying, the root portions could be stacked, and batch scanned on microCT. This would provide 3D data for each sample in a higher Z resolution than possible with LAT, and 3D analysis methods could be more readily utilized than with LAT images. This would have a greatly reduced throughput compared to an experienced LAT user, but could be more readily automated, would not need constant attention, and may overcome many of the challenging aspects of optimizing the LAT images for each sample during scanning. If considering the benefits of the system in terms of image quality and information available from the images captured there are more elements to consider. This LAT system is far from the highest resolution option available for anatomical imaging, and unlike electron microscopy, even at the highest magnification, subcellular features are scarcely visible. It has the same drawback as other fluorescence microscopy techniques, where the accuracy of measurement is hampered by the point spread function, making fluorescent objects appear larger than they are depending on the settings applied to the camera sensor used. Unlike confocal microscopy, different lasers

cannot be employed to differentially excite materials, and the sensor cannot be tuned to the emission range of different wavelengths. Despite this, composition information can be gained from the level of fluorescence of the different materials, and the contrast between tissue types where the difference in cell wall structure is understood. This gives LAT the ability to clearly show difference in secondary thickening levels within a root section image without the need for any additional staining or sample preparation beyond what is required to make samples ready for LAT scanning.

A significant limitation of any 2D scanning approach is the ability to obtain a truly representative single image. Even within a <1mm scanning range there can be major variation in presence or absence of aerenchyma or sclerenchyma, appearance of size of vascular cells, and root diameter. Hypothetically, this could be overcome by a perfectly consistent sampling approach, capturing a single image a fixed distance of root away from the stem combined with a sufficiently large number of biological replicates, however in practice this was not possible with the variation in samples received the occasionally inconsistent image quality from the LAT, and the limited number of replicates possible to harvest.

5.4.3 Future work

This pearl millet work is ongoing and will benefit from genetic analysis of year three data. Derived anatomical traits will be added to this, such as ratios between tissues and relative sizes in order to attempt to distinguish between composition and simple allometric affects. The lines used for leaf anatomical phenotyping were selected based on an initial screen for water use efficiency. Including water use efficiency data as well as the leaf photosynthetic, stomatal, and transpiration data currently being gathered would be of great value and may produce further insight into how anatomy affects these areas.

A further panel of lines, created from an introgression of contrasting for metaxylem size will be phenotyped for transpiration efficiency and metaxylem size with the aim of further uncovering this relationship, and facilitating more precise GWAS studies to identify candidate SNPs responsible for this key trait. This will be done under more controlled conditions, in large pot experiments in a glasshouse, to reduce the uncontrolled environmental variability.

As discussed, there are trade offs in the range of root classes sampled, and their suitability for high throughput anatomical analysis techniques. I feel the approaches used are part of necessary compromises to meet and progress past the challenges of large field trials, especially to use and develop multinational phenotyping approaches. I think the choice of whorl four is suitable, as it was seen to be developing during the period of drought treatment, and as a later developing whorl, the literature supports that it would have a major role in supporting the grain filling growth phase. I would like to have validated this independently as part of this study to better resolve the function of each root class. I think this could be done with a time course of destructive sampling during the root system development, restricting water availability to specific whorls if possible, or utilizing isotope tracing and applying these to specific root classes. Ultimately the reliance on specific whorls will most likely vary significantly across the diversity population, and I would expect this to be different for early or late flowering, and tillering or non-tillering varieties, however I feel establishing a baseline for this would be fundamentally beneficial. With an option to continue this work in a hypothetical expansion or extension of the project, I would like to see an additional year of field data, repeated with the methods that were used for in year three as much as possible, as the methodology for year three introduced several improvements to year two, but meant they were done differently. In this I would like to sample stem and leaf tissue for anatomical analysis from all plants, focusing on xylem

measurement, with the aim of GWAS being employed to find candidate genes that regulate xylem area and plasticity on a whole plant and organ specific level, to better understand what physiological factors contribute to water stress tolerance and water use efficiency.

The organogenesis, architecture, and vascular patterning of adventitious roots in response to the environment is the result of a complex set of traits that are of great importance to plant growth and yield. The mechanism for perception of environmental conditions by the plant with regard to adventitious root production, and whether this is perceived by the extant root system or stem, the mechanism of carriage of this signal, and mechanism of action to this signal is not well resolved, and I feel this would be an interesting and useful area for further investigation.

The analysis of the large number of root anatomical traits would not have been possible in the time frame without the use of AI to increase throughput, though it would still be possible to further improve the quality of this system by increasing the size of the training set, including more diverse images, or training for additional features. These could include cell end wall indications, lateral roots and lateral root primordia, lysed cells as seen in around aerenchyma, and root hairs. This would improve the reliability of the software by reducing incorrect annotations, as well as the number of traits that it could measure, and open the door for application in 3D image stack processing. The LAT method itself could be further revised or improved to increase its utility in this project. Additional excitation lasers (similar to as employed in confocal microscopy) could be fitted to the sample illumination system, and a multispectral or hyperspectral camera could be used in addition or in place of the current unit. These alterations could provide useful additional data, but would come at a level of throughput cost, both in imaging as well as processing and analysis time. With these considerations, I believe that for the use case of this project, the current set up and analysis pipeline is well optimized and uses the best methodological approach available.

5.5 Conclusions

This thesis has met all of its stated initial aims in full. Several novel techniques have been developed in order to investigate anatomical traits and how they relate to a plants relationship with water, and investigations of this relationship have been conducted.

The investigation of duckweed anatomy revealed that there has been a dramatic loss of anatomical traits in the duckweed root, and especially within the vasculature. This has been supported by an analysis of root function which showed that duckweeds roots have lost the majority of their ancestral function, and are well on their way to vestigiality if not already vestigial (Ware et al., 2023). During this investigation many methods of duckweed phenotyping were developed and optimized, and the μCT work was able to be published as the first investigation of aquatic plants using this technique (Jones et al., 2021).

The work developing laser ablation tomography systems and pipelines has produced methods suitable for a greater range of species and tissue types than have previously been used with LAT. This includes the development of an automated image analysis pipeline that will greatly improve the throughput of future LAT work and root image analysis bases experiments and surveys. The LAT methods have been validated through application to investigation of root anatomy in four species and their responses to water stress.

An extensive investigation of water stress response and tolerance in pearl millet was carried out. This included several years of field trials, growing large panels of genotyped pearl millet lines under well-watered and water stress conditions. These were extensively phenotyped for anatomical, physiological, and agronomic traits, using the developed methods presented in Chapter 3. Analysis of this data showed that there were strong relationships between anatomical traits, physiological

traits, and important agronomic characteristics. Genomic analysis has identified QTLs associated with relevant anatomical traits, priming future research in this area.

In conclusion the work presented in this thesis demonstrates the significance of anatomical analysis in enhancing understanding of organ function and adaptation, especially with regard to plants relationship with water.

Publications from this thesis

Jones DH, Atkinson BS, Ware A, Sturrock CJ, Bishopp A and Wells DM (2021) Preparation, Scanning and Analysis of Duckweed Using X-Ray Computed Microtomography. Front. Plant Sci. 11:617830. doi: 10.3389/fpls.2020.617830

Ware A, **Jones DH (Joint first author)**, Flis P, Chrysanthou E, Smith KE, Kümpers BMC, Yant L, Atkinson JA, Wells DM, Bhosale R, Bishopp A, Loss of ancestral function in duckweed roots is accompanied by progressive anatomical reduction and a re-distribution of nutrient transporters. Current Biology. doi: 10.1016/j.cub.2023.03.025

References

Acosta, K., Appenroth, K. J., Borisjuk, L., Edelman, M., Heinig, U., Jansen, M. A. K., et al. (2021). Return of the Lemnaceae: duckweed as a model plant system in the genomics and postgenomics era. *The Plant Cell* 33, 3207–3234. doi: 10.1093/plcell/koab189.

Akapo, A. A.-R., Omidiji, S. O., and Otitoloju, A. A. (2011). Morphological and anatomical effects of crude oil on Pistia stratiotes. *Environmentalist* 31, 288–298. doi: 10.1007/s10669-011-9333-x.

An, D., Zhou, Y., Li, C., Xiao, Q., Wang, T., Zhang, Y., et al. (2019). Plant evolution and environmental adaptation unveiled by long-read whole-genome sequencing of Spirodela. *Proceedings of the National Academy of Sciences* 116, 18893–18899. doi: 10.1073/pnas.1910401116.

Atkinson, J. A., Pound, M. P., Bennett, M. J., and Wells, D. M. (2019). Uncovering the hidden half of plants using new advances in root phenotyping. *Current Opinion in Biotechnology* 55, 1–8. doi: 10.1016/j.copbio.2018.06.002.

Atkinson, J. A., and Wells, D. M. (2017). An Updated Protocol for High Throughput Plant Tissue Sectioning. *Frontiers in Plant Science* 8. Available at: https://www.frontiersin.org/article/10.3389/fpls.2017.01721 [Accessed January 25, 2022].

Awika, J. M. (2011). “Major Cereal Grains Production and Use around the World,” in *Advances in Cereal Science: Implications to Food Processing and Health Promotion* ACS Symposium Series. (American Chemical Society), 1–13. doi: 10.1021/bk-2011-1089.ch001.

Baillie, A. L., and Fleming, A. J. (2020). The developmental relationship between stomata and mesophyll airspace. *New Phytologist* 225, 1120–1126. doi: 10.1111/nph.16341.

Basu, S., Kumari, S., Kumar, A., Shahid, R., Kumar, S., and Kumar, G. (2021). Nitro-oxidative stress induces the formation of roots' cortical aerenchyma in rice under osmotic stress. *Physiologia Plantarum* 172, 963–975. doi: 10.1111/ppl.13415.

Bawa, G., Liu, Z., Wu, R., Zhou, Y., Liu, H., Sun, S., et al. (2022). PIN1 regulates epidermal cells development under drought and salt stress using single-cell analysis. *Frontiers in Plant Science* 13. Available at: https://www.frontiersin.org/articles/10.3389/fpls.2022.1043204 [Accessed March 24, 2023].

Birch, A. N. E., Griffiths, B. S., Caul, S., Thompson, J., Heckmann, L. H., Krogh, P. H., et al. (2007). The role of laboratory, glasshouse and field scale experiments in understanding the interactions between genetically modified crops and soil ecosystems: A review of the ECOGEN project. *Pedobiologia* 51, 251–260. doi: 10.1016/j.pedobi.2007.04.008.

Blatt, M. R., Chaumont, F., and Farquhar, G. (2014). Focus on Water. *Plant Physiology* 164, 1553–1555. doi: 10.1104/pp.114.900484.

Borrell, A. K., Wong, A. C. S., George-Jaeggli, B., van Oosterom, E. J., Mace, E. S., Godwin, I. D., et al. (2022). Genetic modification of PIN genes induces causal mechanisms of stay-green drought adaptation phenotype. *Journal of Experimental Botany* 73, 6711–6726. doi: 10.1093/jxb/erac336.

Bray, A. L., and Topp, C. N. (2018). The Quantitative Genetic Control of Root Architecture in Maize. *Plant Cell Physiol* 59, 1919–1930. doi: 10.1093/pcp/pcy141.

Brück, H., Piro, B., Sattelmacher, B., and Payne, W. A. (2003). Spatial distribution of roots of pearl millet on sandy soils of Niger. *Plant and Soil* 256, 149–159. doi: 10.1023/A:1026246728095.

Burridge, J. D., Grondin, A., and Vadez, V. (2022). Optimizing Crop Water Use for Drought and Climate Change Adaptation Requires a Multi-Scale Approach. *Frontiers in Plant Science* 13. Available at: https://www.frontiersin.org/articles/10.3389/fpls.2022.824720 [Accessed December 15, 2022].

Burton, A. L., Williams, M., Lynch, J. P., and Brown, K. M. (2012). RootScan: Software for high-throughput analysis of root anatomical traits. *Plant Soil* 357, 189–203. doi: 10.1007/s11104-012-1138-2.

Cantó, C. D. la F., Diouf, M. N., Ndour, P. M. S., Debieu, M., Grondin, A., Passot, S., et al. (2021). Genetic control of rhizosheath formation in pearl millet. 2021.11.02.466908. doi: 10.1101/2021.11.02.466908.

Carland, F. M., Berg, B. L., FitzGerald, J. N., Jinamornphongs, S., Nelson, T., and Keith, B. (1999). Genetic regulation of vascular tissue patterning in Arabidopsis. *Plant Cell* 11, 2123–2137.

Chen, Z., Sun, J., Li, D., Li, P., He, K., Ali, F., et al. (2022). Plasticity of root anatomy during domestication of a maize-teosinte derived population. *Journal of Experimental Botany* 73, 139–153. doi: 10.1093/jxb/erab406.

Chimungu, J. G., Brown, K. M., and Lynch, J. P. (2014a). Large Root Cortical Cell Size Improves Drought Tolerance in Maize. *Plant Physiology* 166, 2166–2178. doi: 10.1104/pp.114.250449.

Chimungu, J. G., Brown, K. M., and Lynch, J. P. (2014b). Reduced Root Cortical Cell File Number Improves Drought Tolerance in Maize. *Plant Physiology* 166, 1943–1955. doi: 10.1104/pp.114.249037.

Chimungu, J. G., Loades, K. W., and Lynch, J. P. (2015a). Root anatomical phenes predict root penetration ability and biomechanical properties in maize (Zea Mays). *J. Exp. Bot.* 66, 3151–3162. doi: 10.1093/jxb/erv121.

Chimungu, J. G., Maliro, M. F. A., Nalivata, P. C., Kanyama-Phiri, G., Brown, K. M., and Lynch, J. P. (2015b). Utility of root cortical aerenchyma under water limited conditions in tropical maize (Zea mays L.). *Field Crops Research* 171, 86–98. doi: 10.1016/j.fcr.2014.10.009.

Clark, L. H., and Harris, W. H. (1981). Observations on the Root Anatomy of Rice (Oryza sativa L.). *American Journal of Botany* 68, 154–161. doi: 10.2307/2442846.

Clark, R. B., Alberts, E. E., Zobel, R. W., Sinclair, T. R., Miller, M. S., Kemper, W. D., et al. (1998). Eastern gamagrass (Tripsacum dactyloides) root penetration into and chemical properties of claypan soils. *Plant and Soil* 200, 33–45.

Colombi, T., Chakrawal, A., and Herrmann, A. M. (2022). Carbon supply–consumption balance in plant roots: effects of carbon use efficiency and root anatomical plasticity. *New Phytologist* 233, 1542–1547. doi: 10.1111/nph.17598.

Correa, J., Postma, J. A., Watt, M., and Wojciechowski, T. (2019). Soil compaction and the architectural plasticity of root systems. *Journal of Experimental Botany* 70, 6019–6034. doi: 10.1093/jxb/erz383.

Costa, C., Schurr, U., Loreto, F., Menesatti, P., and Carpentier, S. (2019). Plant Phenotyping Research Trends, a Science Mapping Approach. *Frontiers in Plant Science* 9. Available at: https://www.frontiersin.org/articles/10.3389/fpls.2018.01933 [Accessed March 23, 2023].

Crang, R., Lyons-Sobaski, S., and Wise, R. (2018). “Periderm,” in *Plant Anatomy: A Concept-Based Approach to the Structure of Seed Plants*, eds. R. Crang, S. Lyons-Sobaski, and R. Wise (Cham: Springer International Publishing), 553–575. doi: 10.1007/978-3-319-77315-5_16.

de la Fuente, C., Grondin, A., Sine, B., Debieu, M., Belin, C., Hajjarpoor, A., et al. (2023). Glutaredoxin regulation of primary root growth confers early drought stress tolerance in pearl millet. *bioRxiv*, 2023.02.02.526762. doi: 10.1101/2023.02.02.526762.

de la Fuente Cantó, C., Diouf, M. N., Ndour, P. M. S., Debieu, M., Grondin, A., Passot, S., et al. (2022). Genetic control of rhizosheath formation in pearl millet. *Sci Rep* 12, 9205. doi: 10.1038/s41598-022-13234-w.

De Rybel, B., Adibi, M., Breda, A. S., Wendrich, J. R., Smit, M. E., Novák, O., et al. (2014). Integration of growth and patterning during vascular tissue formation in Arabidopsis. *Science* 345, 1255215. doi: 10.1126/science.1255215.

de Wet, J. M. J., and Harlan, J. R. (1974). TRIPSACUM-MAIZE INTERACTION: A NOVEL CYTOGENETIC SYSTEM. *Genetics* 78, 493–502. doi: 10.1093/genetics/78.1.493.

Dembitzer, B. (2018). *The Famine Next Door: Africa Is Burning, the North Is Watching*. Ethical Events Limited.

Diack, O., Kanfany, G., Gueye, M. C., Sy, O., Fofana, A., Tall, H., et al. (2020). GWAS unveils features between early- and late-flowering pearl millets. *BMC Genomics* 21, 777. doi: 10.1186/s12864-020-07198-2.

Draper, J., Mur, L. A. J., Jenkins, G., Ghosh-Biswas, G. C., Bablak, P., Hasterok, R., et al. (2001). Brachypodium distachyon. A New Model System for Functional Genomics in Grasses. *Plant Physiology* 127, 1539.

Dunn, J., Hunt, L., Afsharinafar, M., Meselmani, M. A., Mitchell, A., Howells, R., et al. (2019). Reduced stomatal density in bread wheat leads to increased water-use efficiency. *Journal of Experimental Botany* 70, 4737–4748. doi: 10.1093/jxb/erz248.

Evans, D. E. (2004). Aerenchyma formation. *New Phytologist* 161, 35–49. doi: 10.1046/j.1469-8137.2003.00907.x.

FAOSTAT (n.d.). Available at: https://www.fao.org/faostat/en/#data/QCL [Accessed March 25, 2023].

Fasoula, D. A., Ioannides, I. M., and Omirou, M. (2020). Phenotyping and Plant Breeding: Overcoming the Barriers. *Frontiers in Plant Science* 10. Available at: https://www.frontiersin.org/articles/10.3389/fpls.2019.01713 [Accessed March 23, 2023].

Fekete, B. M. (2013). "5.02 - State of the World's Water Resources," in *Climate Vulnerability*, ed. R. A. Pielke (Oxford: Academic Press), 11–23. doi: 10.1016/B978-0-12-384703-4.00506-2.

Fonta, J. E., Giri, J., Vejchasarn, P., Lynch, J. P., and Brown, K. M. (2022). Spatiotemporal responses of rice root architecture and anatomy to drought. *Plant Soil* 479, 443–464. doi: 10.1007/s11104-022-05527-w.

Gage, J. L., Jarquin, D., Romay, C., Lorenz, A., Buckler, E. S., Kaeppler, S., et al. (2017). The effect of artificial selection on phenotypic plasticity in maize. *Nat Commun* 8, 1348. doi: 10.1038/s41467-017-01450-2.

Galmés, J., Ochogavía, J. M., Gago, J., Roldán, E. J., Cifre, J., and Conesa, M. À. (2013). Leaf responses to drought stress in Mediterranean accessions of Solanum

lycopersicum: anatomical adaptations in relation to gas exchange parameters. *Plant, Cell & Environment* 36, 920–935. doi: 10.1111/pce.12022.

Gamagrass : USDA ARS (n.d.). Available at: https://www.ars.usda.gov/northeast-area/beltsville-md-barc/beltsville-agricultural-research-center/sustainable-agricultural-systems-laboratory/docs/gamagrass/ [Accessed March 27, 2023].

Genotypic variation and nitrogen stress effects on root anatomy in maize are node specific | Journal of Experimental Botany | Oxford Academic (n.d.). Available at: https://academic.oup.com/jxb/article/70/19/5311/5522258 [Accessed December 8, 2022].

Gilker, R. E., Weil, R. R., Krizek, D. T., and Momen, B. (2002). Eastern Gamagrass Root Penetration in Adverse Subsoil Conditions. *Soil Science Society of America Journal* 66, 931–938. doi: 10.2136/sssaj2002.9310.

Grew, N., Grew, N., Rawlins, W., and Britain), R. S. (Great (1682). *The anatomy of plants :by Nehemiah Grew ...* [London]: Printed by W. Rawlins, for the author doi: 10.5962/bhl.title.4.

Haaland, R. (2011). Crops and Culture: Dispersal of African Millets to the Indian Subcontinent and its Cultural Consequences. *Dhaulagiri Journal of Sociology and Anthropology* 5, 1–30. doi: 10.3126/dsaj.v5i0.6354.

Hall, B., and Lanba, A. (2019). Three-dimensional analysis of biological systems via a novel laser ablation technique. *Journal of Laser Applications* 31, 022602. doi: 10.2351/1.5096089.

Hasterok, R., Catalan, P., Hazen, S. P., Roulin, A. C., Vogel, J. P., Wang, K., et al. (2022). Brachypodium: 20 years as a grass biology model system; the way forward? *Trends in Plant Science* 27, 1002–1016. doi: 10.1016/j.tplants.2022.04.008.

Hazman, M., and Brown, K. M. (2018). Progressive drought alters architectural and anatomical traits of rice roots. *Rice* 11, 62. doi: 10.1186/s12284-018-0252-z.

He, Q., Hsueh, M., Zhang, G., Joy, D. C., and Leapman, R. D. (2018). Biological serial block face scanning electron microscopy at improved z-resolution based on Monte Carlo model. *Sci Rep* 8, 12985. doi: 10.1038/s41598-018-31231-w.

Hegelmaier, F. (1868). *Die Lemnaceen: eine monographische Untersuchung*. Engelmann.

Heymans, A., Couvreur, V., and Lobet, G. (2021). Combining cross-section images and modeling tools to create high-resolution root system hydraulic atlases in Zea mays. *Plant Direct* 5, e00290. doi: 10.1002/pld3.334.

Hillman, W. S. (1961). The Lemnaceae, or Duckweeds: A Review of the Descriptive and Experimental Literature. *Botanical Review* 27, 221–287.

Hu, Z., Mbacké, B., Perumal, R., Guèye, M. C., Sy, O., Bouchet, S., et al. (2015). Population genomics of pearl millet (Pennisetum glaucum (L.) R. Br.): Comparative analysis of global accessions and Senegalese landraces. *BMC Genomics* 16, 1048. doi: 10.1186/s12864-015-2255-0.

Huang, P., Shyu, C., Coelho, C. P., Cao, Y., and Brutnell, T. P. (2016). Setaria viridis as a Model System to Advance Millet Genetics and Genomics. *Frontiers in Plant Science* 7. Available at: https://www.frontiersin.org/articles/10.3389/fpls.2016.01781 [Accessed March 23, 2023].

Ii, G. P. W. G. (2012). New grass phylogeny resolves deep evolutionary relationships and discovers C4 origins. *New Phytologist* 193, 304–312. doi: 10.1111/j.1469-8137.2011.03972.x.

Jones, D. H., Atkinson, B. S., Ware, A., Sturrock, C. J., Bishopp, A., and Wells, D. M. (2021). Preparation, Scanning and Analysis of Duckweed Using X-Ray Computed Microtomography. *Frontiers in Plant Science* 11. Available at: https://www.frontiersin.org/article/10.3389/fpls.2020.617830 [Accessed May 20, 2022].

Jung, J., Lee, S. C., and Choi, H.-K. (2008). Anatomical patterns of aerenchyma in aquatic and wetland plants. *J. Plant Biol.* 51, 428–439. doi: 10.1007/BF03036065.

Kane, E. N. A., Foncéka, D., and Dalton, and T. J. (2022). *Crop Adaptation and Improvement for Drought-Prone Environments*. New Prairie Press Available at: https://kstatelibraries.pressbooks.pub/feed-the-future-innovation/ [Accessed February 7, 2023].

Kellogg, E. A. (2015). Brachypodium distachyon as a Genetic Model System. *Annual Review of Genetics* 49, 1–20. doi: 10.1146/annurev-genet-112414-055135.

Kevin Boyce, C. (2005). "23 - The Evolutionary History of Roots and Leaves," in *Vascular Transport in Plants* Physiological Ecology., eds. N. M. Holbrook and M. A. Zwieniecki (Burlington: Academic Press), 479–499. doi: 10.1016/B978-012088457-5/50025-3.

Kim, I. (2007). Development of the root system inSpirodela polyrhiza (L.) schleiden (Lemnaceae). *J. Plant Biol.* 50, 540–547. doi: 10.1007/BF03030707.

Klein, S. P., Schneider, H. M., Perkins, A. C., Brown, K. M., and Lynch, J. P. (2020). Multiple Integrated Root Phenotypes Are Associated with Improved Drought Tolerance1 [OPEN]. *Plant Physiology* 183, 1011–1025. doi: 10.1104/pp.20.00211.

Kusmec, A., de Leon, N., and Schnable, P. S. (2018). Harnessing Phenotypic Plasticity to Improve Maize Yields. *Frontiers in Plant Science* 9. Available at: https://www.frontiersin.org/articles/10.3389/fpls.2018.01377 [Accessed March 22, 2023].

Laird, R. A., and Barks, P. M. (2018). Skimming the surface: duckweed as a model system in ecology and evolution. *American Journal of Botany* 105, 1962–1966. doi: 10.1002/ajb2.1194.

LANDOLT, E. (1986). *Biosystematic investigations in the family of duckweeds (Lemnaceae), volume 2. The family of Lemnaceae—a monographic study, volume 1*. Geobotanical Institute of the Swiss Federal Institute of Technology, Ruebel Foundation.

Lartaud, M., Perin, C., Courtois, B., Thomas, E., Henry, S., Bettembourg, M., et al. (2015). PHIV-RootCell: a supervised image analysis tool for rice root anatomical parameter quantification. *Frontiers in Plant Science* 5. Available at: https://www.frontiersin.org/article/10.3389/fpls.2014.00790 [Accessed January 25, 2022].

Laser Ablation Tomography 2.0 (n.d.). *Plone site*. Available at: https://plantscience.psu.edu/research/labs/roots/methods/laser-ablation-tomography/laser-ablation-tomography-2-0 [Accessed March 23, 2023].

Lens, F., Gleason, S. M., Bortolami, G., Brodersen, C., Delzon, S., and Jansen, S. (2022). Functional xylem characteristics associated with drought-induced embolism in angiosperms. *New Phytologist* 236, 2019–2036. doi: 10.1111/nph.18447.

Les, D. H., Crawford, D. J., Landolt, E., Gabel, J. D., and Kimball, R. T. (2002). Phylogeny and Systematics of Lemnaceae, the Duckweed Family. *sbot* 27, 221–240. doi: 10.1043/0363-6445-27.2.221.

Li, K., Kamiya, T., and Fujiwara, T. (2015). Differential Roles of PIN1 and PIN2 in Root Meristem Maintenance Under Low-B Conditions in Arabidopsis thaliana. *Plant and Cell Physiology* 56, 1205–1214. doi: 10.1093/pcp/pcv047.

Lipka, A. E., Tian, F., Wang, Q., Peiffer, J., Li, M., Bradbury, P. J., et al. (2012). GAPIT: genome association and prediction integrated tool. *Bioinformatics* 28, 2397–2399. doi: 10.1093/bioinformatics/bts444.

Lucas, P. W., Darvell, B. W., Lee, P. K. D., Yuen, T. D. B., and Choong, M. F. (1995). The Toughness of Plant Cell Walls. *Philosophical Transactions: Biological Sciences* 348, 363–372.

Lynch, J. (1995). Root Architecture and Plant Productivity. *Plant Physiology* 109, 7–13. doi: 10.1104/pp.109.1.7.

Lynch, J. P. (2007). Roots of the Second Green Revolution. *Aust. J. Bot.* 55, 493–512. doi: 10.1071/BT06118.

Lynch, J. P. (2013). Steep, cheap and deep: an ideotype to optimize water and N acquisition by maize root systems. *Ann. Bot.* 112, 347–357. doi: 10.1093/aob/mcs293.

Lynch, J. P. (2022). Harnessing root architecture to address global challenges. *The Plant Journal* 109, 415–431. doi: 10.1111/tpj.15560.

Lynch, J. P., Strock, C. F., Schneider, H. M., Sidhu, J. S., Ajmera, I., Galindo-Castañeda, T., et al. (2021). Root anatomy and soil resource capture. *Plant Soil* 466, 21–63. doi: 10.1007/s11104-021-05010-y.

Mader, A., Langer, M., Knippers, J., and Speck, O. (2020). Learning from plant movements triggered by bulliform cells: the biomimetic cellular actuator. *Journal of The Royal Society Interface* 17, 20200358. doi: 10.1098/rsif.2020.0358.

Maiti, R. K., and Bidinger, F. R. (1981). Growth and Development of the Pearl Millet Plant.

Maiti, R., Satya, P., Rajkumar, D., and Ramaswamy, A. (2012a). Cereals. *Crop plant anatomy*, 44–94. doi: 10.1079/9781780640198.0044.

Maiti, R., Satya, P., Rajkumar, D., and Ramaswamy, A. (2012b). Relevance of anatomical studies in modern crop science. *Crop plant anatomy*, 6–14. doi: 10.1079/9781780640198.0006.

Malpighi, M. (1675). *Anatome plantarum. Cui subjungjungitur appendix, iteratas & auctas ejusdem authoris de ovo incubato observationes continens. Regiae societati, Londini ad scientan naturalem promovendam institutae, dicata*. Londini: J. Martyn doi: 10.5962/bhl.title.20220.

Manning, K., Pelling, R., Higham, T., Schwenniger, J.-L., and Fuller, D. Q. (2011). 4500-Year old domesticated pearl millet (Pennisetum glaucum) from the Tilemsi Valley, Mali: new insights into an alternative cereal domestication pathway. *Journal of Archaeological Science* 38, 312–322. doi: 10.1016/j.jas.2010.09.007.

Mathers, A. W., Hepworth, C., Baillie, A. L., Sloan, J., Jones, H., Lundgren, M., et al. (2018). Investigating the microstructure of plant leaves in 3D with lab-based X-ray computed tomography. *Plant Methods* 14, 99. doi: 10.1186/s13007-018-0367-7.

Matschi, S., Vasquez, M. F., Bourgault, R., Steinbach, P., Chamness, J., Kaczmar, N., et al. (2020). Structure-function analysis of the maize bulliform cell cuticle and its potential role in dehydration and leaf rolling. *Plant Direct* 4, e00282. doi: 10.1002/pld3.282.

McDonough, C., and Rooney, L. (1989). Structural Characteristics of Pennisetum Americanum (Pearl Millet) Using Scanning Electron and Fluorescence Microscopy. *Food Structure* 8. Available at: https://digitalcommons.usu.edu/foodmicrostructure/vol8/iss1/16.

Melaragno, J. E., and Walsh, M. A. (1976). Ultrastructural Features of Developing Sieve Elements in Lemna Minor L.—the Protoplast. *American Journal of Botany* 63, 1145–1157. doi: 10.1002/j.1537-2197.1976.tb13200.x.

Mellor, N., Adibi, M., El-Showk, S., De Rybel, B., King, J., Mähönen, A. P., et al. (2017). Theoretical approaches to understanding root vascular patterning: a consensus between recent models. *Journal of Experimental Botany* 68, 5–16. doi: 10.1093/jxb/erw410.

Mellor, N., Vaughan-Hirsch, J., Kümpers, B. M. C., Help-Rinta-Rahko, H., Miyashima, S., Mähönen, A. P., et al. (2019). A core mechanism for specifying root vascular patterning can replicate the anatomical variation seen in diverse plant species. *Development* 146, dev172411. doi: 10.1242/dev.172411.

Minervini, M., Scharr, H., and Tsaftaris, S. A. (2015). Image Analysis: The New Bottleneck in Plant Phenotyping [Applications Corner]. *IEEE Signal Processing Magazine* 32, 126–131. doi: 10.1109/MSP.2015.2405111.

Molden, D., Vithanage, M., de Fraiture, C., Faures, J. M., Gordon, L., Molle, F., et al. (2011). "4.21 - Water Availability and Its Use in Agriculture," in *Treatise on Water Science*, ed. P. Wilderer (Oxford: Elsevier), 707–732. doi: 10.1016/B978-0-444-53199-5.00108-1.

Muchhal, U. S., Pardo, J. M., and Raghothama, K. G. (1996). Phosphate transporters from the higher plant Arabidopsis thaliana. *Proceedings of the National Academy of Sciences* 93, 10519–10523. doi: 10.1073/pnas.93.19.10519.

Naylor, D., and Coleman-Derr, D. (2018). Drought Stress and Root-Associated Bacterial Communities. *Frontiers in Plant Science* 8. Available at: https://www.frontiersin.org/articles/10.3389/fpls.2017.02223 [Accessed March 27, 2023].

Ndiaye, A., Diallo, A. O., Fall, N. C., Diouf, R. D., Diouf, D., and Kane, N. A. (2022). Transcriptomic analysis of methyl jasmonate treatment reveals gene networks involved in drought tolerance in pearl millet. *Sci Rep* 12, 5158. doi: 10.1038/s41598-022-09152-6.

Neto, I. L. C., Hall, B., Lanba, A., Blosenski, J., and Onyenedum, J. G. (2022). Laser ablation tomography (LATscan) as a new tool for anatomical studies of woody plants. 2022.11.07.515046. doi: 10.1101/2022.11.07.515046.

O'Connor, D. L., Elton, S., Ticchiarelli, F., Hsia, M. M., Vogel, J. P., and Leyser, O. (2017). Cross-species functional diversity within the PIN auxin efflux protein family. *eLife* 6, e31804. doi: 10.7554/eLife.31804.

Omelyanchuk, N. A., Kovrizhnykh, V. V., Oshchepkova, E. A., Pasternak, T., Palme, K., and Mironova, V. V. (2016). A detailed expression map of the PIN1 auxin transporter in Arabidopsis thaliana root. *BMC Plant Biology* 16, 5. doi: 10.1186/s12870-015-0685-0.

Pacheco-Villalobos, D., and Hardtke, C. S. (2012). Natural genetic variation of root system architecture from Arabidopsis to Brachypodium: towards adaptive value. *Philosophical Transactions of the Royal Society B: Biological Sciences* 367, 1552–1558. doi: 10.1098/rstb.2011.0237.

Passot, S., Gnacko, F., Moukouanga, D., Lucas, M., Guyomarc'h, S., Ortega, B. M., et al. (2016). Characterization of Pearl Millet Root Architecture and Anatomy Reveals Three Types of Lateral Roots. *Frontiers in Plant Science* 7. Available at: https://www.frontiersin.org/article/10.3389/fpls.2016.00829 [Accessed February 16, 2022].

Passot, S., Moreno-Ortega, B., Moukouanga, D., Balsera, C., Guyomarc'h, S., Lucas, M., et al. (2018). A New Phenotyping Pipeline Reveals Three Types of Lateral Roots and a Random Branching Pattern in Two Cereals. *Plant Physiology* 177, 896–910. doi: 10.1104/pp.17.01648.

Phong, B. T. (1975). Illumination for computer generated pictures. *Commun. ACM* 18, 311–317. doi: 10.1145/360825.360839.

Pieruschka, R., and Schurr, U. (2019). Plant Phenotyping: Past, Present, and Future. *Plant Phenomics* 2019. doi: 10.34133/2019/7507131.

Poorter, H., Fiorani, F., Pieruschka, R., Wojciechowski, T., van der Putten, W. H., Kleyer, M., et al. (2016). Pampered inside, pestered outside? Differences and similarities between plants growing in controlled conditions and in the field. *New Phytologist* 212, 838–855. doi: 10.1111/nph.14243.

Poudel, M., Mendes, R., Costa, L. A. S., Bueno, C. G., Meng, Y., Folimonova, S. Y., et al. (2021). The Role of Plant-Associated Bacteria, Fungi, and Viruses in Drought Stress Mitigation. *Frontiers in Microbiology* 12. Available at: https://www.frontiersin.org/articles/10.3389/fmicb.2021.743512 [Accessed March 27, 2023].

Pound, M. P., French, A. P., Wells, D. M., Bennett, M. J., and Pridmore, T. P. (2012a). CellSeT: Novel Software to Extract and Analyze Structured Networks of Plant Cells from Confocal Images. *Plant Cell* 24, 1353–1361. doi: 10.1105/tpc.112.096289.

Pound, M. P., French, A. P., Wells, D. M., Bennett, M. J., and Pridmore, T. P. (2012b). CellSeT: Novel Software to Extract and Analyze Structured Networks of Plant Cells from Confocal Images. *The Plant Cell* 24, 1353–1361. doi: 10.1105/tpc.112.096289.

Preibisch, S., Saalfeld, S., and Tomancak, P. (2009). Globally optimal stitching of tiled 3D microscopic image acquisitions. *Bioinformatics* 25, 1463–1465. doi: 10.1093/bioinformatics/btp184.

Prince, S. J., Murphy, M., Mutava, R. N., Durnell, L. A., Valliyodan, B., Shannon, J. G., et al. (2017). Root xylem plasticity to improve water use and yield in water-stressed soybean. *J Exp Bot* 68, 2027–2036. doi: 10.1093/jxb/erw472.

Purushothaman, R., Zaman-Allah, M., Mallikarjuna, N., Pannirselvam, R., Krishnamurthy, L., and Gowda, C. L. L. (2013). Root Anatomical Traits and Their

Possible Contribution to Drought Tolerance in Grain Legumes. *Plant Production Science* 16, 1–8. doi: 10.1626/pps.16.1.

Rebouillat, J., Dievart, A., Verdeil, J. L., Escoute, J., Giese, G., Breitler, J. C., et al. (2009). Molecular Genetics of Rice Root Development. *Rice* 2, 15–34. doi: 10.1007/s12284-008-9016-5.

Saengwilai, P., Nord, E. A., Chimungu, J. G., Brown, K. M., and Lynch, J. P. (2014). Root Cortical Aerenchyma Enhances Nitrogen Acquisition from Low-Nitrogen Soils in Maize. *Plant Physiology* 166, 726–735. doi: 10.1104/pp.114.241711.

Saito, S., Niki, T., and Gladish, D. K. (2020). Evaluation of Metaxylem Vessel Histogenesis and the Occurrence of Vessel Collapse during Early Development in Primary Roots of Zea mays ssp. mexicana: A Result of Premature Programmed Cell Death? *Plants (Basel)* 9, 374. doi: 10.3390/plants9030374.

Sattler, F. T., Pucher, A., Kassari Ango, I., Sy, O., Ahmadou, I., Hash, C. T., et al. (2019). Identification of Combining Ability Patterns for Pearl Millet Hybrid Breeding in West Africa. *Crop Science* 59, 1590–1603. doi: 10.2135/cropsci2018.12.0727.

Satyavathi, C. T., Ambawat, S., Khandelwal, V., and Srivastava, R. K. (2021). Pearl Millet: A Climate-Resilient Nutricereal for Mitigating Hidden Hunger and Provide Nutritional Security. *Frontiers in Plant Science* 12. Available at: https://www.frontiersin.org/article/10.3389/fpls.2021.659938 [Accessed April 20, 2022].

Schäfer, E. D., Ajmera, I., Farcot, E., Owen, M. R., Band, L. R., and Lynch, J. P. (2022). In silico evidence for the utility of parsimonious root phenotypes for improved vegetative growth and carbon sequestration under drought. *Frontiers in Plant Science* 13. Available at:

https://www.frontiersin.org/articles/10.3389/fpls.2022.1010165 [Accessed December 2, 2022].

Schindelin, J., Arganda-Carreras, I., Frise, E., Kaynig, V., Longair, M., Pietzsch, T., et al. (2012). Fiji: an open-source platform for biological-image analysis. *Nat Methods* 9, 676–682. doi: 10.1038/nmeth.2019.

Schneider, H. M., Klein, S. P., Hanlon, M. T., Kaeppler, S., Brown, K. M., and Lynch, J. P. (2020). Genetic control of root anatomical plasticity in maize. *The Plant Genome* 13, e20003. doi: 10.1002/tpg2.20003.

Schneider, H. M., Lor, V. S., Zhang, X., Saengwilai, P., Hanlon, M. T., Klein, S. P., et al. (2023). Transcription factor bHLH121 regulates root cortical aerenchyma formation in maize. *Proceedings of the National Academy of Sciences* 120, e2219668120. doi: 10.1073/pnas.2219668120.

Schneider, H. M., and Lynch, J. P. (2020). Should Root Plasticity Be a Crop Breeding Target? *Frontiers in Plant Science* 11. Available at: https://www.frontiersin.org/articles/10.3389/fpls.2020.00546 [Accessed March 22, 2023].

Schneider, H. M., Strock, C. F., Hanlon, M. T., Vanhees, D. J., Perkins, A. C., Ajmera, I. B., et al. (2021). Multiseriate cortical sclerenchyma enhance root penetration in compacted soils. *Proceedings of the National Academy of Sciences* 118, e2012087118. doi: 10.1073/pnas.2012087118.

Scoffoni, C., Albuquerque, C., Brodersen, C. R., Townes, S. V., John, G. P., Cochard, H., et al. (2017a). Leaf vein xylem conduit diameter influences susceptibility to embolism and hydraulic decline. *New Phytologist* 213, 1076–1092. doi: 10.1111/nph.14256.

Scoffoni, C., Albuquerque, C., Brodersen, C. R., Townes, S. V., John, G. P., Cochard, H., et al. (2017b). Leaf vein xylem conduit diameter influences susceptibility to

embolism and hydraulic decline. *New Phytologist* 213, 1076–1092. doi: 10.1111/nph.14256.

Sehgal, D., Skot, L., Singh, R., Srivastava, R. K., Das, S. P., Taunk, J., et al. (2015). Exploring potential of pearl millet germplasm association panel for association mapping of drought tolerance traits. *PLoS One* 10, e0122165. doi: 10.1371/journal.pone.0122165.

Seleiman, M. F., Al-Suhaibani, N., Ali, N., Akmal, M., Alotaibi, M., Refay, Y., et al. (2021). Drought Stress Impacts on Plants and Different Approaches to Alleviate Its Adverse Effects. *Plants* 10, 259. doi: 10.3390/plants10020259.

Shannon, E. L. (1953). The Production of Root Hairs by Aquatic Plants. *The American Midland Naturalist* 50, 474–479. doi: 10.2307/2422106.

Šidák, Z. (1967). Rectangular Confidence Regions for the Means of Multivariate Normal Distributions. *Journal of the American Statistical Association* 62, 626–633. doi: 10.1080/01621459.1967.10482935.

Sidhu, J. S., Ajmera, I., Arya, S., and Lynch, J. P. (n.d.). RootSlice—A novel functional-structural model for root anatomical phenotypes. *Plant, Cell & Environment* n/a. doi: 10.1111/pce.14552.

Silva, S. A. e, Techio, V. H., de Castro, E. M., de Faria, M. R., and Palmieri, M. J. (2013). Reproductive, Cellular, and Anatomical Alterations in Pistia stratiotes L. Plants Exposed to Cadmium. *Water Air Soil Pollut* 224, 1454. doi: 10.1007/s11270-013-1454-z.

Simpson, M. G. (2019). “10 - Plant Anatomy and Physiology,” in *Plant Systematics (Third Edition)*, ed. M. G. Simpson (Academic Press), 537–566. doi: 10.1016/B978-0-12-812628-8.50010-9.

Song, J., Wang, Y., Pan, Y., Pang, J., Zhang, X., Fan, J., et al. (2019). The influence of nitrogen availability on anatomical and physiological responses of Populus alba × P. glandulosa to drought stress. *BMC Plant Biology* 19, 63. doi: 10.1186/s12870-019-1667-4.

Strock, C. F., Schneider, H. M., Galindo-Castañeda, T., Hall, B. T., Van Gansbeke, B., Mather, D. E., et al. (2019). Laser ablation tomography for visualization of root colonization by edaphic organisms. *Journal of Experimental Botany* 70, 5327–5342. doi: 10.1093/jxb/erz271.

Strock, C. F., Schneider, H. M., and Lynch, J. P. (2022). Anatomics: High-throughput phenotyping of plant anatomy. *Trends in Plant Science* 27, 520–523. doi: 10.1016/j.tplants.2022.02.009.

The William Henry Fox Talbot Catalogue Raisonné (n.d.). Available at: https://talbot.bodleian.ox.ac.uk/search/catalog/artifact-1483 [Accessed March 25, 2023].

Tyree, M. T., Fiscus, E. L., Wullschleger, S. D., and Dixon, M. A. (1986). Detection of Xylem Cavitation in Corn under Field Conditions 1. *Plant Physiology* 82, 597–599. doi: 10.1104/pp.82.2.597.

Uga, Y., Ebana, K., Abe, J., Morita, S., Okuno, K., and Yano, M. (2009). Variation in root morphology and anatomy among accessions of cultivated rice (*Oryza sativa* L.) with different genetic backgrounds. *Breeding Science* 59, 87–93. doi: 10.1270/jsbbs.59.87.

Uga, Y., Okuno, K., and Yano, M. (2008). QTLs underlying natural variation in stele and xylem structures of rice root. *Breeding Science* 58, 7–14. doi: 10.1270/jsbbs.58.7.

Vanhees, D. J., Loades, K. W., Bengough, A. G., Mooney, S. J., and Lynch, J. P. (2020). Root anatomical traits contribute to deeper rooting of maize under compacted

field conditions. *Journal of Experimental Botany* 71, 4243–4257. doi: 10.1093/jxb/eraa165.

Vanhees, D. J., Schneider, H. M., Sidhu, J. S., Loades, K. W., Bengough, A. G., Bennett, M. J., et al. (2022). Soil penetration by maize roots is negatively related to ethylene-induced thickening. *Plant, Cell & Environment* 45, 789–804. doi: 10.1111/pce.14175.

Vejchasarn, P., Lynch, J. P., and Brown, K. M. (2016). Genetic Variability in Phosphorus Responses of Rice Root Phenotypes. *Rice* 9, 29. doi: 10.1186/s12284-016-0102-9.

Wahl, S., Ryser, P., and Edwards, P. J. (2001). Phenotypic Plasticity of Grass Root Anatomy in Response to Light Intensity and Nutrient Supply. *Annals of Botany* 88, 1071–1078. doi: 10.1006/anbo.2001.1551.

Walter, A., Liebisch, F., and Hund, A. (2015). Plant phenotyping: from bean weighing to image analysis. *Plant Methods* 11, 14. doi: 10.1186/s13007-015-0056-8.

Wang, J., and Zhang, Z. (2021). GAPIT Version 3: Boosting Power and Accuracy for Genomic Association and Prediction. *Genomics, Proteomics & Bioinformatics* 19, 629–640. doi: 10.1016/j.gpb.2021.08.005.

Wang, W., Haberer, G., Gundlach, H., Gläßer, C., Nussbaumer, T., Luo, M. C., et al. (2014). The Spirodela polyrhiza genome reveals insights into its neotenous reduction fast growth and aquatic lifestyle. *Nature Communications* 5, 1–13. doi: 10.1038/ncomms4311.

Ware, A., Jones, D. H., Flis, P., Chrysanthou, E., Smith, K. E., Kümpers, B. M. C., et al. (2023). Loss of ancestral function in duckweed roots is accompanied by

progressive anatomical reduction and a re-distribution of nutrient transporters. *Current Biology* 0. doi: 10.1016/j.cub.2023.03.025.

Warner, D. A., and Edwards, G. E. (1988). C4 photosynthesis and leaf anatomy in diploid and autotetraploid Pennisetum americanum (pearl millet). *Plant Science* 56, 85–92. doi: 10.1016/0168-9452(88)90190-2.

Watanabe, Y., Kabuki, T., Kakehashi, T., Kano-Nakata, M., Mitsuya, S., and Yamauchi, A. (2020). Morphological and histological differences among three types of component roots and their differential contribution to water uptake in the rice root system. *Plant Production Science* 23, 191–201. doi: 10.1080/1343943X.2020.1730701.

Water Uptake and Transport in Vascular Plants | Learn Science at Scitable (n.d.). Available at: https://www.nature.com/scitable/knowledge/library/water-uptake-and-transport-in-vascular-plants-103016037/ [Accessed March 23, 2023].

Watt, M., Schneebeli, K., Dong, P., Wilson, I. W., Watt, M., Schneebeli, K., et al. (2009). The shoot and root growth of Brachypodium and its potential as a model for wheat and other cereal crops. *Functional Plant Biol.* 36, 960–969. doi: 10.1071/FP09214.

Xiao, Y., Sloan, J., Hepworth, C., Fradera-Soler, M., Mathers, A., Thorley, R., et al. (2023). Defining the scope for altering rice leaf anatomy to improve photosynthesis: a modelling approach. *New Phytologist* 237, 441–453. doi: 10.1111/nph.18564.

Y, L., J, Z., L, W., Y, S., Y, W., and C, M. (2019). Functional Divergence of PIN1 Paralogous Genes in Rice. *Plant & cell physiology* 60. doi: 10.1093/pcp/pcz159.

Yasrab, R., Atkinson, J. A., Wells, D. M., French, A. P., Pridmore, T. P., and Pound, M. P. (2019). RootNav 2.0: Deep Learning for Automatic Navigation of Complex Plant Root Architectures. *bioRxiv*, 709147. doi: 10.1101/709147.

York, L. M., Galindo-Castañeda, T., Schussler, J. R., and Lynch, J. P. (2015). Evolution of US maize (Zea mays L.) root architectural and anatomical phenes over the past 100 years corresponds to increased tolerance of nitrogen stress. *J Exp Bot* 66, 2347–2358. doi: 10.1093/jxb/erv074.

Yu, P., Gutjahr, C., Li, C., and Hochholdinger, F. (2016). Genetic Control of Lateral Root Formation in Cereals. *Trends in Plant Science* 21, 951–961. doi: 10.1016/j.tplants.2016.07.011.

Zhang, Q., Li, J., Zhang, W., Yan, S., Wang, R., Zhao, J., et al. (2012). The putative auxin efflux carrier OsPIN3t is involved in the drought stress response and drought tolerance. *The Plant Journal* 72, 805–816. doi: 10.1111/j.1365-313X.2012.05121.x.

Zhao, C., Zhang, Y., Du, J., Guo, X., Wen, W., Gu, S., et al. (2019). Crop Phenomics: Current Status and Perspectives. *Front Plant Sci* 10. doi: 10.3389/fpls.2019.00714.

Zhu, J., Brown, K. M., and Lynch, J. P. (2010). Root cortical aerenchyma improves the drought tolerance of maize (Zea mays L.). *Plant, Cell & Environment* 33, 740–749. doi: 10.1111/j.1365-3040.2009.02099.x.

Appendices

Appendix 1 : LAT Imaging resolutions and Image Sizes

Lens	Pixels Per Micron	Microns per Pixel	Micron Image Size Dimension X	Micron Image Size Dimension Y
1X	0.2615395	3.82351423	15661.11429	11470.54269
2X	0.5831	1.714971703	7024.524095	5144.915109
5X	1.4709	0.679855871	2784.689646	2039.567612
10X	3.018	0.331345262	1357.190192	994.0357853
20X	5.9403	0.168341666	689.5274649	505.0249987

Appendix 2: Excerpts from gamagrass and maize grant

Objective 1: Identify soil metagenome features associated with historical exposure to drought

Objective 1 | APPROACH: Broadly, we plan to sequence DNA from soils spanning two steep, naturally-occurring precipitation gradients to identify metagenomic signatures of historical legacies of water limitation. In one of these gradients, we will sample from both consistently-irrigated and never-irrigated environments to aid our inference about the role of water in shaping soil metagenomes. To control for other factors that likely affect the soil microbiota, we will also collect detailed data on chemical and physical soil properties and other environmental parameters.

Acquisition of soil samples: We will use portable, hand-held DNA sequencing equipment (Oxford Nanopore MinION), available from the University of Nottingham (UoN; letter of support—M. Loose), to sequence soil metagenomes at the collection sites. At five points along the Kansas gradient, we will collect soils from pristine (never-cultivated) prairie remnants as well as active grain farms (Figure 3). We will also sample two additional prairies at the far eastern and western ends of the gradient. The Kansas collection sites are already well-established as part of an active, large-scale, collaborative NSF EPSCoR grant (OIA #1656006) that investigates how links between microbiomes of surface water, plant communities, and soil affect ecosystem resilience. This active NSF grant does not involve maize or gamagrass directly, nor does it address our motivating questions about microbial adaptation in free-living vs. host-associated contexts. Rather, it is complementary to our proposed work and will provide important context on the microbiomes of natural and agricultural landscapes across Kansas, including in bulk soils and in other grass species, over four years. As a result, our proposed work and the ongoing NSF project have high potential for synergy of results, interpretation, and future directions. Dr. Wagner will coordinate this effort with her KU colleagues who are personnel on the EPSCoR project (letter of support—J. Bever). From all 26 locations (12 in Cape Verde and 14 in Kansas), five soil samples will be taken for analysis (N=130 total) (Figure 3). The contrast between prairie and farm soils will clarify how agricultural disturbance—including irrigation—has impacted the microbial gene content of Kansas soils.

Objective 2 | RATIONALE AND PRELIMINARY DATA: Due to their short generation times and taxonomic and functional diversity, microbial lineages and communities can adapt rapidly to environmental challenges including drought, with functional consequences for plant hosts [67]. Understanding the mechanisms and dynamics of such microbiome adaptation--both with and without a plant host--is a critical step toward understanding how plant-microbiome interactions may have evolved, and how we might leverage microbiome adaptation to mitigate negative effects of rapid climate change.

Responses of free-living vs. host-associated microbiomes to stress: In Objective 1, we will have identified soil metagenome properties that correlate with the historical severity of water stress. Those data, although taken from bulk soil samples, likely include microbial lineages with some history of living in close association with a host plant. Therefore, we assume that any patterns in those data will reflect outcomes of microbial evolution in both free-living contexts and host-associated contexts, in some unknown combination. Next, in Objective 2, we will experimentally test whether the mechanisms of microbial adaptation to water stress differ in free-living versus host-associated conditions (Figure 5).

Previous work demonstrated that the selective pressures acting on free-living Ensifer bacteria in soil differ from those acting on the same species during colonization of root nodules [20]. During adaptation of a community of 101 Ensifer strains to contrasting environments (plant-free soil and two host genotypes), strain

fitness in soil was only weakly correlated with fitness in planta. Adaptation to each environment involved shifts in allele frequency for different sets of genes. Many advantageous alleles in the plant environment were either deleterious or conditionally neutral in the soil environment [20]. That is, bacterial adaptation to a host-associated environment involved different mechanisms than adaptation of the same species to a free-living environment. Another recent project revealed that changes in community composition due to drought were strongest within plant roots, moderate in the rhizosphere, and weakest in bulk soil [77].

In Objective 2, we aim to test whether similar dynamics exist for free-living vs. host-associated microbes in the context of drought. The complexity of our focal soil communities restricts our ability to analyze fitness at the strain level. However, shotgun metagenome and metatranscriptome sequencing can still tell us the relative frequency and expression levels of different types of genes and functional groups within the community. That is, we can use the select-and-resequence approach to assess metagenome-level mechanisms of adaptation to prolonged drought.

Objective 2 | APPROACH: We will assess how rapid adaptation to drought affects metagenome content and gene expression in both free-living and host-associated soil microbial communities. To do this, we will use an “evolve and resequence” greenhouse experiment, sequencing soil mesocosms both before and after experimental evolution to quantify changes in gene and transcript abundances.

Greenhouse experiment: To characterize microbiome adaptation to drought, we will use six of the Kansas prairie soils from Objective 1–three from the driest sites and three from the wettest sites—to create replicate soil mesocosms that vary in drought legacy (N = 2 drought legacies [dry/wet] x 3 soils x 16 replicates = 96 pots). We will then divide these mesocosms among four conditions in a fully-factorial design: with or without a host, and either water-stressed or well-watered (Figure 5). Thus, this experiment will reveal how adaptation to drought proceeds in both free-living and host-associated soil communities. Half the pots will be planted with seedlings of the native prairie grass T. dactyloides; the rest will remain unplanted. Drought-treated pots will be watered once per 2 weeks to simulate natural cycles of drought and rewetting, which have been shown to substantially alter soil microbiome composition [40]; control pots will be watered every other day. All mesocosms will be allowed to adapt to their watering regimes for 4 months under controlled conditions in the KU greenhouse (letter of support—K. Sadler).

Objective 3. Test how drought-adapted and non-adapted microbiota affect plant phenotype and drought resistance.

Objective 3 | RATIONALE AND PRELIMINARY DATA: Recent findings suggest that soil microbiota is important for plant drought tolerance. Nevertheless, the mechanism of how plant-associated microbes engage with plant

drought responses remains unknown. To understand how microbiome adaptation to drought stress influences plant performance under water-limited conditions, we will conduct a greenhouse experiment using two host plants: Zea mays (maize; a major crop grown in both Kansas and Cape Verde) and Tripsacum dactyloides (eastern gamagrass; a close relative of maize and a native of Kansas tallgrass prairies).

Objective 3 | APPROACH: Broadly, we will use re-inoculation experiments to assay the effects of microbial drought adaptation on host plant phenotype, gene expression, and drought tolerance. We will use microbial communities from the previous objectives as inocula in growth chamber experiments to test the effects of historical drought legacy (Obj. 1) and rapid drought adaptation (Obj. 2) of free-living and host-associated microbial communities on the performance of wild and domesticated grasses.

Growth chamber experiment: To evaluate the relationship between soil microbiome adaptation and plant physiology and drought tolerance, we will grow maize and eastern gamagrass in sterile sand supplemented with drought-adapted or non-adapted microbiota from the experimental evolution mesocosms in Obj. 2 (Figure 5). Sand is an inert substrate with a very low nutrient content, an excellent system to isolate the microbiota effect from other complex edaphic factors present in natural soils. It also enables clean and efficient extraction of root systems for analysis after the experiment.

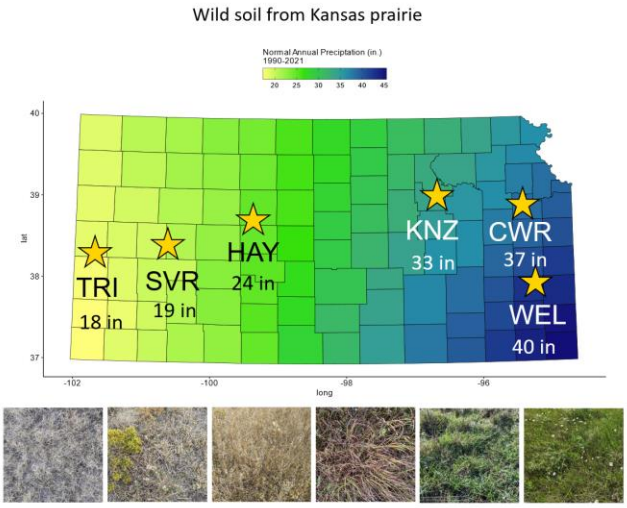
Microbes will be isolated from mesocosm soils using a protocol that we use routinely in our labs consisting of several washes with MES pH 6.0 [83], and then re-inoculated into sand fortified with Hoagland solution [84]. To maintain independence of the experimental replicates from Obj. 2, the microbial component of each mesocosm will be used to inoculate two pots in Obj. 2—one planted with maize (genotype B73 or Mo17), and the other with clones from the T. dactyloides cultivar “Pete” (N = 2 species * 96 soil mesocosms from Obj. 2 = 192 plants). Plants will be grown under standard controlled conditions for one month in the Wagner lab’s growth chambers and exposed to two-week cycles of drought and re-wetting (Figure 6).

Plant physiological and performance measurements: To characterize microbiome effects on host phenotype under drought conditions, we will measure a suite of physiological traits related to water regulation. During the four weeks of growth, we will measure absolute chlorophyll concentration of leaves—a reliable indicator of drought stress [85]—twice weekly using the Wagner lab’s MC-100 chlorophyll meter (Apogee Instruments; Figure 6d). Photosynthetic rates and stomatal conductance will be measured weekly using a LI-6800 portable photosynthesis system borrowed from the Castrillo lab.

After four weeks, we will destructively sample roots and shoots and aliquot the tissues for a variety of physiological and molecular assays. The topmost lateral root will be subsampled, homogenized in liquid nitrogen, divided into two aliquots, and stored at -80C for later RNA and DNA extraction. The second lateral root will also be subsampled and shipped to UoN for measurement of the deposition of lignin and suberin in the root—barriers to water and ionic diffusion—using laser ablation tomography (LAT; Figure 8; letter of support—M. Bennett, UoN Houndsfield facility). Shoots will be dried and weighed for biomass. Root system architecture will be quantified using high-resolution flatbed scanners and the dedicated analysis software IJ_Rhizo [86]. Finally, root biomass will be measured and dried root samples will be shipped to UoN for ionomic measurement using ICP-MS as described in Objective 1.

Appendix 3: Map showing soil sampling sites

Obj 1 – Soil metagenome features associated with drought historical exposure



Appendix 4: Macros for leaf image processing

Whole leaf

```
for (a = 0; a < 161; a++) {
b=""+a+"_1X";
path="C:/Users/stxdj6/Documents/PM_Leaf_All/PM_Leaf_1XStitched1to115/";
c="image_directory=U:/Dylan/PM_Leaf/"+a+"_1X ";
//y="U:/Dylan/PM_Leaf/"+a+"_1X/";
y="C:/Users/stxdj6/Documents/PM_Leaf_All/PM_Leaf/"+a+"_1X";
list = getFileList(y);
z = list.length;
text= "" + z;
print(text);
if (z>1) {
```

```
d="output_file_name=TileConfiguration.txt rgb_order=rgb
channels_for_registration=[Red, Green and Blue] fusion_method=[Linear
Blending] fusion_alpha=1.50 regression_threshold=0.30
max/avg_displacement_threshold=2.50 absolute_displacement_threshold=3.50";

e="image_directory=C:/Users/stxdj6/Documents/PM_Leaf_All/PM_Leaf/"+a+"_1
X ";

//newImage("Blank", "8-bit black", 10, 10, 1);

//f="Blank";

//saveAs("Tiff",e+"Blank");

//selectWindow("Blank.tif");

//close();

run("Stitch Directory with Images (unknown configuration)", e+d);

saveAs("Tiff", path+b);

selectWindow(b+".tif");

close();

run("Close All");

}

else {

open(y);

saveAs("Tiff", path+b);

selectWindow(b+".tif");

close();

run("Close All");

}

}
```

Lamina-Median

```
for (a = 116; a < 161; a++) {

b=""+a+"_10X";

c="open=C:/Users/stxdj6/Documents/PM_Leaf_All/PM_Leaf_10X/"+a+"_10X";

run("Image Sequence...", c);

run("Z Project...", "projection=Median");

run("Enhance Local Contrast (CLAHE)", "blocksize=127 histogram=256 maximum=3 mask=*None* fast_(less_accurate)");

y="U:/Dylan/PM_Leaf/"+a+"_1X/";

path="C:/Users/stxdj6/Documents/PM_Leaf_All/PM_Leaf_10X_median/";

saveAs("Tiff", path+b);

selectWindow(b+".tif");

close();

run("Close All");

}
```

Appendix 5: List of pearl millet lines in PGiMAP and used during thesis

PGiMAP Panel					List of Lines used			
Accession code	IP no.	Alternate accession identifier	Origin/Source	Inferred subpop.	Full field trial	pilot year	leaf anatomy	Nottinghan
AP88	IP 10820	Acc 615	Sudan	E*	ICML-197189	IP-3175	IP-10964	GB-8735
AP84	IP 10964		Kenya	F	ICML-197217	IP-5438	IP-11346	E-14
AP81	IP 3098		India	D/E**	ICML-197222	IP-6060	IP-12116	PLS-05
AP90	IP 8949	P 3254; PL 73; Yoei	Togo	A/F	ICML-197287	IP-6460	IP-12395	SL-28

AP77	IP 13154	Maiwa local 2-1	Niger	E	ICML-197296	IP-6882	IP-13459	G-3a
AP76	IP 9407		Ghana	C	ID-132	IP-8166	IP-15872	
AP95	IP 20349		Yemen	B	ID-220	IP-8174	IP-17150	
AP92	IP 11229		Zimbabwe	A/B	ID-249	IP-8767	IP-21169	
AP74	IP 13370	Msungu-mukufi	Tanzania	B	ID-337	IP-8949	IP-3110	
AP83	IP 11353	CVP 298	Burkina Faso	F	IP-2058	IP-9446	IP-3122	
AP91	IP 8181	IP 338-1	ICRISAT-patencheru	C	IP-3098	IP-10811	IP-3389	
AP85	IP 18157	Souna	Mali	B	IP-3110	IP-11310	IP-4952	
AP89	IP 13964		Zimbabwe	E	IP-3122	IP-11763	IP-5695	
AP86	IP 4965	Serere 53	Uganda	E	IP-3125	IP-12925	IP-7922	
AP97	ICMB 90111-P6		ICRISAT-patencheru	C	IP-3175	IP-15857	IP-8426	
AP66	IP 17690		Togo	D	IP-3389	IP-16096	IP-8767	
AP70	IP 6101	P 936	Niger	B	IP-3564	IP-17099	IP-9301	
AP69	IP 10488		Zimbabwe	D	IP-3757	IP-17554	IP-9651	
AP71	IP 13149	P 932-1	Niger	F	IP-3865	IP-19584	Souna3	
AP72	IP 15533		Burkina Faso	F	IP-4927	IP-22420	Tif23DB	
AP68	IP 10140	P 5510; Chowuguile	Mali	E	IP-4952			
AP67	IP 3890		India	A/F	IP-4974			
AP64	IP 11677	100; Dukhun	Sudan	F	IP-5031			
AP65	IP 11984		Nigeria	E	IP-5131			
AP58	IP 3175	Chadi	India	B	IP-5272			

AP55	W 504-1-P1		India	B	IP-5438
AP57	IP 22455	ICMV-IS 89305	ICRISAT	D	IP-5695
AP46	IP 16096		India	E	IP-5713
AP49	IP 6060	P 175; Tein	Central African Republic	B	IP-5816
AP47	IP 7633	S 195	India	B/E	IP-5900
AP60	IP 19386		Namibia	B	IP-5923
AP42	IP 6112	P 949	Niger	A	IP-6037
AP33	IP 10811	Acc 604	Sudan	B	IP-6060
AP41	IP 3757		India	E	IP-6098
AP38	IP 18147		Pakistan	C	IP-6099
AP43	IP 19448		Namibia	B/D	IP-6103
AP37	ICMS 7703	ICMS 7703	ICRISAT-patencheru	B	IP-6417
AP35	IP 11577	P 6041; Yan nane	Burkina Faso	E	IP-6584
AP36	GB 8735	GB 8735	ICRISAT	A/E	IP-6682
AP44	ICML 22		Chad	F	IP-6882
AP45		Okashana 1 (ICMV 88908)	ICRISAT-Patancheru	D/E	IP-6891
AP31	IP 9446		Ghana	D	IP-6892
AP32	IP 21155	Tift 23DAS	USA	B	IP-7108
AP24	IP 11211	PSR 49-1	India	E/C	IP-7470
AP22	IP 6745		Malawi	F	IP-7536
AP21	IP 6769		Malawi	D	IP-7633
AP25	IP 10705	CMM 540; Haini	Mali	B	IP-7910
AP26	IP 22274	GICKV 93191 (ICMP 93191)	India	D	IP-7922

AP27	IP 22272	AIMP 92901	India	E	IP-7942
AP17	IP 18132		Pakistan	E/F	IP-7952
AP15		PRLT 2	ICRISAT-Patancheru	A	IP-7953
AP16	IP 4020		India	F	IP-8002
AP11	IP 13971		Zimbabwe	B	IP-8166
AP8	IP 8767		Botswana	B	IP-8172
AP9	IP 12298		Nigeria	B	IP-8174
AP10		863B-P2	ICRISAT-patencheru	D	IP-8181
AP4		ICTP 8203	ICRISAT-Patancheru	E	IP-8187
AP3	IP 4542		India	F	IP-8276
AP6	IP 17720		Togo	E	IP-8280
AP2		H 77/833-2-P5(NT)	ICRISAT-patencheru	B	IP-8294
AP1		843B	ICRISAT-patencheru	B	IP-8426
AP196	IP 6102	P 938	Niger	E	IP-8761
AP195	IP 3616	Periya	India	C	IP-8767
AP184	IP 18389		Namibia	D	IP-8786
AP194	IP 9824	Mexioera	Mozambique	E	IP-8863
AP204	IP 18293	P152		D	IP-8949
AP203	IP 22419	ICML 1; ICMPE 13-6-27	ICRISAT	D	IP-9242
AP155	IP 11765	Arnold 2141	South Africa	F	IP-9301
AP156	IP 6869	Acc 106	Kenya	D	IP-9347
AP159	IP 10085	P 5439;Tiotioni	Mali	A	IP-9351
AP160	IP 10394	IC 46963	India	C	IP-9446
AP172	IP 21517	Sadore local	Niger	B	IP-9496
AP164		ICMV-IS 92222	ICRISAT	F	IP-9651
AP161	IP 12839		Botswana	A	IP-9692

AP168	IP 3732		India	B	IP-9710
AP167	IP 8210	IP 1739 L-1	ICRISAT	B/E	IP-9840
AP158	IP 7108		India	A	IP-9854
AP157	IP 5272	D 258	Niger	A/D	IP-9969
AP166	IP 7910	D 89 C-1-1	Niger	C/D	IP-10085
AP169	IP 9391		Ghana	F	IP-10343
AP170	IP 3471	Podi cumbu	India	F	IP-10471
AP148	IP 3636	Mochai	India	E	IP-10539
AP135	IP 9710	PI 287043	Nigeria	A	IP-10701
AP137	IP 3122		India	B	IP-10705
AP136	IP 6037	P 152; Tein	Central African Republic	F/A	IP-10759
AP140	IP 5713	45-349	Nigeria	D	IP-10811
AP138	IP 6146	P 42; Mefie	Cameroon	F	IP-10820
AP142		ICMB 89111-P2	ICRISAT-patencheru	B/E	IP-10953
AP141	IP 10953	BM 8	Kenya	A	IP-10964
AP131	IP 6460	P 482	Mali	E	IP-11310
AP52		ICMV 221ICMV 88904	ICRISAT	E	IP-11346
AP130	IP 4979	700164	Nigeria	A	IP-11353
AP132	IP 9351		Ghana	B/C	IP-11358
AP133	IP 10539	CSM 51	Senegal	C	IP-11577
AP153		Tift 238D1-P158	USA	E/F	IP-11584
AP152	IP 11310	CVP 152	Burkina Faso	B/E	IP-11670
AP154	IP 15344		India	A	IP-11763

AP120	IP 12058		Nigeria	E/D	IP-11929
AP118	IP 19626	C 90-133; Zongo	Niger	E	IP-11984
AP108		Tift 186	USA,	F	IP-12128
AP126	IP 16403	Halale	Zimbabwe	F/E	IP-12298
AP128	IP 2058		Nigeria	B/C	IP-12322
AP99	IP 10486		Zimbabwe	A	IP-12364
AP125	IP 12845	Saouga local 2-1	Burkina Faso	F	IP-12395
AP104	IP 5695	45-327	Nigeria	D	IP-12840
AP101	IP 4962	Serere 50	Uganda	F	IP-12967
AP124	IP 15320		India	E	IP-13016
AP105	IP 12768	SM 3646	ICRISAT-patencheru (India)	C	IP-13154
AP114	IP 8280	Souna 57-1	ICRISAT	E	IP-13180
AP106	IP 6179	P 75; Midougen	Cameroon	E	IP-13324
AP100	IP 3557	Mathuravellai	India	D	IP-13344
AP116	IP 10271	EC 134725	Nigeria	B	IP-13459
AP109	IP 8761		Botswana	B	IP-13817
AP112	IP 9532		Ghana	B	IP-13964
AP110	IP 8955	P 3271; PL 80; Ignie	Togo	F	IP-13971
AP117	IP 12322	Gero	Nigeria	E	IP-14210
AP119	IP 3564	Umi	India	B	IP-14624
AP102	IP 8344		India	B/E	IP-15320
AP113	IP 8275	IP 1881-1	ICRISAT-patencheru	B/C	IP-15533
AP115	IP 10379	EC 134857	Nigeria	B	IP-15553
AP107	IP 7095		India	E	IP-15857
AP111	IP 9406		Ghana	F/E	IP-15872

AP79	IP 17554		Togo	D	IP-15917
AP75	IP 11311	CVP 159	Burkina Faso	E	IP-16096
AP258	IP 8166	GS 148	ICRISAT	D/F	IP-16120
AP246	IP 9969	1769	Zambia	E	IP-16289
AP245	IP 10543	CMM 374; Sanio	Mali	C	IP-16403
AP256	IP 7930	IP 5300-2; Maiwa local 1-2	ICRISAT	E	IP-17028
AP255	WSIL-P8		ICRISAT-patencheru	C/D	IP-17099
AP252	IP 18090		Pakistan	F	IP-17150
AP253	P 1449-2-P1			C	IP-17554
AP257	IP 4927	Souna D2	Senegal	B	IP-17611
AP247	IP 6882	Acc 124	Kenya	F	IP-17690
AP259	IP 5253	D 202	Niger	C	IP-18062
AP263	IP 18500		Namibia	D	IP-18168
AP262	IP 8863		Zambia	F	IP-18246
AP264	IP 11346	CVP 278	Burkina Faso	C	IP-18293
AP250	IP 8069	DS 279	India	F/E	IP-18500
AP238	IP 4828	Bareilly 10	India	F	IP-18621
AP242	IP 19584	C 90-90; Enele	Niger	F	IP-19334
AP240	IP 5207	D 110	Niger	B/E	IP-19361
AP239	IP 11275	CVP 9	Burkina Faso	E	IP-19386
AP241	SOSAT-C88		ICRISAT	C	IP-19388
AP243	IP 6417	P 424; Sanio barbu	Mali	E	IP-19612
AP234	IP 14439	Mouri	Cameroon	F	IP-19613

AP233	IP 9651	PI 286865	Nigeria	D	IP-19626
AP235	LGD 1-B-10			C	IP-21020
AP222	IP 5131	D 235; Zongo	Niger	D	IP-21142
AP227	IP 8187	IP 2695-1	ICRISAT	E	IP-21169
AP225	WC-C75		ICRISAT	D	IP-21206
AP224	81B-P6		ICRISAT-patencheru	C/E	IP-21517
AP228	IP 13927		Zimbabwe	A/C	IP-22274
AP223	IP 12967		Malawi	F	IP-22420
AP230	ICMP 451-P8		ICRISAT-Patancheru	A	IP-22423
AP231	ICMP 85410-P7		ICRISAT-Patancheru	A	IP-22424
AP229	IP 15872	P 15	Tanzania	A	IP-22455
AP208	IP 9971	1806	Zambia	F/A	IP-22494
AP211	IP 22420	ICML 2; ICMPE 13-6-30	ICRISAT	D	ISMI-21014
AP209	IP 8074	GS 8	ICRISAT	C	ISMI-21348
AP212	Tift 383		USA,	F/C	ISMI-21376
AP216	IP 10632	CMM 465; Haini beri	Mali	B/C/F	ISMI-21481
AP217	IP 13817	CVP 230	Burkina Faso	F	SOSAT-C88
AP205	IP 13180	No. 2-1	Nigeria	E	Souna3
AP213	IP 7953	IP 6191-1; P 87-1	ICRISAT	F	Tif23DB
AP215	IP 10701	CMM 536; Haini	Mali	D	
AP210	IP 21169	P 1449-3	ICRISAT	A/B/C/D/E/F	
AP218	IP 8129	GS 112	ICRISAT	E	
AP221	ICMP 451-P6		ICRISAT-Patancheru	A	
AP220	IP 11593	P 6062; Da M'Lare	Burkina Faso	D	

AP219	IP 10471		Zimbabwe	D
AP176	IP 7952	IP 6578-1; Kolala local 7-1	ICRISAT	D
AP192	IP 9282	P 3279; Ignari	Togo	B
AP198	IP 17611		Togo	A
AP185	IP 7886	J 1357-1	India	E
AP189		ICMV-IS 89305	ICRISAT	E
AP191		Raj 171 (ICMV 85404RBC-IC 9)	ICRISAT-Patancheru	C
AP188	IP 13384	Serere 2A-1	Uganda	C/E
AP202	IP 13344	Acc 736-1	Sudan	D
AP178	IP 16638		Zimbabwe	A
AP180	IP 8972	P 3369; PL 97; Olikon	Togo	F
AP200	IP 7967	IP 6342-1; P 337-2	ICRISAT	F
AP177	IP 5441	P 2731; Zongo	Niger	E
AP186	IP 16289		Zimbabwe	F
AP187	IP 6682		Malawi	B
AP175	IP 3138		India	B
AP182	IP 11584	P 6050; Sanio	Burkina Faso	E
AP201	IP 8172	GS 154	ICRISAT-patencheru	B
AP343	IP 11218		Zimbabwe	A
AP342	IP 18412		Namibia	D
AP346	IP 8174	GS 156	ICRISAT-Patancheru	A
AP345	IP 6110	P 946	Niger	A

AP332	IP 5438	P 2727; Guerguera	Niger	D
AP334	IP 11378	CVP 409	Burkina Faso	D
AP325	IP 13608	Kala	India	F
AP328	IP 8647	Dukhun	Sudan	A
AP327	IP 7364		Tanzania	E
AP336	IP 10759	Acc 509	Sudan	F
AP337	IP 15536		Burkina Faso	F
AP330	IP 6125	P 15	Cameroon	C
AP331	IP 14624		Cameroon	D
AP333	IP 12020	Dauro	Nigeria	F
AP324	IP 13290	CSM 27-1	Senegal	A/B
AP329	IP 11763	Arnold 2131	South Africa	B
AP322	IP 13520	Bhilodi	India	B
AP335	IP 14398		Cameroon	E
AP317	IP 12128		Nigeria	F/C
AP316	IP 14311		Cameroon	B
AP318	IP 15857		Tanzania	F
AP320	IP 12364		Nigeria	B
AP315	IP 18292	D2 WS Gl. yellow	ICRISAT-Patancheru	A/D
AP309	IP 13840		Burkina Faso	E
AP310	IP 5931	P 1538/Sl. 305; Souna	Senegal	C
AP311	IP 4378		India	F
AP304	IP 11929	Belenguine	Sierra Leone	D/C
AP299	IP 10945	Acc 816	Sudan	D
AP301	IP 7941	IP 5447-1; P 2737-1	ICRISAT	D

AP303	IP 17150		Zimbabwe	E
AP298	IP 13459	Pitta ganti	India	F
AP302	IP 8182	IP 406-B-1	ICRISAT	D/C
AP305	IP 14849		Cameroon	F
AP306	IP 5900	P 1505/Sl. 228; Souna	Senegal	D
AP308	IP 19334		Namibia	D
AP307	IP 3110		India	F
AP296	IP 7536	K 46	India	C/D
AP297	IP 12395		South Africa	D
AP295	IP 14418	Mouri	Cameroon	C
AP289	IP 17493		Togo	A
AP288	IP 6415	P 422; Souna	Mali	C
AP290	IP 16120		India	F
AP292	IP 5560	P 2857-1; Bakin hiri	Niger	D
AP291	IP 12138	Maiwa	Nigeria	C/D/F
AP294	IP 15512		Burkina Faso	E
AP280	IP 10579	CMM 410; Souna	Mali	E
AP269	IP 17099		Zimbabwe	B
AP281	IP 13324	Acc 9-1	Sudan	F
AP276	IP 19405	TCD 9; Arkoum	Chad	D
AP268	IP 17125		Zimbabwe	B/E
AP266	IP 5031	700482	Nigeria	D
AP267	IP 11358	CVP 311	Burkina Faso	B

AP275	IP 7660	S 395	India	C/D/F
AP273	IP 15553		Burkina Faso	E
AP271	IP 18168	Sounari	Mali	C/D
AP283	IP 13363		Tanzania	B
AP265	IP 6310	P 286	Mali	F
AP278	IP 20679	Maiwa	Nigeria	D
AP286	IP 10339	EC 134799	Nigeria	B
AP282	IP 3201		India	F
AP254	P 310-17-B		ICRISAT-patencheru	C
AP248	IP 14148		Zimbabwe	E
AP244	IP 4952	Serere 41	Uganda	A

Appendix 6: R Script used for spatial field correction and to generate BLUPs

```
##############################################

remotes::install_github("Biometris/statgenSTA", ref = "develop", dependencies = TRUE)

install.packages("statgenSTA")

StagenSTA ("Single trial analysis")

library(statgenSTA)

library(dplyr)

setwd("C:/Users/Dylan/Documents/spatbluptest")

Anatomics21 <- read.csv("togrwe.csv", sep=(","), header=T)

nrow(Anatomics21)

Anatomics21$rowId <- as.factor(Anatomics21$Variety_ID)

Anatomics21$colId <- as.factor(Anatomics21$Plot)

Anatomics21_ETM <- Anatomics21 %>% filter(Scenario!="STR")
```

```
Anatomics21_ETM <- na.omit(Anatomics21_ETM)

nrow(Anatomics21_ETM)

Anatomics21_STR <- Anatomics21 %>% filter(Scenario!="ETM")

Anatomics21_STR <- na.omit(Anatomics21_STR)

nrow(Anatomics21_STR)

############################                                    RCA_ETM
####################################

######################### spats_RCA

spats_Anatomics21_ETM_RCA <- Anatomics21_ETM

spats_Anatomics21_ETM_RCA <- spats_Anatomics21_ETM_RCA %>%
filter(XY!="20_8")

spats_Anatomics21_ETM_RCA <- spats_Anatomics21_ETM_RCA %>%
filter(XY!="15_16")

spats_Anatomics21_ETM_RCA <- spats_Anatomics21_ETM_RCA %>%
filter(XY!="29_16")

nrow(spats_Anatomics21_ETM_RCA)

imaging_count <- spats_Anatomics21_ETM_RCA %>%

 group_by(Variety_ID) %>%

 summarise(nb = n())

spats_Anatomics21_ETM_RCA_clean <- spats_Anatomics21_ETM_RCA %>%
group_by(Variety_ID) %>% filter(n() > 1)

nrow(spats_Anatomics21_ETM_RCA_clean)

imaging_count_1 <- spats_Anatomics21_ETM_RCA_clean %>%

 group_by(Variety_ID) %>%

 summarise(nb = n())
```

```
spats_TD_Ana21_RCA <- createTD(data = spats_Anatomics21_ETM_RCA_clean,
                        genotype = "Variety_ID",
                        rowCoord = "Variety_ID",
                        colCoord = "Plot",
                        rowId = "rowId",
                        colId = "colId",
                        subBlock = "Bloc",
                        repId = "Rep",
                        plotId = "Plot")
spaMod_RCA <- fitTD(TD = spats_TD_Ana21_RCA,
              design = "res.ibd",
              traits = "Tot_Grain_Weight_raw",
              what = "random")
summary(spaMod_RCA)
## Create spatial plots of the results.
plot(spaMod_RCA, plotType = "spatial", spaTrend = ("percentage"))
## Detect outliers in the standardized residuals of the fitted model.
spats_outliers <- outlierSTA(STA = spaMod_RCA, traits = “RCA”, what = "random")

## Extract all available statistics from the fitted model.
spats_extr <- extractSTA(spaMod_RCA, what = "heritability")
spats_extr
#extr_lme4 <- extractSTA(spaMod, what=c("sMEANs"),  restoreColNames = TRUE,
keep=c("repId","plotId","subBlock","rowCoord","colCoord"))
spats_TDGxE <- STAtoTD(STA = spaMod_RCA, what = c("BLUPs", "seBLUPs"))
```

```
spats_TDGxE

spats_TDGxE_Var <- extractSTA(STA = spaMod_RCA, what = "varGen")

spats_TDGxE_Var

spats_TDGxE_Var <- extractSTA(STA = spaMod_RCA, what = "varErr")

spats_TDGxE_Var

### Genotype fixed

spats_Anatomics21_ETM_RCA_cleanf <- spats_Anatomics21_ETM_RCA_clean
%>% filter(XY!="34_10")

spats_TD_Ana21_RCAf <- createTD(data = spats_Anatomics21_ETM_RCA_cleanf,

                        genotype = "Variety_ID",

                        rowCoord = "Line",

                        colCoord = "Position",

                        rowId = "rowId",

                        colId = "colId",

                        subBlock = "BLOC",

                        repId = "Rep",

                        plotId = "Plot")

spaMod_RCAf <- fitTD(TD = spats_TD_Ana21_RCAf,

                design = "res.ibd",

                traits = “RCA”,

                what = "fixed")

spats_outliers <- outlierSTA(STA = spaMod_RCAf, traits = “RCA”, what = "fixed")

spats_TDGxEf <- STAtoTD(STA = spaMod_RCAf, what = c("BLUEs", "seBLUEs"))

spats_TDGxEf
```

```
########################                                    RCA_STR
###################################

######################## spats_RCA

spats_Anatomics21_STR_RCA <- Anatomics21_STR

spats_Anatomics21_STR_RCA <- spats_Anatomics21_STR_RCA %>% filter(XY!="10_16")

nrow(spats_Anatomics21_STR_RCA)

imaging_count <- spats_Anatomics21_STR_RCA %>%

 group_by(Variety_ID) %>%

 summarise(nb = n())

spats_Anatomics21_STR_RCA_clean <- spats_Anatomics21_STR_RCA %>% group_by(Variety_ID) %>% filter(n() > 1)

nrow(spats_Anatomics21_STR_RCA_clean)

imaging_count_1 <- spats_Anatomics21_STR_RCA_clean %>%

 group_by(Variety_ID) %>%

 summarise(nb = n())

spats_TD_Ana21_RCA <- createTD(data = spats_Anatomics21_STR_RCA_clean,

                    genotype = "Variety_ID",

                    rowCoord = "Line",

                    colCoord = "Position",

                    rowId = "rowId",

                    colId = "colId",

                    subBlock = "BLOC",

                    repId = "Rep",

                    plotId = "Plot")

spaMod_RCA <- fitTD(TD = spats_TD_Ana21_RCA,
```

```
            design = "res.ibd",
            traits = “RCA”,
            what = "random")
summary(spaMod_RCA)
## Create spatial plots of the results.
plot(spaMod_RCA, plotType = "spatial", spaTrend = ("percentage"))
## Detect outliers in the standardized residuals of the fitted model.
spats_outliers <- outlierSTA(STA = spaMod_RCA, traits = “RCA”, what = "random")
## Extract all available statistics from the fitted model.
spats_extr <- extractSTA(spaMod_RCA, what = "heritability")
spats_extr
#extr_lme4 <- extractSTA(spaMod, what=c("sMEANs"),  restoreColNames = TRUE,
keep=c("repId","plotId","subBlock","rowCoord","colCoord"))
spats_TDGxE <- STAtoTD(STA = spaMod_RCA, what = c("BLUPs", "seBLUPs"))
spats_TDGxE
spats_TDGxE_Var <- extractSTA(STA = spaMod_RCA, what = "varGen")
spats_TDGxE_Var
spats_TDGxE_Var <- extractSTA(STA = spaMod_RCA, what = "varErr")
spats_TDGxE_Var


# Genotype fixed
spats_Anatomics21_STR_RCA_cleanf <- spats_Anatomics21_STR_RCA_clean %>%
filter(XY!="16_14")
```

```
spats_Anatomics21_STR_RCA_cleanf <- spats_Anatomics21_STR_RCA_cleanf %>%
filter(XY!="23_14")

spats_Anatomics21_STR_RCA_cleanf <- spats_Anatomics21_STR_RCA_cleanf %>%
filter(XY!="40_9")

spats_TD_Ana21_RCAf <- createTD(data = spats_Anatomics21_STR_RCA_cleanf,

                    genotype = "Variety_ID",

                    rowCoord = "Line",

                    colCoord = "Position",

                    rowId = "rowId",

                    colId = "colId",

                    subBlock = "BLOC",

                    repId = "Rep",

                    plotId = "Plot")


spaMod_RCAfs <- fitTD(TD = spats_TD_Ana21_RCAf,

                  design = "res.ibd",

                  traits = “RCA”,

                  what = "fixed")


spats_outliers <- outlierSTA(STA = spaMod_RCAfs, traits = “RCA”, what = "fixed")

spats_TDGxEf <- STAtoTD(STA = spaMod_RCAfs, what = c("BLUEs", "seBLUEs"))

spats_TDGxEf
```

Appendix 7: R Script used for GWAS

```
# FarmCPU - iteraltively uses fixed and random effect models for powerful and efficient genome-wide association studies (GWAS)

## Launching libraries and functions

source("http://zzlab.net/GAPIT/GAPIT.library.R")

source("http://zzlab.net/GAPIT/gapit_functions.txt")

source("gapit_functions.txt")

library(data.table)

#install.packages("devtools")

#install.packages("cli")

#devtools::install_github("YaoZhou89/BLINK")

library(BLINK)

## NOTE 1: It is important that each taxa name is spelled, punctuated, and capitalized (R is case sensitive) the same way in each of the input data sets. If this is not done, they will be excluded from the analysis. Additionally, the taxa names must not be numeric.

## NOTE 2 : The SNPs in the “myGD” and “myGM” files NEED to be in the same order.

## NOTE 3 : Missing data should be indicated by either “NaN” or “NA”.

## Prelim Analysis I : If genotype (SNP) data is not in numeric format, then run GAPIT to generate

setwd("/Users/Dylan/Documents/UoN/Pearl_Millet_GWAS")

myG <- read.table("PMHMP.txt", head = FALSE)

myY <- read.csv("Total_MX_Area_Plasticity.csv", head = TRUE, sep = ",")

#Step 2: Run GAPIT

myGAPIT <- GAPIT( Y=myY,

          G=myG,
```

```
PCA.total=2,

#SNP.MAF = 0.05,

Multiple_analysis=TRUE,

model=c("FarmCPU")
```

Appendix 8: Agronomic, physiological, and architectural measurements used in field trials

Meta_trait	Trait	Description
Agro	Biom1	shoot biomass measured at 42 days after sowing
Agro	Biom2	shoot biomass measured at maturity
Agro	Hauteur	Height until last leaf
Agro	Hauteur_tot	Height until panicle apex
Agro	Nb_tige	Number of tillers
Agro	Nb_tot_épis	Number of panicles
Flo	DSF	Days to 50% flowering
Flo	DSM	Days to maturity
Roots	StemDia	Stem diameter measured with ObjectJ
Roots	RootDia	Root diameter measured with ObjectJ
Roots	Angle	Angle (front view) measured with ObjectJ
Roots	Excised_Length	Length of the excised root measured with ObjectJ
Roots	NumBranch	Number of branches (lateral) on the excised root measured with ObjectJ
Roots	AngleP	Angle (side view) measued with ObjectJ
Roots	Root_density	Root density on the excised root (NumBranch/Excised_Length)

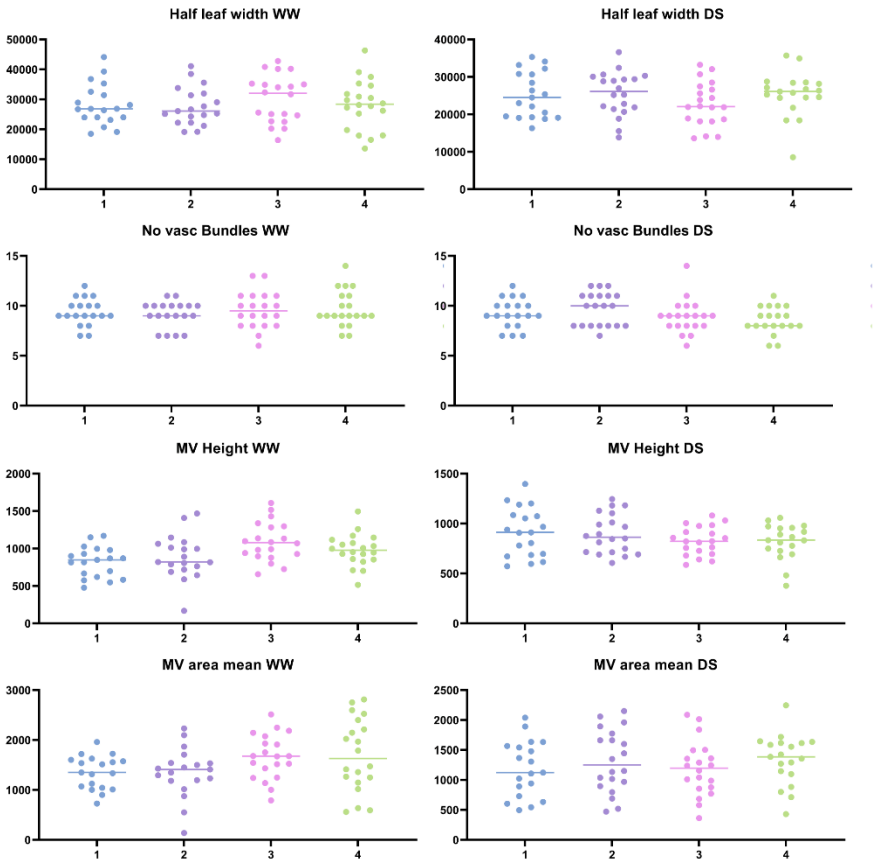
Appendix 9: Leaf anatomical trait measurements

Label	Imaging Region	Measurement Description
HL_MVB_Median_Distance	Half Leaf	median distance between major vascular bundles
HL_MVB_Number	Half Leaf	Number of major vascular bundles
HL_Width	Half Leaf	Width of leaf from Midpoint to tip

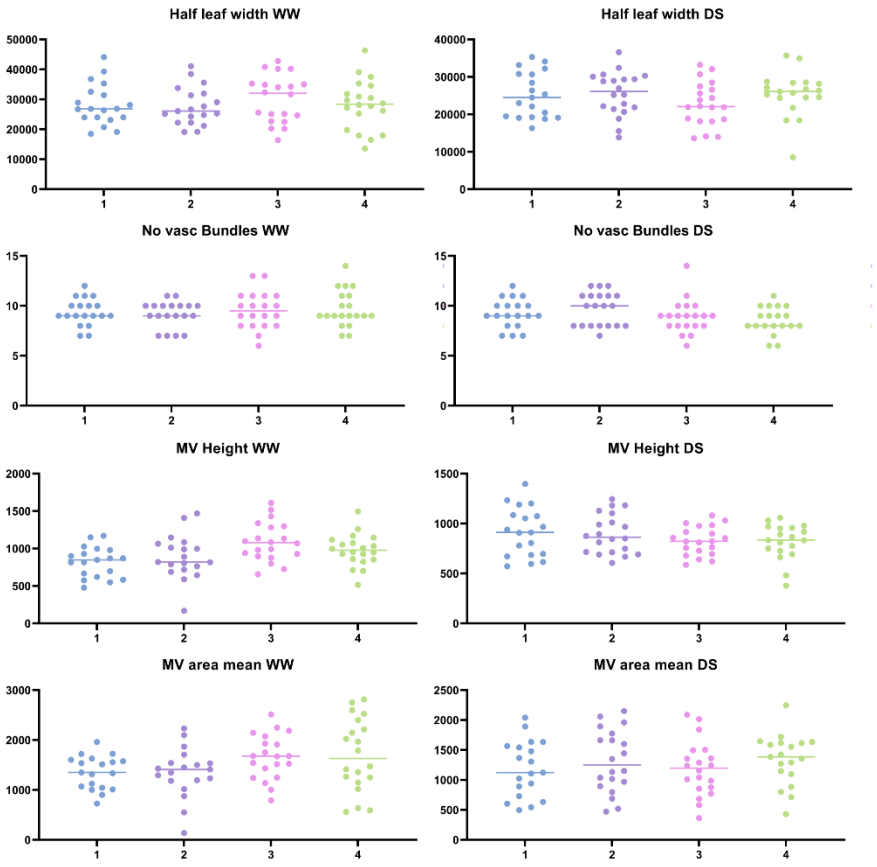
La_MVB_Circle_area	Lamina	area of ellipse fitted to major vascular bundle
La_MVB_Circle_Diameter	Lamina	Max Diameter of ellipse fitted to major vascular bundle
La_MVB_Leaf_Thickness	Lamina	Thickness of leaf at major vascular bundle
La_MVB_LMX_Area	Lamina	Max diameter of single Late/Large meta-xylem in major vascular bundle
La_MVB_LMX_Max_Diameter	Lamina	Area of single Late/Large meta-xylem in major vascular bundle
La_SVB_Abaxial_Epidermis_Thickness	Lamina	thickness of abaxial epidermis at position of bulliform/small vascular bundle
La_SVB_Bulliform_Thickness	Lamina	thickness of bulliform at position of bulliform/small vascular bundle
La_SVB_Leaf_Thickness	Lamina	total leaf thickness at position of bulliform/small vascular bundle
La_SVB_Mesophyll_Thickness	Lamina	thickness of mesophyll at position of bulliform/small vascular bundle
La_VB_Count	Lamina	Number of all types of vascular bundle in image
La_VB_Median_Distance	Lamina	Median distance between all types of vascular bundle in image
La_VB_Sum_Distance	Lamina	Sum of distance between all types of vascular bundle in image
MR_MVB_LMX_Median_area	Midrib	Median area of Late/Large meta-xylem in major vascular bundles
MR_MVB_LMX_Number	Midrib	Number of Late/Large meta-xylem in major vascular bundles
MR_MVB_LMX_Sum_area	Midrib	Sum Area of Late/Large meta-xylem in major vascular bundles
MR_Thickness	Midrib	Maximum thickness of adaxial-abaxial surface
St_Abaxial_File_Count	Stomata	Number of Abaxial stomatal files in image
St_Abaxial_File_Mean_Distance	Stomata	Mean distance between abaxial stomatal files
St_Abaxial_File_Sum_Distance	Stomata	Sum distance between abaxial stomatal files
St_Adaxial_File_Count	Stomata	Number of Adaxial stomatal files in image
St_Adaxial_File_Mean_Distance	Stomata	Mean distance between adaxial stomatal files
St_Adaxial_File_Sum_Distance	Stomata	Sum distance between adaxial stomatal files

Appendix 10: Leaf anatomical trait block effect visualization

2021


Half leaf width WW
Half leaf width DS
No vasc Bundles WW
No vasc Bundles DS
MV Height WW
MV Height DS
MV area mean WW
MV area mean DS

2022


Half leaf width WW
Half leaf width DS
No vasc Bundles WW
No vasc Bundles DS
MV Height WW
MV Height DS
MV area mean WW
MV area mean DS